Diss. ETH NO. 26497

Lipid Nanoparticles as MRI Contrast Agents for the Detection of Atherosclerotic Plaques

A thesis submitted to attain the degree of

DOCTOR OF SCIENCES of ETH Zurich

(Dr. sc. ETH Zurich)

presented by

Alessandro Fracassi

M. Sc., Sapienza University of Rome

born on 19.04.1988
citizen of Italy

accepted on the recommendation of

Prof. Dr. Yoko Yamakoshi, examiner
Prof. Dr. Jean-Christophe Leroux, co-examiner
Prof. Dr. Peter Johann Walde, co-examiner

2020

Acknowledgements

I would like to express my gratitude to Prof. Dr. Yoko Yamakoshi for providing me the opportunity to work and study in the stimulating academic environment offered in her group at ETH. The interdisciplinary nature of the projects in which I was involved strongly influenced my scientific and personal development. I really thank you for the generous support, motivation and trust during and beyond this work.

I thank Prof. Dr. Jean-Christophe Leroux and Prof. Dr. Peter Johann Walde for being co-examiners of my dissertation and for their interest in my project.

Many thanks to Prof. Dr. Bode for his constant support throughout all the PhD, for all the fruitful discussion and the time he has spent for me.

I am grateful to Prof. Dr. Rong Zhou for our collaboration, and for giving me the opportunity to work in her laboratory at University of Pennsylvania.

I would like to thank all the collaborators that made this work possible, Dr. Corey Archer (ETH Zurich), Mr. Jianbo Cao (University of Pennsylvania), Dr. Hisao Masai and Dr. Naoko Yoshizawa-Sugata (Tokyo Metropolitan Institute of Medical Science), Prof. Dr. Éva Jakab Tóth (University of Orléans), Dr. Stephan Handschin (ScopeM, ETH Zurich), Prof. Dr. Jean-Pascal Bourgeois (University of Applied Sciences and Arts Western Switzerland), Mr. Olivier Gröninger and Prof. Dr. Wendelin Stark (ETH Zurich).

I would like to acknowledge Mr. Mario Kessinger for his administrative assistance and for his daily “Buongiorno Signor Fracassi”.

It is difficult to find the right words to thank properly all the past and present members of the Yamakoshi group. Rakesh, Safwan, Rita, Oriana, Masa, Elisha, Olesya, Tamas, Ankita, Korinne, Gabriele, Hanna, I thank them for all the moments we shared, I am grateful for our friendships. I wish them all the best and a great future.

I wish to extend my special thanks to all the members of the Bode group for the nice time spent together, and for all the insights that helped me during this work. In particular, I would like to thank Dr. Vijay Pattabiraman for all the precious advices and the support; Yi-Chung for the countless discussion and for the proofreading of this thesis; Raphael, Iain, Dino, Alberto and Samuele for all the help and moral support; Dominik, Matthias and Kevin for the good collaborations, and Ice and Moritz for the nice atmosphere of our lab.

I am grateful for the support of the NMR and MS service. In particular, I thank Dr. Bertran Rubi for his patience and the advices, and Mr. Daniel Wirz for his help.

I thank all the staff of the HCI shop for all the support and the professional assistance. I thank Carmela for all the nice words and enthusiasm.

Many thanks to all the friends who supported me during my PhD thesis. There is no need to say your name, that's the best part of being friends. Thank you for being part of my life.

I would like to thank my family members for being with me during these five years in Zurich. I am grateful to the distance that brought me much closer to all of them.

I thank all the people that with their curiosity and kindness make the human condition joyful and worth living.

List of Publications and Presentations

Additional manuscripts are currently under preparation.

Portions of this dissertation are reproduced with the permission from:

1. Oriana, S.[†]; **Fracassi, A.**[†]; Archer, C.; Yamakoshi, Y., Covalent Surface Modification of Lipid Nanoparticles by Rapid Potassium Acyltrifluoroborate Amide Ligation. *Langmuir* **2018**, *34* (44), 13244-13251 († equal contribution).
2. Royappa, A. R.; Ayer, M.; **Fracassi, A.**; Ebert, M. O.; Aroua, S.; Yamakoshi, Y., Conformationally Selective Synthesis of Mononitrocalix[4]arene in Cone or Partial Cone. *Helv. Chim. Acta* **2017**, *100*, *5*.
3. Giansanti, L.; Bozzuto, G.; **Fracassi, A.**; Bombelli, C.; Stringaro, A.; Molinari, A.; Piozzi, A.; Sennato, S.; Mancini, G., Effect of preparation protocol on physicochemical features and biointeractions of pegylated liposomes. *Colloids and Surfaces A* **2017**, *532*, 444–450.
4. Mauceri, A.; **Fracassi, A.**; D'Abramo, M.; Borocci, S.; Giansanti, L.; Piozzi, A.; Galantini, L.; Martino, A., D'Aiuto, V.; Mancini, G., Role of the hydrophilic spacer of glucosylated amphiphiles included inliposome formulations in the recognition of Concanavalin A. *Colloids and Surfaces B: Biointerfaces* **2015**, *136*, 232-239.

Oral Presentations

- "Preparation of Synthetic Low Density Lipoprotein (sLDL) with an On-Surface Chemoselective Ligation", Nanomediciene Rome, Italy, **2018**.

Poster Presentations

- "Efficient Nanoparticles Surface Fabrication by a Chemoselective Ligation", International Symposium on Macrocyclic and Supramolecular Chemistry (ISMSC) in conjunction with ISACS: Challenges in Organic Materials and Supramolecular Chemistry, Cambridge, UK, **2017**.
- "On-Particle Chemical Functionalization of Synthetic Low-Density Lipoprotein (sLDL)" Scholarship Fund of the Swiss Chemical Industry (SSCI), Zurich, Switzerland, **2017**.
- "Synthetic Low-Density Lipoprotein (sLDL) for *in vivo* Imaging" Nanomedicine Viterbo, Italy, **2016**.

Table of Contents

List of Common Terms or Abbreviations

Å	angstrom 1 Å = 10^{-10} m
AFM	atomic force microscopy
Ala	alanine
apoB100	apolipoprotein B100
Arg	arginine
ATR	attenuated total reflection
$B(OMe)_3$	trimethyl borate
BHT	butylated hydroxytoluene
Boc	tert-butyloxycarbonyl
°C	Celsius
CA	contrast agent
calcd	calculated
$CDCl_3$	deuterated chloroform
CO	cholesteryl oleate
Cys	cysteine
CVD	cardiovascular diseases
d	doublet (NMR)
DIPEA	N,N-diisopropylethylamine
DLS	dynamic light scattering
DMAP	4-dimethylaminopyridine
DMF	dimethylformamide
DMSO	dimethyl sulfoxide
DO3A	1,4,7,10-tetraazacyclododecane-1,4,7-triacetate
DTPA	diethylenetriaminepentaacetic acid
equiv	equivalent
ESI	electrospray ionisation
Et	ethyl
Et_2O	diethyl ether
Et_3N	triethylamine
Fmoc	fluorenylmethyloxycarbonyl
Gd	gadolinium
Gly	glycine

h	hour(s)
HA	hydroxylamine
HATU	(1-[Bis(dimethylamino)methylene]-1H-1,2,3-triazolo[4,5-b]-Pyridinium 3-oxid hexafluorophosphate
HCCA	alpha-cyano-4-hydroxycinnamic acid
HCTU	O-(6-chlorobenzotriazol-1-yl)-N,N,N’,N’-tetramethyluronium hexafluorophosphate
HDL	high-density lipoprotein
HPLC	high-performance liquid chromatography
HRMS	high resolution mass spectrometry
Hz	Herz
IR	infrared
J	Coupling constant (NMR)
KAT	potassium acyltrifluoroborate
LC	liquid chromatography
LC-MS	liquid chromatography-mass spectrometry
LDL	low-density lipoprotein
LNP	lipid nanoparticles
Leu	leucine
Lys	lysine
M	molarity
m	multiplet (NMR)
m/z	mass to charge ratio
MALDI	matrix-assisted laser desorption/ionization
Me	methyl
CH_3CN	acetonitrile
MeOH	methanol
min	minute(s)
MRI	magnetic resonance imaging
MRI-CA	magnetic resonance imaging contrast agent
MS	mass spectrometry
Mw	molecular weight
MWCO	molecular weight cut-off
NaOPh	sodium phenoxide

n-BuLi	n-butyllithium
NHS	N-hydroxysuccinimide
nm	nanometer
NMM	4-methylmorpholine
NMR	nuclear magnetic resonance
OA	oleic acid
OBz	O-benzoyl
Pbf	2,2,4,6,7-pentamethyldihydrobenzofuran-5-sulfonyl
PC	phosphatidylcholine
PEG	polyethylene glycol
Pro	proline
PTFE	polytetrafluoroethylene
q	quartet (NMR)
quin	quintet (NMR)
rt	room temperature
s	singlet (NMR)
sLDL	synthetic low-density lipoprotein
SPSS	solid-phase peptide synthesis
t	triplet (NMR)
TEM	transmission electron microscopy
TFA	trifluoroacetic acid
THF	tetrahydrofuran
TIPS	triisopropylsilane
TLC	thin-layer chromatography
TO	triolein
TOF	time of flight
Tris	tris(hydroxymethyl)aminomethane
Tris.HCl	tris(hydroxymethyl)aminomethane hydrochloride
Trt	trityl
UV-vis	ultraviolet-visible light
Val	valine
VLDL	very low-density lipoprotein
δ	chemical shift (ppm)
μ	micro (10^{-6})

Abstract

Low-density lipoprotein (LDL) has been widely recognized as a useful natural system for the delivery of drugs and imaging probes in cancer and other inflammatory diseases. In particular, natural LDL has been successfully employed as a carrier for magnetic resonance imaging contrast agents (MRI-CA) for the *in vivo* detection of atheroplaques. However, the progress in the use of natural LDL has been hampered by the necessity of isolation from fresh blood plasma of donors, and by the laborious drug loading process often involve, which limits the therapeutic applications of LDL and their use in clinic. The development of completely synthetic LDL (sLDL) may be able to overcome these problems.

The sLDL can be constituted by lipid nanoparticles (LNPs). LNPs have attracted significant attention as biocompatible delivery vehicles of both diagnostic and therapeutic agents. A major challenge in the preparation of sLDL from LNPs is the development of chemical reactions that can efficiently attachment biomolecules and imaging probes onto the LNPs surface, by stable covalent bond formation. This thesis presents the preparation of LNP-based natural LDL mimetic nanoparticles, achieved by efficient covalent functionalization of the LNPs surface with an apolipoprotein-mimetic peptide and imaging probes (MRI-CA and optical probes). The surface functionalization method relies on the use of a chemoselective amide-forming ligation reaction, namely potassium acyltrifluoroborate (KAT) ligation.

As a meterial for LNPs preparation, a KAT derivative of oleic acid (OA-KAT) was synthesized and added to a mixture of three lipid components (phosphatidylcholine, triolein, cholesteryl oleate). The mixture of lipids was sonicated and extruded in Tris-HCl buffer (pH 8.0), to provide LNPs equipped with KAT functional group (**LNP-KAT**). The obtained **LNP-KAT** particle was characterized by DLS and cryo-TEM, indicating a uniform dispersion with an average diameter of ca. 50 nm. For the preliminary test on the efficiency of the ligation reaction on particles surface, **LNP-KAT** with different amounts of OA-KAT (0, 2.5, 5, 10 mol%) were prepared and subjected to KAT ligation with a hydroxylamine derivative of fluorescein (HA-fluorescein) in phosphate buffer (pH 5.8) at room temperature. The UV-vis and fluorescence spectra of the obtained particles clearly indicated that fluorescein was stably attached onto the nanoparticles surface dependently on the amount of OA-KAT incorporated in the **LNP-KAT**. The quantification of boron (determined by inductively coupled plasma mass spectrometry) and fluorescein (determined by fluorescence)

in the particles, before and after KAT ligation, indicated that the **LNP-KAT** surface functionalization proceeded efficiently in a yield of 40-50%.

Subsequently, the KAT ligation of **LNP-KAT** nanoparticle and HA derivatives was used in the preparation of LDL-mimetic nanoparticles bearing an apolipoprotein-mimetic peptide and imaging probes (a Gd-chelate MRI-CA and optical probes), aiming the selective detection of atheroplaques. Hydroxylamine derivatives of apoB100-mimetic peptide, Gd(DO3A) and fluorescein were synthesized and used in the KAT ligation with **LNP-KAT**. As assessed by MALDI-MS (to detect the ligation products) and ICP-MS (to determine the Gd^{3+} amount) analyses, sLDL carrying both an apolipoprotein-mimetic peptide moiety and a Gd-chelate (**sLDL-Gd**) was prepared efficiently by KAT ligation. The conjugation of the Gd(DO3A) derivative onto the **LNP-KAT** nanoparticles provided **sLDL-Gd** with high payload, providing a relaxivity (r_1 = 22.0 $s^{-1}mM^{-1}$ per Gd^{3+}, at 1.5 T, 25 °C) much higher than the small molecules MRI-CA (ProHance, r_1 = 4.0 $s^{-1}mM^{-1}$ per Gd^{3+}, at 1.5 T, 25 °C).

The obtained **sLDL-Gd** nanoparticles were preliminary tested *in vitro* using monocyte and macrophage derived cell lines, and subsequently *in vivo* on an atherosclerosis mouse model (*apoE*$^{-/-}$). A **sLDL-Gd** dispersion was injected intravenously in *apoE*$^{-/-}$ mice, and MR images of the aortic arch were acquired pre- and post-injection. The images obtained indicated a clear contrast enhancement of the left common carotid artery wall, observed 48 h post-injection of **sLDL-Gd**. Aorta segments containing atheroma were finally dissected and subjected to ICP-MS analysis, revealing the accumulation of significant amount of Gd^{3+} in the targeted atheroplaques.

The use of KAT ligation was further investigated for the surface functionalization of self-assembled monolayers (SAMs) on gold surfaces. A dialkyl thioether molecule, bearing a terminal KAT group, was synthesized and used for the preparation of SAM on gold. Subsequently, the obtained SAMs were subjected to surface KAT ligation with a water soluble hydroxylamine derivative of PEG12 (HA-PEG) in phosphate buffer (pH 5.5). The SAM on gold before and after the ligation was characterized by XPS, contact angle, and ellipsometry, clearly confirming the covalent modification of the surface. The reaction process of KAT ligation for the modification of SAMs was also evaluated by quartz crystal microbalance (QCM), indicating the modification of SAMs at very low concentration. The results suggested that KAT ligation can be potentially used for the modification of surfaces with biomolecules such as proteins and nucleic acids, which often require the use of very low concentrations of reagents.

Sommario

Le lipoproteine a bassa densità (LDL) sono ampiamente riconosciute come un utile sistema naturale per la somministrazione selettiva di farmaci nei casi di cancro e di altre malattie infiammatorie. In particolare, le LDL naturali sono state impiegate con successo come vettori di agenti di contrasto nell' *imaging* a risonanza magnetica (MRI-CA) per il rilevamento di placche ateromasiche *in vivo*. Tuttavia, i progressi nell'uso delle LDL naturali sono stati ostacolati sia dalla necessità di isolare le LDL dal plasma di donatori che dai complicati processi di funzionalizzazione, che ne limitano le applicazioni terapeutiche sfavorendone l'utilizzo in *trial* clinici. Lo sviluppo di nanoparticelle di origine interamente sintetica può aiutare a superare queste problematiche.

Un buon materiale di partenza per la preparazione di nanoparticelle sintetiche in grado di imitare l'azione delle LDL (sLDL) è costituito da nanoparticelle lipidiche (LNPs), le quali hanno attirato molta attenzione per il loro possibile utilizzo come veicoli biocompatibili per la somministrazione di agenti diagnostici e terapeutici. Una delle maggiori difficoltà nell'uso di LNPs per la preparazione di sLDL è lo sviluppo di reazioni chimiche che possano essere utilizzate per la coniugazione di biomolecole sulla superficie delle LNPs, mediante formazione di un legame covalente stabile. In questa tesi viene presentata la preparazione di LNPs mimetiche delle LDL naturali, ottenute mediante funzionalizzazione covalente della superficie di LNPs con un peptide che mima l'azione di un'apolipoproteina e di sonde di *imaging* (MRI-CA e sonde ottiche). Il metodo di funzionalizzazione della superficie si basa sull'uso di una reazione di legatura che conduce chemoselettivamente alla formazione di un'ammide, la legatura di potassio aciltrifluoroborato (KAT).

Come substrato per la preparazione di LNP, un derivato KAT dell'acido oleico (OA-KAT) è stato sintetizzato e aggiunto a una miscela di tre componenti lipidici (fosfatidilcolina, trioleina, colesterolo oleato). La miscela di lipidi è stata sonicata ed estrusa in tampone Tris-HCl (pH 8.0), per fornire LNPs dotate di KAT (**LNP-KAT**). Le **LNP-KAT** così ottenute sono state caratterizzate con DLS e crio-TEM, indicando la formazione di una dispersione uniforme, con un diametro medio di ca. 50 nm. Per testare l'efficienza della funzionalizzazione delle particelle, **LNP-KAT** con diverse quantità di OA-KAT **1** (0, 2,5, 5, 10 mol%) sono state preparate e sottoposte a legatura KAT con un derivato idrossilaminico della fluoresceina (HA-fluoresceina) in tampone fosfato (pH 5.8) a temperatura ambiente. I risultati delle misurazioni ad UV-vis e a fluorescenza hanno indicato chiaramente che la fluoresceina era legata stabilmente sulla superficie delle nanoparticelle in modo dipendente

dalla quantità di OA-KAT incorporata nel **LNP-KAT**. La quantificazione del boro (determinata mediante spettrometria di massa a plasma accoppiato induttivamente) e la fluoresceina (determinata da spettroscopia di fluorescenza) nelle particelle, prima e dopo la legatura KAT, hanno indicato che la funzionalizzazione della superficie **LNP-KAT** é proceduta in modo efficiente, con una resa del 40-50%.

Successivamente, la legatura KAT tra nanoparticelle **LNP-KAT** e derivati HA è stata utilizzata nella preparazione di nanoparticelle mimetiche delle LDL, funzionalizzate con un peptide apolipoproteico e sonde di imaging (MRI-CA e sonde ottiche), mirando alla rilevazione selettiva di atheroplacche. Derivati di idrossilammina di un peptide mimetico della proteina apoB100, di Gd(DO3A) e fluoresceina sono stati sintetizzati e usati come miscela nella legatura KAT con **LNP-KAT**. La reazione è proceduta in modo efficiente, come valutato dalle analisi MALDI-MS (per l'identificazione dei prodotti di reazione) e ICP-MS (per la determinazione di Gd^{3+}), fornendo sLDL recanti sia un complesso di Gd che un gruppo peptidico mimetico della proteina apoB100 (**sLDL-Gd**). La coniugazione del derivato Gd(DO3A) sulle LNP-KAT ha prodotto sLDL-Gd con una relassività (r_1 = 22,0 $s^{-1}mM^{-1}$ per Gd^{3+}, a 1,5 T, 25 °C) molto più elevata degli MRI-CA a basso peso molecolare (ProHance, r_1 = 4.0 $s^{-1}mM^{-1}$ per Gd^{3+}, a 1,5 T, 25 °C).

L'uso della legatura KAT è stato ulteriormente studiato per la funzionalizzazione di superfici di monostrati auto-assemblati (SAMs) su superfici di oro. Una molecola di dialchil tioetere, recante un gruppo KAT terminale, è stata sintetizzata e utilizzata per la preparazione di SAMs su oro. Successivamente, i SAMs ottenuti sono stati sottoposti a legatura KAT superficiale con un derivato idrossilammina solubile in acqua di PEG12 (HA-PEG) in tampone fosfato (pH 5.5). I SAMs su oro così ottenuti sono stati caratterizzati con XPS, angolo di contatto ed ellipsometria prima e dopo la legatura KAT, confermando chiaramente l'avvenuta modifica covalente della superficie. Il processo di reazione della legatura KAT per la modifica dei SAMs è stato studiato anche mediante microbilancia a cristallo di quarzo (QCM), indicando che la modifica covalente dei SAMs può avvenire in condizioni di diluzione elevate. I risultati hanno suggerito che la legatura KAT può essere utilizzata per la modifica di superfici con biomolecole come proteine e acidi nucleici, che spesso richiedono l'uso di concentrazioni molto basse di reagenti.

Chapter 1

Background and Introduction

1. Background and Introduction

1.1 Atherosclerosis

Cardiovascular diseases (CVD) are the leading cause of death worldwide.[1] One of the major causes of cardiovascular disorders involves atherosclerosis, an inflammatory disease of the arteries, characterized by the deposition of fatty material on their inner wall.[2] Although the etiology of atherosclerosis is complex, recently developed investigation tools, including genetically modified mouse models of atherosclerosis, enabled a clearer elucidation of the pathway that leads to the development of atherosclerotic plaques. The onset of arterial lesions can be observed in the aorta already in the first decade of life by the generation of fatty streaks, that also appear in other arteries such as the coronary arteries and cerebral arteries during the second and third decade, respectively.[2] The development of fatty streaks is reversible and thus is not a clinically significant process, but it can set the condition for the progression to atherosclerosis. Figure 1 represent the progression of atherosclerosis. The formation of an atherosclerotic plaque comprises (1) the accumulation of lipoproteins and fatty material in the artery wall, which is induced by endothelial damages promoted by cardiovascular risk factors, such as tobacco consumption, unhealthy diet, stress, sedentary life, high blood cholesterol level, and hereditary factors.[3] The deposition of lipids is followed by (2) the adhesion of monocytes on the damaged site, which (3) transmigrate into the intima, differentiating into macrophages that uptake the accumulated lipoproteins, forming "foam cells". Such foam cells, engorged with lipids, begin to die and release their content forming a necrotic core.[4] At the same time (4) vascular smooth muscle cells migrate through the intima, towards the endothelium, and proliferate resulting in the formation of a fibrous cap, which can protrude into the arterial lumen causing a stenosis. A major complication of atherosclerosis is the rupture of the fibrous cap, which leads to formation of platelets aggregates and thrombi that can occlude arteries.[5–7]

One of the main concerns related to atherosclerosis is the absence of symptoms that reveal the existence of the underlying progress of the disease.[8] Although several indicators of higher possibility of developing an atherosclerotic pathological condition (intermediate risk factors) such as high blood pressure, diabetes, and obesity have been identified and can be easily monitored, frequently the first symptom of atherosclerosis is a major cardiovascular event such as a sudden heart attack or a stroke.[9] The development of efficient diagnostic tools for the detection of the disease in early stage will allow efficient treatment and monitoring of

the progression of atherosclerosis. Together with the implementation of regulations and taxes to discourage the use of unhealthy dietary products, and the promotion of a healthy lifestyle, molecular probes for diagnosis of early-stage atherosclerosis will contribute to decrease the burden of atherosclerosis worldwide.

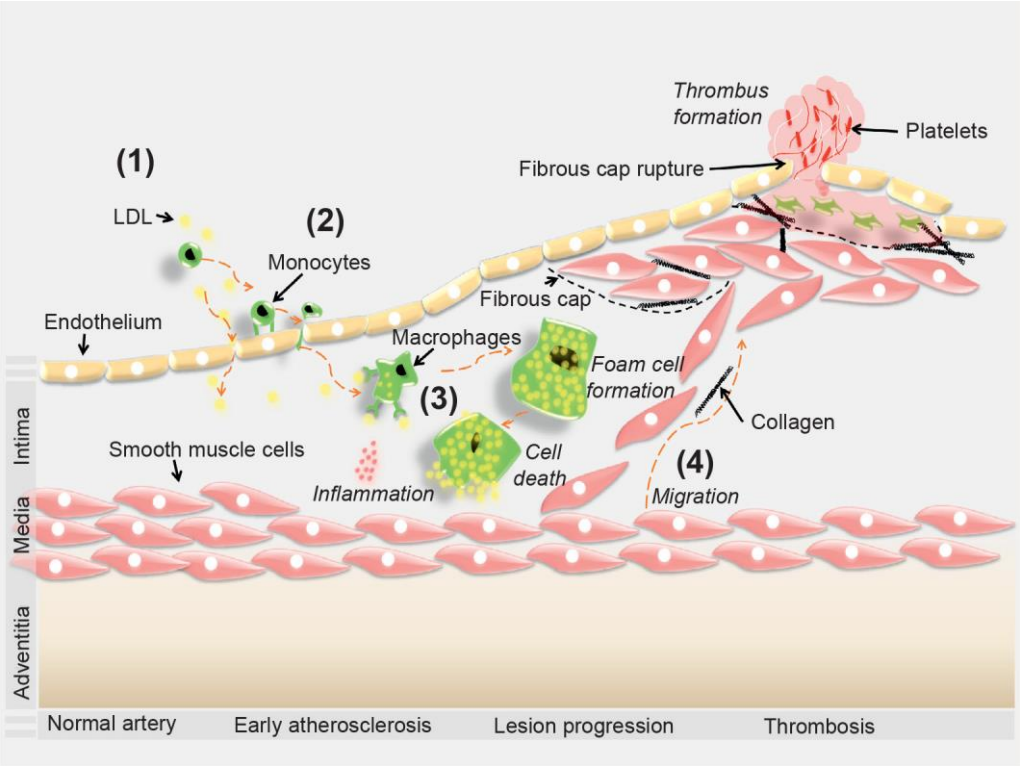

Figure 1. Atherogenesis of an atheroplaque: (1) lipoproteins and fatty material deposition initiate an inflammation. (2) Monocytes permeate in the intima, and (3) transform to macrophages that uptake lipoproteins yielding to foam cells. (4) Vascular smooth muscle cells migrate to form a fibrous cap that can eventually break causing the formation of thrombi in the lumen of the artery. Adapted from Athanasiou *et al*.[6]

1.2 Imaging of Atherosclerotic Plaques

The development of efficient and cost-effective imaging methods for detecting atherosclerosis will provide better pharmacological treatment options. Traditionally, the progression of atherosclerosis was assessed by inspecting the narrowing of the artery or by evaluating the effect of arterial stenosis on organs perfusion.[10] Nowadays, several imaging techniques such as ultrasound imaging (USI), chest X-rays and X-rays angiography are routinely used to diagnose atherosclerosis.[11] These techniques are fast and efficient in

revealing artery stenosis and wall thickness. In particular, the use of non-invasive X-rays angiography techniques with intravenous injection of a contrast agent has become a common clinical practice used to outline the degree of stenosis of the carotid, renal and peripheral arteries, and aorta.[12] However, the luminal diameter of the arteries may appear normal despite the significant occurring of the disease. Therefore, these imaging methods are efficient only in an advanced stage of atherosclerosis, and are unable to detect atheroplaques that do not protrude in the luminal space of arteries. After the development of imaging methods for atherosclerosis such as computer tomography (CT) and magnetic resonance imaging (MRI),[13] it became possible to obtain more information about the morphology and composition of atheroplaques including fibrous cap thickness, which correlates to atheroplaques rupture.[11] Together with the techniques already commonly employed clinically, these methods provide measures of disease severity, which are becoming essential to everyday clinical practice and cardiovascular research. Several imaging modalities for atherosclerosis detection, based on these recent developments, have been considered (Table 1).

Table 1. Imaging methods for atherosclerosis. Adapted from Albeda *et al*.[14]

Imaging Technique	Spatial resolution	Depth	Sensitivity	Acquisition time	Radiation employed	Cost
CT	50-200 µm	No limit	µmol (10^{-6})	min	X-rays	Medium
USI	50-500 µm	mm to cm	nmol (10^{-8})	From s to min	High-frequeny sound	Medium
OI	1-5 mm	>1-2 mm	pmol (10^{-12})	From s to min	Vis-NIR light	Low-medium
PET	1-2 mm	No limit	fmol (10^{-15})	From s to h	γ-rays	High
SPECT	1-2 mm	No limit	fmol (10^{-14})	From min to h	γ-rays	Medium
MRI	10-100 µm	No limit	nmol (10^{-9})	From min to h	Radiowaves	High

CT is a powerful non-invasive technique routinely used for anatomical imaging of coronary artery disease.[15,16] The high sensitivity of CT allows quick evaluations of stenosis and plaque morphology providing information on the severity of the disease. Due to the low electrodensity of soft tissues, CT is usually utilized in combination with a contrast agent, which can absorb electromagnetic waves in the wavelength range of X-rays.[17] Despite high resolution

and short acquisition time of CT, the use of ionizing radiations remains a concern. Therefore, CT is not recommended to be used for regular checks.

USI is one of the most common and non-invasive techniques for detecting atherosclerosis. The reconstruction of the image is based on the reflection of ultrasound waves emitted from an ultrasound transducer.[18] The reflection of the ultrasound wave in angiography is correlated to blood flow, therefore this technique provides information about the effect of arterial stenosis on hemodynamics. Although, USI is very useful as diagnostic and prognostic tool for atherosclerosis, it is applicable only in an advanced stage of the disease. Better morphological and structural information can be obtained using an intravascular ultrasound catheter (IVUS), which are unfortunately invasive.[19]

Optical imaging (OI) have also been used to characterize atherosclerosis.[20,21] Light with wavelengths in the region of the near-infrared (NIR) is used, since those radiation are less energetic, and therefore less harmful to patients. Importantly, NIR light can penetrate biological tissues deeper than light with shorter wavelength, due to minor absorbance and scattering.[22] Nevertheless, the penetration capacity of NIR is still very limited and the OI is mainly used in research. For clinical applications the use of catheters is required, making this imaging method invasive.

Positron emission tomography (PET) and single photon emission computed tomography (SPECT) are extremely sensitive imaging techniques (fmol level, Table 1). These methods make use of γ-ray emissions from a radionuclide and are particularly promising for the molecular imaging of atheroplaques, allowing the non-invasive evaluation of the plaque inflammation by targeting specific biomarkers.[23–25] Disadvantages of PET and SPECT are the limited spatial resolution (1-2 mm), long acquisition time, and high costs of the instruments.[14]

MRI is a non-invasive imaging method with a very high spatial resolution that does not involve the use of ionizing radiation. Therefore, it can be used to monitor the progression of diseases such as multiple sclerosis and Alzheimer's disease in patients under treatment.[26,27] MRI images are obtained based on the different relaxivity of protons in water and soft tissues.[28] Since the high intensity signal provided from the blood, MRI imaging of atherosclerosis is not a trivial task. However, this imaging technique can provide many important information on atherosclerotic plaques on the basis of biophysical and biochemical parameters such as chemical composition, water content, molecular motion or diffusion.[12] The "black-blood" MRI sequences have been developed in order to suppress the blood signal,

allowing to visualize the arterial wall and to reveal the size and morphology of atheroplaques with sub-millimeter resolution.[29] In order to achieve a clear distinction between adjacent soft tissues, MRI often requires the use of contrast agents (MRI-CAs), that affect the relaxation time of the protons in the tissues, causing a difference of contrast in the obtained image. The main limitations in the use of MRI are long acquisition times and the high cost of instrumentation. From a chemical perspective, the development of high relaxivity contrast agents able to specifically target atheroplaques can help solve these problems, allowing to acquire images with a higher contrast in a shorter time. The details of this method are described in the following section.

1.3 Magnetic Resonance Imaging (MRI)

1.3.1 General

MRI relies on nuclear magnetic resonance (NMR), which is extensively used in chemistry for the structure determination of organic compounds. For medical applications, the use of the word "nuclear" was dropped to avoid that patients may associate it with radioactivity. NMR is based on atomic nuclei quantum property of spin.[30] When placed in an external magnetic field, the nuclei start precessing, generating a magnetization vector in the direction of the magnetic field. The frequency of the precession is proportional to the nature of the nuclei and to the strength of the magnetic field, and it is mathematically expressed by the Larmor equation:

$$\nu_0 = - (\gamma /2\pi) B_0$$

where ν_0 is the Larmor frequency, γ is the gyromagnetic ratio, and B_0 is the magnetic field. For protons, there are only two possible energy states, corresponding to the precession in the directions parallel (lower energy) and antiparallel (higher energy) to the magnetic field. Thus, a net magnetization in the direction of the applied magnetic field is generated.

As shown in Figure 2, by the application of a radiofrequency (RF) pulse, it is possible to tilt the magnetization in an orthogonal plane. When the RF pulse stops, the magnetization goes back to equilibrium following an exponential increase in the z axis (relaxation time T_1) and an exponential decrease in the xy plane (relaxation time T_2). This process induces an electric current in a detector coil in the xy plane and after conversion of the signal from

analog to digital, a signal function called Free Induction Decay (FID) is obtained and converted into a spectrum by Fourier transformation of this signal.

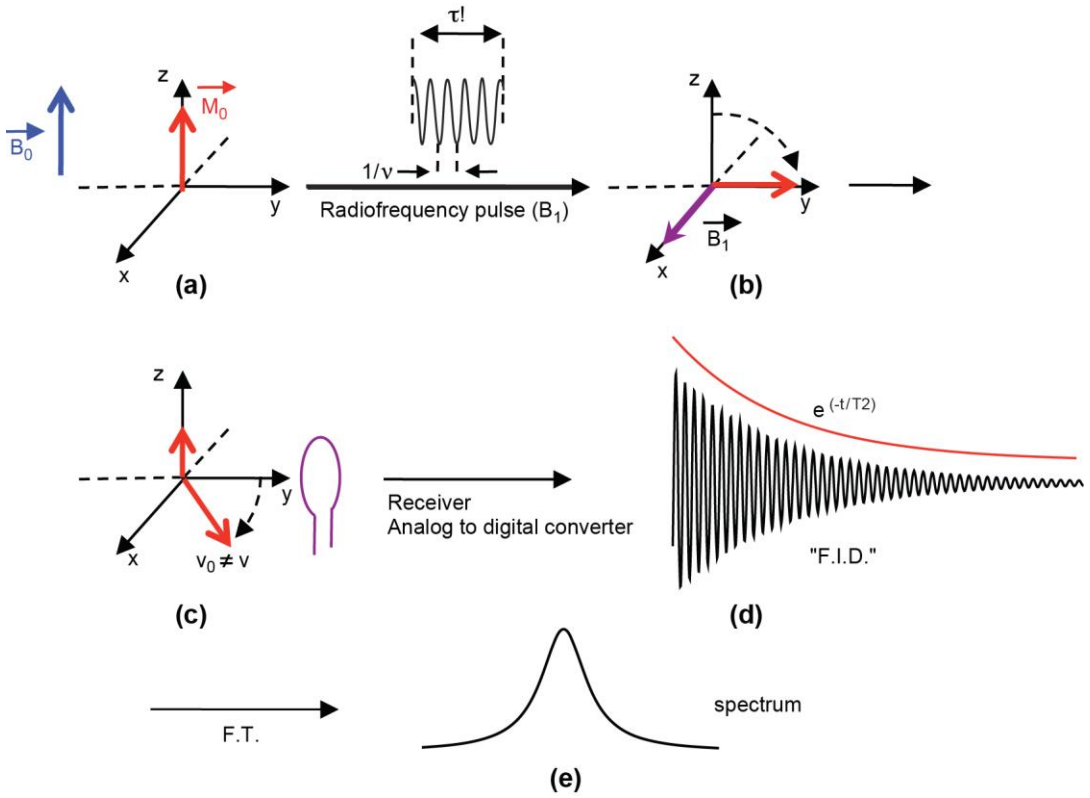

Figure 2. (a) Net magnetization in the direction of B_0 (b) a radio frequency (RF) pulse, induced by a perpendicular B1 magnetic field, tilts the magnetization into the xy plane. (c) The system relaxes back to the equilibrium state and loss of magnetization in the xy plane over time is recorded; (d) Free Induction Decay (FID) function; (e) spectrum obtained by the Fourier transform of FID. Adapted from Merbach *et al.*[30]

For medical application of MRI, proton (^{1}H) imaging is used in most cases due to its high abundance and relatively strong magnetic moment. MR images are generated by the spatial distribution of the spin density. Since the resonance frequency is proportional to the strength of the magnetic field, the generation of a field gradient allows to correlate the signal obtained with the position in space of the nuclei. Those gradients are superimposed with the static magnetic field B_0 (Figure 3).

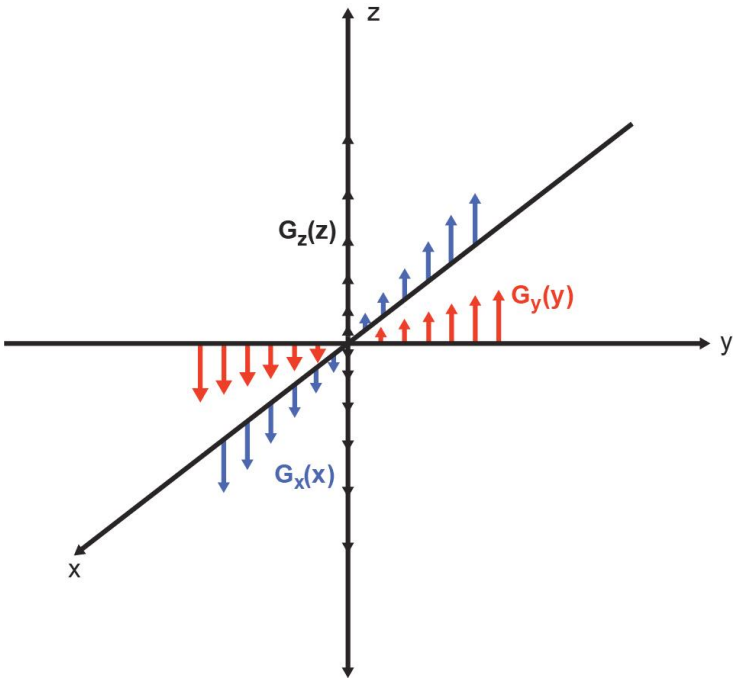

Figure 3. Magnetic field gradients used to localize spins in MRI. Gx, Gy, Gz = magnetic field gradients along the x, y and z axis respectively. Adapted from Merbach *et al.*[30]

The contrast of a MRI image is dependent on the difference of the signal intensity detected from the different tissues. This intensity can be affected by using an MRI-CA to alter the relaxation of water contained in the tissue. MRI-CAs are either paramagnetic metals or superparamagnetic materials that are able to decrease T_1 and T_2.[31] The most widely used MRI-CAs are gadolinium-based metal chelates, which shorten T_1 causing the brightening of the area in which they are accumulated.

1.3.2 Gadolinium-Based Metal Chelate as MRI contrast agent (MRI-CA)

Gadolinium is a lanthanide metal with atomic number 64. The gadolinium cation (Gd^{3+}) is highly paramagnetic, with seven unpaired electrons in its 4f orbital, and it possesses high magnetic moment. The strong positive charge of the Gd^{3+} cation, and its ionic radius (0.100 Å), that is similar to the one of Ca^{2+} (0.103 Å),[32] make Gd^{3+} able to interact strongly with Ca^{2+} binding proteins causing therefore highly toxic effects. For this reason, it can be used *in vivo* only when it is tightly chelated with organic ligands that shield the exchange with Ca^{2+}. An extremely important parameter in the evaluation of the safety of Gd^{3+}-chelates is their kinetic inertness, which denotes how slow Gd^{3+} is released from the chelate. All the clinically approved Gd^{3+}-based MRI-CAs utilize octadentate ligands with only one

coordination site left for the coordination with water. Two types of structures are used for the chelation of Gd^{3+}; a cyclic structure based on cyclen derivatives (A-C in Figure 4) and a linear structure based on diethylenetriamine derivatives (D-I in Figure 4).[33] In the macrocyclic cyclen derivative, Gd^{3+} is entrapped in a cage-like structure between the preformed central cavity of cyclen and four carboxylic acid residues, whereas in the linear structure, the ion Gd^{3+} is coordinated by the three nitrogen of the diethylenetriamine backbone, and by five carbonyl residues that wrap the ion around avoiding its release.

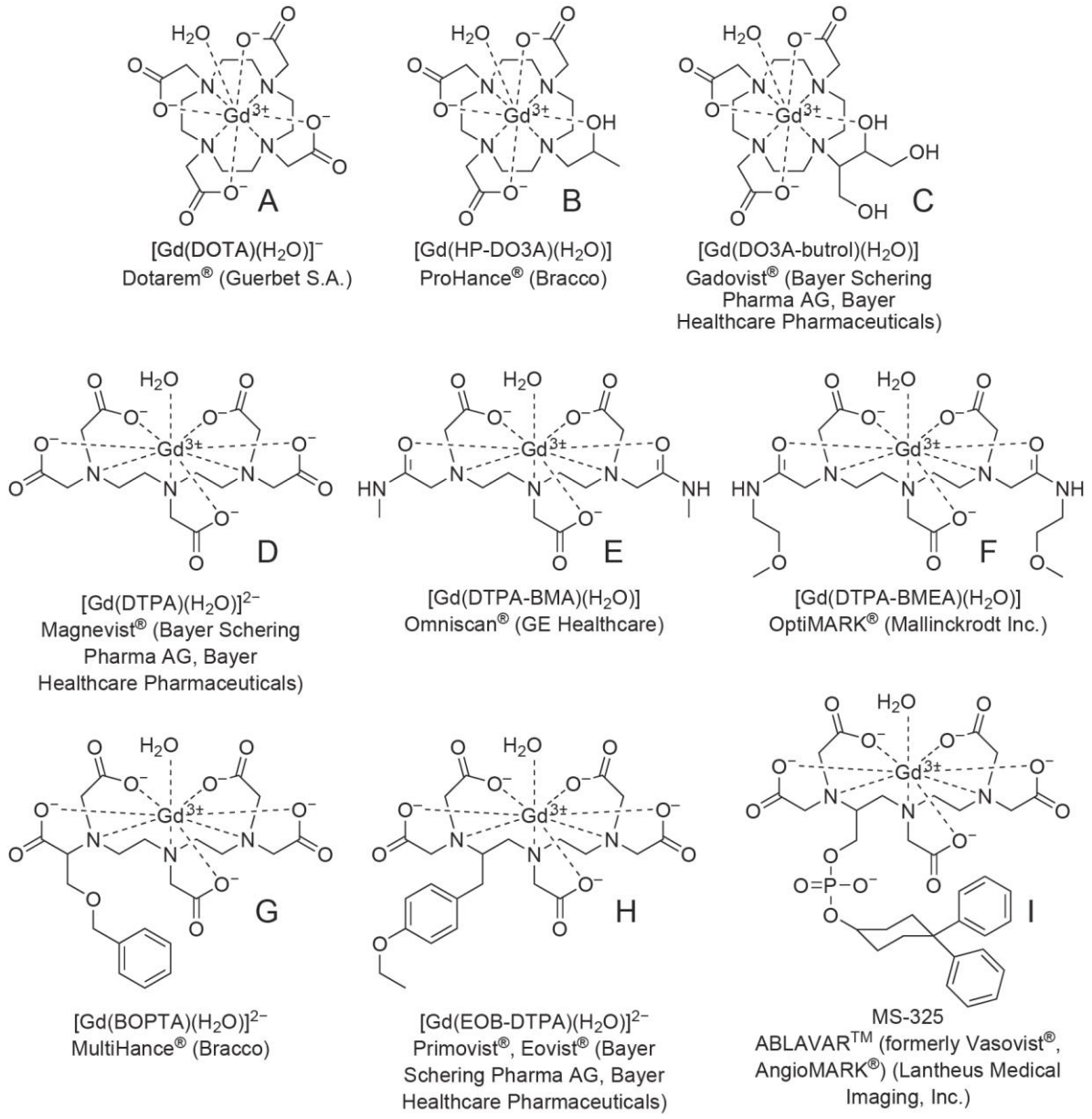

Figure 4. Structures of FDA-approved Gd^{3+}-chelates for MRI-CA. Adapted from Merbach *et al.*[30]

The parameter that defines the contrast enhancement efficiency of MRI-CAs is the relaxivity (r_1) (Table 2). The r_1 is defined as the inverse of T_1 for a 1 mM aqueous solution of MRI-CA. The r_1 values are reported in mM^{-1} s^{-1} and it is dependent on both magnetic field and temperature.[31,34]

Table 2. Relaxivity of the most common Gd^{3+} contrast agents.

	Trademark	Abbreviation	Structure	Ionicity	r_1 ($mM^{-1}s^{-1}$)
A	Dotarem®	Gd(DOTA)	Macrocyclic	Ionic	4.2
B	ProHance®	Gd(HP-DO3A)	Macrocyclic	Non-ionic	4.4
C	Gadovist®	Gd(BT-DO3A)	Macrocyclic	Non-ionic	5.3
D	Magnevist®	Gd(DTPA)	Linear	Ionic	4.3
E	Omniscan®	Gd(DTPA-BMA)	Linear	Non-ionic	4.6
F	OptiMark®	Gd(DTPA-BMEA)	Linear	Non-ionic	5.2
G	MultiHance®	Gd(BOPTA)	Linear	Ionic	6.7
H	Primovist®	Gd(EOB-DTPA)	Linear	Ionic	7.3
I	Vasovist®	Gd(MS-325)	Linear	Ionic	19

The r_1 is generated by the interactions of water molecules with Gd^{3+}. These interactions can be direct, like for water molecules coordinated to Gd^{3+} that are quickly exchanged with other water molecules (inner sphere), or indirect (outer sphere), as shown in Figure 5.

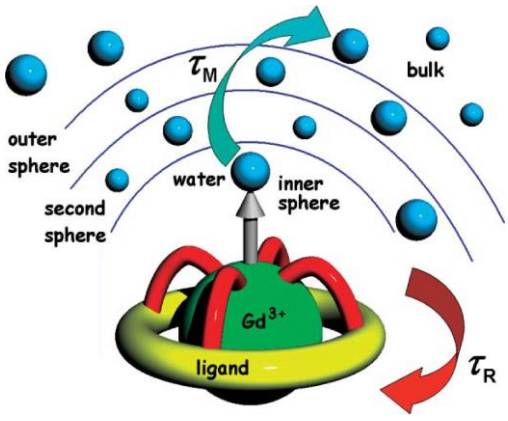

Figure 5. Model of the interaction between Gd^{3+} and water. Adapted from Hermann *et al.*[33]

The r_1 values depend on several parameters such as (1) the number of water molecules directly bound to Gd^{3+} (q), (2) the exchange rate of the water coordinated to Gd^{3+} (τ_M) (3) the rotational correlation time (τ_r), as described below.

1. Higher q results in an increase of r_1. However, the chelates with higher q are more prone to Gd^{3+} release and transmetallation with consequent safety concerns.
2. An optimal value for τ_M is a compromise between the minimum residence time needed to efficiently affect the bound molecule of water and the exchange rate. It is estimated that an ideal value for τ_M at 1.5 T is 10 ns.[30] To increase τ_M values, modification of the ligand structure are often efficient. For example, the addition of bulky groups, which can hinder the approach of water to Gd^{3+} provide fast water exchange. However, the introduction of bulky groups can cause unpredictable structural changes that will affect τ_M, therefore this strategy is generally avoided.
3. The molecular motion of the entire molecule generates local changes in the magnetic field, significantly affecting the relaxivity. Consequently, slowing down the rotation rate of CAs can cause the increasing of r_1 values.[35] This effect has been observed in CAs with increased molecular size, by linking small molecules CA to larger structures such as proteins, polymers and nanoparticles.[35–38]

1.4 Delivery of MR Imaging Probes to Atheroplaques

Artery wall thickness in healthy humans ranges between 1 mm (coronary artery) and few mm for the carotid and aorta, whereas the thickness of diseased arteries ranges between 1.5 mm up until 10 mm in advanced atherosclerotic stage.[39] In light of its submillimeter spatial resolution, MRI is one of the best imaging techniques for characterizing atheroplaques. However, for an advanced characterization of the atheroplaques, MRI has to provide a significant contrast between the diseased tissue and its surrounding. In order to have a more effective contrast enhancement, CAs able to target atherosclerotic diseased tissue need to be developed. Such CAs would allow to obtain better MRI images with lower administration doses, thus reducing the concerns related to side effects.[40] So far, only a few target-specific MRI-CAs have been approved by FDA for clinical use (e.g. gadofosveset, which binds to albumin) and several promising new agents are under study (e.g. elastin and fibrin binding contrast agents).[41] The typically injected clinical dose is in the range of 0.1 mmol/kg but can be even lower for target specific contrast agents, due to the increased relaxivity upon binding. One of the most promising approaches for the

preparation of MRI-CAs able to target atheroplaques is the use of nanoparticles as delivery systems. Indeed, nanoparticles can be modified modified with specific targeting moieties, which enable the selective delivery of the MRI-CAs to the diseased tissue.[42] In general, the use of nanoparticles has the advantage of offering prolonged circulation time, providing increased stability and aqueous solubility of diagnostic agents together with therapeutic compounds and targeting moieties, which can allow high binding and uptake efficiency in the target tissue.[43] Therefore, the last decade has seen a fast development of nanoparticles as diagnostic tools for detecting atherosclerotic plaques.[44] These nanoparticles include polymers and dendrimers, metallic nanoparticles, micelles, liposomes and lipoproteins.[45]

Dendrimers are highly branched synthetic polymers, which can be prepared as core of nanostructure-based Gd MRI-CA and several dendrimer materials, such as polyamidoamine (PAMAM) and diaminobutane (DAB), have been employed for MRI applications.[46,47] Despite their broad applicability, dendrimers present some toxicity concerns deriving from their polycationic surfaces, which can be reduced by the functionalizion with negatively charged or neutral functional groups. Furthermore, even though the synthesis of dendrimers allows to fine-tune their chemical and physical properties, the high production costs are still a concern and hamper their clinical use.

Among the metals, gold and silica nanoparticles are well explored to be coated with molecules that are able to induce high stability and the suitable environment for a subsequent functionalization.[48] For the delivery of such nanoparticles to atherosclerosis, gold nanoparticles have been coated with lipids and targeting agents.[49–51] However, the toxicity of gold nanoparticles is a crucial issue that can limit their biomedical applications prior to clinical use, the whole body effect of gold nanoparticles must be accurately assessed. When metal nanoparticles are used, the comparison between the possible toxicity to the overall health benefit still remains a crucial task to be addressed.

Lipid-based nanoparticles (LNP) such as micelles, liposomes and lipoproteins, bear the advantage of being less toxic, with consequent less concerns for *in vivo* applications. Micelles are nanoparticles formed by amphiphilic molecules that spontaneously aggregate in water in order to hide their hydrophobic moieties from the aqueous media, forming a spherical shape structure. Micelles represent an ideal system for the delivery of hydrophobic and poorly water soluble drugs, but they can also be used as delivery system of hydrophilic material by the modification of the amphiphilic molecules that constitute the aggregate. The use of micelles as delivery system to atheroplaques is still limited,[52–54] with the main concern derived from the

stability of micelles in the blood stream, where critical micelle concentration could be reduced by blood dilution, resulting therefore in the disassembly of the micelles, with consequential reduction of the circulation half-life and total loss of targeting ability.[55]

Liposomes are spherical vesicles formed by either natural or synthetic amphiphilic lipids, which are able to carry both lipophilic molecules in their lipid bilayer, and hydrophilic molecules, such as small molecules MRI-CA, in their inner aqueous core. Since the interaction between the CA and the water of the tissues is limited by the water permeability of the liposomes bilayer, the direct encapsulation of polar MRI-CA is not effective.[56] Paramagnetic liposomes have been prepared, and used for the detection of atherosclerosis, by the modification amphiphilic lipids with an MRI-CA.[57,58] In order to obtain the best contrast with the same amount of MRI-CA, the lipid modification should ideally take place after the formation of the liposomes, in order to have all the molecules of CA oriented in the outer sphere, available for the interaction with the water molecules of the tissues that have to be imaged.

Since a large deposition of lipoproteins and fatty material is involved in the formation and progression of atheroplaques, lipoproteins could be used as delivery system of CAs for the specific target of atherosclerosis.[59,60] This nanoparticle type is addressed in the next section.

1.5 Lipoproteins for the Delivery of MR Imaging Probes to Atheroplaques

1.5.1 Lipoproteins and atherosclerosis

Lipoproteins are natural nanoparticles formed by lipids and proteins that are responsible for the transport of fatty molecules in the bloodstream. Lipoproteins are formed by a lipid core of triglycerides and cholesteryl esters, that is surrounded by a monolayer of phospholipids, with an embedded amphiphilic protein called apolipoprotein.[61–63] The most abundant lipoproteins in the blood are high-density lipoprotein (HDL),[64] which carries away the excess of cholesterol from the cells to the liver, and low-density lipoproteins (LDL), which is the major supplier of cholesterol and fatty acids to the cells (Figure 6). Thus, the concentration of both HDL and LDL play a crucial role in the regulation of lipids content and development of atherosclerosis.

In order to modify lipoproteins with drugs or imaging probes, natural lipoproteins have to be isolated from blood donors and reconstituted with other lipid material. The

reconstitution process consists in the delipidation of the lipoproteins, to obtain the apolipoprotein free of lipids in solution. Subsequently, a microemulsion of lipids functionalized with a drug or an imaging probe is added and the lipoprotein can be reconstituted with the new lipids.[65,66]

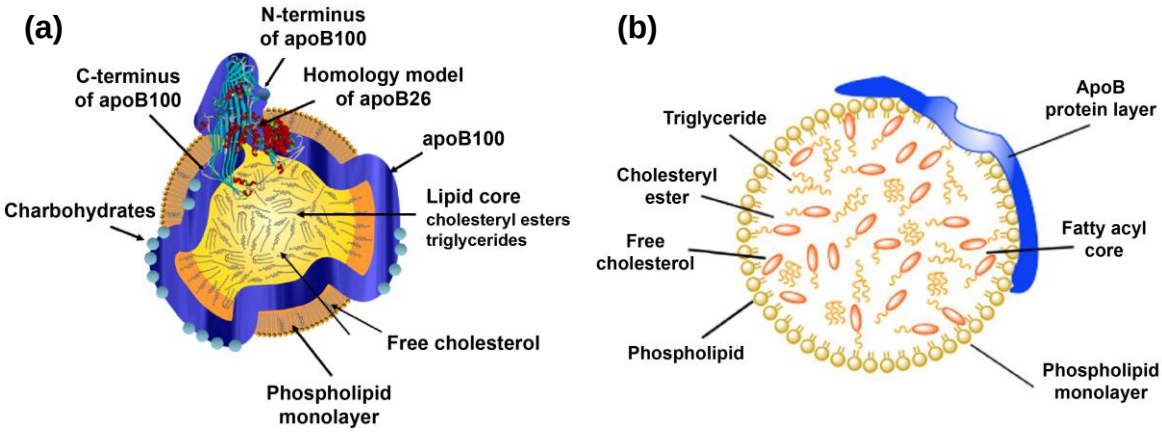

Figure 6. Schematic representations of the structure of a low-density-lipoprotein (LDL). LDL are formed by a lipid core of triglycerides and cholesteryl esters, surrounded by a phospholipids monolayer, with an amphiphilic protein (apoB100) embedded in the lipid structure. (a) Adapted from Prassl *et al.*[63], (b) adapted from Maric *et al.*[67]

1.5.2 HDL for the detection of atherosclerosis

The possibility to reconstitute HDL with different fat derivatives has been applied to the preparation of an MRI diagnostic tool for the imaging of atherosclerosis.[68] In initial studies, Fayad *et al.* reported on the preparation of reconstituted HDL (rHDL) that selectively targets atheroplaques (Figure 7). Natural HDL were isolated, delipidated and reconstituted with a mixture of lipids which included phospholipid-based CA of Gd(DTPA) derivative and fluorescent lipids.[69] The obtained rHDL were able to accumulate in the atherosclerotic plaques of the abdominal aorta of apolipoprotein E knockout model mice (*ApoE*$^{-/-}$), a murine model for atherosclerosis, revealing the presence of atheroplaques on the arterial wall.[70]

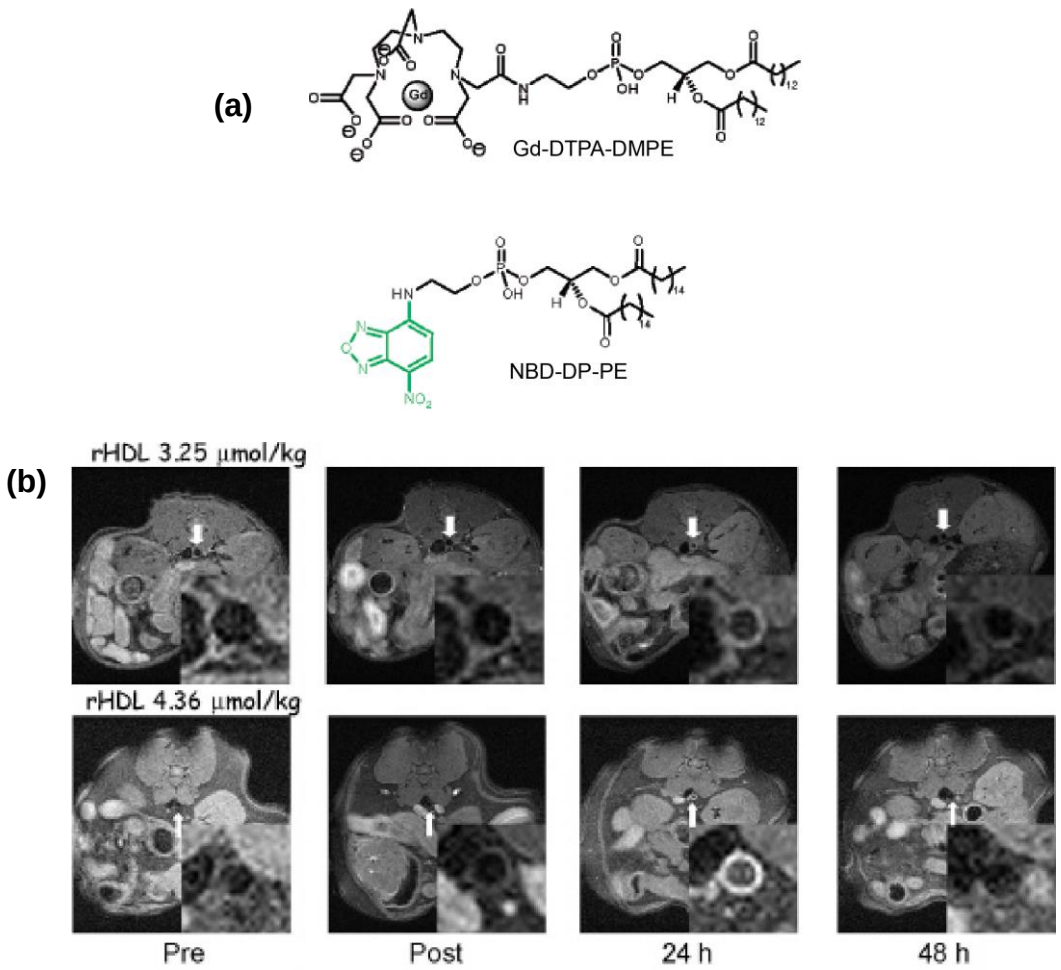

Figure 7. (a) Structure of the Gd(DO3A) and fluorescent lipid used in the reconstitution of the rHDL (DMPE = 1,2-dimyristoyl-sn-glycero-3-phosphoethanolamine; NBD-DP-PE = nitrobenzodiazole-dipalmitoyl-phosphoethanolamine (b) *In vivo* MR images of the abdominal aorta of *ApoE*$^{-/-}$ mice recorded pre- and post-injection (0 h, 24 h, 48 h) of reconstituted HDL (rHDL) bearing a Gd-chelate CA (doses: 3.25 and 4.36 µmol/Kg of Gd^{3+}). All the images are a transversal section of the abdominal aorta at kidneys level. In every image the abdominal aorta is pointed out by a white arrow, with an expansion of the interested area at the bottom right corner. Adapted from Frias *et al*.[69]

1.5.3 LDL for the detection of atherosclerosis

LDL is a major bloodstream carrier of cholesterol and fatty acid in blood. Despite its potential, very few studies have been reported on the use of LDL for the detection of atherosclerosis. Our group reported the first use of natural LDL loaded with an MRI-CA for the *in vivo* detection of atheroplaques.[71,72] LDL were isolated from healthy human blood and modified with a Gd(DO3A) derivative bearing a long oleyl anchor, which can intercalate into

the lipid monolayer of LDL. *In vivo* MR imaging of the aortic arch was performed both on ApoE$^{-/-}$ mice and LDL receptor knockout (*LDLr*$^{-/-}$) mice, clearly revealing the presence of atheroplaques (Figure 8).

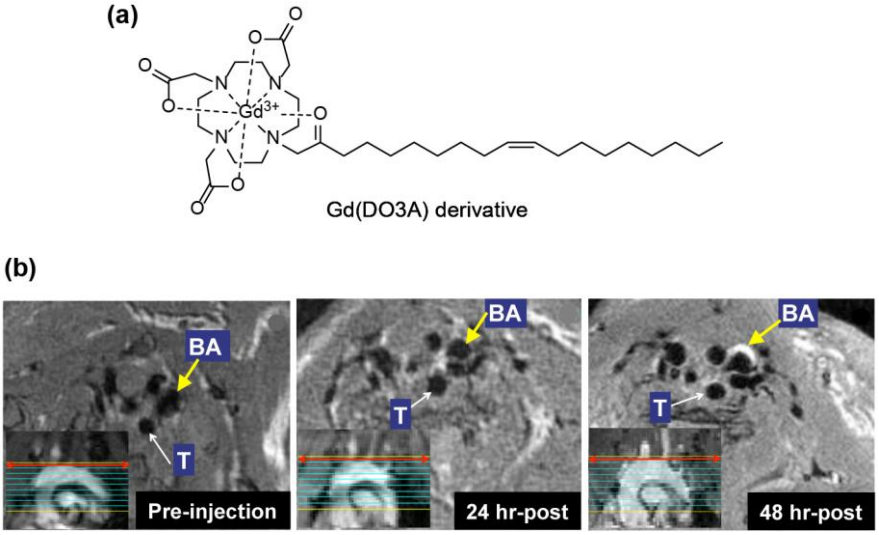

Figure 8. (a) Structure of Gd(DO3A) oleyl derivative (b) *In vivo* MR images of the aortic arch of *ApoE*$^{-/-}$ mice recorded pre- and post-injection (24 h, 48 h) of LDL modified with a Gd-chelate contrast agent. The images are transversal sections of the aortic arch, with the section of the heart reported at the bottom left corner. (T: trachea, BA: brachiocephalic artery). Adapted from Lowell *et al.*[72]

1.5.4 Approach to lipoprotein-mimetic MRI-CAs for atherosclerosis detection

For the preparation of reconstituted lipoproteins as presented above, the isolation of natural lipoproteins from blood donors is required, which hinders the scale up of the process, and increases the infectious risk, limiting therefore their therapeutic applications and the transition to clinic.[73] One of the ways to solve these problems is to develop completely synthetic lipoprotein-mimetic nanoparticles.[74] Towards the development of such synthetic systems, HDL-mimetic nanoparticles were prepared by mixing 1,2-dimyristoyl-*sn*-glycero-3-phosphocholine (DMPC) with a Gd-chelate lipid derivative, and two kind of synthetic peptides (18A or 37pA) able to mimic apoA-I, the main protein of HDL (Figure 9). Those synthetic HDL (sHDL) were tested *in vivo* on *ApoE*$^{-/-}$ providing a discrete enhancement of the contrast in the MR images of the abdominal aorta.[75–80]

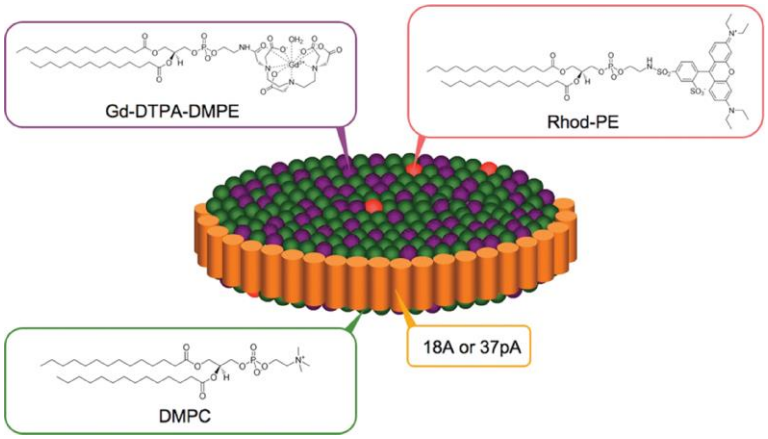

Figure 9. Structure of a synthetic HDL-mimicking particle (sHDL), formed by dimyristoylphosphatidylcholine (DMPC), a Gd-lipid derivative of diethylenetriamine pentaacetic acid (Gd-DTPA-DMPE), a lipid derivative of sulphorhodamine B (Rhod-PE), and two kinds of apoA-I mimicking peptides (18A or 37pA). Adapted from Cormode *et al*.[77]

Despite LDL being the major bloodstream carrier of cholesterol and fatty acid, synthetic LDL (sLDL) have been used only for the selective delivery to cancer tissues, and there are no reports about their use for the detection of atheroplaques. Compared to HDL, LDL has a larger size and contains a higher lipid content, possibly allowing a higher payload of drugs and imaging probes. However, due to the voluminous inner lipid core, the preparation of a stable protein-free particle analogous of LDL, which can be further modified with a peptide mimetic of the apoB100 protein, is challenging.[81] Halbert group reported on the preparation of a synthetic microemulsion, formed by a core of cholesterol ester and triolein, surrounded by a monolayer of phospholipids.[82,83] The protein apoB100 can be grafted to the microemulsion after particles formation, but the process still requires a source of protein from fresh plasma.[84] Furthermore, apoB100 is one of the largest protein (550 kDa), with very low solubility in aqueous media, and therefore hard to handle. However, it is reported that the LDL receptor binding domain of apoB100 consists of only a nine-amino-acid peptidic segment, and can be used for the preparation of synthetic LDL (sLDL).[85,86] Using this amphipathic peptide sequence, the first sLDL particles were successfully prepared, and showed the ability to accelerate the proliferation of U937 cell line in a similar way as LDL.[87,88] Importantly, using fluorescently labelled sLDL, it was shown that the sLDL were able to directly interact with the LDL receptor.[89–91] In order to obtain sLDL as an efficient diagnostic tool for atherosclerosis detection, the development of strategies that allow the surface functionalization of the sLDL particles is necessary. Such strategies would allow the

concurrent attachment of a variety of organic molecules onto the sLDL surface enabling the versatile preparation of particles for multiple application, and ensuring the correct exposure of MRI-CA and targeting moieties towards the bulk water. In particular, particles obtained by the attachment of apoB100 mimetic peptides and MRI-CAs would represent a useful tool for the *in vivo* detection of atheroplaques.

1.6 Lipid Nanoparticles (LNP) Surface Functionalization

Lipid-based nanoparticles (LNPs), including vesicles, micelles and lipoproteins, represent one of the most promising delivery systems for bioactive organic molecules. The main advantages of using LNP are their biocompatibility and easy access to starting materials for the preparation. However, the potential success of LNP in the clinic relies on parameters such as nanoparticle fabrication strategies, loading efficiencies, stability related to possibility of storage, and safety.[92] Common strategies for the preparation of LNP often include surface modifications to increase biological half-life by reducing the interaction with the immune system,[93] and to enable highly stable loading of drugs and imaging probes.[94] The surface functionalization of LNP allows to tailor their properties according to the specific use they are designed for, therefore allowing the realization of peculiar LNP design to aid a specific imaging modality approach. LNP surface can be modified by non-covalent interactions, based on intermolecular interactions between the LNP surface and the moiety to be attached, or by covalent bond formation. Non-covalent surface modification of LNP is rather simple to carry out, since it usually requires simple incubation of the LNP and the chemical moiety that has to be bound on the surface.[95,96] In addition, the great advantage is that no chemical modifications on the attached molecules are required, with a reduced risk to decrease the original biological activity. However, non-covalent modifications are strictly dependent on the binding affinity between the LNP surface and the organic molecules to be attached and may cause the detachment of the loaded molecules. For this reason, the covalent modification is preferred for the preparation of LNP with stably attached moieties. The formation of a covalent bond allows the stable loading of molecules and it is in general more reproducible compared to the non-covalent approach.[48] The chemical reaction for such covalent surface functionalization of LNP should fulfill the following criteria: (1) the reaction should proceed with high chemoselectivity in the presence of unprotected functional groups; (2) the starting material should be biocompatible; (3) no toxic coupling agents or catalysts should be required; (4) the reaction should proceed without the formation of toxic byproducts. (5) The

reaction should proceed with high reaction rate and high yield at low concentration, since the biomolecules to attach are often expensive and soluble only at low concentration; (6) The product formation should not cause aggregation of the LNP. Towards the development of systems able to fulfill these requirements, functionalization reactions such as Michael addition,[97] Cu(I)-catalyzed azide-alkyne cycloaddition (CuAAC),[98] and strain promoted azide-alkyne cycloaddition (SPAAC)[99] have been employed.

1.6.1 Thiol-Michael ligation

The thiol-Michael ligation is a reaction between a thiol and an α,β-unsaturated carbonyl compound (Scheme 1). This reaction can proceed in extremely high reaction rates[100] (> 700 M^{-1} s^{-1} at physiological pH), and has found wide applications in chemistry, biology[101] and material science.[97] However, the thiol-Michael ligation has some drawbacks such as that ligation does not proceed in highly orthogonal manner, since thiols are often found in biological molecules such as peptides or proteins. Also, adducts are often prone to undergo hydrolysis or retro-Michael in the presence of other thiols.[102]

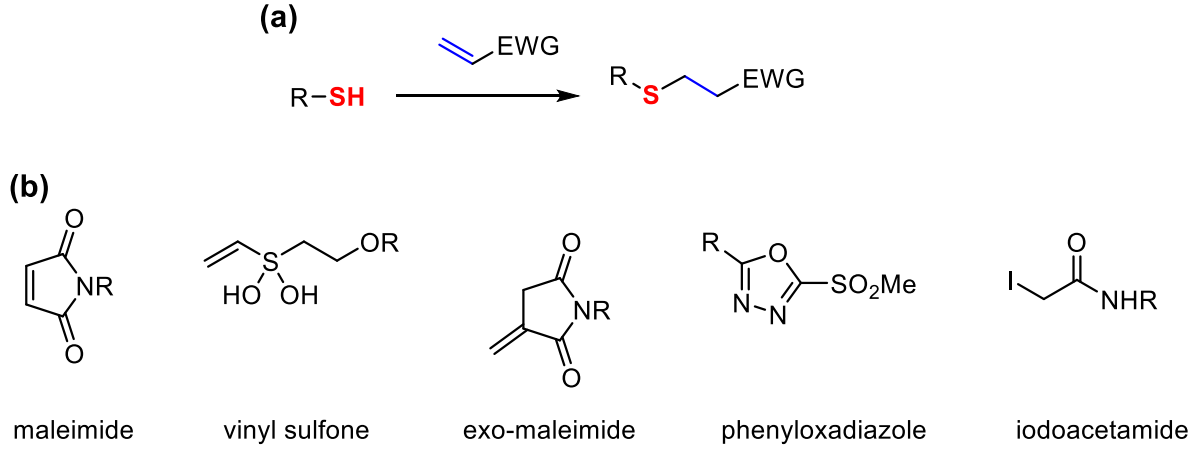

Scheme 1. (a) Thiol-Michael ligation. (b) Commonly used Michael acceptors for thiol-Michael ligation.

1.6.2 Cu(I)-Catalyzed Alkyne-Azide Cycloaddition (CuAAC)

In 2002, Sharpless[103] and Meldal[104] independently reported the Cu(I)-catalyzed alkyne-azide cycloaddition (CuAAC) as a modification of Huisgen cycloaddition (Scheme 2). It has been observed that CuAAC proceeds with a second order rate constant respect to Cu. A first atom

of copper (I) binds the terminal alkyne increasing significantly its acidity and enabling the formation of a Cu-acetylide intermediate, whereas a second copper (I) is coordinated by both the Cu-acetylide and the azide, bringing together the two reactants.[105]

Due to the outstanding bioorthogonality of this reaction, CuAAC rapidly became one of the most used bioconjugation reactions.[106] This ligation provides exclusively 1,4-substituted triazole at room temperature under aqueous conditions. One of the major drawbacks of CuAAC is the cytotoxicity of Cu(I)[107] by the generation of reactive oxygen species (ROSs) due to the interaction of Cu(I) with oxygen in living organisms.[108] Despite this problem, CuAAC has been widely used in nanoparticle modification,[98] and its high potential has resulted in the development of a reaction with a better biocompatibility.

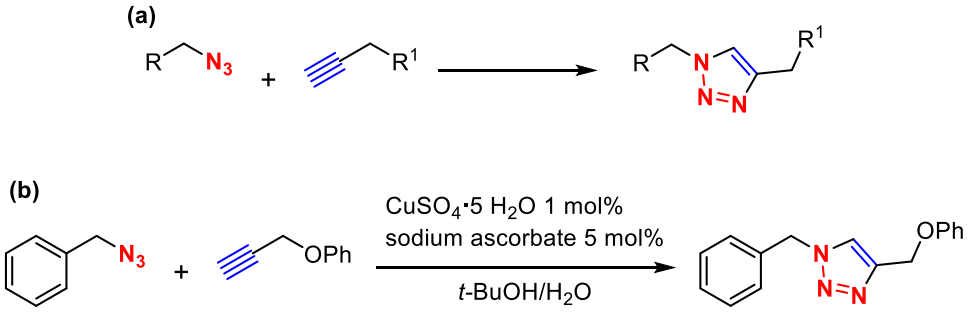

Scheme 2. (a) Cu(I)-catalyzed alkyne-azide cycloaddition (CuAAC); (b) CuAAC originally reported by Sharpless and Meldal[103,104].

1.6.3 Strain-Promoted Alkyne-Azide Cycloaddition (SPAAC)

Towards the development of a more biocompatible version of CuAAC, in 2004 Bertozzi and coworkers reported on the strain-promoted alkyne-azide cycloaddition (SPAAC), which does not require Cu(I) catalyst, therefore is more suitable for applications in biological systems (Scheme 3).[109] This cycloaddition proceeds between cyclooctyne and azide driven by the geometrical constraints of the cyclic alkyne. The azide is orthogonal to many functional groups present in living organisms as it is generally absent from biological systems. Compared to CuAAC, SPAAC can be better applied in biology due to the absence of Cu(I). However, it presents the potential issue that cyclooctynes can be vulnerable to nucleophilic attack by other functional groups such as thiols that are often present in biological targets.[110] In addition, the bulky linkage part of SPAAC products may alter the bioactivity of molecules which undergoe this bioconjugation.

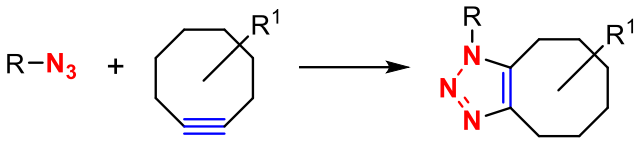

Scheme 3. Strain-promoted alkyne-azide cycloaddition (SPAAC) reported by Bertozzi.

1.7 Potassium Acyltrifluoroborate (KAT) Ligation

In the covalent surface functionalization of LNP, the linker bearing the chemical functional moiety that takes part in the bioconjugation should be small in order not to affect the activity of the conjugated molecules. The formation of an amide bond represents one of the ideal solutions, since amides are usually stable under the variety of conditions in which LNP are stable, they are not bulky and they do not constitute an exotic functional group for living organisms.

Two of the most promising chemoselective amide-forming ligations were developed by the Bode group.[111] In 2006, the Bode group reported the ligation between an α-ketoacid and a hydroxylamine (HA) that chemoselectively form an amide bond in aqueous media (KAHA ligation) as shown in Scheme 4.[112] KAHA ligation does not require any coupling agent or catalyst, generating CO_2 and water as the only by-productsThis reaction has been predominantly used for the chemical synthesis of proteins.[113,114]

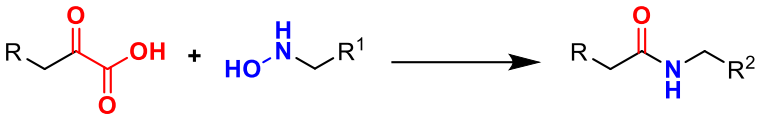

Scheme 4. α-ketoacid-hydroxylamine (KAHA) ligation reported by Bode.

In 2012 a new type of amide forming ligation was reported by Bode and coworkers.[115] This ligation reaction proceeds between a potassium acyltrifluoroborate (KAT) and HA to form an amide bond as shown in Scheme 5. This bioconjugation reaction can meet all the requirements mentioned for the LNP surface modification (Section 1.5). KAT ligation proceeds at room temperature, under aqueous conditions at near physiological pH. It is highly chemoselective, tolerating all the common unprotected functional groups, it provides stable and natural occurring amide bonds linkages, and both starting materials and by-products have been proven to be biocompatible.[116] KAT ligation was employed in the conjugation of unprotected peptides using a 1:1 molar ratio of starting materials, providing full conversion to

products without any side reaction.[117] KAT ligation was successfully used for the PEGylation and dimerization of proteins.[118] Due to its orthogonal nature, it was used for the immobilization of proteins onto synthetic hydrogels.[116,119]

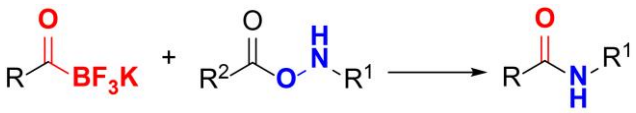

Scheme 5. Potassium acyltrifluoroborate (KAT) ligation reported by Bode.

The first synthesis of the potassium acyltrifluoroborate functional group was reported in 2010 by Molander.[120] This work was followed by the development of a robust protocol for the synthesis of a variety of KAT molecules by the Bode group in collaboration with Molander.[121] The strategy was based on the Katritzky benzotriazole N,O-acetal approach,[122,123] which upon treatment with *n*-BuLi leads to the formation of acyl anions. The anion is trapped by trimethyl borate, which undergoes hydrolysis in aqueous KHF_2 providing the corresponding KAT compound (Scheme 5). The choice of potassium derives from the nice size match between the K^+ cation and the BF_3^- anion, which allows KATs to solidify nicely or reside in the organic layer together during phase extraction purification. This methodology was successfully used to prepare both aliphatic and aromatic KAT compounds.

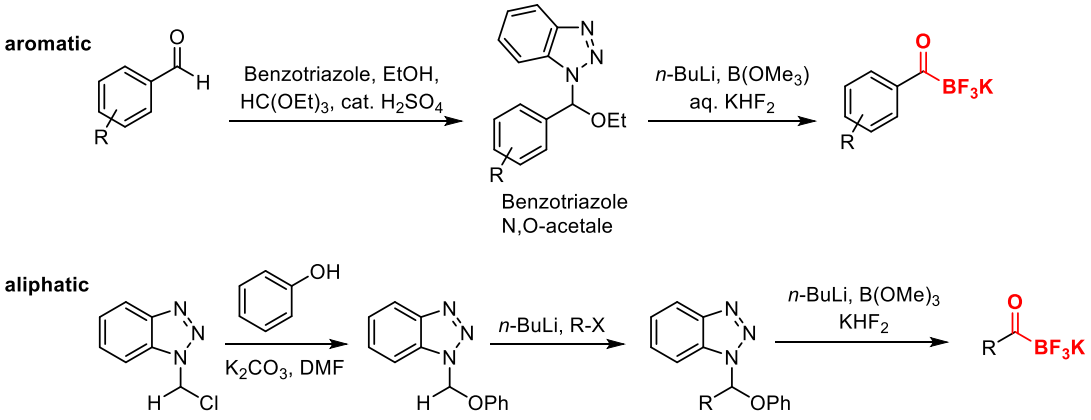

Scheme 6. Benzotriazole N,O-acetal approach for the synthesis of KAT.

The second approach for the synthesis of aromatic and heteromatic KAT was also developed in the Bode group (Scheme 7). In this method, aryl halide are first lithiated by *n*-BuLi and then trapped by (Ethylthio-trifluoroborate)-methane dimethyliminium in a one-pot

procedure.[124] Recently this strategy has also been successfully extended to the synthesis of aliphatic KAT from organocuprates.[125]

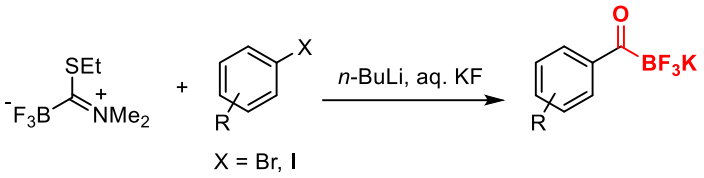

Scheme 7. Synthetic approach using (Ethylthio-trifluoroborate)-methane dimethyliminium for the synthesis of KAT.[124]

Initially, O-benzoyl HA was used as a reaction partner for KAT. However, the benzoyl leaving group exhibits several stability issues, in particular towards hydrolysis under basic and acidic pH and in the presence of primary and secondary amines. After screening, N,N-diethylcarbamoyl HAs were found to have increased stability and reactivity under the same reaction conditions (Scheme 8a).[117] N,N-diethylcarbamoyl HAs can be synthesized by alkylic substitution of N-Boc protected (diethylcarbamoyl)-carbamate as shown in Scheme 8b.

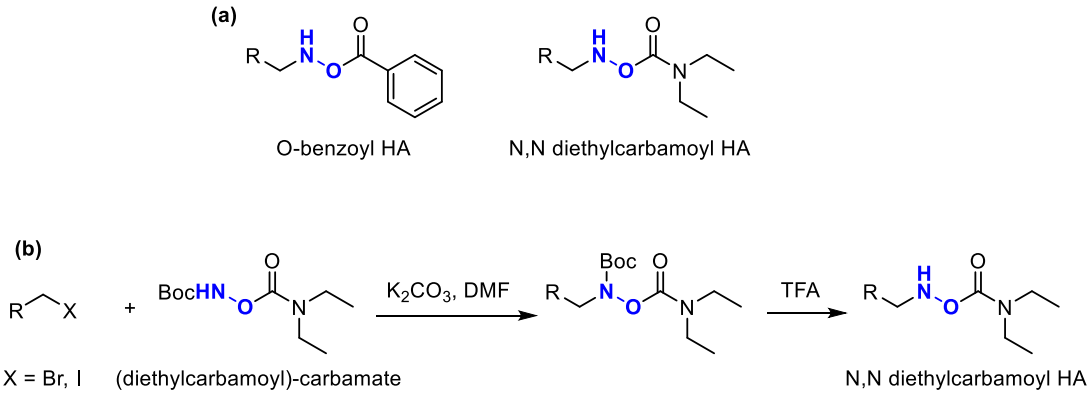

Scheme 8. (a) Structure of the hydroxylamine reaction partner for KAT (b) Synthetic approach towards for the synthesis of N,N-diethylcarbamoyl HA.

Due to the high chemoselectivity and efficiency at low concentration of reagents of KAT ligation, this reaction has a large potential in the application for the covalent surface modification of LNP, also allowing the attachment of multiple ligands. Importantly, the formation of an amide bond enables a stable attachment of biological molecules to the LNP surface, limiting the risk of altering the bioactivity of the molecules attached.

1.8 Concluding remarks

LNPs represent one of the most promising *in vivo* delivery system for drugs and imaging probes. A crucial aspect in the preparation of LNPs is their surface modification through the formation of stable covalent bonds, which provides the ability to tailor the LNP properties such as targeting ability, loading of drugs or imaging probes, and biological half-life. Therefore, for the preparation of LNPs, the use of new chemoselective and biocompatible bioconjugation reactions, that enable the versatile surface functionalization with a variety of organic molecules, providing high loading, is required.

This dissertation describes the application of KAT ligation for the surface functionalization of LNPs. Chapter 2 describes the development of a new LNP bearing the chemically reactive KAT moiety on the surface and the subsequent surface KAT ligation with a standard fluorescent compound. Chapter 3 focuses on the LNP surface functionalization with a peptide and a Gd-chelate as a targeting moiety and MRI-CA, to develop a LDL-mimetic LNP nanoparticles. *In vitro* cellular assay and *in vivo* MRI using atherosclerosis mice models are also described. In Chapter 4, surface KAT ligation was carried out on self-assembly monolayers on gold, to test the efficiency of this chemical ligation method and potential applications to other surface devices.

Chapter 2

Preparation of LNP with KAT group and KAT ligation with fluorescein derivative

The work presented in this chapter was done in collaboration with Dr. Sean Oriana. We thank Dr. Corey Archer (ETH Zurich) for the assistance with the ICP-MS measurements. A manuscript containing a portion of the presented data has been published in Langmuir: Covalent Surface Modification of Lipid Nanoparticles by Rapid Potassium Acyltrifluoroborate Amide Ligation.[126]

2. Preparation of LNP with KAT group and KAT ligation with fluorescein derivative

2.1 Background

Considering the potential of LNP as delivery vehicle of imaging probes, the development of strategies that enable the stable surface functionalization of the LNP with functional moieties is a crucial aspect. The reported surface modification methods take place either by non-specific physical adsorption (non-covalent approach) or by the formation of covalent bonds.

One of the advantages of non-covalent methods is the simpler preparation protocol, which, not requiring any chemical modification, allow to preserve the original chemical properties of the attached molecules. On the other hand, non-covalent surface modification suffers from several drawbacks such as lack of reproducibility and scarcity of control over the quantity of substrates attached to the LNP. Furthermore, it is not always applicable to surface modification, especially when there is no chemical affinity between LNP surface and the molecules to be attached. Furthermore, it may lead to the formation of unstable bonds which easily causes the detachment of molecules from the LNP surface.

Covalent modification is the method of choice for the preparation of more stable chemical functionalization of LNP surfaces.[48,127] In general, two strategies can be used in the preparation of nanoparticles with covalent bond formation, and these involve (1) the assembly of LNP with pre-functionalized molecules and (2) the attachment of functional group onto the preformed LNP.

In this study, the latter strategy was chosen for the preparation of LNP bearing a reactive functional group for the attachment of biorelevant molecules by a chemoselective reaction. Taking advantage of KAT ligation (section 1.6), this approach allowed the attachment of water-soluble moieties or biomolecules such as peptides and imaging probes to the LNP surface.

2.2 Design of LNP with KAT group

For the preparation of LNP equipped with a functionalizable chemical group, we decided to rely on KAT ligation. This reaction is an amide bond forming ligation that takes place

between KAT groups and HA-derivatives (Scheme 4). Advantages of KAT ligation include high chemoselectively in aqueous media under diluted conditions with high yield, using equimolar amount of reagents, and without the requirement of coupling agents. Importantly, this reaction can proceed in an orthogonal manner to common unprotected functional groups and it has been shown to couple peptides with unprotected side chains.[115,117]

In order to obtain LNP mimetic of LDL, LNP were prepared by mixing the main components of the LDL structure, such as phosphatidyl choline (PC), triolein (TO), and cholesteryl oleate (CO). Similar to the LDL structure, it was expected that the amphiphilic PC molecules could form a monolayer in the outer edge of the particle, with the polar head facing to the bulk water while the hydrophobic tails point towards the center of the particle. At the same time, the hydrophobic core of the structure was expected to be filled with triolein and cholesteryl oleate which are apolar compounds and can be in this way separated from the bulk water. (Figure 10).

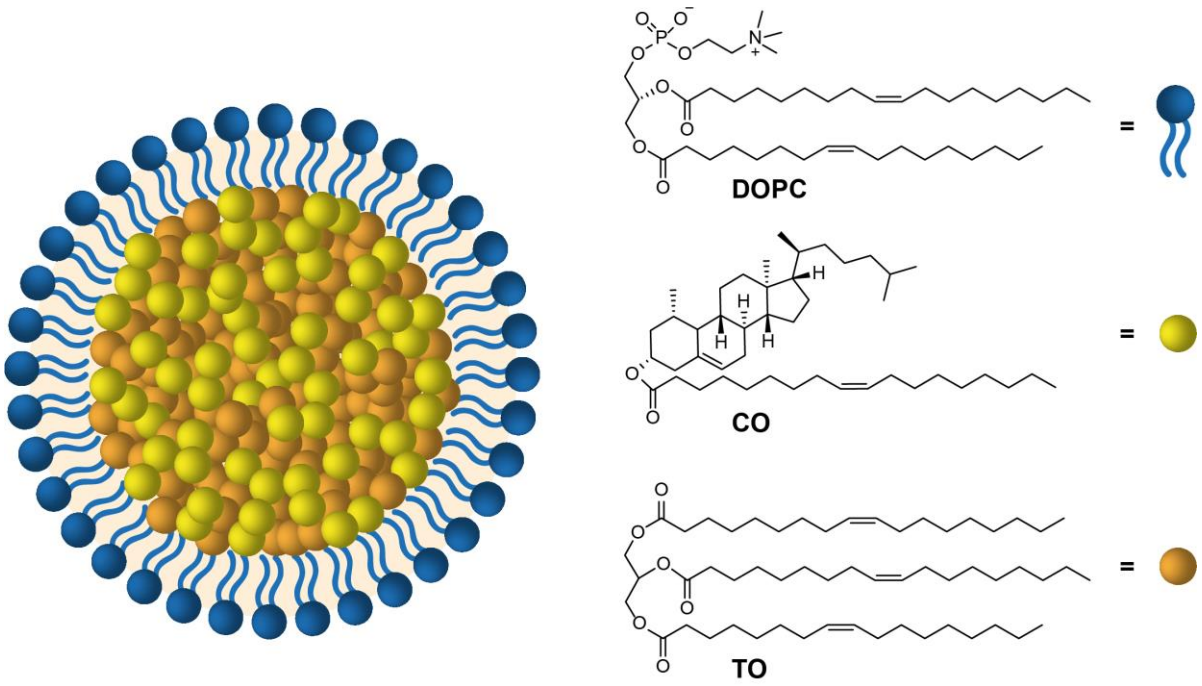

Figure 10. Schematic illustration of LNP structure. PC: phosphatidylcholine, CO: cholesteryl oleate, TO: triolein.

To the lipid components above, a KAT derivative of oleic acid (OA-KAT) was added in the particle formulation in order to obtain nanoparticles possessing KAT functional groups for the covalent surface functionalization (**LNP-KAT**). It was expected that OA-KAT would

be incorporated into the lipid monolayer of LNP through hydrophobic interactions between the long oleic chains of PC and OA-KAT, while leaving the polar salt KAT group exposed to the bulk water, available for the KAT ligation with HA derivatives (Figure 11).

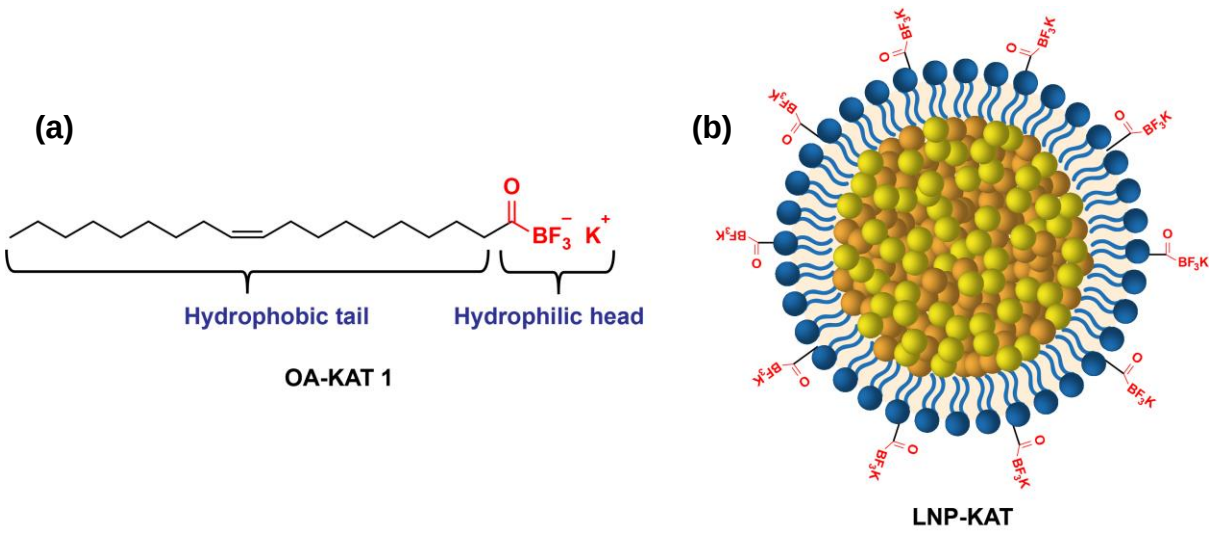

Figure 11. (a) Chemical structure of the oleic acid derivative of KAT (OA-KAT) **1**. (b) Schematic illustration of the **LNP-KAT** structure.

2.3 Synthesis of KAT Derivative of Oleic Acid (OA-KAT)

The OA-KAT **1** was synthesized based on the previously reported protocol of the synthesis of KAT derivatives (Scheme 9).[121] The commercially available (chloromethyl)-1H-benzotriazole **2** was substituted with sodium phenoxide to provide compound **3**. The oleyl iodide, obtained from the commercially available oleyl chloride by substitution with NaI in acetone under reflux conditions, was used for the alkylation of compound **3** to provide the key intermediate **4** as a direct precursor of the KAT group. This hemiaminal compound was deprotonated by *n*-BuLi and converted to OA-KAT **1** by trapping the obtained anion with $B(OMe)_3$, followed by the addition of an aqueous saturated solution of KHF_2. The low yield in this last step (26%) is due to both the solubility of the starting material **4** and the low stability of its anion form in THF. Since benzotriazole-based hemiaminal anions have been reported to be unstable at temperature higher than – 40 °C,[128] the last step was carried out at – 78 °C. It was expected that the deprotonation could proceed better by increasing the amount of *n*-BuLi, but this caused the formation of the $BuBF_3K$ byproduct, which derives from the direct attack of *n*-BuLi to the $B(OMe)_3$, and it is extremely difficult to separate from the KAT product.

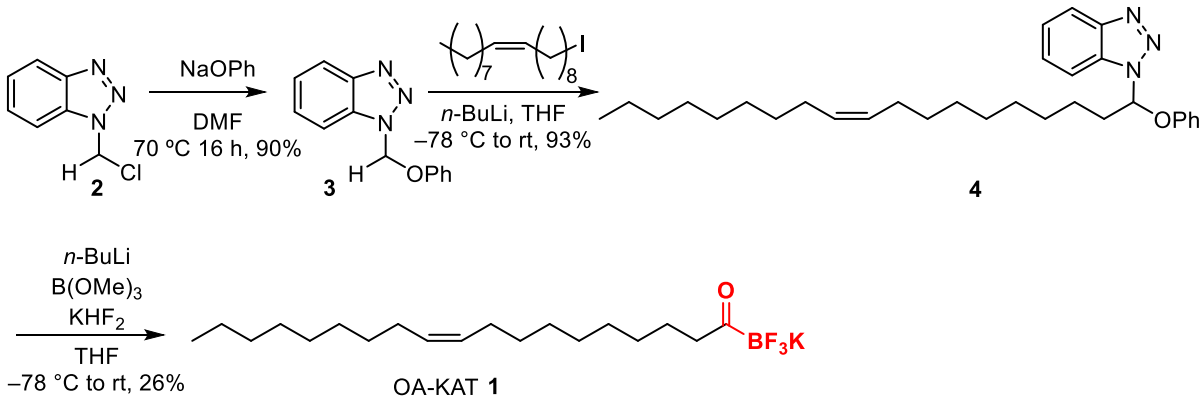

Scheme 9. Synthesis of the KAT oleic acid derivative (OA-KAT) **1**.

2.4 Preparation of LNP with KAT group

2.4.1 Preparation of LNP

LNP was prepared based on the previously reported protocol for the production of LDL-mimetic microemulsion of synthetic LDL (sLDL), with slight modifications.[82,87] Three commercially available lipid components, PC, TO, and CO were used in a ratio of 3:2:1 (mol/mol). They were initially solubilized in a mixture of $CHCl_3$-MeOH-acetone (2:1:1, v/v) and evaporated in a round-bottom-flask to form a thin film. The obtained lipid film was lyophilized overnight to remove every trace of organic solvents. The thin film was hydrated with 10 mM Tris-HCl buffer (pH 8.0, containing 10 mM KF and 1 mg/L BHT), sonicated at 0 °C for 2 h and extruded 10 times through two stacked polycarbonate membrane filters of 0.1 and 0.05 μm pore sizes at 55 °C.

2.4.2 Preparation of LNP with KAT group

The same procedure described in 2.4.1 was used for the preparation of **LNP-KAT**, with OA-KAT **1** added to the lipid mixture of PC, TO and CO in the ratio of 2.5, 5 and 10 mol% of total lipid. The addition of OA-KAT **1** to the lipid mixture often caused polydispersity in the particle size, as observed by dynamic light scattering (DLS) experiments, especially when relatively large amount of OA-KAT **1** (10 mol%) was employed. This observation was in line with the previous reports, in which as a consequence of the increasing of the mol% ratio between the amphiphilic PC and the hydrophobic lipids, the formation of larger polydispersed lipid aggregates was observed. The reason of this observation is unclear, but the concomitant formation of lipid vesicles may be the cause.[82] Based on these observations,

LNP-KAT were prepared keeping the same the same mol% ratio of amphiphilic lipids (PC, OA-KAT) relative to the hydrophopic lipids (CO, TO) (details are shown in Table 3). The **LNP** and **LNP-KAT** were washed with the same Tris-HCl buffer by spin-filtration to remove free lipids components, which were not incorporated in the nanoparticles, and were characterized by DLS and cryoTEM.

Table 3. Amount of lipid in **LNP-KAT** (4 mL), with 0, 2.5, 5, 10 mol% of OA-KAT **1**.

	Lipid components (mg) (µmol)			
LNP-KAT	**PC**	**TO**	**CO**	**OA-KAT 1**
0	37.6 (49.5)	29.2 (33)	9.4 (16.5)	-
2.5	35.7 (46.5)	29.2 (33)	9.4 (16.5)	0.95 (2.5)
5	33.8 (44.5)	29.2 (33)	9.4 (16.5)	1.9 (5.0)
10	30.1 (39.6)	29.2 (33)	9.4 (16.5)	3.8 (10.0)

2.4.3 Dynamic light scattering, TEM, cryoTEM and Zetapotential of LNP and LNP-KAT.

Dynamic light scattering (DLS) results indicated that all the **LNP** and **LNP-KAT** samples containing 0, 2.5, 5, or 10 mol% of OA-KAT **1** showed similar diameter size around 50-60 nm with no significant aggregation (Figure 12).

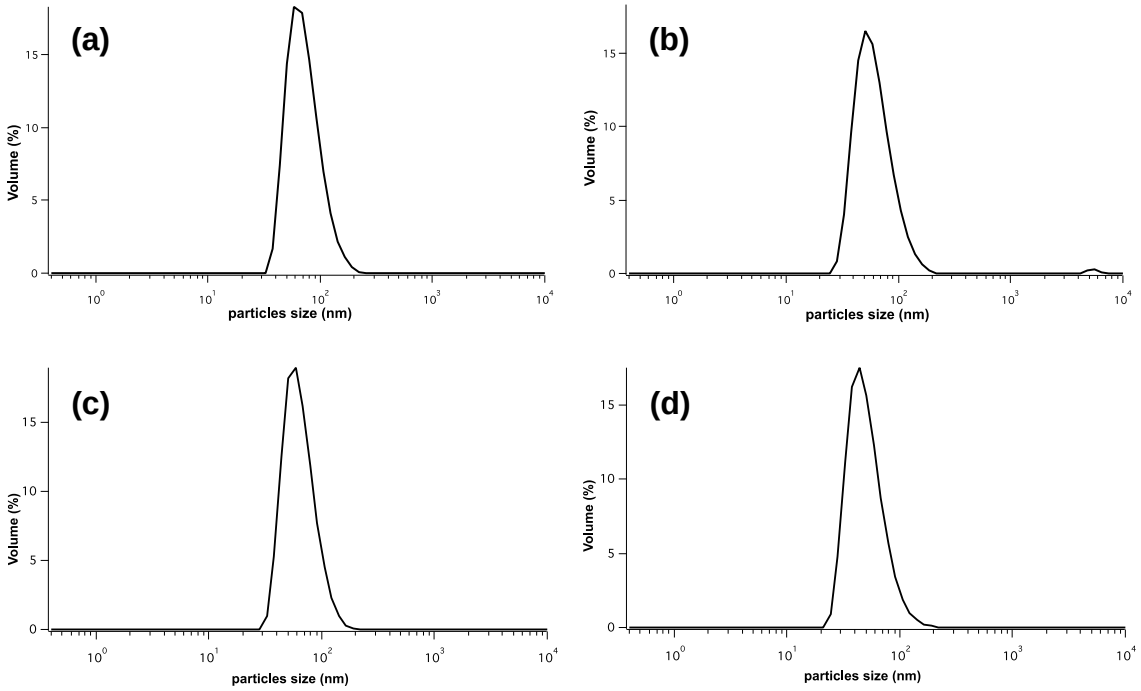

Figure 12. DLS analyses of LNP nanoparticles containing OA-KAT (0, 2.5, 5, 10 mol%) in Tris-HCl buffer (pH 8.0) at 25 °C. DLS mean (width): (a) LNP 70 nm (27 nm); (b) **LNP-KAT** (2.5 mol%) 60 nm (25 nm); (c) **LNP-KAT** (5 mol%) 63 nm (24 nm); (d) **LNP-KAT** (10 mol%) 49 nm (20 nm).

To assess the stability of LNP and **LNP-KAT**, DLS measurements were performed on the nanoparticle suspensions 7 and 14 days after preparation. As shown in Figure 13, all the samples showed a unimodal distribution, without significant differences. The DLS result showed that the particles can be stored as suspension in Tris buffer (pH 8.0) at 4 °C for at least 14 days without the occurring of particles aggregation.

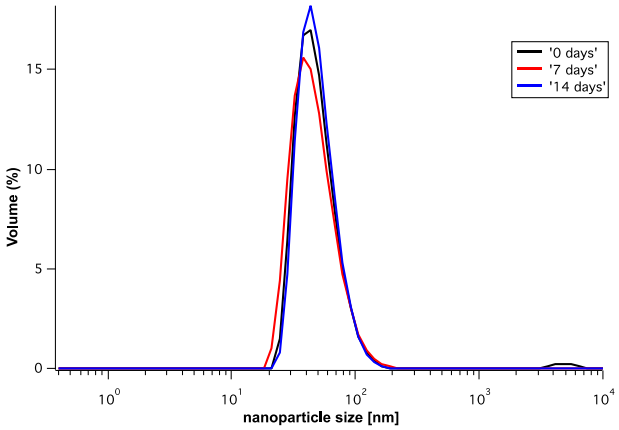

Figure 13. DLS of **LNP-KAT** (5 mol%) stored in Tris buffer (pH 8.0) at 4 °C, after 0, 7, 14 days from the preparation.

The TEM and cryoTEM images of LNP and **LNP-KAT** (0, 10 mol% KAT) were recorded (Figure 14). TEM images were obtained by negative staining technique,[129,130] in which the specimen is surrounded by heavy metal atoms that constitute an electron barrier. In principle, the electron beam can pass through the low electron density of the specimen but not through the metallic background, resulting in a negative stained image with a bright specimen against a dark background. The condition (pH and concentration) of the staining solution and the duration of the staining varies according to specimen types. LNP nanoparticles were initially stained with a solution of uranyl acetate at pH 4.0 as an initial trial, but the formation of big aggregates was observed, presumably due to the acidic pH of the aqueous media.[131] In order to avoid such aggregation, the TEM images of LNP and **LNP-KAT** (10 mol%) were recorded using a solution of sodium phosphotungstate at pH 8.0 as a stain, resulting in images showing well-dispersed particles with a round morphology and suggesting the presence of an oily core in the nanoparticles (Figure 14a, b).

However, the protocol used for the LNP preparation it is reported to provide the concomitant formation of nanoparticles formed by a lipid monolayer surrounding an apolar lipid core and of vesicular structures. To further investigate about the coexistence of both kind of structures, LNP were also analyzed by cryoTEM technique. The samples were prepared by plunge freezing on grids and imaged at –180 °C. Often, sorting of the nanoparticles by size was observed in cryoTEM images (Figure 14d), with increasingly larger nanoparticles observed from the center to the edge of the cryoTEM grid. This observation can be explained by the grid support wettability, which causes an increase of the thickness of the frozen layer on the edge of the grid rather than at the center of the grid hole, thus determining

a size-dependent distribution of the nanoparticles on the grid.[132] The cryoTEM images showed the presence of particles with very similar morphologies both for LNP and **LNP-KAT**, confirming that the addition of OA-KAT **1** in the LNP formulation does not significantly affect their shape. Furthermore, the images indicated the contemporary presence of both nanoparticles with monolayer lipid structure, characterized by the presence of a uniform dark contrast, and of vesicular structures.

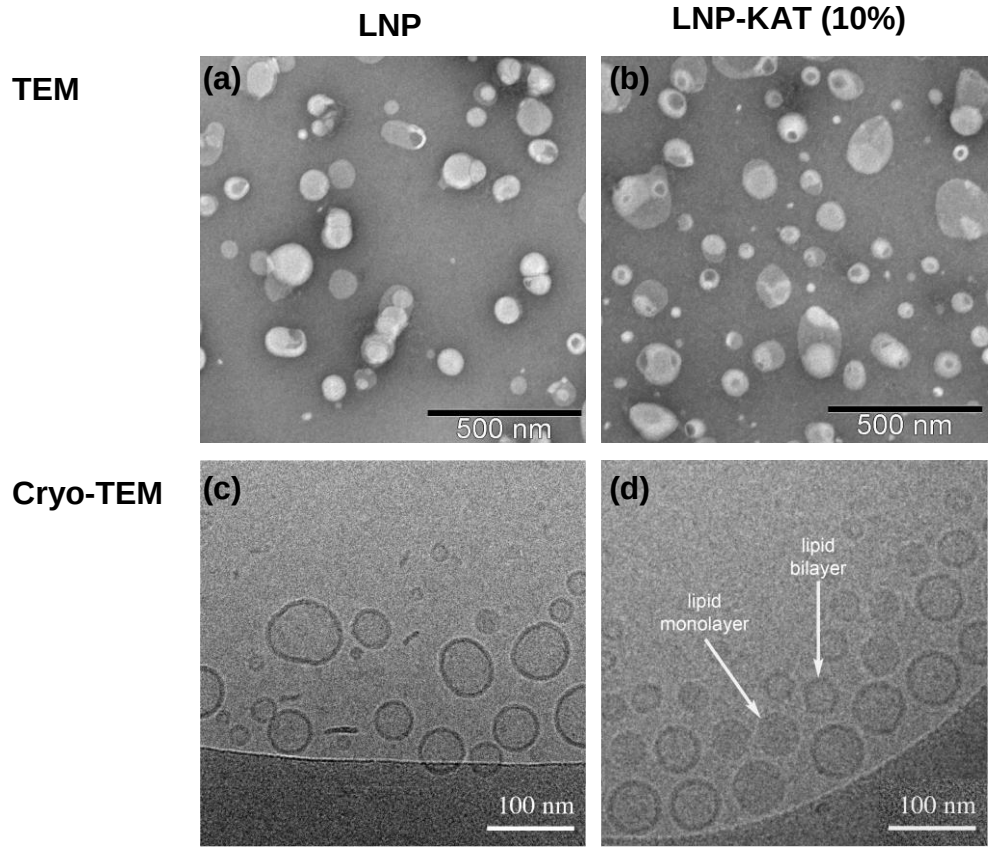

Figure 14. TEM and cryoTEM images of LNP (a, c) and **LNP-KAT** 10 mol% of OA-KAT **1** (b, d).

The effect of the presence of OA-KAT **1** on the LNP surface was also studied by measuring the Zetapotential. It was expected that magnitude of the Zetapotential would increase depending on the amount of OA-KAT **1** added in the **LNP-KAT**, since the potassium salt of acyltrifluoroborate was expected to be mostly dissociated in aqueous solution, thus determining a higher number of negative charges on the nanoparticles surface. The measurements were carried out in Tris-HCl buffer at the same conditions of pH, temperature and ionic strength. A clear trend was observed for the Zeta potential data of

LNP-KAT, showing that the Zeta potential increased with the amount of OA-KAT added in the **LNP-KAT** (Table 4).

Table 4. Zetapotential of LNP and **LNP-KAT** in TRIS-HCl buffer pH 8.0.

OA-KAT 1 (mol %)	Zeta Potential (mV)
0	– 15.0
2.5	– 17.0
5	– 27.2
10	– 68.2

2.5 Synthesis of carboxylate-terminated hydroxylamine linker (HA-COOH)

The Boc protected derivative **8** was prepared according to a literature protocol with slight modifications, (Scheme 9).[116] Briefly, the N-Boc protected hydroxylamine **5** was subjected to the reaction with diethylcarbamoyl chloride to provide compound **6**, which was further alkylated with ethyl 4-bromobutanoate, to give compound **7**. In the last step, the ester was hydrolyzed to provide the free hydroxylamine carboxylic acid (HA-COOH) **8** that was used to synthesize HA-derivatives.

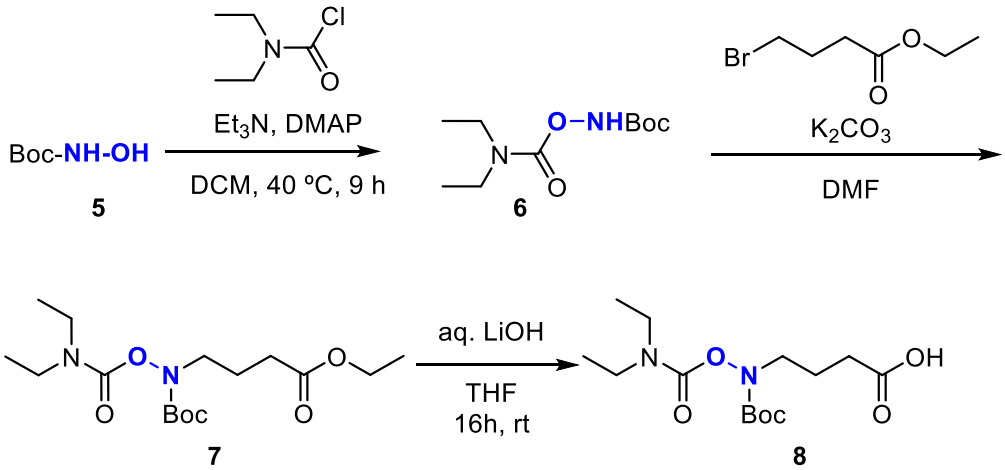

Scheme 10. Synthesis of the HA-linker **8**.

2.6 Synthesis of Hydroxylamine Fluorescein Derivative (HA-Fluorescein)

The HA derivative of fluorescein **13ab** was synthesized starting from the commercially available mixture of isophthalic and terephthalic carboxylfluoresceins as shown in Scheme 11. A fluorescein amine derivative **11ab** was prepared by amide coupling between N-Boc protected ethylenediamine and the carboxylfluoresceins **9ab**, followed by the TFA deprotection of the terminal amine. The obtained fluorescein derivative **11ab** was coupled with the Boc-protected HA-COOH **8** (synthesis described in 2.5) to provide **12ab** as a direct precursor of the HA-fluorescein **13ab**. The deprotection of compound **12ab** was carried out with a mixture of TFA-$CHCl_2$ (1:1) and the reaction was completed in 15 min (Figure 15 a,b). HA-fluorescein was stored in its protected form **13ab** and deprotected right before use. It was possible to isolate by HPLC the two isomeric forms of HA-fluorescein **13ab**. Since the UV and fluorescence spectra of both isomers were found to be identical, HA-fluorescein **13ab** was used as a mixture of the two isomers in KAT ligation.

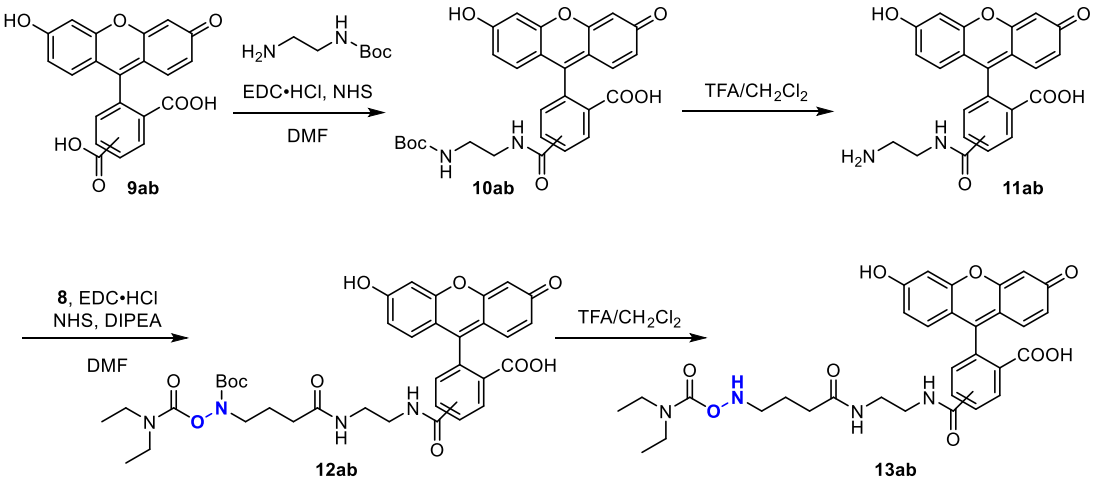

Scheme 11. Synthesis of the HA-fluorescein **13ab**.

2.7 KAT Ligation of OA-KAT and HA-fluorescein in Solution Phase

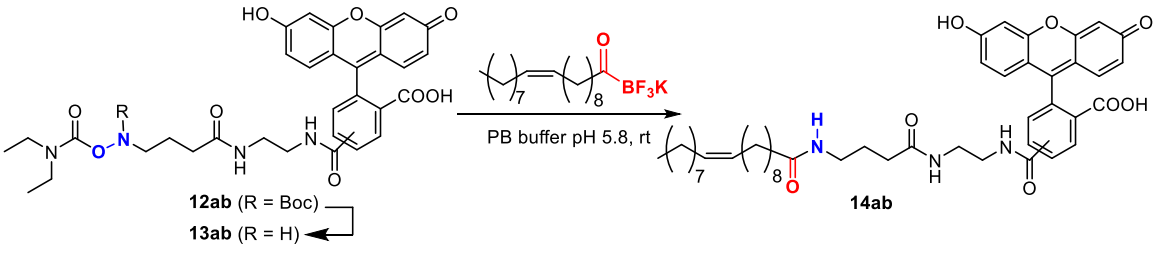

Scheme 12. KAT ligation of HA-fluorescein **13ab** with OA-KAT **1** in solution phase.

Prior to the reaction on **LNP-KAT** surface, KAT ligation between HA-fluorescein **13ab** and OA-KAT **1** (Scheme 12) was tested in solution phase. An equimolar concentration of **13ab** and **1** (50 µM) was used and the reaction was monitored by the LC-MS (Figures 15, 16). The Boc-protected HA-fluorescein **12ab** was deprotected by TFA to provide HA-fluorescein **13ab**, that was dissolved in a mixture of MeOH - 10 mM phosphate buffer (pH 5.8) (1:2, v/v). In parallel, a second solution of OA-KAT **1** in acetone -10 mM phosphate buffer (pH 5.8) (2:1, v/v) was prepared. An aliquot of each solution was added to 10 mM phosphate buffer (pH 5.8) to have a 1:1 mole ratio of each reagent (50 µM) and the reaction mixture was analyzed immediately. As clearly indicated by the LC-MS traces in Figures 15b, c and 16b, c, the ligation reaction between **1** with **13ab** completed in a couple of minutes at room temperature to quantitatively provide the oleyl fluorescein derivative **14ab** as a single product. No significant amount of side product was observed. Based on this rapid and efficient result obtained for KAT ligation in solution phase, this reaction was also tested for the direct functionalization of **LNP-KAT** surface.

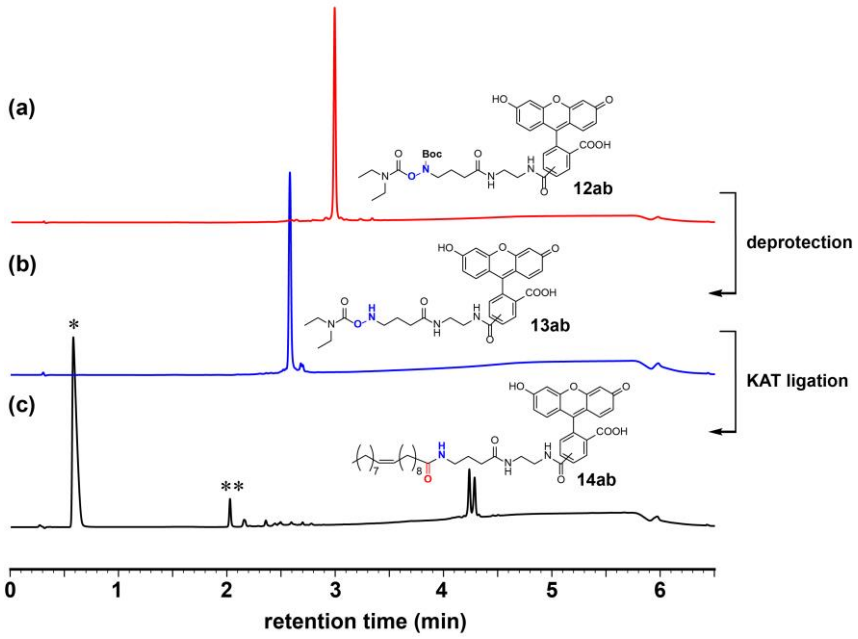

Figure 15. HPLC chromatogram of KAT ligation between OA-KAT **1** and HA-fluorescein **13ab** in solution phase (column: Aquity UPLC BEH C_{18} 1.7 µm (Φ 2.1 x 50 mm); eluent: MeCN-H_2O (2 – 98% in 4 min), 0.1% HCOOH; flow rate: 0.5 mL/min; detection: 254 nm). Chromatogram of (a) compound **12ab**, (b) reaction mixture of the deprotection step of HA-fluorescein **13ab**, (c) reaction mixture of KAT ligation showing the formation of **14ab** (*: solvent peaks and **: trace amount of impurity of benzotriazole from the previous reaction).

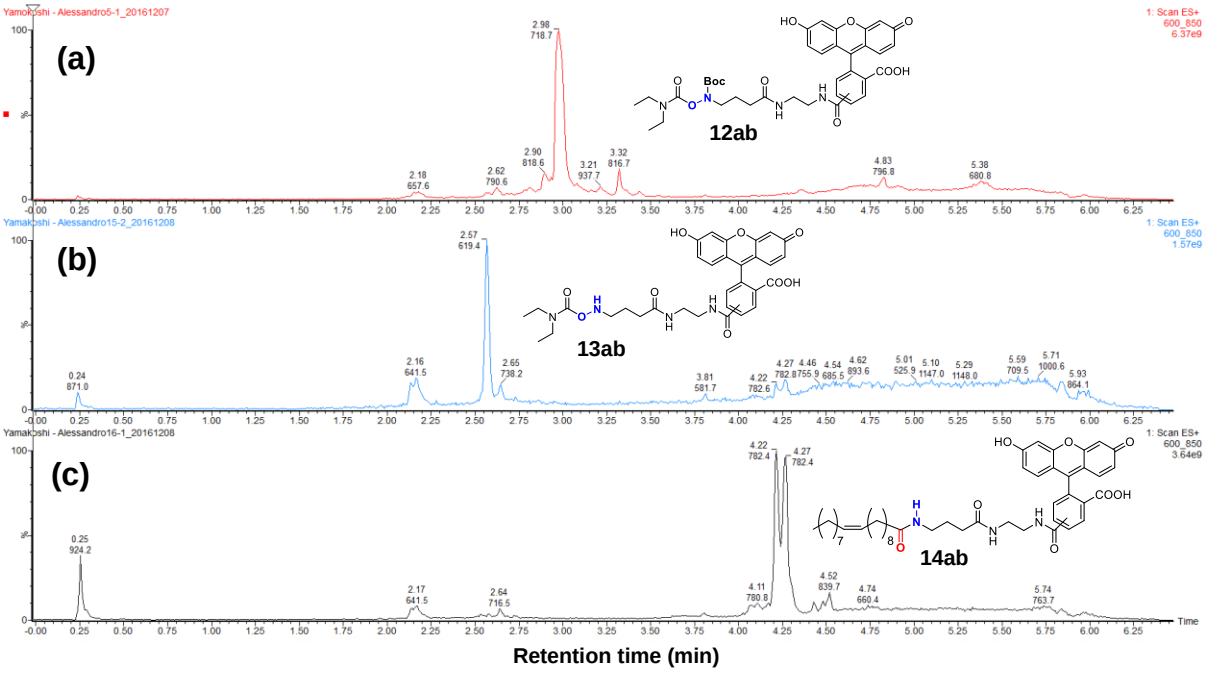

Figure 16. Extracted ion chromatograms (*m/z* 600 - 850 Da) of (a) Compound **12ab**, (b) reaction mixture of the deprotection of HA-fluorescein **13ab**, and (c) reaction mixture of KAT ligation showing the formation of the product **14ab**. (Micromass Autospec Ultima-EI-Sector-MS LC-MS system, column: Aquity UPLC BEH C_{18} 1.7 µm (Φ 2.1 x 50 mm), eluent: MeCN-H_2O (2 – 98% in 4 min), 0.1% HCOOH, flow rate: 0.5 mL/min.

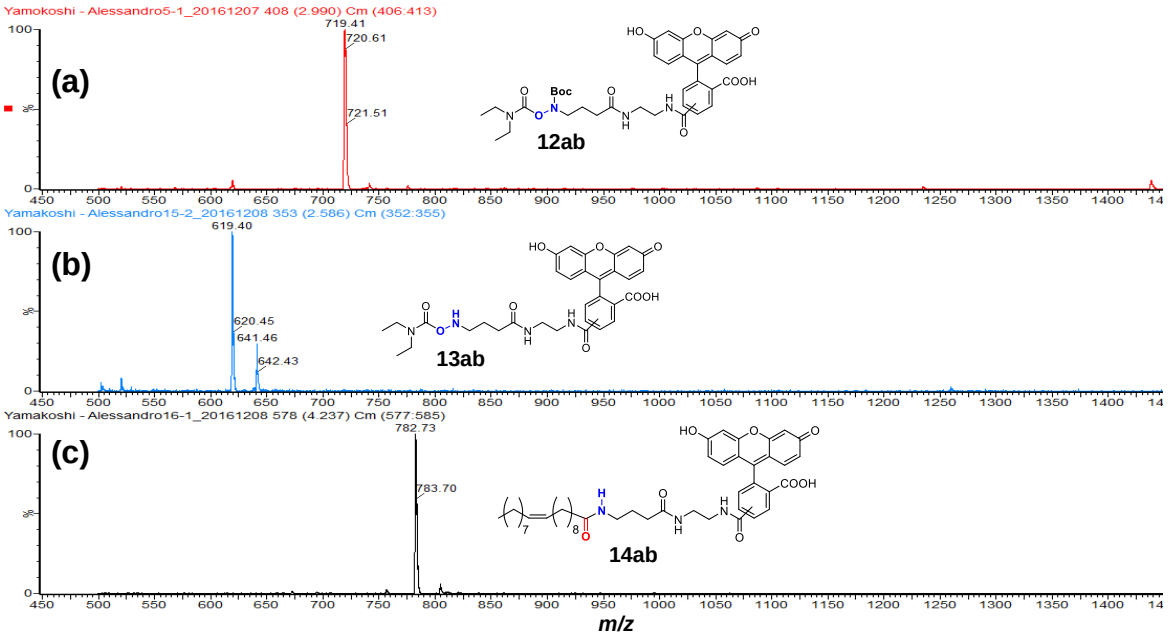

Figure 17. ESI mass spectra corresponding to the peaks of the chromatograms shown in Figure 16; (a) Compound **12ab**, (b) reaction mixture of the deprotection of HA-fluorescein **13ab**, and (c) reaction mixture of KAT ligation showing the formation of the product **14ab**.

2.8 Surface KAT ligation of LNP-KAT with HA-fluorescein

After the KAT ligation test in solution phase, KAT ligation was used for the LNP surface modification of **LNP-KAT** with HA-fluorescein **13ab** as substrate. **LNP-KAT** suspensions with 0, 2.5, 5, or 10 mol% of OA-KAT **1** were diluted 5 times with phosphate buffer (pH 5.8) and the pH was adjusted to pH 5.2. Immediately after deprotection of compound **12ab**, the obtained HA-fluorescein **13ab** was dried under nitrogen stream, dissolved in MeOH, and added to the **LNP-KAT** nanoparticles in a final concentration of 250 µM. Each reaction was carried out in the presence of the same amount of HA-fluorescein **13ab**, equivalent to the amount of OA-KAT **1** incorporated in **LNP-KAT** prepared with 10 mol% of OA-KAT **1**. The incorporated amount of **1** was estimated by boron ICP-MS as shown in Table 5. Each reaction mixture was stirred at room temperature for 12 h and the obtained LNP functionalized with fluorescein (**LNP-Fl**) was washed to remove the non-specifically bounded compound **13ab**. The initial attempt of washing **LNP-Fl** by dialysis was ineffective, presumably due to the hydrophobicity of the fluorescein attached. The purification was carried out by dialysis cassettes (ThermoScientific) with 20 kDa MW cutoff against a 500 times volume of phosphate buffer (pH 8.0), but even after 3 days of dialysis, changing the dialysis buffer every 24 hours, the excess of HA-fluorescein **13ab** could not be removed. Therefore, the use of different a dialysis membrane with a bigger pore size was also tried (SpectraLab, 100 kDa MW cutoff), but the yield of the fluorescein functionalization was unexpectedly low (around 10%, calculated based on the amount of boron in the **LNP-KAT** measured by ICP-MS). After the dialysis, the membranes were visibly yellow, and it was therefore hypothesized that the low yield obtained after this dialysis purification method was due to the adsorption of **LNP-Fl** onto the dialysis membrane due to the different chemical composition of the membrane material (cellulose) that have affinity with **LNP-Fl**. To address this problem, the spin centrifuge filtration was attempted as purification method. This strategy allowed to use the same membranes material utilized in the first dialysis (polyethersulfone), which did not show affinity for the particles, and a much bigger MW cutoff (100 kDa MW cutoff). The particles were washed 5 times with 10 mM phosphate buffer (pH 8.0) providing a yield of surface KAT ligation around 50% (Table 5). The obtained **LNP-Fl** were characterized by UV-vis, fluorescence spectroscopy, and DLS (Figure 18).

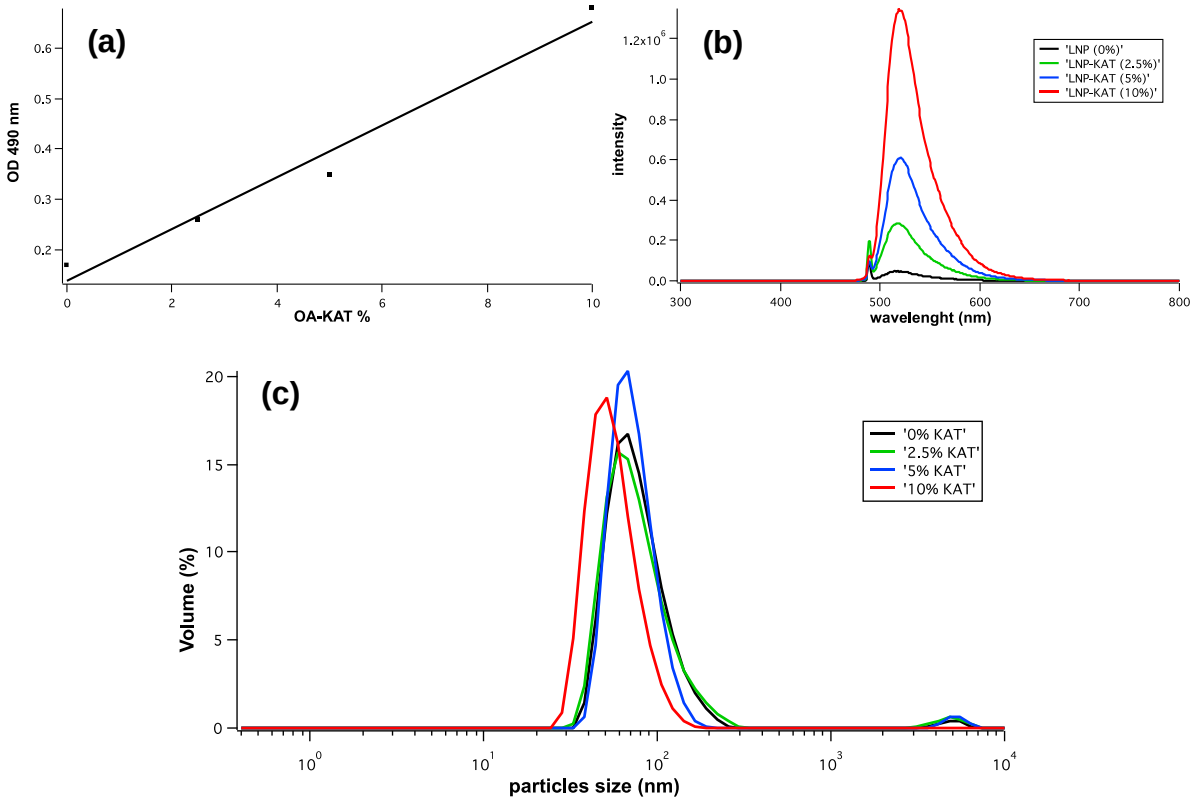

Figure 18. Characterization of **LNP-KAT** (0, 2.5, 5, and 10 mol% of OA-KAT **1**) functionalized by KAT ligation with HA-fluorescein derivative **13ab**. (a) OD_{490} (y = 0.052x + 0.1 (Pr = 0.98)); (b) fluorescence spectra, (excitation: 490 nm) and (c) DLS of the obtained **LNP-Fl**. DLS mean (width): OA-KAT 0 mol% 74 nm (30 nm); 2.5 mol% 72 nm (30 nm); 5 mol% 71 nm (25 nm); 10 mol% 55 nm (18 nm).

The UV-vis measurement of the **LNP-Fl** samples showed absorbance with maximum at 490 nm corresponding to the one of the fluorescein moieties. The fluorescent emission was obtained at 520 nm. In both UV-vis and fluorescence spectra, the intensities were in good correlation to the relative amount of OA-KAT **1** in the LNP, indicating that the fluorescein moiety was covalently bound to the LNP surface *via* KAT ligation (Figure 18a, b). The size of all **LNP-Fl** was determined again by DLS after KAT ligation in order to verify that no aggregation occurred during the reaction. All the **LNP-Fl** in 10 mM phosphate buffer showed a unimodal distribution of **LNP-Fl** resulted with particle size of about 40-70 nm (Figure 18c). This result indicated that the functionalization of the particle surface with fluorescein moiety proceeded fast and efficiently in aqueous solution under diluted condition. Taken together, these results show that the covalent surface modification was possible by KAT ligation in a dose dependent manner, and that the obtained functionalized LNP resulted well-dispersed without detectable aggregation.

To further evaluate the efficiency of surface KAT ligation, quantitative analyses were performed to compare the amount of the attached fluorescein in **LNP-Fl** (determined by fluorescence), to the B contents in the LNP before and after KAT ligation (determined by ICP-MS). The reaction yield obtained by the two complementary methods indicated that ca. 50% of the OA-KAT incorporated in **LNP-KAT** reacts in the surface KAT ligation. This reaction yield is in accordance with the cryoTEM data, further suggesting the presence of vesicles in the LNP formulation. Indeed, all the OA-KAT **1** incorporated in the inner layer of vesicular structures would be unable to react with the HA-Fluorescein **13ab** added to the LNP dispersion. Furthermore, the amide bond formation to produce the OA-fluorescein product **14ab** in **LNP-Fl** was confirmed by LC-MS measurements of **LNP-Fl** dissolved in MeOH (Figure 19).

In conclusion, the surface KAT ligation of **LNP-KAT** has shown to be a useful method for the functionalization of LNP through stable covalent amide bond. Importantly, the attachment of the fluorescein onto the LNP surface shows that **LNP-KAT** can be used as a platform LNP for the preparation of nanoparticles functionalized with a variety of organic molecules, such as drugs and imaging probes, for the preparation of lipid-based delivery systems.

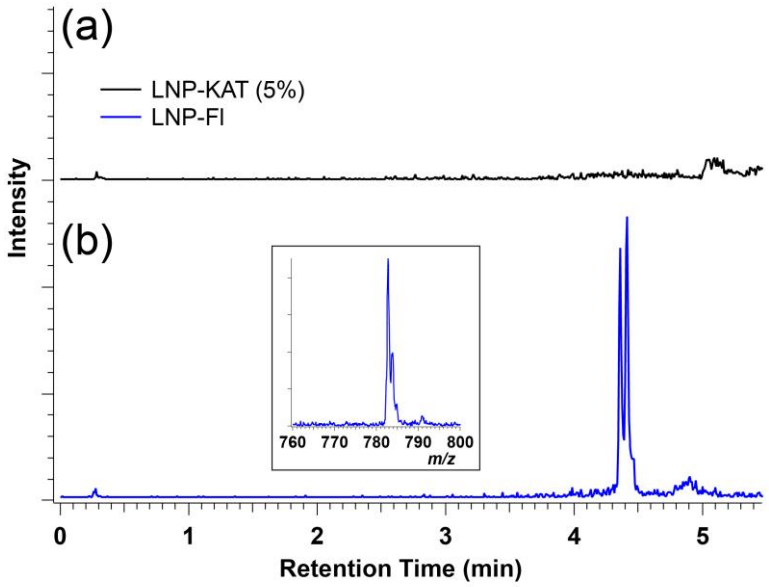

Figure 19. Extracted ion chromatograms (*m/z* 782 ±2 Da, corresponding to the mass of OA-fluorescein **14ab**) of (a) **LNP-KAT**, and (b) **LNP-Fl** measured by LC-MS (Micromass Autospec Ultima-EI-Sector-MS LC-MS system, column: Aquity UPLC BEH C_{18} 1.7 µm (Φ 2.1 x 50 mm), eluent: MeCN-H_2O (2 – 98% in 4 min), 0.1% HCOOH, flow rate: 0.5 mL/min.

Table 5. Quantitative analyses of **LNP-KAT** and **LNP-Fl** by ICP-MS and fluorescence.

LNP-KAT (before ligation)			**LNP-Fl (after ligation)**			
OA-KAT (mol%) initially added (μM)[a]	B content by ICP-MS (μM)[b]	incorporation yield of OA-KAT (%)	B contents by ICP-MS (μM)[c]	% of reacted KAT[d]	conc. of fluorescein (μM)[e]	yield fluorescein addition (%)[f]
2.5 (625)	230	37	120	48	110	48
5 (1250)	502 ±7.5	40 ±0.6	253 ±7.2	50	240 ±20	48 ±4.7
10 (2500)	1200	48	430	64	523	44

Concentration of B [a]initially added for the preparation of **LNP-KAT** nanoparticles, [b]in the **LNP-KAT** nanoparticles at the end of the preparation protocol, [c]in the **LNP-Fl** particles after functionalization. [d]Calculated from the difference of B contents before and after the reaction. [e]Based on fluorescence emission at λ_{em} = 520 nm. [f]Calculated from the fluorescein amount found after the reaction.

2.9 Conclusion

In conclusion, lipid nanoparticles equipped with a chemically active moiety (KAT) for the covalent surface modification were prepared by mixing OA-KAT **1** with three kinds of lipids (PC, TO, and CO), followed by sonication and extrusion. The obtained **LNP-KAT** showed uniform diameter of ca. 50 nm determined by DLS and TEM, in a suitable size range for the delivery of drugs and imaging probes. **LNP-KAT** was stable for at least 2 weeks in 10 mM Tris buffer in the presence of KF and BHT. The KAT ligation on **LNP-KAT** with the HA-fluorescein derivative **13ab** efficiently provided **LNP-Fl** with covalently attached fluorescein in a dose dependent manner as clearly detected by UV-vis absorption and fluorescent emission. The formation of covalent linkage between the OA and fluorescein product was further confirmed by LC-MS. The efficiency of the reaction was further evaluated by quantifying the amount of fluorescein attached and the boron contents before and after the surface functionalization, to provide a yield of ca. 50% relative to the total amount of OA-KAT **1,** detected in LNP-KAT. These results indicate that the **LNP-KAT** nanoparticle can be efficiently covalently functionalized by KAT ligation, suggesting that a

variety of biorelevant molecules may be stably attached on its surface through amide bond formation.

Chapter 3

Preparation of low-density lipoprotein (LDL) mimetic lipid nanoparticles by KAT ligation, and application as MRI-CA for the targeted imaging of atheroplaques in vivo

The work presented in this chapter was conducted in collaboration with Prof. Dr. Rong Zhou and Jianbo Cao (University of Pennsylvania), who performed all the *in vivo* animal tests. Cell culture studies were performed by Dr. Naoko Yoshizawa-Sugata and Dr. Hisao Masai (Tokyo Metropolitan Institute of Medical Science). Relaxivity measurements were carried out by Prof. Dr. Éva Tóth (University of Orléans). A manuscript is in preparation for publication.

3. Preparation of low-density lipoprotein (LDL) mimetic lipid nanoparticles by KAT ligation, and application as MRI-CA for the targeted imaging of atheroplaques *in vivo*

3.1 Background

Chapter 2 describes the preparation of **LNP-KAT** particles and their covalent functionalization by HA-fluorescein, showing that **LNP-KAT** can be used as a convenient method for the surface functionalization of LNP with HA derivatives. Based on the results showed in chapter 2, in this study the same KAT ligation LNP modification strategy was applied for the preparation of LNP as LDL-mimetic particles (sLDL), covalently attaching an apolipoprotein-mimetic peptide with affinity to atherosclerotic plaques. Furthermore, the use of the surface KAT ligation was expanded towards the multiple and simultaneous LNP functionalization by the attachment of a Gd-chelate moiety together with the mimetic peptide, in order to prepare atherosclerosis-selective MRI-CA. Ideally, MRI-CAs should be (1) easy to prepare from economic and biocompatible materials, (2) sterile (3) stable over long-term storage, (4) suitably sized for *in vivo* delivery, (5) suitable for a high payload of MRI-CAs (6) with high relaxivity at the imaging conditions used *in vivo*.

3.2 Design of sLDL with MRI-CA (sLDL-Gd)

A suitable design of sLDL can enable (1) easy preparation and purification of the sLDL; (2) high yield in the particles surface modification providing high MRI-CAs payload; (3) high exposure of the Gd-chelate to the water bulk, in order to favor their interaction with the water molecules of the tissues. In this work, in order to target atherosclerotic plaques, LNP bearing an apoB100-mimetic peptide and a Gd-chelate derivative of DOTA (Gd(DO3A-MA)) was designed as shown in Figure 20 (**sLDL-Gd**). The final nanoparticle structure was achieved through amide formation reaction (KAT ligation) on the LNP surface, between the OA-KAT **1** and HA-derivatives of the Gd(DO3A-MA) **15** or the mimetic peptide **16**. The design of the structure of HA-Gd(DO3A-MA) **15** was based on the structure of Gd(DOTA), with three carboxylic acids and one amide connected to the HA moiety, which can be used for the reaction with the **LNP-KAT**. In the Gd(DO3A-MA) moiety, the Gd^{3+} was coordinated to the four nitrogen atoms of the cyclen, to three oxygen atoms of the carboxylate and to one oxygen atom of the carbonyl group of the amide appendage (Figure 20), to provide the stable

Gd-chelate **15**. An apoB100-mimetic peptide, Gly-Thr-Thr-***Arg-Leu-Thr-Arg-Lys-Arg-Gly-Leu-Lys***-Leu-Ala, was used as a surrogate of the apoB100 lipoprotein. The peptide sequence highlighted in bold is the apoB100 peptide sequence responsible for the interaction with the LDL receptor.[85,133] The other amino acids are also part of the original sequence of the apoB100 protein and were added in the design of the mimetic peptide sequence in the current study in order to distance the targeting peptide from the LNP surface. This late-stage surface functionalization enables the peptide and the MRI-CA to be bound exclusively to the outer edge of the particles, allowing the targeting peptide to interact with the LDL receptor and the MRI-CA to be exposed to the bulk water which is necessary in MRI contrast enhancement.

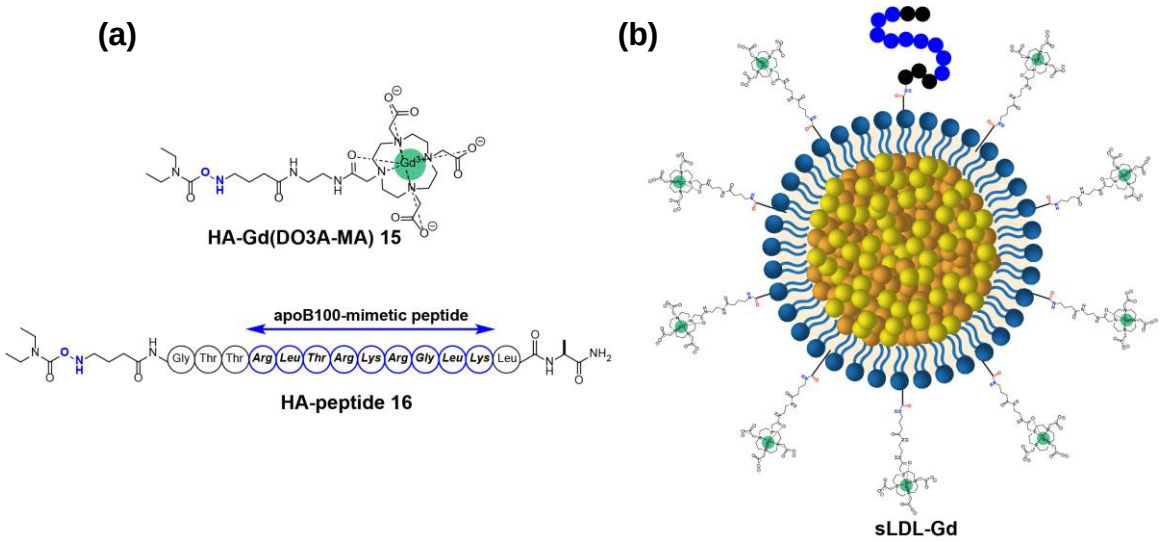

Figure 20. (a) Structures of HA- derivatives of Gd(DO3A-MA) **15** and apoB100 mimetic peptide **16**. (b) Schematic illustration of the **sLDL-Gd**.

3.3 Synthesis of hydroxylamine linker with NH_2-terminal (HA-NH_2)

The HA-NH_2 **18**, with a terminal free primary amine, was prepared as shown in Scheme 13. Briefly, compound **8** was subjected to the reaction with benzyl (2-aminoethyl)carbamate to provide a Cbz-protected amine **17**. The subsequent Cbz deprotection with H_2 and Pd/C provided the free primary amine HA derivative **18**, which can be used for the coupling of the HA-moiety with functional molecules that need to be attached to the LNP surface by KAT ligation.

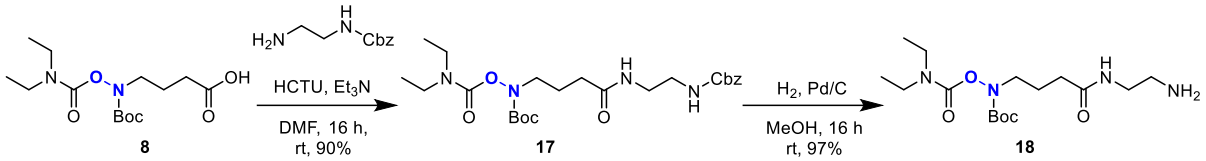

Scheme 13. Synthesis of HA-NH_2 **18**

3.4 Synthesis of hydroxylamine-Gd(DO3A-MA) derivative (HA-GdDO3A-MA)

The HA derivative of Gd(DO3A-MA) **15** was synthesized by the common strategy using orthogonal protective groups of carboxylic acids such as benzyl and *t*-butyl groups as shown in Scheme 14. The cyclen starting compound **19** was subjected to reaction with benzyl bromoacetate and *t*-Bu bromoacetate to provide the intermediate **21**. After selective deprotection of the *t*-Bu group, and coupling with HA derivative **18**, all the carboxylic acids of **23** were deprotected to provide compound **24** as a ligand to Gd^{3+}. Compound **25** was obtained by subsequent Gd^{3+}-chelation as an *N*-Boc protected direct precursor of the HA-(GdDO3A-MA) **15**. Compound **25** was purified by HPLC (Figure 21) and identified by HR-ESI-MS (Figure 22). The final step of deprotection of compound **25** with TFA quantitatively provided HA-(GdDO3A-MA) **15**, as monitored by LC-MS (Figure 23). The identification of the final compound HA-(GdDO3A-MA) **15** was further confirmed by HR-MALDI-MS (Figure 24).

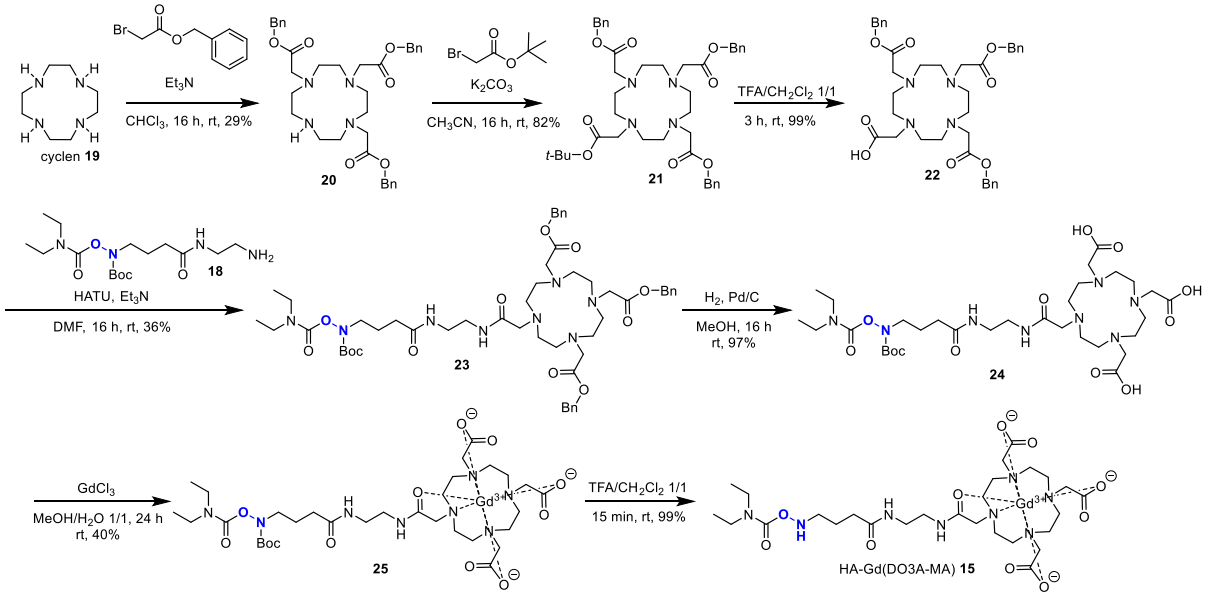

Scheme 14. Synthesis of HA-Gd(DO3A-MA) **15**

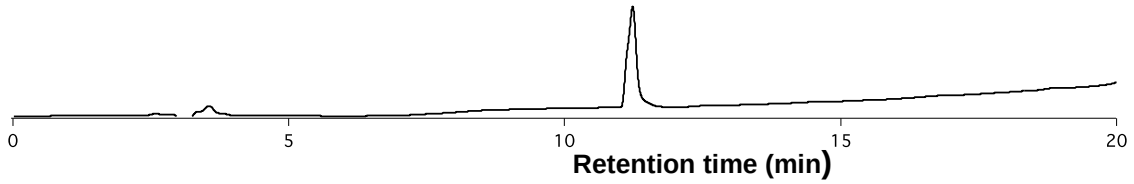

Figure 21. Analytical HPLC diagram of the purified compound **25** (column: Shiseido Capcell Pak C18 column (Φ 4.6 mm x 250 mm), eluent: gradient solvent system of CH_3CN-H_2O (10:90 to 98:2, over 20 min) in the presence of 0.1% TFA. Detection: 220 nm).

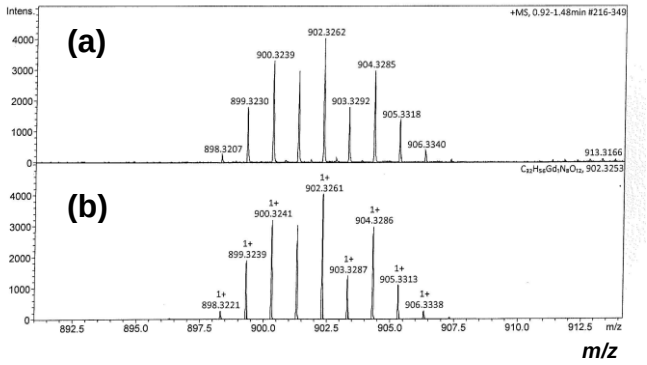

Figure 22. (a) Measured and (b) simulated HR-ESI spectra of compound **25**.

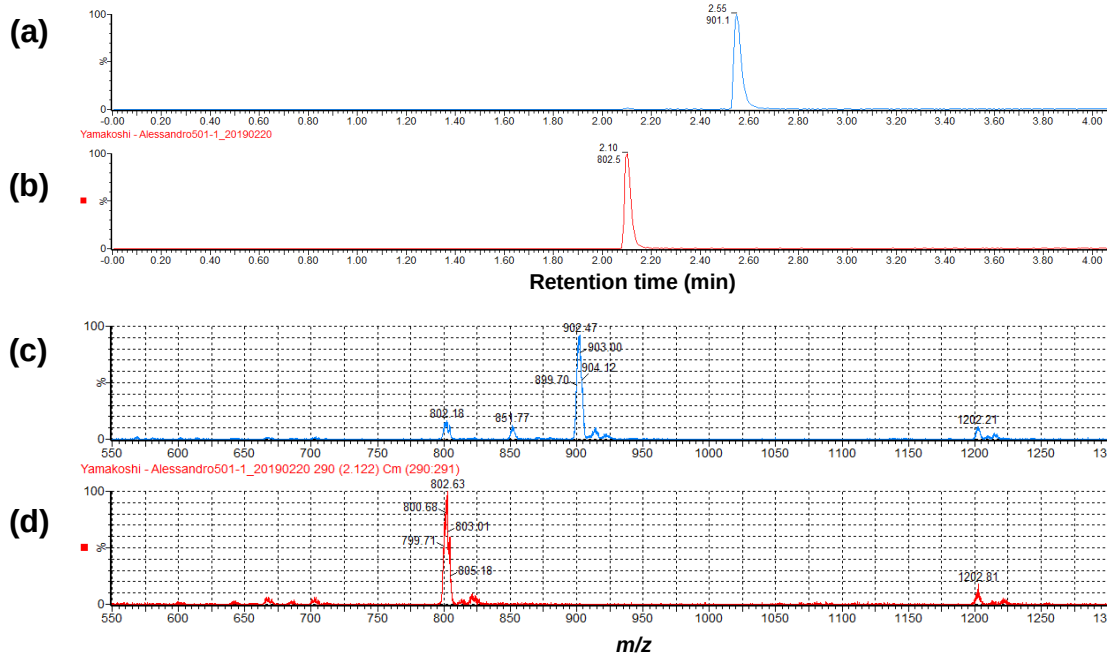

Figure 23. Extracted ion chromatogram (*m/z* 750-950) of (a) compound **25** and (b) crude deprotection reaction mixture after 15 min, with the corresponding (c,d) ESI-MS spectra of each peak. LC-MS detector: Micromass Autospec Ultima-EI-Sector-MS LC-MS system, column: Aquity UPLC BEH C18 (1.7 μm, Φ 2.1 mm x 50 mm); elution: CH_3CN-H_2O (2-98% in 4 min) with 0.1% (v/v) HCOOH, flow rate: 1.0 mL/min.

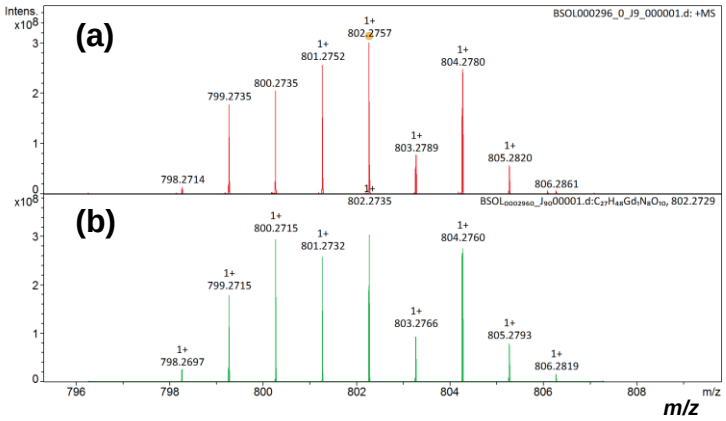

Figure 24. (a) Measured and (b) simulated HR-MALDI spectra of HA-Gd(DO3A-MA) **15**.

3.5 Synthesis of hydroxylamine derivative of apoB100-mimetic peptide (HA-peptide)

The HA-peptide **16** was synthesized by a standard solid phase peptide synthesis (SPPS) as shown in Scheme 15. The peptide **27** was obtained from the reaction of Rink-amide MBHA resin **26** with Fmoc-protected amino acids in the presence of HCTU as a coupling agent. After the addition of each Fmoc-protected amino acid, the Fmoc group at the N-terminus of the peptide was deprotected by 20% (v/v) piperidine in DMF, prior to the subsequent addition of the next Fmoc-amino acid. After completing the peptide synthesis, the N-Boc-protected HA-COOH **8** was attached to the N-terminus of the peptide **27** to obtain the HA-peptide derivative **28** on resin, as a direct precursor of HA-peptide **16**. In the last step, peptide **28** was treated with TFA and TIPS for the simultaneous (1) deprotection of all the amino acid side chains and N-Boc group of the HA moiety, and (2) cleavage of the peptide from the resin to provide HA-peptide derivative **16**. The purification of the fully deprotected peptide **16** was carried out by reverse phase HPLC (Figure 25) with confirmation by HR-MALDI-MS (Figure 26).

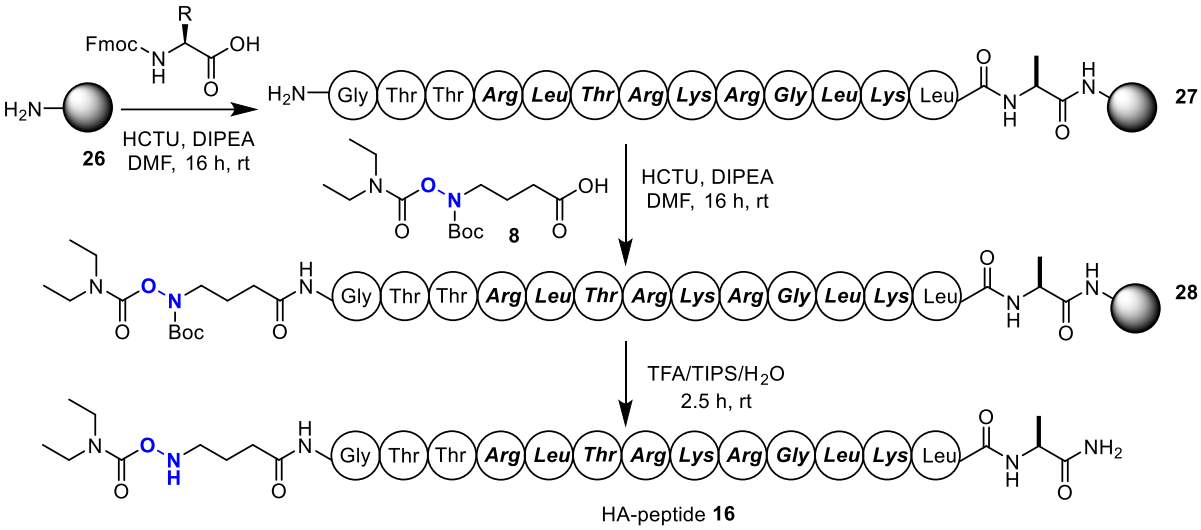

Scheme 15. Synthesis of HA-peptide **16**.

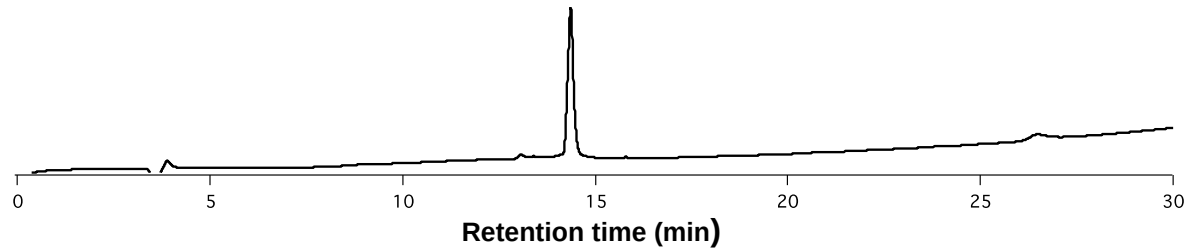

Figure 25. HPLC diagram of the purified HA-peptide **16** (column: Shiseido Capcell Pak C18 column (Φ 4.6 mm x 250 mm); solvent system: CH_3CN-H_2O with 0.1% TFA and a gradient of CH_3CN-H_2O (10:90 to 98:2, over 30 min); detection: 220 nm; flow rate, 1 mL/min).

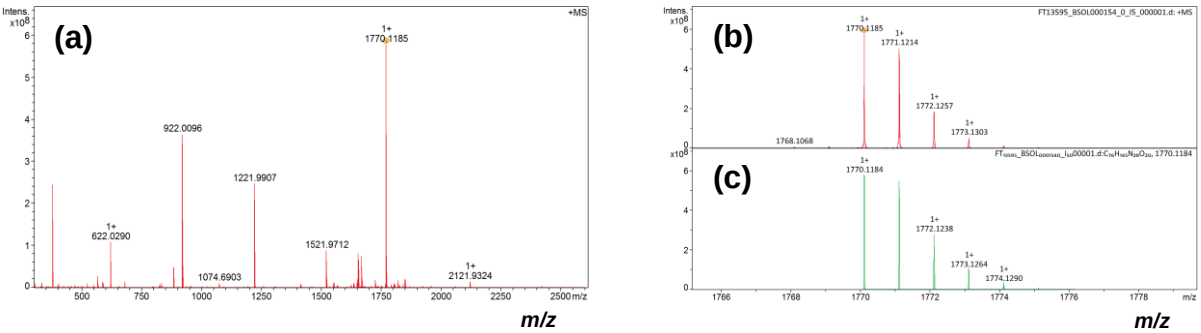

Figure 26. (a) HR-MALDI-MS of the purified HA-peptide **16**; (b) expansion of the measured and (c) simulated molecular ion peaks.

3.6 Preparation of sLDL-Gd by KAT ligation

3.6.1 KAT ligation of LNP-KAT with HA-Gd(DO3A-MA) 15 and HA-peptide 16

For the preparation of sLDL, the **LNP-KAT** with 5 mol% of OA-KAT (see section 2.4) was subjected to KAT ligation with a mixture of HA-Gd(DO3A-MA) **15** and HA-peptide **16** in mol ratio 9:1, for the simultaneous surface functionalization (Figure 27).

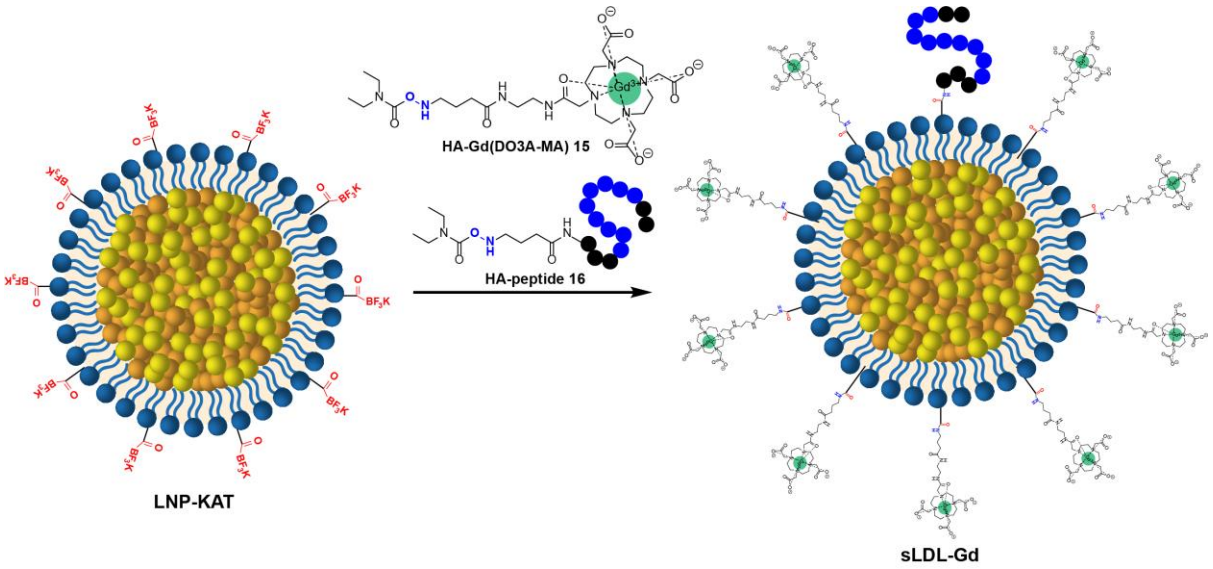

Figure 27. Illustration of the **LNP-KAT** functionalization.

Based on the ICP-MS quantitative analysis of the boron content (Table 6) in **LNP-KAT** for the determination of the incorporated OA-KAT, 1.2 equiv of HA derivatives were used in the reaction. The reaction was performed at rather low concentration of HA-derivatives (120 µM) since unfavorable aggregation of LNP was observed in the presence of higher concentration of HA-peptide **16** (Figure 28). The aggregation was presumably due to electrostatic interaction between the negatively charged BF_3^- moieties on the **LNP-KAT** surface and the positively charged HA-peptide **16**. Those interactions could not be disrupted by increasing the ionic strength of the aqueous media. The presence of high concentration of salt caused the **LNP-KAT** to precipitate, as monitored by DLS (Figure 29). The aggregation problem was solved performing the **LNP-KAT** functionalization under very diluted conditions, with a concentration of HA-peptide **16** (10 µM). The ligation was carried out at room temperature for 16 h under aqueous conditions (pH 5.2) and the obtained **sLDL-Gd** were washed by spin filtration with PBS (-) (pH 7.4) to remove the unreacted and non-specifically bound HA derivatives. The characterization of the **sLDL-Gd** was carried out by

DLS, AFM, cryoSEM, cryoTEM, ICP-MS, and MALDI-MS as described in the following sections.

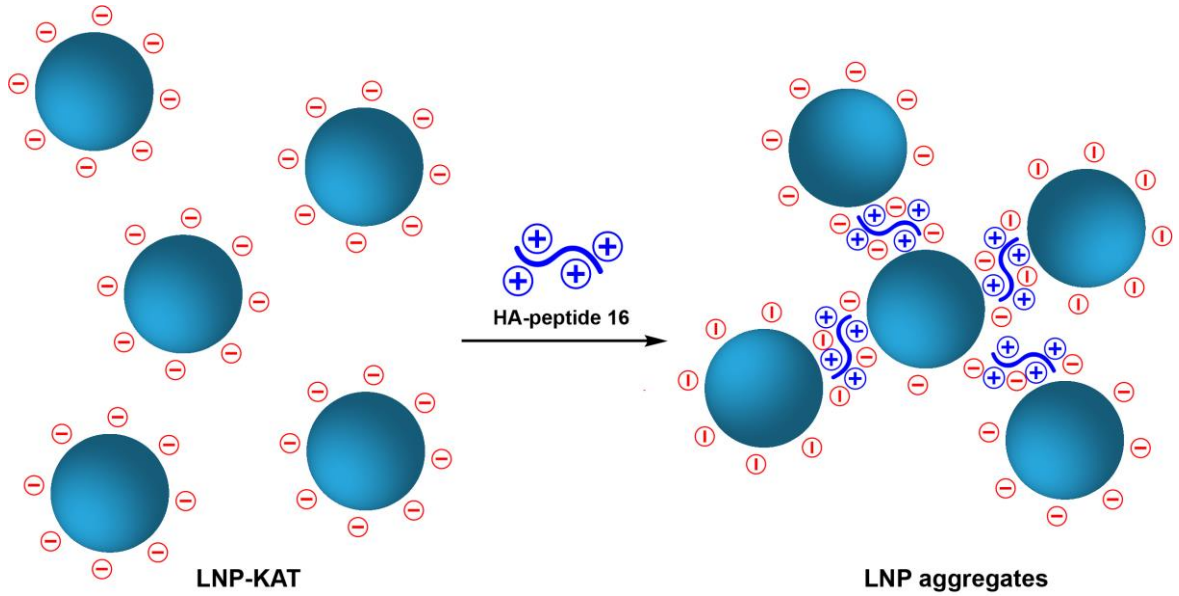

Figure 28. Schematic of LNP aggregation in the presence of HA-peptide **16**.

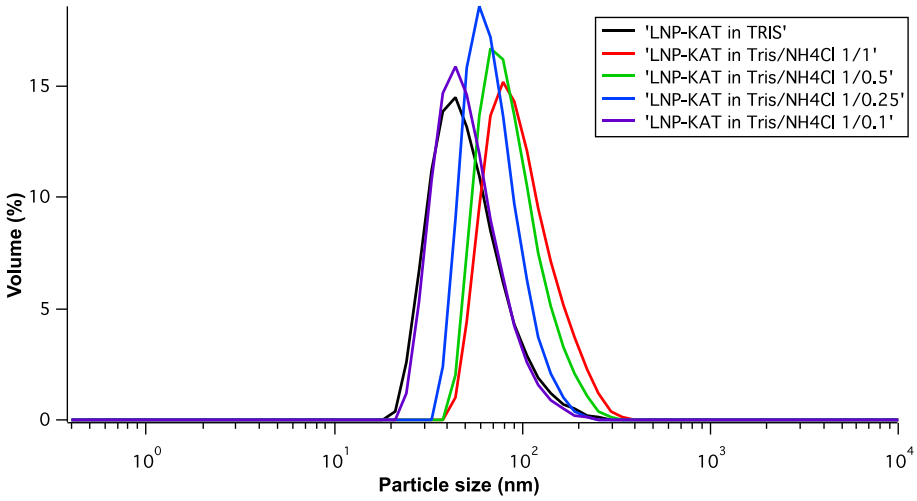

Figure 29. DLS of **LNP-KAT** in Tris buffer after adding a solution 3.73 M of NH_4Cl in several ratio (1/0.1, 1/0.25, 1/0.5, 1/1) showing that aggregation occurs with the increasing of the concentration of NH_4Cl. DLS mean (width): only Tris buffer, 50 nm (23 nm); Tris buffer-NH4Cl 1-1, 95 nm (42 nm); Tris buffer-NH_4Cl 1-0.5, 83 nm (34 nm); Tris buffe-NH4Cl 1-0.25, 68 nm (26 nm); Tris buffer-NH_4Cl 1-0.1, 51 nm (22 nm).

3.6.2 Characterization of sLDL-Gd

Size determination by DLS. To verify that no aggregation occurs upon KAT ligation, the size distributions of **LNP-KAT** and **sLDL-Gd** were determined by DLS. As shown in Figure 30, both particles revealed a unimodal distribution of diameter size around 50 nm, within the appropriate range for the *in vivo* delivery. The stability of **sLDL-Gd** was tested by dispersion over time. The DLS was measured on **sLDL-Gd** particles after 7 and 14 days of storage at 4 °C in PBS (-). The results indicate that **sLDL-Gd** were stably dispersed after 7, 14 days (Figure 31).

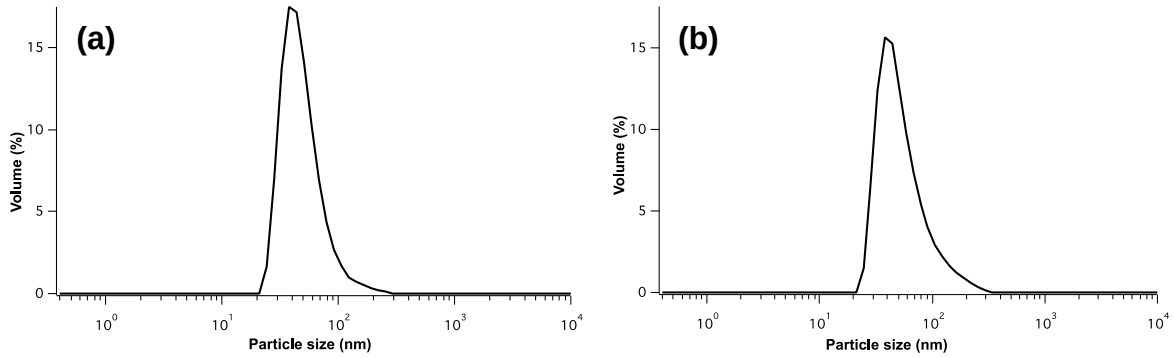

Figure 30. Size distribution of LNP before and after the surface functionalization. DLS mean (width) of (a) **LNP-KAT** 45 nm (18 nm) and (b) **sLDL-Gd** 47 nm (19 nm).

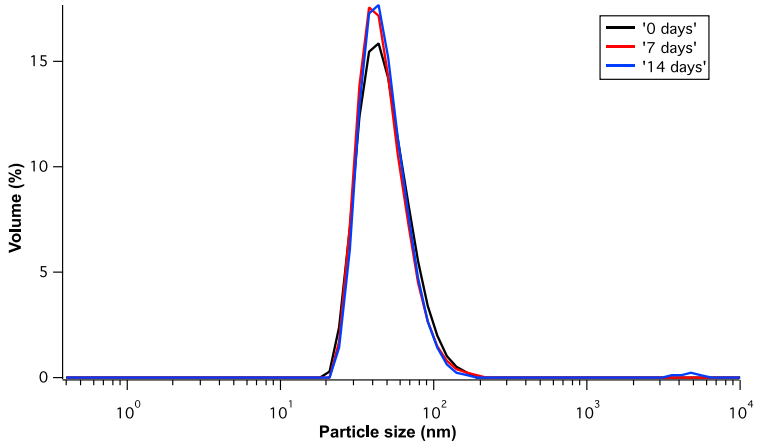

Figure 31. DLS stability test of **sLDL-Gd** after 0, 7 and 14 days of storage at 4 °C in PBS (-) buffer. DLS mean (width): 0 days, 48 nm (21 nm); 7 days, 46 nm (18 nm); 14 days, 47 nm (19 nm).

Microscopic analyses of the particles. To directly visualize if the LNP surface modification through KAT ligation affects the morphology of the LNP, microscopy analyses by AFM, cryoSEM and cryoTEM were performed on both **LNP-KAT** and **sLDL-Gd**. The samples for liquid-AFM were prepared by deposition onto a mica substrate and subsequent fixation with formalin. As shown in Figure 32a, b the particles were uniformly dispersed without any significant aggregation. In the cryoSEM images, the concentration of visible particles was lower compared to the other methods. In freeze-fractured samples, the topography represents only one random plane of the frozen volume. The fracture through the bulk reveals only the dispersed particles present in the plane, where the fracture passes through. The fracture goes along the interface between the particles and the medium, leaving either the negative imprint or the topography of protruding particles (Figure 31c, d). For the cryoTEM imaging, the samples were prepared by plunge freezing on grids and imaged at – 180 °C without staining (Figure 32e, f). The results of the microscopy analyses indicate that the morphology and size of the particles are retained after the surface modification through KAT ligation, in good agreement with the DLS data.

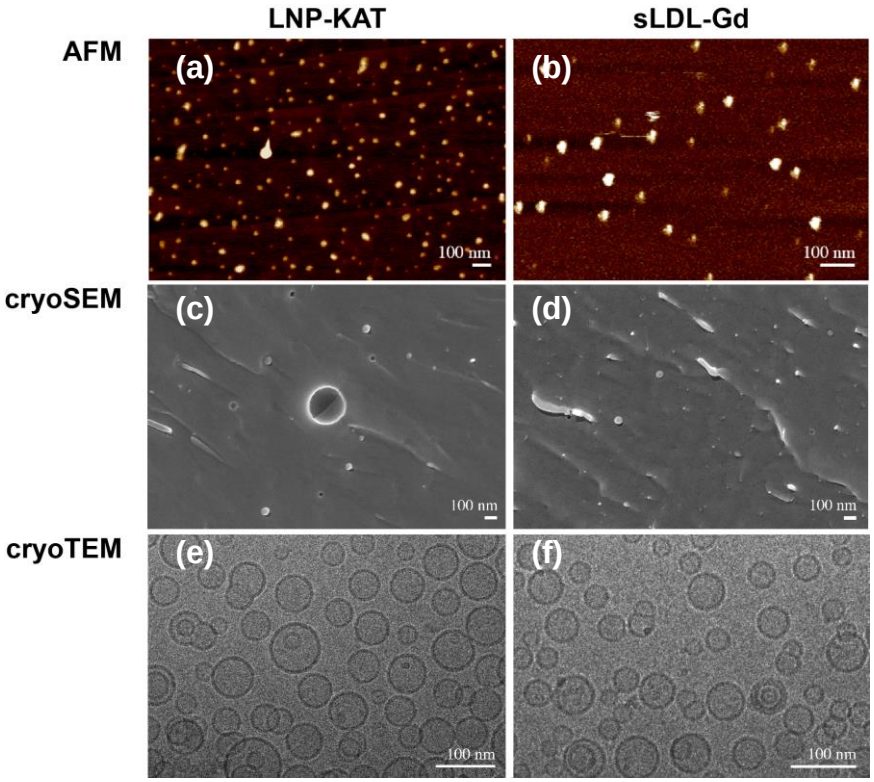

Figure 32. Microscopy images of (a, c, e) **LNP-KAT** and (b, d, f) **sLDL-Gd** measured by (a, b) AFM, (c, d) cryo SEM and (e, f) cryoTEM.

Reaction efficiency of surface KAT ligation by ICP-MS. To evaluate the efficiency of the LNP surface modification, quantitative analyses of B (starting material) and Gd (product) contents were performed by ICP-MS on the **LNP-KAT** and **sLDL-Gd** before and after KAT ligation. It was expected that, if no side reaction occurred, the decrease of the B amount in the **sLDL-Gd** would be comparable to the amount of the attached Gd. As summarized in Table 6, the B content of the **LNP-KAT** (514 µM) and **sLDL-Gd** (227 µM) indicated that ca. 56% of the OA-KAT **1** initially incorporated in the **LNP-KAT** was consumed during the reaction, in reasonable agreement with the Gd content found in the **sLDL-Gd** (217 µM**)**, which provided a yield of 47%. The yields obtained for the preparation of **sLDL-Gd** are in agreement with the expectations, and confirm the results reported in the section 2.8 for the surface functionalization of LNP with HA-fluorescein **13ab**. Furthermore, the conversion yield of the particles functionalization, calculated taking into account that the HA derivatives were used in a 9:1 mixture of HA-Gd(DO3A-MA) **15** and HA-peptide **16**, provided a value of 85% suggesting that no side reaction took place during the surface modification. These results clearly indicated that KAT ligation proceeded efficiently at room temperature under dilute aqueous conditions (120 µM of HA derivatives, 1.2 equiv) without the occurring of any significant side reactions.

Table 6. ICP-MS analyses of **LNP-KAT** and **sLDL-Gd** for the determination of B and Gd.

	Contents of B^{3+} (µM)	**Consumed B^{3+} (%)**	**Contents of Gd^{3+} (µM)**	**Reaction yield (%)**	**Conversion yield (%)**
LNP-KAT	514[a]	–	–	–	–
sLDL-Gd-5 (n = 3)	227 ±20[b]	56 ±3.8	217 ±5.2[c]	47 ±1.0[d]	85 ±6.8[e]

[a]Total amount of B in the **LNP-KAT** before the reaction. [b]Amount of B in **sLDL-Gd**, after the reaction. [c]Amount of Gd^{3+} in **sLDL-Gd**, after the reaction. [d]Reaction yield and [e]conversion yield of Gd^{3+} attachment, taking into account that 10% of HA derivatives in the reaction was HA-peptide **16**.

MALDI-MS analyses of sLDL-Gd. To confirm that the LNP surface modification proceeded covalently, the MALDI-MS analysis for the detection of the KAT ligation products of **sLDL-Gd** particles was carried out. An aliquot of **sLDL-Gd** was dried by N_2 flow, mixed with a matrix, and subjected to the HR-MALDI-MS measurements. Molecular

peaks corresponding to both ligation products, OA-Gd(DO3A-MA) and OA-peptide, were clearly observed, whereas no residual trace of HA-derivatives **15** or **16** was detected, as shown in Figure 33. These results indicate that all the unreacted starting materials could be efficiently washed away, confirming that the Gd content in Table 6 solely corresponded to the covalently bound Gd(DO3A-MA), further validating the high yield of the surface modification obtained.

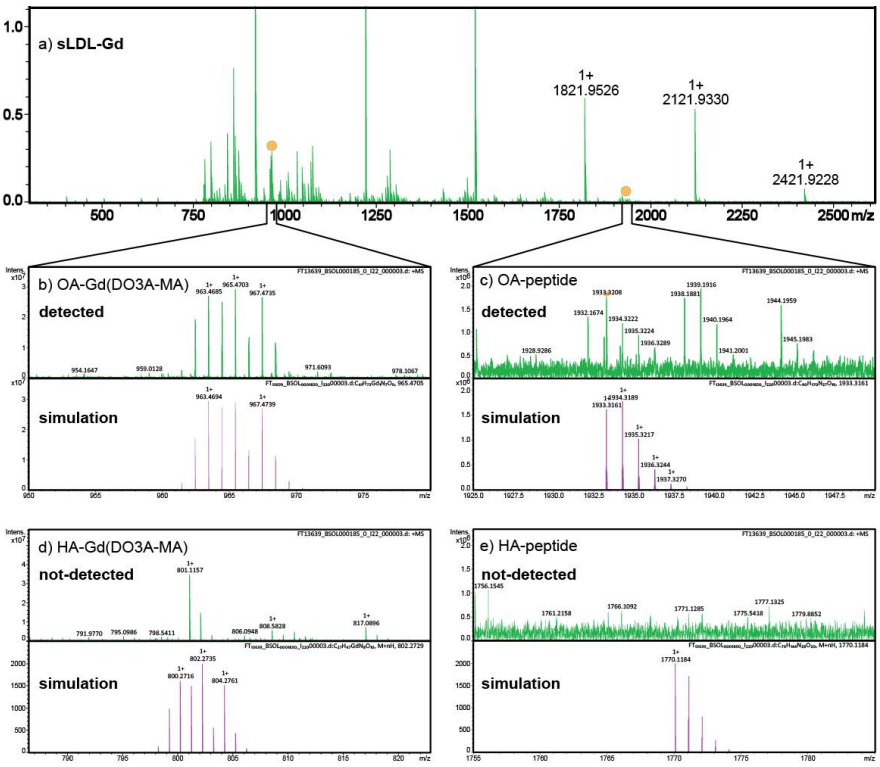

Figure 33. HR-MALDI-MS spectrum of the KAT ligation products in **sLDL-Gd** (a) Spectrum with a broader molecular weight range, (b) expansion at the molecular peak of OA-Gd(DO3A-MA) (*m/z*: $[M+H]^+$ found 965.4703), (c) and OA-peptide (*m/z*: $[M+H]^+$ found 1933.3208). The (d) and (e) show that there are no detectable peaks of unreacted compounds HA-Gd(DO3A-MA) **15** and HA-peptide **16**.

Relaxivity of sLDL-Gd. Relaxivity measurements were carried out in the laboratory of Prof. Dr. Éva Jakab Tóth at the Centre de Biophysique Moléculaire, CNRS, France. The ability of an MRI-CA to induce a contrast enhancement is highly correlated to its r_1 value. It is known that shortening of the rotational correlation time of the Gd^{3+}-chelate significantly increases r_1 relaxivity value of the contrast agents (see section 1.3.1). The **sLDL-Gd** was therefore expected to have a higher r_1 than small molecules CA. As expected, the proton longitudinal

relaxation rate ($1/T_1$) of **sLDL-Gd** at 1.4 T / 60 MHz at 25 °C provided an r_1 of 22.0 $s^{-1}mM^{-1}$, which was much higher than the small molecule contrast agent, ProHance® (Bracco Spa, Milano, Italy), with r_1 = 4.0 $s^{-1}mM^{-1}$ (1.4 T / 60 MHz at 25 °C). The relaxivity of a CA changes with the experimental conditions. In particular, r_1 decreases with the increasing of the magnetic field and temperature employed for the MRI scanning. Consequently, it is very important to determine the r_1 value at the same conditions used for the *in vivo* tests. The relaxivity of **sLDL-Gd** was measured at 9.4 T / 400 MHz at 37 °C providing a value of 8.2 $s^{-1}mM^{-1}$, which was also significantly higher than the r_1 of ProHance® (2.6 $s^{-1}mM^{-1}$ at 9.4 T / 400 MHz, 37 ºC). These results show the convincing potential of this **sLDL-Gd** for the *in vivo* detection of atheroplaques, with both functions of targeted delivery to the atherosclerosis diseased tissue and the higher relaxivity.

3.6.3 *In vitro cellular* incorporation of sLDL-fluorescein

In cellulo assays were carried out in the laboratory of Dr. Masai and Dr. Yoshizawa-Sugata at the Tokyo Metropolitan Institute of Medical Science, Tokyo, Japan. The internalization of the functionalized LNP was evaluated by using two cell lines, THP-1 (a human monocyte cell line) and RAW 264.7 (a mouse macrophage cell line). A fluorescent sLDL (**sLDL-Fl**), prepared using a 9:1 mixture of HA-fluorescein **13ab** and HA-peptide **16**, was used in this assay. THP-1 and RAW 264.7 cells in log-phase were co-incubated with **sLDL-Fl** for 5 h or overnight. After removing the culture media, the cells were washed thoroughly with PBS (-) to remove non-specifically-bound particles on the surface of the cells and the incorporation of **sLDL-Fl** was evaluated by fluorescence microscopy. As shown in Figure 34, **sLDL-Fl** particles were significantly incorporated in both THP-1 and RAW 264.7 cell lines without significant cytotoxicity. In order to verify the effect of HA-peptide **16** on the cellular uptake of **sLDL-Fl**, control experiments using **LNP-Fl** without peptide were carried out on both cell lines. Interestingly, in the experiment with THP-1, the incorporation of **sLDL-Fl** was significantly more efficient than the experiments with **LNP-Fl** (2.05-fold fluorescence intensity [p value = 0.003] from three images taken by 20x magnification of Figure 34b, c), whereas no significant difference was observed in the experiments of RAW 264.7. These data indicate that the efficient incorporation of **sLDL-Fl** in undifferentiated THP-1 cells was presumably caused by the presence of the peptide on the particles. In comparison, mouse macrophage cell line RAW 264.7 cells quickly incorporated either **sLDL-Fl** or the control **LNP-Fl** without peptide after 5 h incubation, suggesting that the presence of the peptide did

not affect the cellular uptake of the **sLDL-Fl**. RAW264.7 are cells with massive phagocytic ability that may not distinguish LNP with or without apoB100 mimetic peptide. In summary, the data indicate that **sLDL-Fl** did not induce any cytotoxicity and their incorporation in certain types of cells like monocytic cells can be dependent on the associated peptide. On the other hand, the cells with massive phagocytic ability, e.g. RAW264.7 cells, did not distinguish the nanoparticles with or without the mimetic peptide in terms of particle internalization.

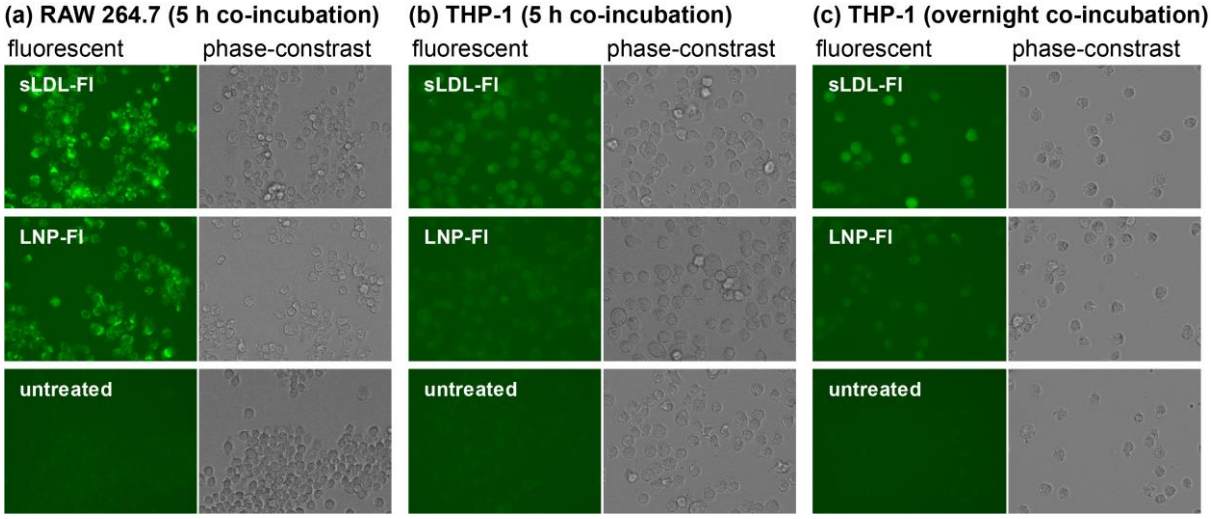

Figure 34. Incorporation of **sLDL-Fl** (top), **LNP-Fl** (middle), and untreated cells (bottom) into (a) RAW 267.4 after 5 h of co-incubation, (b) THP-1 after 5 h of co-incubation and (c) overnight co-incubation. The incorporation of the particles was observed by fluorescent microscopy. Magnification: x60 (including x3 digital zoom).

3.7 In Vivo MR imaging of atheroplaques in ApoE$^{-/-}$ mouse model

3.7.1 ApoE$^{-/-}$ atherosclerosis mouse model

In vivo MRI experiments were carried out in the laboratory of Prof. Dr. Rong Zhou at the University of Pennsylvania, Philadelphia, USA. To test the contrast enhancement by **sLDL-Gd** for the detection of atheroplaques, three atherosclerotic *apoE*$^{-/-}$ mice, fed on high fat diet (HFD) for 2 months, were subjected to MR imaging of the aortic arch. As a control experiment, the commercially available ProHance® was used. The experiment design involved (1) an initial MR imaging of the baseline of each mouse; (2) MRI of the mice 48 h post-injection of ProHance® (Gd^{3+} dose = 0.085 mmol/Kg); (3) MRI of the mice 48 h post-injection of **sLDL-Gd** (Gd^{3+} dose = 0.0176-0.051 mmol/Kg). For both ProHance® and

sLDL-Gd, 250 µL of each sample was administered *via* tail vein injection. To reduce the sample volume to 250 µL, the **sLDL-Gd** were concentrated by spin filtration right before the injection. Due to long intervals between MRI sessions, we relied on the unique anatomy of the aortic arch and its branching points and other thoracic arteries in the imaging plane for the comparison of pre- and post-injection images. To properly identify the trachea and better visualize the aortic arch branches, we acquired both white blood (WB) images (Figures 35, 36, 37 (a, b, e, f, i, j)), in which the MR signal from the blood appears white, and black blood (BB) images (Figures 35, 36, 37 (c, d, g, h, k, l)), in which the blood signal was suppressed, thus appearing black. For images acquired after **sLDL-Gd** injection, BB was further combined with fat suppression option in the MRI protocol although such option is not necessary to detect enhancement. The baseline images show that it was not possible to distinguish the atheroplaques from the arterial wall without the use of a contrast agent (Figures 35, 36, 37). In addition, very little enhancement was observed in aortic wall 48 h post-injection of ProHance®, suggesting that ProHance® was not retained in atherosclerotic lesion (Figure 35 c-h). In contrast, 48 h after the **sLDL-Gd** injection, a clear enhancement of the left carotid wall was detected for two of the three mice (yellow arrow in Figure 35, 36 i-l). Interestingly, an intense contrast enhancement was observed in a nearby structure (pointed by a yellow arrowhead in Figure 35k, l), which is unknown but is suspected to be a cluster of lymph nodes or inflammatory tissue that might have taken up **sLDL-Gd**. In the case of the third mice, no clear contrast enhancement of the atheroplaques could be observed but similarly to the other two mice, a strong enhancement of the nearby structures was observed.

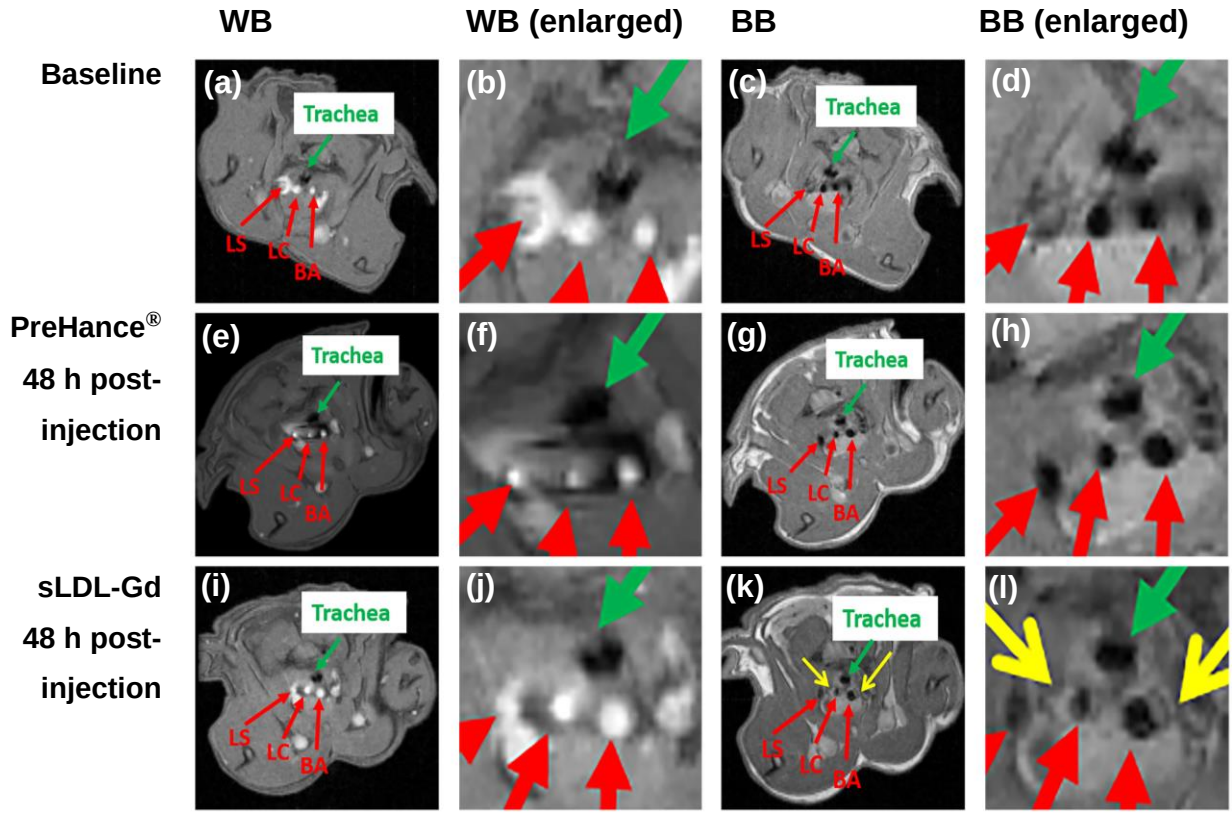

Figure 35. *In vivo* MR images of the aortic arch of the *apoE*$^{-/-}$ mouse 1, taken pre-injection (a-d), 48 h post-injection of ProHance (e-h), and 48 h post-injection of **sLDL-Gd** particle (i-l). WB images (a, b, e, f, i, j) and BB images (c, d, g, h, k, l). The three branches of the aortic arch were identified by red arrows: BA = brachiocephalic artery; LC = left carotid artery; LS = left subclavian artery. Yellow arrow points to enhancement of atheroplaque in the LC wall.

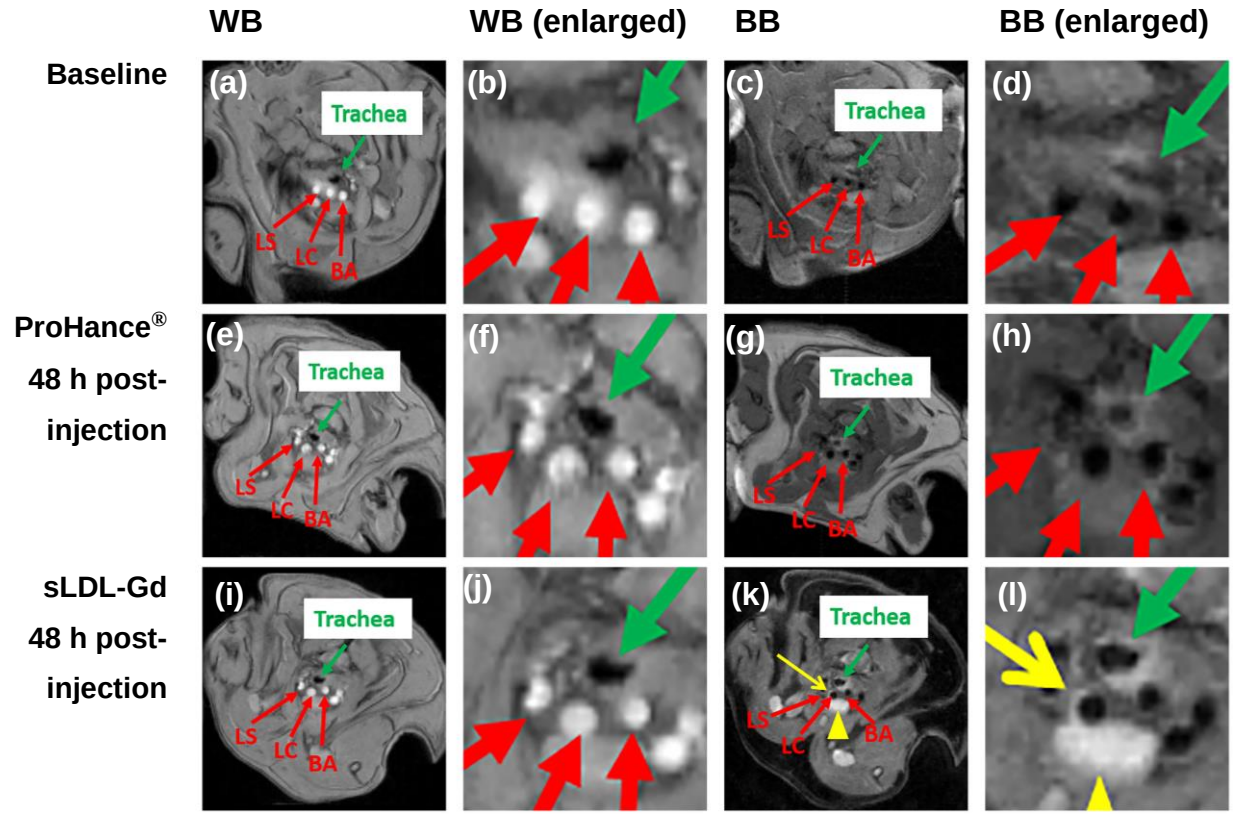

Figure 36. *In vivo* MR images of the aortic arch of the *apoE*$^{-/-}$ mouse 2, taken pre-injection (a-d), 48 h post-injection of ProHance (e-h), and 48 h post-injection of **sLDL-Gd** particle (i-l). WB images (a, b, e, f, i, j) and BB images (c, d, g, h, k, l). The three branches of the aortic arch were identified by red arrows: BA = brachiocephalic artery; LC = left carotid artery; LS = left subclavian artery. Yellow arrow points to enhancement of atheroplaque in the LC wall. Yellow arrow-heads point to an enhancement with unknown structure.

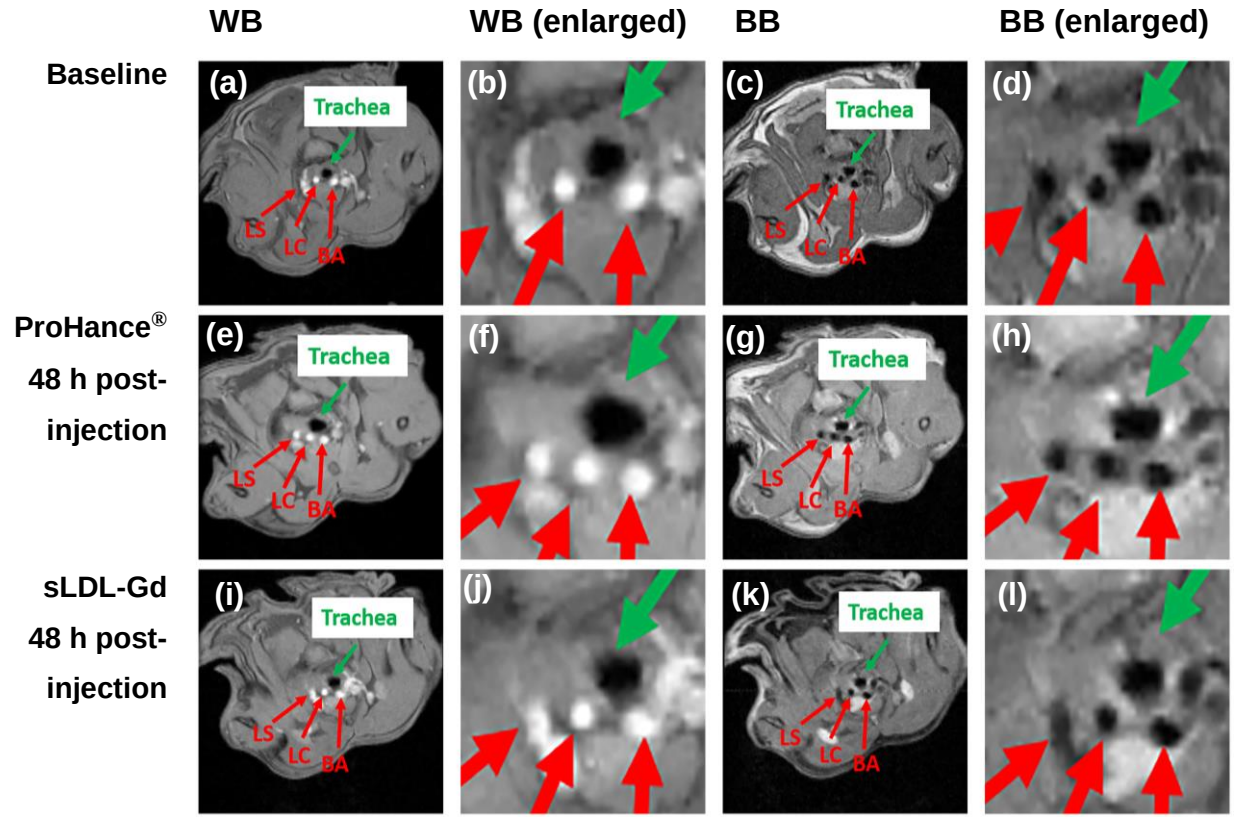

Figure 37. *In vivo* MR images of the aortic arch of the *apoE*$^{-/-}$ mouse 3, taken pre-injection (a-d), 48 h post-injection of ProHance (e-h), and 48 h post-injection of **sLDL-Gd** particle (i-l). WB images (a, b, e, f, i, j) and BB images (c, d, g, h, k, l). The three branches of the aortic arch were identified by red arrows: BA = brachiocephalic artery; LC = left carotid artery; LS = left subclavian artery.

3.7.2 ICP-MS analysis of mouse tissue received sLDL-Gd.

To further evaluate the delivery efficiency of the nanoparticles to the atheroplaques, the aorta of the three *apoE*$^{-/-}$ mice 48 h post-injection of **sLDL-Gd** was harvested, and the Gd content determined by ICP-MS. Significant accumulation of Gd was observed in all the three mice, which resulted to be higher than the previous study, in which natural LDL were used as a carrier of MRI-CA to the atheroplaques. In particular, mouse No. 2 had the highest Gd content (14.6 ppm), in good agreement with the highest enhancement observed in the *in vivo* MR images (Figure 36). This result is also consistent with its high body weight and atheroplaques burden, which was observed during the dissection. Indeed, body weight can be considered as an indicator of fat ingestion and therefore of the extent of inflammation induced by such diet.

Table 7. ICP-MS analysis of dissected aorta of *apoE*$^{-/-}$ 48 h post-injection of **sLDL-Gd**.

***apoE*$^{-/-}$ mice**	**Mouse body weight [g]**	**dose of Gd^{3+} [mmol / kg]**	**dry weight of tissue used [mg]**	**Gd^{3+} content by ICP-MS [ppm]**
No. 1	34	0.018	0.8	3.66
No. 2	49	0.051	0.7	14.6
No. 3	38	0.042	0.9	4.26
average of 1-3	40	0.037±0.010	0.80±0.058	8.51±3.55

3.8 Conclusion

A synthetic analogue of LDL was developed and used as MRI probe for the *in vivo* detection of atherosclerotic plaques. The **LNP-KAT** particles, was used as a platform system for the simultaneous surface functionalization with HA-Gd(DO3A-MA) **15** and HA-peptide **16** in a ratio of 9:1 by KAT ligation, to produce **sLDL-Gd**. As observed by DLS, AFM, cryoSEM and cryoTEM, the surface modification did not affect the size and morphology of the particles, and **sLDL-Gd** resulted as uniformly dispersed without significant aggregation. The KAT ligation products were clearly detected by HR-MALDI-MS analysis of the **sLDL-Gd**, whereas no HA derivatives could be observed, confirming that the surface modification happened through covalent bond formation and not by non-specific binding. The efficiency of the reaction was further evaluated by ICP-MS analyses for the determination of the B and Gd content in the particles before and after the surface modification. Those results indicate that the reaction proceeds efficiently in aqueous diluted conditions and in particular the high conversion yield obtained (>85%) suggested that no side reactions took place. The successful addition of two different types of molecules demonstrated the versatility and the efficacy of KAT ligation as a general tool for the surface functionalization of LNP with biorelevant molecules. *In cellulo* studies, using two different cell lines (THP-1 and RAW 264.7) indicated a significant uptake of **sLDL-Fl** in THP-1 cells in comparison to **LNP-Fl**. The difference observed is presumably due to the presence of the peptide on the LNP surface that can induce cellular uptake. The relaxivity of **sLDL-Gd** was evaluated prior to the *in vivo* studies by measuring the r_1 value of **sLDL-Gd** at 1.4 T / 60 MHz, 25 °C. As expected, the obtained relaxivity value (r_1 = 22.0 $s^{-1}mM^{-1}$) resulted to be much higher than the small molecule ProHance® (r_1 = 4.0 $s^{-1}mM^{-1}$) at the same experimental conditions. More

importantly, the determined relaxivity value of **sLDL-Gd** (r_1 = 8.2 $s^{-1}mM^{-1}$) was significantly higher than ProHance® (r_1 = 2.4 $s^{-1}mM^{-1}$) also under the conditions used in the *in vivo* study (9.4 T / 400 MHz, 37 °C). The *in vivo* MRI studies on *apoE*$^{-/-}$ atherosclerosis mice model indicated an increase of contras of the aortic walls bearing atheroplaque. The MR images were recorded 48 h post-injection of the **sLDL-Gd**, and the images compared with MRI images recorded without the administration of any MRI-CA or 48 h after injecting ProHance®. Interestingly, the MR images showed a significant contrast enhancement of the area alongside the aortic arch, presumably corresponding to a limp node. It should be pointed that the contrast enhancement observed in the animal model studies needs to be further investigated in a larger number of mice. Histological analysis can shed light on the localization of the particles in the atheroplaques and biodistribution of Gd studies can provide information about accumulation in specific organs. However, the *in vivo* results were corroborated by the high Gd^{3+} retention in the atheroplaques revealed by ICP-MS analysis of the aorta harvested right after the imaging.

Chapter 4

Covalent functionalization of self-assembled monolayer (SAM) by KAT ligation

The work presented in this chapter was done in collaboration with Ankita Ray, who contributed in the preparation and characterization of the gold surfaces, Prof. Dr. Antonella Rossi (ETH Zurich) and Dr. Cristiana Passiu (ETH Zurich), who carried out the characterization of the surfaces by XPS. I wish to thank Prof. Dr. Nicholas Spencer (ETH Zurich) for the access provided to ellipsometry, contact angle and QCM instruments. A manuscript is in preparation for publication.

4. Covalent functionalization of self-assembled monolayer (SAM) by KAT ligation

4.1 Background

As described in Chapters 2 and 3, the surface modification of **LNP-KAT** particles by KAT ligation was successfully achieved, indicating that **LNP-KAT** can be versatile scaffold for the preparation of nanoparticles bearing a variety of bioactive molecules such as imaging probes and targeting peptide moieties. In this study, KAT ligation was used to modify the surface of lipid self-assembled monolayers (SAMs) on gold surface. SAM are molecular assemblies that form monolayers organized into ordered domains through spontaneous adsorption on surfaces. The formation of SAM is usually accomplished by exposing the gold surface to molecules with a functional group that interacts with gold such as thiols, disulfides, thioethers.[134,135]

In order to prepare SAMs with designated properties, specific molecules can be synthesized and used for the self-assembly onto the surface. However, well-oriented SAMs can only be obtained with a suitable molecular design that allow proper intermolecular interactions in the assembling process. For instance, the surface immobilization of polymers can be hampered by unfavorable geometry and shape of the assembling molecules, resulting in a disordered surface assembly.[136,137] Chemical modification of preformed monolayers offers a better alternative, since it allows to form stable and well-packed monolayer scaffolds, that can be subsequently modified with different molecules. The ideal reaction for the SAM modification should be compatible with the presence of most common functional groups providing high yield under mild conditions. In this Chapter, the preparation of SAM with a KAT moiety and further SAM modification by KAT ligation is described.

4.2 Design of the KAT terminated thioether molecule for the SAM preparation

To test the surface modification by KAT ligation, a molecule (**33**) was designed for the formation of SAMs on gold surfaces and the subsequent KAT ligation with HA-derivatives. As shown in Figure 38, the design of the KAT molecule includes the presence of (1) a thiother group for the interaction with the gold surface, (2) two alkylic chains that enable the formation of the SAM, and (3) a KAT group at the end of one of the two alkylic chains,

which allows the SAM modification. The thioether KAT (S-KAT) **33** was expected to form well-ordered SAMs (Figure 38b) through van der Waals interactions between the alkyl chains, leaving the KAT groups exposed to the bulk solution, ready to undergo KAT ligation.

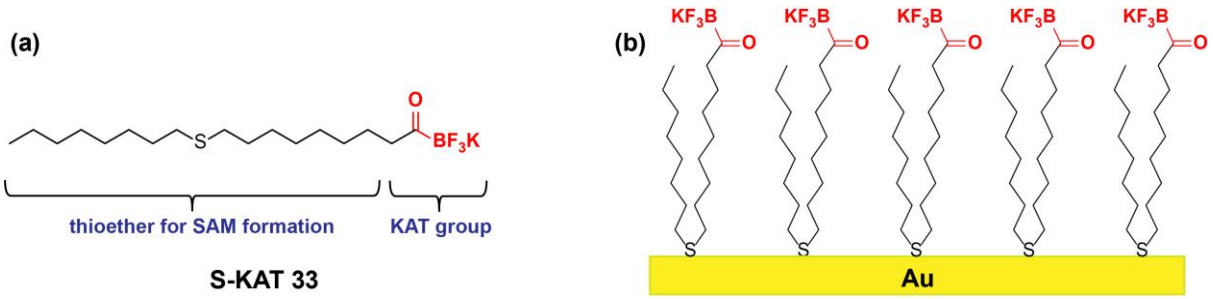

Figure 38. (a) Chemical structure of S-KAT **33**; (b) Self-assembled monolayer (SAM) with S-KAT **33** on bare gold substrate.

4.3 Synthesis of thioether KAT (S-KAT)

The S-KAT **33** was synthesized based on previously reported synthesis of KAT derivatives (Scheme 16).[121] The commercially available 1,8-dibromooctane **29** was converted to the corresponding iodide **30** by substitution with NaI in acetone. Subsequently, the mono-substitution with the octanthiol provided compound **31**, which already contained the basic structure for the SAM forming molecule. The following alkylation of compound **2** provided the key intermediate **32** as a direct precursor of the KAT group. This hemiaminal compound was deprotonated by *n*-BuLi and converted to S-KAT **33** by trapping the obtained anion with $B(OMe)_3$, followed by the addition of an aqueous saturated solution of KHF_2. Similarly to the synthesis of OA-KAT **1** (section 2.3), the low solubility of benzotriazole-based hemiaminal precursors of KAT at low temperature was a limiting factor to this reactions. Indeed, similar attempts to synthesize didodecyl-thiother KAT was not successful and resulted in the starting material recovery. In order to overcome this problem, the target molecule was redesigned with shorter alkylic chains, which allowed to obtain the completely soluble starting material **32**.

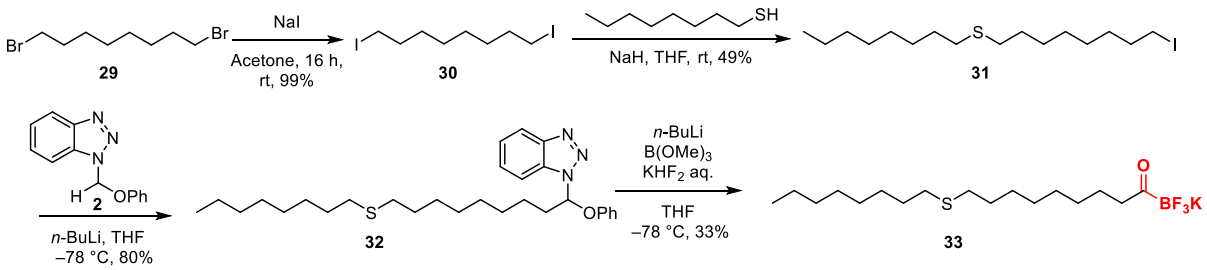

Scheme 16. Synthesis of the thioether KAT (S-KAT) **33**.

4.4 Synthesis of hydroxylamine-PEG (HA-PEG)

The HA-PEG **36** and **39** were synthesized with similar protocols as shown in Scheme 17 and 18. Starting materials amino PEG **34** or **37** were coupled with compound **8** to provide compounds **35** or **38** respectively. The final deprotection by TFA provided compounds HA-PEG **36** or **39** which were used as reaction partners for the surface KAT ligation.

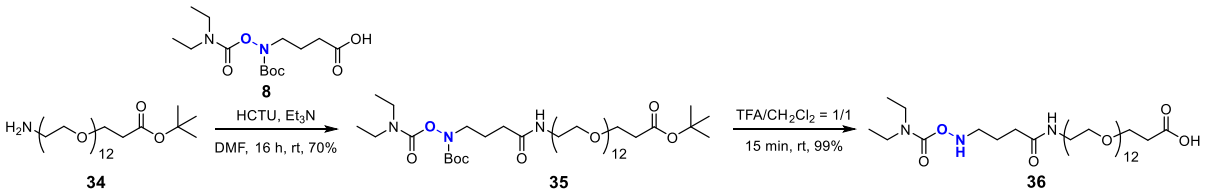

Scheme 17. Synthesis of the HA-PEG **36**.

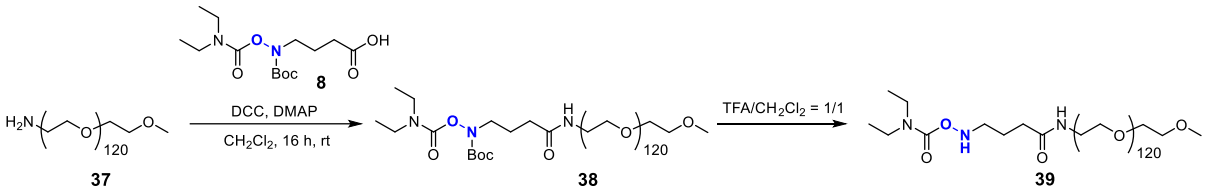

Scheme 18. Synthesis of the HA-PEG **39**.

4.4 KAT ligation between S-KAT 33 and HA-PEG 36 in solution phase

KAT ligation of HA-PEG **36** was carried out initially in solution phase as shown in Scheme 19. Just prior to KAT ligation, compound **36** was prepared by deprotection of **35** with TFA in both the N-Boc HA and the terminal *t*-Bu ester being monitored by LC-MS (Figure 39a, b). The crude product containing HA-PEG **36** was dried under N_2 flow and reconstituted in 3 mL solution of a 2:1 mixture of phosphate buffer (pH 5.5) and acetone. To this solution, S-KAT **33** in acetone was added in an equimolar ratio, with a final concentration of 5 mM in a 1:1

mixture of phosphate buffer (pH 5.5) and acetone. As clearly indicated by the LC-MS trace in Figure 39b, c, KAT ligation of S-KAT **33** with HA-PEG **36** completed quantitatively at room temperature to neatly provide the thioether PEG derivative **40**.

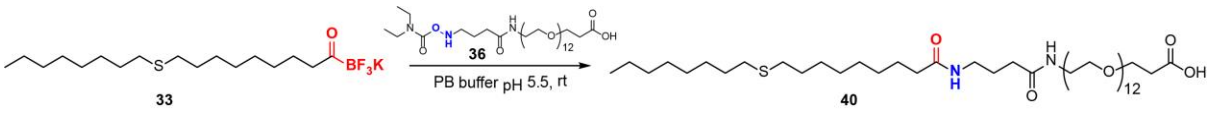

Scheme 19. KAT ligation of S-KAT **33** and HA-PEG **36** in solution phase.

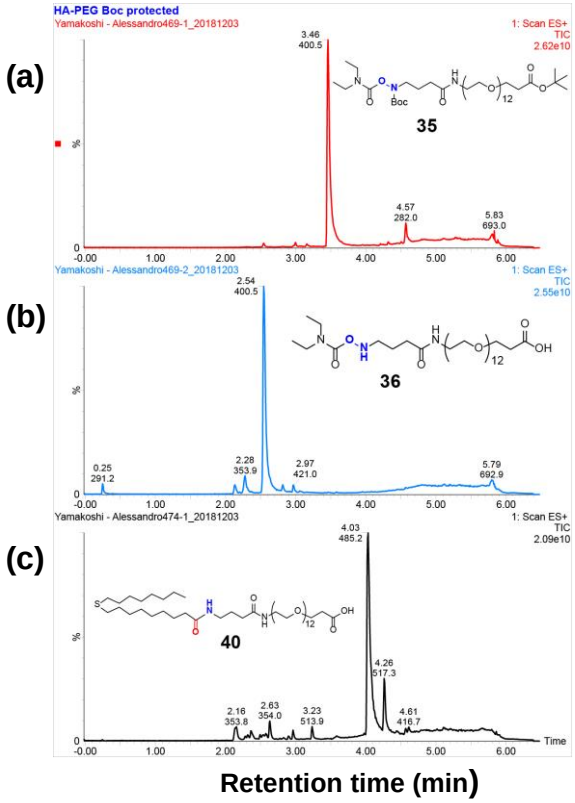

Figure 39. Extracted ion chromatograms (*m/z* 300 - 1000 Da) of (a) compound **35**, (b) reaction mixture of deprotection of **35** with a peak corresponding to HA-PEG **36**, and (c) reaction mixture of KAT ligation of **33** and **36** with a peak corresponding to the ligation product, monitored by LC-MS (Micromass Autospec Ultima-EI-Sector-MS LC-MS system, column: Aquity UPLC BEH C_{18} 1.7 µm (Φ 2.1 x 50 mm); eluent: MeCN-H_2O (2 – 98% in 4 min), 0.1% HCOOH; flow rate: 0.5 mL/min.

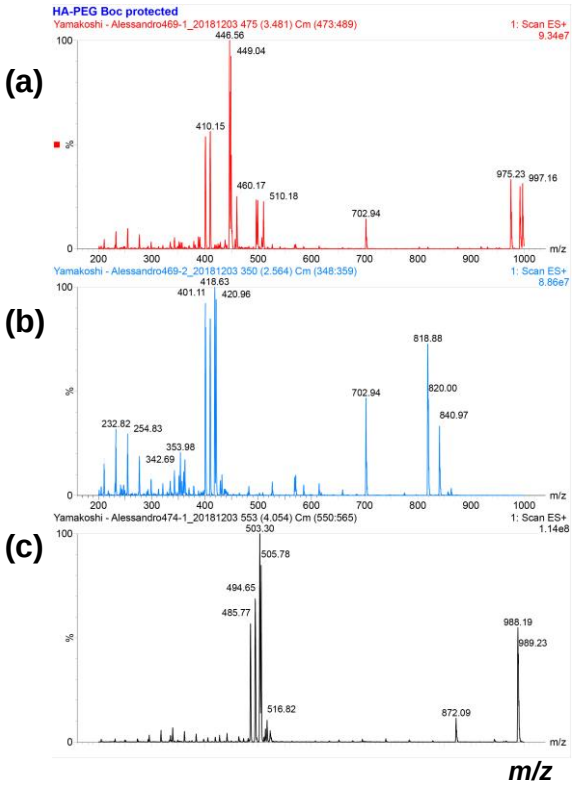

Figure 40. ESI mass spectra corresponding to the peaks of the chromatograms shown in Figure 39; (a) Compound **35** (retention time: 3.45 min), (b) reaction mixture of deprotection of **35** showing the molecular peak of HA-PEG **36** (retention time 2.54 min), and (c) reaction mixture of **33** and **36** showing the molecular peak of **40** (retention time: 4.03 min).

4.5 SAM modification by KAT ligation and surface characterization

SAM of S-KAT **33** was prepared by soaking gold substrates in an ethanol solution of **33** (1 mM) for 20 h at room temperature in the dark. Subsequently, the surfaces were rinsed with ethanol to remove non-specifically bound molecules from the surface. For KAT ligation on surface (Figure 41), the above prepared samples were immersed in a 0.5 mM solution of HA-PEG **36** in phosphate buffer (10 mM, pH 5.5, containing 10 mM of KF) at room temperature for 16 h. The samples were then washed with MilliQ water and ethanol to remove any residual HA-PEG **36**, that were not covalently bound to the surface. These modified surfaces were stored under Ar atmosphere before characterisation by XPS, contact angle, and ellipsometry.

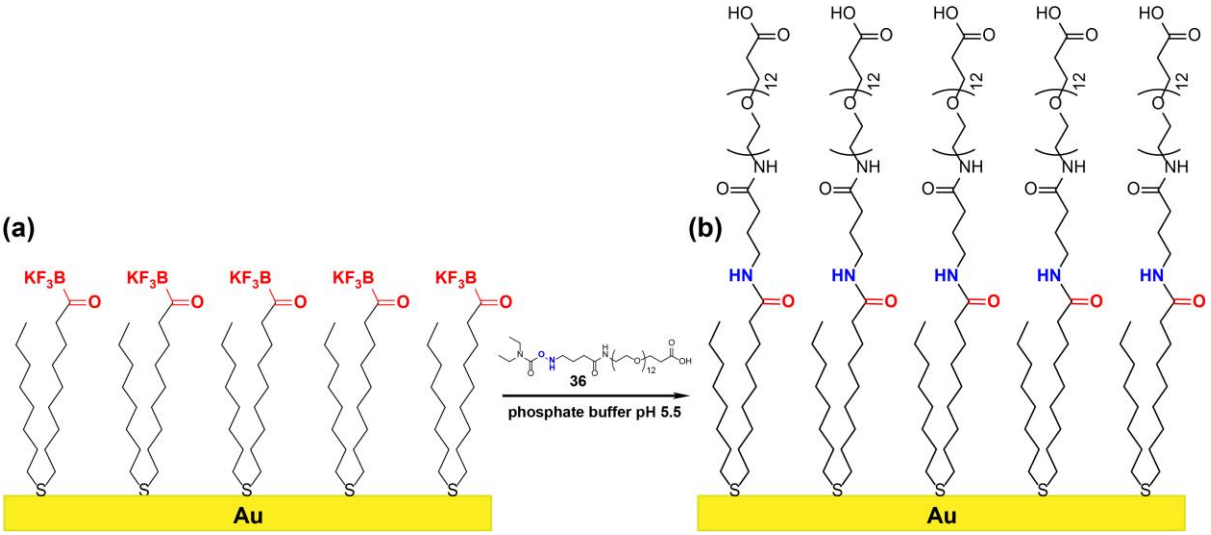

Figure 41. SAM modification by KAT ligation with HA-PEG **36**.

4.5.1 X-ray Photoelectron Spectroscopy analyses of modified gold surfaces

X-ray photoelectron spectroscopy (XPS) is a surface characterization technique to determine the elemental composition of the surface.[138] XPS analyses make use of X-rays to eject electrons from the inner-shell of the samples. The kinetic energy of the ejected electrons is measured by the spectrometer, and converted to the binding energy. The photoelectron intensity (electron yield) spectra are plotted against binding energy which is determined by (effective) nuclear charge, thus allowing the reconstruction of the elemental composition of the sample.

In this study, XPS was used to observe changes of the elemental composition of gold surfaces before and after surface KAT ligation between the SAM of S-KAT **33** and the HA-PEG **36**. The corresponding spectra are shown in Figure 42. With the formation of the amide bond on surface, it was expected that the contents of potassium and fluorine would significantly decrease while, due to amide bond formation, nitrogen and oxygen contents were expected to increase significantly. Based on the observed peaks area, the relative percentage of potassium decreased from 9.4% to 0% together with fluorine decrease from 13% to 0% (Table 8). At the same time, the relative percentage of nitrogen increased from 1.7% to 3.8% and the oxygen from 13.7% to 18.5%. Importantly, as shown in Figure 42b, a clear peak corresponding to the binding energy of N in the amide bonds was detected. Furthermore, a slight increase in the thickness of SAM was observed by XPS, with values of 1.2 nm before KAT ligation and 1.4 nm after the reaction.

Table 8. Theoretical and measured XPS values of the relative elemental percentages based on peaks areas.

	Theoretical (%)					
	C	**K**	**N**	**S**	**O**	**F**
S-KAT **33**	70.8	4.2	0	4.2	4.2	12.5
HA-PEG **36** applied to S-KAT **33**	71.6	0	4.2	1.5	23.9	0
Dioctyl sulfide	94.1	0	0	5.9	0	0

	Measured (%)					
	C	**K**	**N**	**S**	**O**	**F**
S-KAT **33**	58.2 ±0.4	9.4 ±0.6	1.7 ±0.1	3.7 ±0.4	13.7 ±0.7	3.75 ±0.05
HA-PEG **36** applied to S-KAT **33**	74 ±0.9	0	3.75 ±0.05	3.7 ±0.6	18.5 ±0.3	0
Dioctyl sulfide	91 ±1.0	0	0	4.5 ±0.2	4 ±1	0

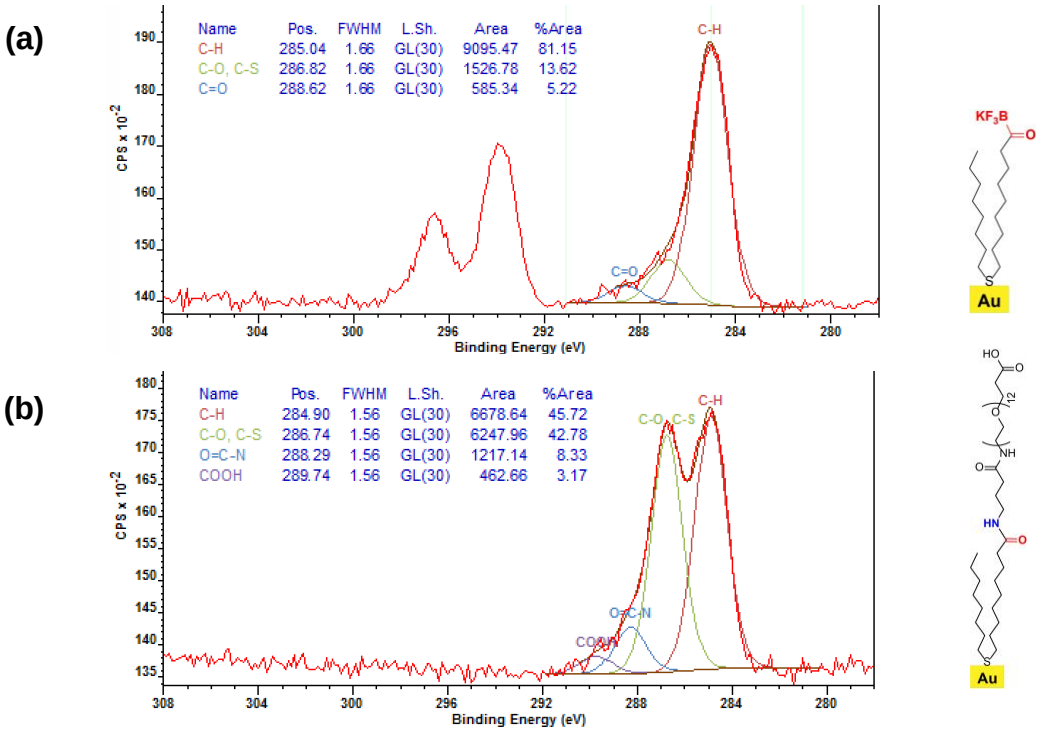

Figure 42. Peak fitting analyses of XPS with functional group identification of SAM on gold surface (a) before and (b) after KAT ligation.

4.5.2 Static Contact Angle of modified gold surfaces

Contact angle is a convenient and straightforward method to measure the wettability of a surface.[139] A hydrophilic surface will show a smaller contact angle than a hydrophobic one. The results of contact angle measurements are summarized in Table 9. The SAM with S-KAT **33** with polar KAT functional group at the end terminus of the alkyl chain provided a lower contact angle value (55°) indicating a more hydrophilic surface compared to the value of the control SAM (87°), with dioctyl sulfide. The contact angle of the SAM surface after KAT ligation showed a rather small value (44°) reflecting the surface hydrophilicity retention after the polar PEG attachment. In contrast, the addition of HA-PEG **36** to the control SAM monolayer did not show any change of hydrophilicity (86°), indicating that there was no non-specific physical adsorption of HA-PEG **36**.

Table 9. Static contact angle measurements.

Surface SAM	Contact angle (±3°)
S-KAT **33**	55°
S-KAT **33** + HA-PEG **36**	44°
S-KAT **33** + HA-PEG **39**	46°
dioctyl sulfide	87°
dioctyl sulfide + HA-PEG **36**	86°

4.5.3 Ellipsometry analysis of modified gold surface

Ellipsometry is a method for the determination of the thickness of thin films on solid surfaces[140] based on the measurement of the phase and amplitude of elliptically polarized visible light after it is reflected from the sample surface. In this study, ellipsometry was used to determine the film thicknesses before and after KAT ligation. The obtained thickness values were compared to the one obtained by forming the SAM using directly the KAT ligation products (Table 10), showing a good agreement. It was expected that the attachment of PEG to the surface would determine an increase of the thickness of the SAM. As shown in Table 10, S-KAT **33** formed a monolayer of 1.2 nm thickness. After KAT ligation, a slight increase of the thickness was observed in the case of HA-PEG **36** (1.4 nm), while a more

significant increase was observed with HA-PEG **39** (1.9 nm), due to the different MW of the two PEG molecules. Importantly, these results are consistent with the thickness values obtained by XPS analyses (1.2 nm before, and 1.4 nm after KAT ligation).

Table 10. Monolayer thickness determined by ellipsometry analyses.

Surface SAM	**thickness (±0.1 nm)**
S-KAT **33**	1.3
S-KAT **33** + HA-PEG **36**	1.4
S-KAT **33** + HA-PEG **39**	1.9
dioctyl sulfide	1.2
dioctyl sulfide + HA-PEG **36**	1.4
KAT ligation product **40** (from **36**)	1.4
KAT ligation product (from **39**)	1.7

4.5.4 Quartz Crystal Microbalance (QCM) measurements

Quartz crystal microbalance (QCM) is a mass sensing technique. The core of the QCM is a piezoelectric quartz crystal that is attached to two metal electrodes. When an alternating electric field is applied, a mechanical oscillation of a specific resonant frequency, that depends on the mass and shape of the crystal, is produced. When some material is deposited to the surface of the electrode metal, the mass variation is detected by monitoring changes in the resonant frequency. The signal is reported as the difference between the fundamental frequency of the crystal and the new frequency $\Delta f_n/n$, where n is the vibrational mode and Δf_n is the difference in frequency for that specific vibration mode.[141,142] The instrument also reports ΔD (change in dissipation), the dissipated energy per cycle of vibration. When the layer of material deposited on the metal surface is thin and elastic, it is possible to neglect the energy dissipation and the Δf_n detected is directly correlated to the mass of material deposited according to the Sauerbrey equation $\Delta m = C \times \Delta f_n/n$ where Δm is the mass difference, C is an instrument constant and Δf_n and n are as previously defined. For thick viscoelastic films, energy dissipation is observed and therefore it is not possible to correlate

the mass of material attached to the surface with the observed Δf*n*. For such films, QCM is not a simple mass sensor but can still provide valuable insights about the effectiveness of reactions on surface.

To monitor the formation of SAM with S-KAT **33** molecules on the gold surface, and to study the efficiency of the surface KAT ligation reaction, QCM analyses were undertaken. A representative QCM trace is shown in Figure 43.

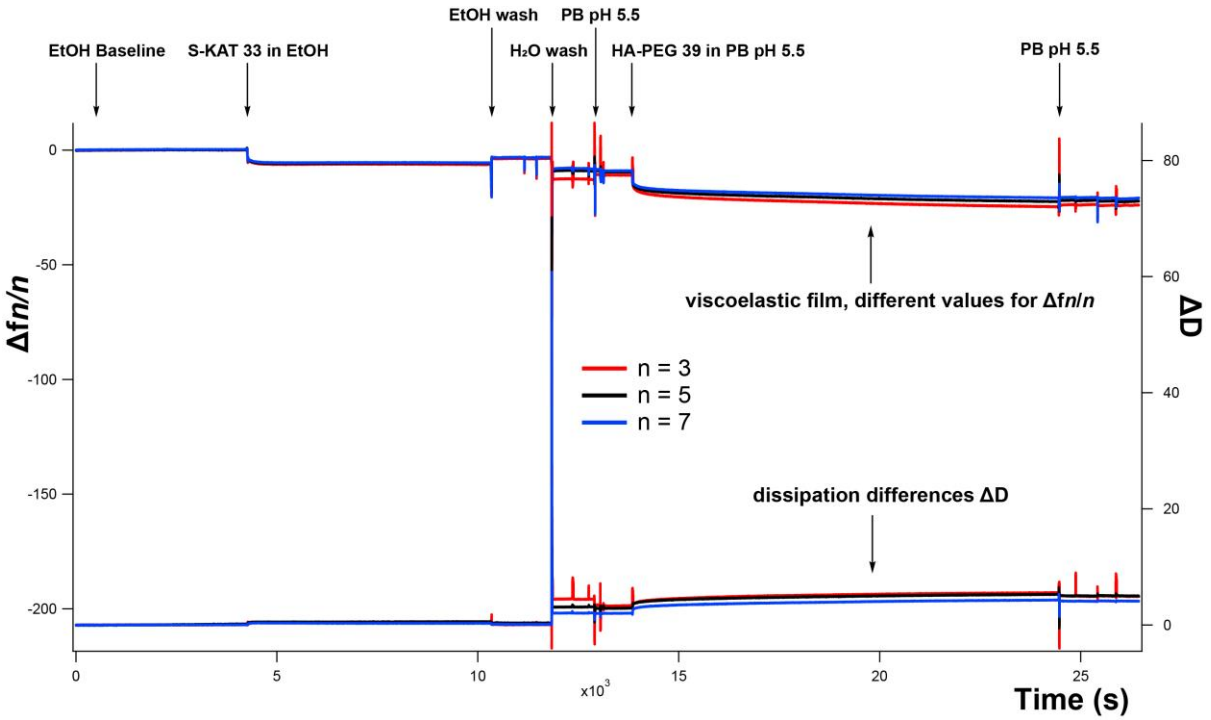

Figure 43. QCM curves upon treatment with S-KAT **33** and subsequent KAT ligation with HA-PEG **39** in phosphate buffer pH 5.5. When a viscoelastic film is formed, Δf*n*/*n* have different values depending on the considered *n*.

The QCM experiments were carried out as shown in Figure 43. (1) Pure ethanol was added to the gold-coated quartz crystal in the cell, to obtain a stable baseline. (2) A filtered solution of S-KAT **33** in ethanol (1 mM) was injected, and a decrease in the oscillation frequency was observed. (3) Pure ethanol was injected again to remove the unbound molecules, and no further change was observed, indicating the stable formation of the SAM. Prior to KAT ligation of the S-KAT **33**, SAM on the gold-coated quartz crystal, ethanol in the cell was replaced by (4) water and (5) then phosphate buffer pH 5.5 (the first water injection was necessary to avoid eventual precipitation of phosphate salts due to the mixing of the buffer with ethanol). A frequency decrease was observed in this process, presumably due to the higher density of H_2O compared to

ethanol. To avoid other crucial aspect observed by replacing the solvent, phosphate buffer was degassed prior to use. Indeed, when non-degassed buffer was used, a huge increase of Δf*n* was observed, possibly due to the formation of air bubbles that affect the surface of the gold sensor (Figure 44). This problem was circumvented by the use of degassed solvents. (6) Subsequently, a filtered solution of HA-PEG **39** (0.01 mM in the same buffer) was injected, and gradual lowering of the frequency over time was recorded. Upon washing the crystal with excess buffer to remove non-covalently bound material, the frequency changed only slightly, which confirms the successful covalent attachment of **39** by KAT ligation on SAM on gold surface.

The attachment of PEG polymers to solid surfaces is known to lead to the formation of thick viscoelastic films and, as a further proof of the surface KAT ligation, the formation of such film was observed upon the addition of HA-PEG **39** (Figure 43). When viscoelastic films are formed, a significant change of the dissipation ΔD is observed and Δf*n*/*n* have different values depending on the considered *n*.

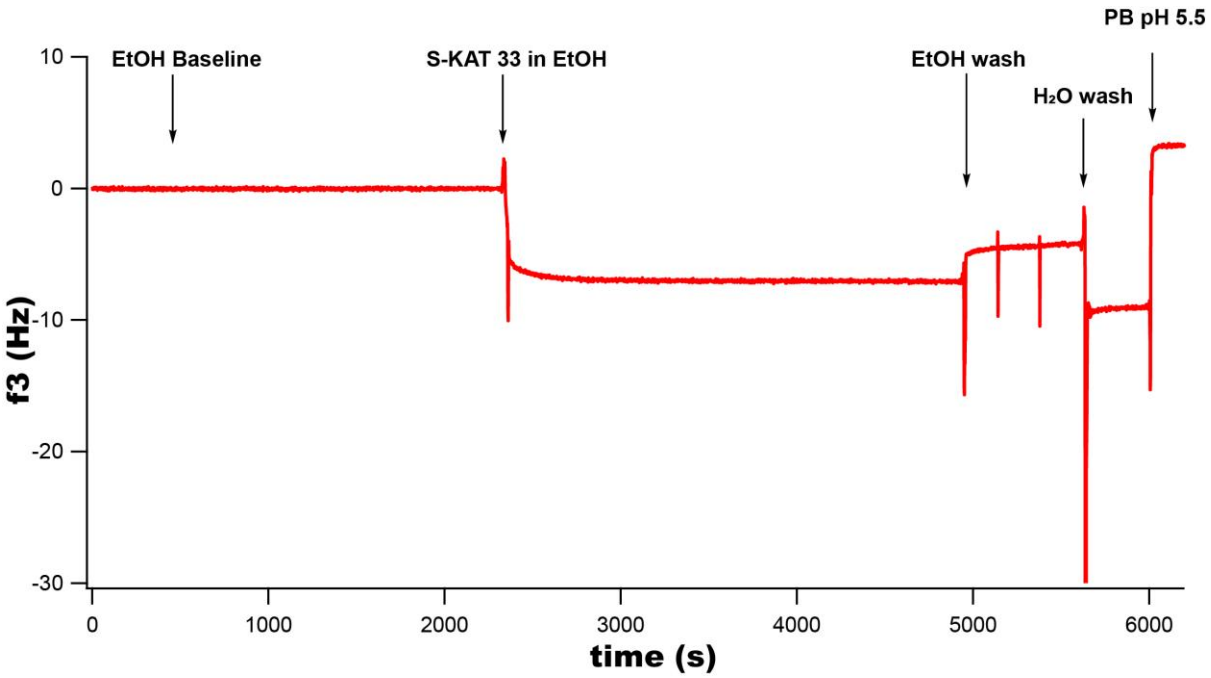

Figure 44. QCM curves upon treatment with S-KAT **33** and subsequent injection of non-degassed phosphate buffer pH 5.5.

To further confirm the covalent bond formation, control experiment using the amino-PEG **37** was carried out. Compound **37** was chosen as a control compound since its structural similarity with HA-PEG **39**. On the one hand, the absence of the HA moiety does not allow

the formation of a covalent bond with the S-KAT **33** on surface and, on the other hand, the presence of the long PEG chain guarantees the same non-specific interaction with the SAM surface. The QCM trace of this control experiment resulted in a similar frequency drop to the one observed when HA-PEG **39** was used (Figure 45). The reason for this observation is not clear and two possible explanations were speculated. (1) Non-specific binding could occur due to chemisorption of the amine group onto the gold surface.[143] Part of the gold could be uncovered by S-KAT 33, leaving part of the gold surface free to interact with the PEG-amine. (2) It is reported that free amine can react with the KAT group leading to the formation of the iminium KAT.[144] Nevertheless, even though iminium KAT are stable in acidic aqueous environment such as the one used for this surface KAT ligation, the formation of the iminium was only suspected and never directly observed in these conditions. We speculated that in the QCM experiment setup its formation could be possible since the strong excess of equivalents of amino-PEG **37** compared to the S-KAT **33** on surface. To verify that the non-specific binding was ascribable to the amino functional group, a control experiment was carried out with the truly inert amino protected compound **41**, resulting in a much minor surface binding (Figure 46).

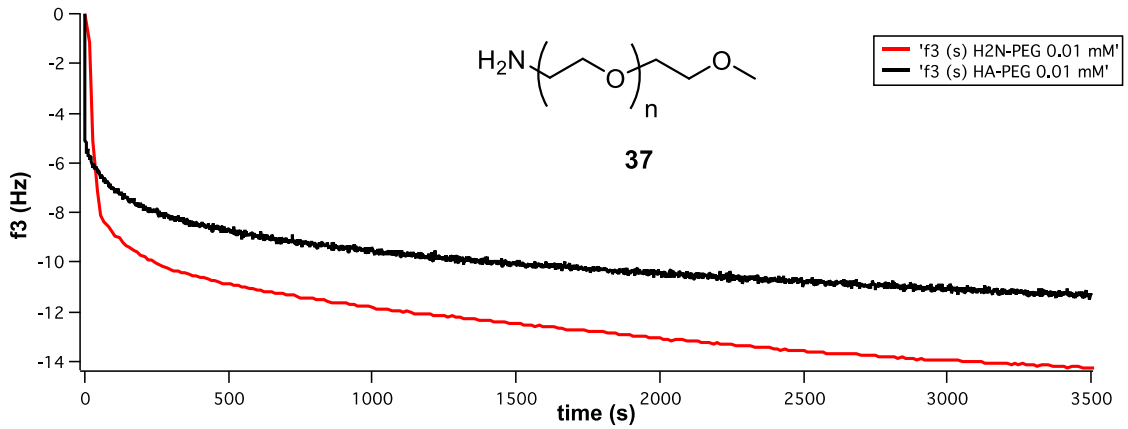

Figure 45. Extracted of QCM trace of KAT ligation with HA-PEG **39** (black) and control experiment with H_2N-PEG **37** (red).

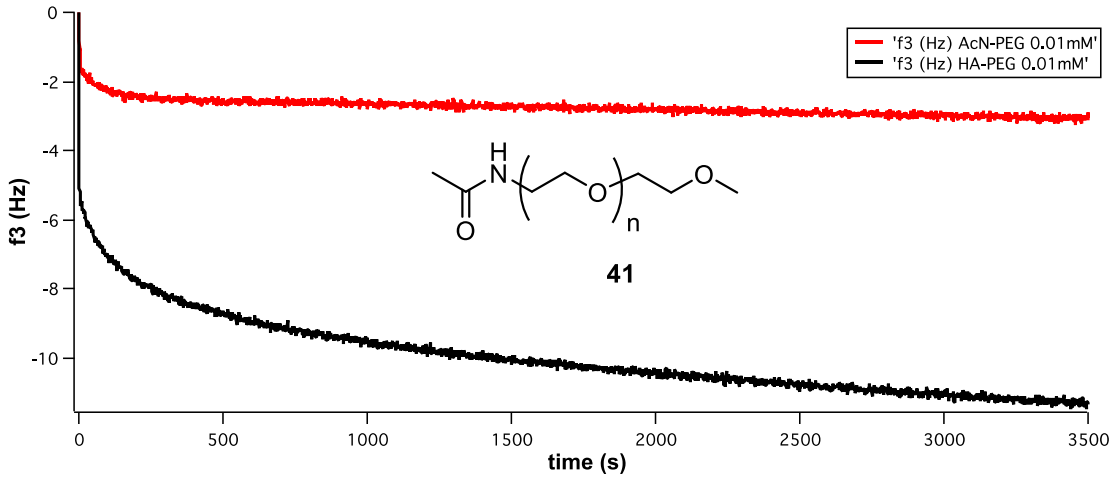

Figure 46. Extracted of QCM trace of KAT ligation with HA-PEG **39** (black) and control experiment with AcN-PEG **41** (red).

It is known that KAT ligation in solution phase generally provides faster kinetics under acidic conditions.[117] The effect of pH on the current surface KAT reaction was tested using QCM. As shown in Figure 47, for KAT ligation in pH 3.2 citrate buffer, an abrupt drop of the resonance frequency was observed right after the injection of HA-PEG **39**. This result indicated that reaction kinetic of the surface KAT ligation was much higher at pH 3.2 in comparison to pH 5.5.

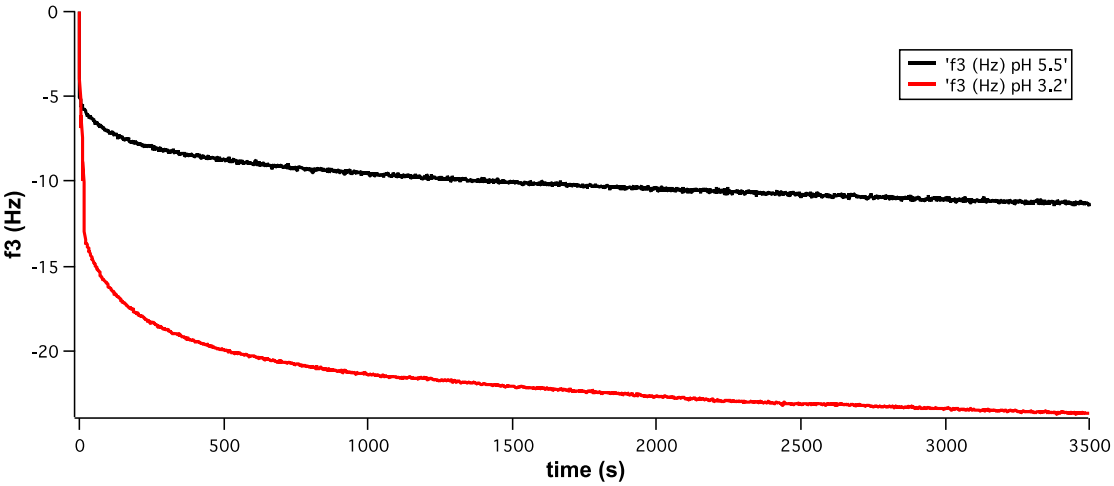

Figure 47. KAT ligation at different pH. Extracted of QCM trace of KAT ligation with HA-PEG **39** in phosphate buffer pH 5.5 (black) and citrate buffer pH 3.2 (red).

From the results presented above, KAT ligation has shown to be an effective method for the modification of SAM, and can be used as a convenient method to tailor the properties

of the surface by covalent attachment of well-defined molecules. For instance, this ligation method could be employed for the immobilization of macromolecules on surfaces, and for the study of the properties of proteins associated to the surface.[145] Indeed, the function of proteins can be affected by their immobilization onto surfaces, and the development of new immobilization methods is required for the study of this phenomena. To test the conjugation of a protein to the gold surface by KAT ligation, a HA derivative of the green fluorescent protein (HA-GFP) **42** was used as a reaction partner, and the reaction was monitored by QCM. Since it is known that HA-GFP **42** tolerates acidic condition,[118] KAT ligation was performed in citrate buffer at pH 4.0 with a final concentration of protein of 0.015 mM. After the injection of the protein solution in the QCM chamber, a dramatic frequency change was immediately observed (– 120 Hz), suggesting that the protein was successfully attached to the SAM by fast covalent bond formation (Figure 48).

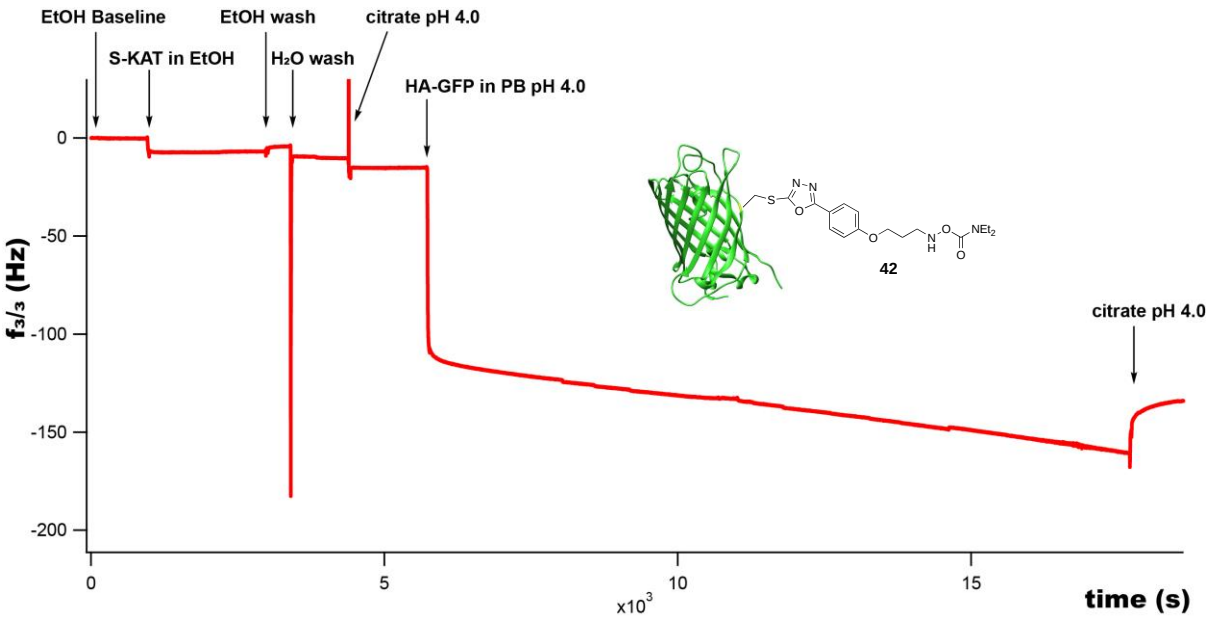

Figure 48. QCM trace with HA-GFP **42**. KAT ligation was performed in citrate buffer pH 4.0. In these reaction condition it was possible to have fast reaction kinetic, avoiding the degradation of the protein compound HA-GFP **42** deriving from an excessively acidic pH.

4.5 Conclusion

In this study, KAT ligation was used for the surface modification of SAM on gold substrates. SAM of S-KAT **33** was initially formed on gold substrates and subjected to KAT ligation with a 0.5 mM solution of HA-PEG **36** in phosphate buffer (pH 5.5) at room temperature for

20 h. After the reaction, the samples were thoroughly washed and characterized by XPS, contact angle, and ellipsometry. XPS provided the elemental composition of the SAM before and after surface KAT ligation confirming the formation of a covalent amide bond. The values of the thickness of SAMs determined by ellipsometry showed a clear increase of the SAM thickness, also indicating that surface KAT ligation occurred. Finally, contact angle data clearly showed the surface hydrophilicity due to the presence of S-KAT **33** on gold surface (55°). More importantly, it was observed that the hydrophilicity increases with the attachment of polar PEG by KAT ligation, further confirming the successful SAM functionalization (44°). The reaction process of KAT ligation for surface functionalization was monitored by QCM at very low concentration of HA-PEG **39** (10 μM). The frequency change observed indicated that, despite the low concentration of reactant, the PEG was covalently attached to the surface. In addition, when a more acidic pH was used (pH 3.2) it was observed a clear increase of the kinetic of the surface KAT ligation. Reactions involving biomolecules such as proteins and nucleic acids often require the use of very low concentrations. Therefore, the suitability of KAT ligation for the attachment of such biomolecules was also tested and monitored by QCM, using an HA-derivative of GFP (**42**) as a substrate. The immediate frequency drop observed upon injection of HA-GFP **42** in the QCM chamber (pH 4.0) indicated a fast attachment of the protein to the SAM, by covalent bond formation. The method developed in this work should find applications in the modification of surfaces with proteins for the study of the retention of their structure, activity and functionality once conjugated on surfaces.

Chapter 5

Conclusion and Outlook

5. Conclusion and Outlook

The development of safe and efficient imaging methods for the detection of atheroplaques in an early stage can help in the prevention of cardiovascular diseases. MRI as a non-invasive imaging modality that uses low-frequency radiations is an emerging and promising technique for the detection and the monitoring of the progression of atherosclerosis. In addition to the imaging of the artery lumen, MRI can provide detailed information about atherosclerotic lesions, allowing for a better assessment of disease severity and medical treatment options. However, the low sensitivity of MRI can hamper the proper distinction between different body tissues, impeding the clear identification of the diseased tissues. This problem can be solved by inducing additional contrast by the use of MRI-CA. A major challenge for the detection of atherosclerosis is the development of MRI-CA able to accumulate selectively in atheroplaques, resulting in a preferential enhancement of the inflamed regions. Since a large deposition of lipoproteins is involved in the formation and progression of atheroplaques, lipoproteins have attracted attention as biocompatible nanocarriers for drugs and imaging probes to atherosclerosis. In this study, lipid-based nanoparticles (LNP) was developed as synthetic LDL-mimetic system for the delivery of imaging probes to atheroplaques. First step towards the preparation of such LNP was the implementation of a versatile method for the covalent functionalization of the LNP surface.

As described in chapter 2, LNP bearing a chemically active KAT moiety on the nanoparticle surface was developed as a platform system for the covalent surface modification through KAT ligation reaction with hydroxylamine derivative of biorelevant molecules. The oleic acid derivative (OA-KAT), with a potassium acyltrifluoroborate (KAT) functional group, was synthesized and mixed together with other commercially available lipids (phosphatidylcholine, triolein, cholesteryl oleate) for the preparation of LNP. The amphiphilic OA-KAT **1** derivative was expected to be oriented with the long alkylic chain embedded in the apolar lipid layer of the LNP, with the polar KAT group exposed in the bulk water, accessible for the KAT ligation reaction with hydroxylamines. The availability of the KAT groups on the LNP surface was tested by performing KAT ligation on **LNP-KAT** with different amounts of OA-KAT (0, 2.5, 5, 10%), using the same amount of HA-fluorescein as a reaction partner. (Figure 49).

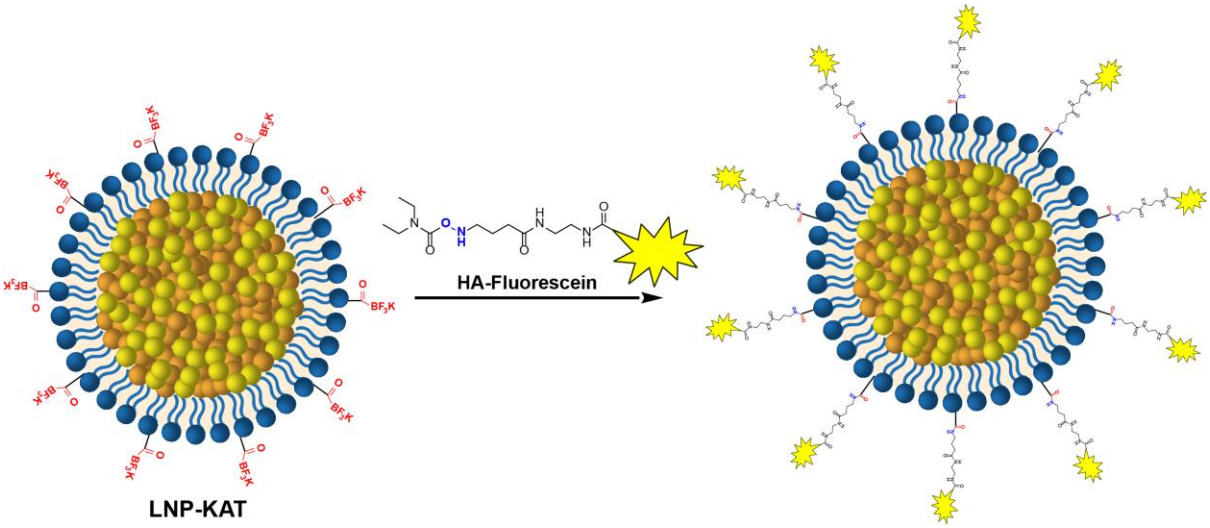

Figure 49. Schematic illustration of **LNP-KAT** functionalization with HA-Fluorescein.

After the reaction, DLS and electron microscopy were performed on the obtained nanoparticles, showing size, morphology and aggregation state similar to the one of **LNP-KAT** (diameter of ca. 50 nm). Both UV-vis and fluorescence analyses were in good correlation to the relative amount of OA-KAT in the **LNP-KAT**, indicating that the fluorescein moiety was covalently bound to the LNP surface *via* KAT ligation. The efficiency of KAT ligation was assessed by quantitative analysis of the fluorescein covalently bounded onto the LNP, and of the boron contents before and after KAT ligation (yield of ca. 50%). The obtained reaction yields were in accordance with the cryoTEM images, which suggested the contemporary presence of both lipid vesicular structures and lipid droplets in the nanoparticles dispersion. Indeed, all the OA-KAT incorporated in the inner phospholipid layer of vesicles would be not available for the reaction with the HA-Fluorescein added to the LNP dispersion. A crucial aspect for the development of good delivery systems is the cargo loading ability. In order to increase the payload of the LNP system reported in this work, strategies to increase the yield of KAT ligation have to be developed. Currently, studies based on the variation of the molar lipids ratio for the preparation of LNP dispersions with a reduced amount of vesicular structures are ongoing. In conclusion, the surface KAT ligation of **LNP-KAT** has shown to be a useful method for the functionalization of LNP through stable covalent amide bonds. The initial **LNP-KAT** reaction with HA-fluorescein indicated that **LNP-KAT** can be used as a platform system for the preparation of particles functionalized with a variety of organic molecules, such as drugs and imaging probes, for the preparation of LNP delivery systems.

In chapter 3 it is described the use of **LNP-KAT** for the preparation of LDL-mimetic LNPs for the *in vivo* MR imaging of atheroplaques. The preparation of the LNPs required the surface functionalization both with an MRI-CA and an apoB100 mimetic peptide for atheroplaques targeting. In particular, **LNP-KAT** was simultaneously modified through KAT ligation, with a mixture of HA-Gd(DO3A-MA) **15** and HA-peptide **16**, to produce **sLDL-Gd** (Figure 50a). The covalent functionalization of LNP was confirmed by the detection of the KAT ligation products by HR-MALDI-MS analysis of the **sLDL-Gd**. The efficiency of the KAT functionalization was evaluated by ICP-MS analyses, for the determination of B and Gd contents. The reaction proceeded efficiently in diluted aqueous conditions with yields similar to the ones obtained for the reaction with HA-fluorescein **13ab** described in chapter 2 (ca. 50%). In addition, the obtained high conversion yield (>85%) suggested that no side reactions took place. The relaxivity of **sLDL-Gd** measured at 1.4 T / 60 MHz, 25 °C provided a value of r_1 = 22.0 $s^{-1}mM^{-1}$, which was much higher than the one of the small molecule ProHance® (r_1 = 4.0 $s^{-1}mM^{-1}$). Importantly, the relaxivity of **sLDL-Gd** measured at the same conditions of the *in vivo* experiments provided an r_1 = 8.2 $s^{-1}mM^{-1}$, also in this case significantly higher than the ProHance® (r_1 = 2.4 $s^{-1}mM^{-1}$). Prior to the *in vivo* study, the *in cellulo* internalization study was carried out using fluorescent particles prepared through KAT ligation of **LNP-KAT** with HA-peptide and HA-fluorescein. The obtained **sLDL-Fl** was tested on two cell lines (THP-1 and RAW 264.7). The results indicated that no cytotoxicity was observed and that the uptake of **sLDL-Fl** in THP-1 cells was significantly higher than the control **LNP-Fl** without peptide, suggesting that the presence of the peptide on the LNP surface could induce cellular uptake. Subsequently, **sLDL-Gd** were tested *in vivo* on *apoE*$^{-/-}$ mice models, showing a clear contrast enhancement of aortic walls with atheroplaque (Figure 50b). Interestingly, the MR images showed a significant contrast enhancement of the area alongside the aortic arch, presumably corresponding to a limp node. After imaging, the aorta was harvested for the Gd^{3+} content quantification by ICP-MS analysis, showing significant retention of Gd^{3+} in the atheroplaques. Taken together, these results suggest that **sLDL-Gd** represent a promising diagnostic tool for the detection and characterization of atheroplaques. However, it should be pointed that the accumulation of nanoparticles proved by animal model studies needs to be reproduced on a higher number of animals, and compared with the accumulation nanoparticles without peptide as control. Furthermore, the realization of an optimal nanoparticles system still faces substantial challenges: (1) a better control over the LNP structure may lead to LNP functionalization strategies that provide a higher MRI-CA payload; (2) studies about the role of the apoB100 mimetic peptide in the LNP cellular uptake

would be of great help in tailoring of the LNP targeting ability. So far, very little has been established and the literature contains only a few reports with hypotheses regarding such peptide targeting; (3) histological analysis is necessary to shed light on the localization of the particles in the atheroplaques and biodistribution studies can provide information about accumulation in specific organs.

The LNP functionalization method through KAT ligation developed in this study is a powerful tool for the functionalization of LNP, where a variety of biomolecules can be simultaneously stably attached on LNP surface through covalent amide bonds formation. Such method can find application in the preparation of delivery systems for the *in vivo* multimodal imaging and transport of therapeutic compounds.

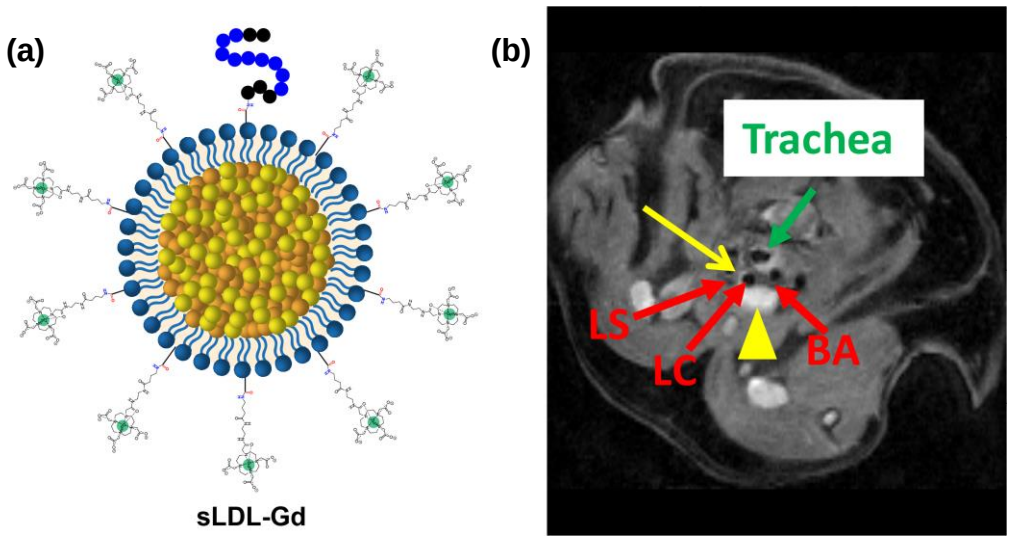

Figure 50. (a) Schematic illustration of **sLDL-Gd** after functionalization with Gd(DO3A-MA) **15** and HA-peptide **16**. (b) In vivo black-blood and fat-suppressed MR image of aortic arch region of an apoE$^{-/-}$ mouse 48 h post injection of **sLDL-Gd**. LS= left subclavian artery; LC= left common carotid artery, BA= brachiocephalic artery. Yellow arrow points to enhanced wall of LC.

In chapter 4, the use of KAT ligation was extended to the covalent surface modification of self-assembled monolayer (SAM) on gold surfaces. A thioether molecule with two alkylic chains and a terminal KAT group (S-KAT **33**) was synthesized and used for the formation of SAMs on gold surfaces. The functionalization of the obtained SAMs was carried out by immerging a 0.5 mM solution of HA-PEG **36** in phosphate buffer (pH 5.5) at room temperature for 16 h. After the reaction, the surfaces were characterized by XPS,

ellispsometry and contact angle. XPS provided information about the elemental composition of the surfaces clearly showing the formation of a covalent amide bond. Ellipsometry measurements provided additional indication of the occurring of KAT ligation on surface, revealing a significant increase of the SAMs thickness upon the reaction. The surfaces were also analyzed by contact angle measurements, which clearly showed the increased surface hydrophilicity of SAMs formed by S-KAT **33** (55°) compared to the SAMs formed by dioctyl sulfide, used as a control (87°). Importantly, contact angle showed that the surface hydrophilicity increases with the attachment of polar PEG by KAT ligation (44°), further confirming the occurring of the SAMs modification. The progression of KAT ligation on surface was monitored over time by QCM. At pH 5.5 in buffer phosphate and in very dilute concentration of HA-PEG **39** (10 μM) the reaction proceeded efficiently, with a significant increase of the reaction kinetic when more acidic conditions (pH 3.2) were used. The occurring of KAT ligation in the conditions used in the QCM experiments suggests that KAT ligation can be used as a bioconjugation method for modifying surface with substrates that require mild and and dilute aqueous reaction conditions, such as proteins and nuclei acids. To test this hypothesis, the HA derivative of GFP **42** was used as a reaction partner for KAT ligation, and the reaction in citrate buffer at pH 4.0 with a final concentration of protein of 15 μM was monitored by QCM. After the injection of the protein solution in the QCM chamber, a dramatic drop of the frequency was immediately observed (– 120 Hz), suggesting the successful attachment of the protein to the SAM by fast covalent bond formation. Subsequently a steady frequency decrease was observed, probably due to non-specific adsorption of HA-GFP **42** onto the modified surface. Nevertheless, upon washing with the same reaction buffer, the frequency value was restored, indicating the reversibility of the process, and the surface covered only with covalently conjugated GFP was obtained. In conclusion, KAT ligation has shown to be an effective and convenient method for the covalent modification of SAMs, which may enable to tailor the properties of the surface by covalent attachment of well-defined molecules. This KAT ligation functionalization approach can be applied to a vast range of molecules, allowing the surface modification with small molecular appendages, but also the immobilization of polymers and biomolecules such as peptides and proteins. We envision the use of this surface ligation method for the preparation of surfaces for biological applications. In particular, the method developed in this work should find applications in the modification of surfaces with proteins for the study of the retention of their structure, activity and functionality once conjugated on surfaces.

Chapter 6

Experimental and Spectra

6. Experimental and Spectra

6.1 Synthesis

6.1.1 General

NMR spectra were recorded on Varian 300 spectrometer (Varian Inc., CA, USA), Bruker 400 spectrometer, and Bruker 600 spectrometer (*Bruker BioSpin* GmbH, Rheinstetten, Germany). The residual peak of the deuterated solvent was used as a reference in all the spectra. HRMS were recorded on Bruker SolariX-FTICR 9.4 T MS (Bruker Daltonics, Bremen, Germany). FT-IR spectra were recorded on a JASCO 4100 FT-IR Spectrometer equipped with an ATR Pro One (JASCO, Inc., Tokyo, Japan). UV–vis was recorded on Infinite M200 microplate reader (Tecan Ltd., Männedorf, Switzerland) using Costar 96 well Clear Polystyrene Microplate (flat bottom, polystyrene, cat. no. 3370, Corning, NY, USA). Fluorescence spectra were recorded on Jobin Yvon Horiba Spex Fluorolog-3 spectrophotometer (Horiba. Ltd., Kyoto, Japan) using a quartz cell (F15-UV-10, cat. no. 621017506, GL Sciences Inc., Tokyo, Japan). HPLC analyses were carried out using JASCO PU-2080 Plus HPLC pump, JASCO MD-2018 Plus detector, and ChromNAV Chromatography Data System (JASCO, Tokyo, Japan). Solvents were purchased from Acros Organic (Thermo Fischer Scientific, Inc., Geel, Belgium) and HPLC-grade solvents were purchased from Sigma-Aldrich Co. LLC (Merck KGaA), and dried by solvent system (Innovative Technology Inc., FL, USA) or distilled when needed. All water used were from Millipore purification system. Column chromatography and analytical TLC were performed on SILICYCLE SilicaFlash® F60 (230 – 400 mesh) and Silica gel 60 F254 TLC (Merck KGaA), respectively. All the reagents were purchased from Sigma-Aldrich Co. LLC (Merck KGaA, Darmstadt, Germany) unless described, and purified as described when needed.

6.1.2 Synthesis of the compound in Chapter 2 and spectra

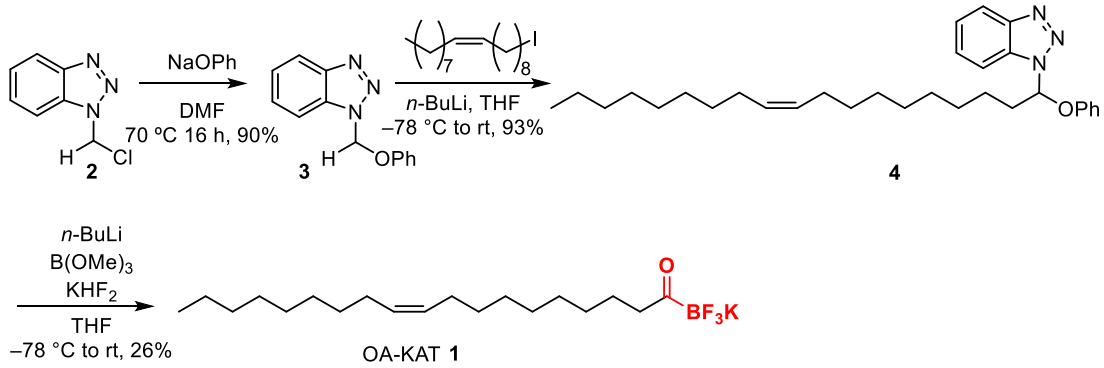

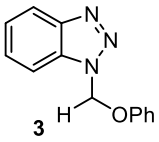

1-(Phenoxymethyl)-1*H*-benzo[*d*][1,2,3]triazole (2). To a solution of **2** (500 mg, 2.98 mmol, 1 equiv) in 10 mL of DMF, NaOPh (0.346 g, 2.98 mmol, 1 equiv, abcr GmbH, Karlsruhe, Germany) was added. The reaction was stirred at 70 °C for 16 h. After cooling down to room temperature, the reaction mixture was poured slowly into ice-water, stirred vigorously for 20 min, filtered, and the resulting white solid was washed three times with water. After drying under high vacuum, compound **3** was obtained as a fluffy colorless powder (0.38 g, 1.69 mmol, y = 57%); ^{1}H NMR (400 MHz, in $CDCl_3$): δ 8.10 (d, *J* = 8.3 Hz, 1H), 7.73 (d, *J* = 8.4 Hz, 1H), 7.56 (t, *J* = 8.0 Hz, 1H), 7.43 (t, *J* = 8.2 Hz, 1H), 7.30 (m, 2H), 7.11 (d, *J* = 8.1 Hz, 2H), 7.05 (t, *J* = 7.3 Hz, 1H), 6.58 (s, 2H). ^{13}C-NMR (100 MHz, $CDCl_3$): δ 156.2, 146.3, 132.8, 129.8, 128.2, 124.5, 123.1, 120.2, 116.3, 109.9, 75.0.

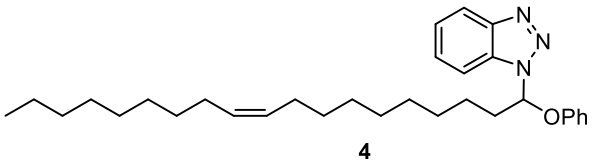

(*Z*)-1-(1-Phenoxynonadec-10-en-1-yl)-1*H*-benzo[*d*][1,2,3]triazole (3). To a solution of **3** (1.0 g, 4.40 mmol, 1 equiv) in 40 mL of THF, 4.1 mL of *n*-BuLi (1.6 M in hexane, 6.6 mmol, 1.5 equiv) was added slowly down the side of the flask at -78 °C and stirred for 1 h. Subsequently, neat oleyl iodide (2.51 g, 6.6 mmol, 1.5 equiv) was slowly added, and the reaction mixture was stirred overnight under N_2 atmosphere, letting it gradually warming up to room temperature. Subsequently, the solvent was evaporated and the crude mixture

extracted in H_2O-CH_2Cl_2. The combined organic layers were washed with brine, dried over Na_2SO_4, filtered and concentrated *in vacuo*. The crude mixture was purified by a silica gel flash chromatography (hexane - EtOAc (3:1)) to provide brown oil **4** (1.95g, 4.10 mmol, y = 93%); IR (cm^{-1}): 2923.6, 2853.3, 1451.2, 1493.3, 1590.6, 1278.8, 1153.9, 1079.5, 1071.0, 1001.2, 888.4, 746.7, 691.0, 666.7, 628.3, 557.6; ^{1}H NMR (400 MHz, $CDCl_3$): δ 8.03 (d, *J* = 8.3 Hz, 1H), 7.81 (d, *J* = 8.2 Hz, 1H), 7.45 (t, *J* = 7.8 Hz, 1H), 7.35 (t, *J* = 7.8 Hz 1H), 7.18 (t, *J* = 8.0 Hz, 1H), 6.95 (m, 3H), 6.83 (t, *J* = 6.8 Hz, 1H), 5.34 (m, 2H), 2.49-2.32 (m, 2H), 2.00 (m, 4H), 1.27 (m, 24H) 0.88 (t, *J* = 5.9 Hz, 3H); ^{13}C NMR (100 MHz, $CDCl_3$): δ 156.2, 146.7, 131.1, 129.7, 127.7, 124.3, 122.9, 120.2, 116.2, 111.2, 88.3, 34.8, 34.0, 32.8, 32.6, 31.9, 29.7, 29.5, 29.3, 29.3, 29.2, 29.2, 28.9, 28.8, 28.2, 27.2, 27.2, 24.7, 22.7, 14.1; HRMS (MALDI) *m/z*: $[M+H]^+$ calcd for $C_{31}H_{46}N_3O^+$, 476.3635; found, 476.3634.

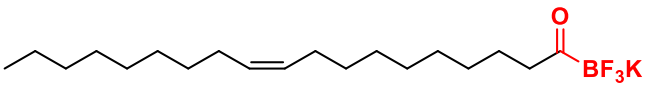

OA-KAT **1**

Potassium oleyltrifluoroborate (1). To compound **4** (4.53 g, 9.6 mmol, 1.1 equiv), dissolved in 100 mL of THF at -78°C, *n*-BuLi (1.6 M in hexane, 5.45 mL, 8.73 mmol, 1 equiv) was added slowly down the side of the flask and stirred for 30 min. Subsequently, neat $B(OMe)_3$ (1.81 g, 17.45 mmol, 2 equiv, Sigma-Aldrich) was added dropwise into the solution. The resulting reaction mixture was kept stirring for 1 h in the dry-ice/acetone bath and then removed from the bath to stir at room temperature for 5 min. The septum cap was then removed from the flask and KHF_2 aqueous solution were added slowly (9 mL x 4). The reaction mixture was stirred overnight, concentrated *in vacuo*, and then dried under high vacuum. The resulting solid was stirred in acetone and then filtered (repeated 3 times). The combined acetone filtrates were concentrated and diluted in Et_2O and stirred until precipitates formed. The precipitates were filtered, washed twice with Et_2O, and dried under high vacuum to give **1** as a white wax (0.94 g, 2.43 mmol, y = 26%); IR (cm^{-1}): 2922, 2853, 1661, 1466, 2404, 1362, 1155, 1026, 969, 929, 747, 722, 670, 667, 590, 558, 568; ^{1}H NMR (600 MHz, Acetone-d_6): δ 5.35 (m, 2H), 2.37 (t, *J* = 7.4 Hz, 2H), 1.44 (p, *J* = 7.4 Hz, 2H), 1.29 (m, 22H), 0.88 (t, *J* = 6.8 Hz, 3H); ^{13}C NMR (150 MHz, Acetone d_6): δ 130.6, 130.5, 32.6, 30.6, 30.5, 30.5, 30.4, 30.3, 30.2, 30.2, 30.0, 30.0, 27.8, 27.7, 23.3, 23.3, 14.3; ^{19}F NMR (470 MHz, Acetone d_6): δ -150.8, ^{11}B NMR (160 MHz, Acetone d_6): δ -1.67, HRMS (MALDI) *m/z*: $[M-K]^-$ calcd for $C_{19}H_{35}BF_3O^-$, 347.2738; found, 347.2739.

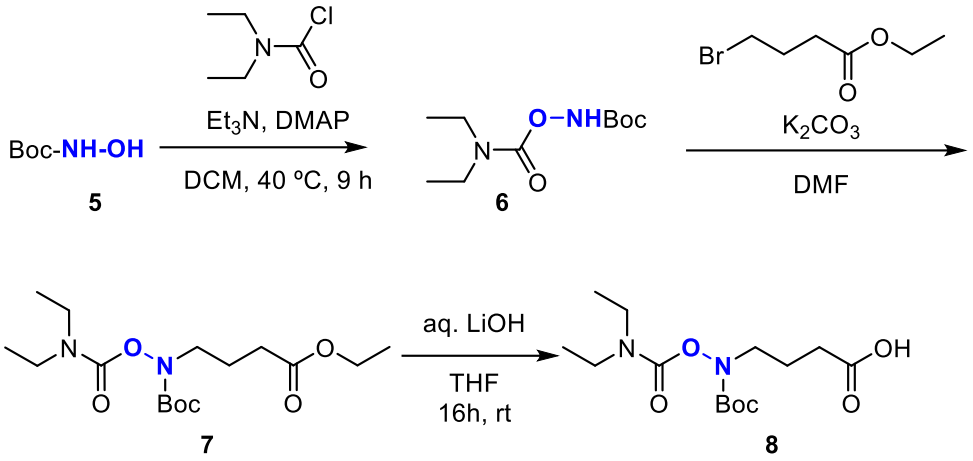

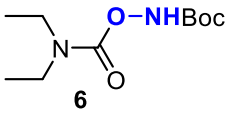

***tert*-Butyl (diethylcarbamoyl)oxycarbamate (6).** To a solution of Boc-NH-OH **5** (10 g, 0.075 mol, 1 equiv, Tokyo Chemical Industry, Co., LTD., Tokyo, Japan), triethylamine (26 mL, 0.187 mol, 2.5 equiv) and DMAP (1.00 g, 0.008 mol, 0.1 equiv) in 100 mL of CH_2Cl_2, diethylcarbamic chloride (12.51 g, 0.092 mol, 1.2 equiv) was added and the reaction mixture was stirred at room temperature overnight. The mixture was diluted with CH_2Cl_2 and washed with water. The organic layer was washed with brine, dried over Na_2SO_4, filtered and concentrated *in vacuo*. The crude extract was purified by a silica gel flash column chromatography (hexane-EtOAc (8:2), to give compound **6** (14.2 g, 0.061 mol, y = 82%); ^{1}H NMR (300 MHz, $CDCl_3$): δ 7.77, (s, 1H, NH), 3.34 (q, *J* = 7.1 Hz, 4H, CH_3-CH_2), 1.49 (s, 9H, *tert*-butyl), 1.19 (m, 6H, CH_2-CH_3 methyl protons); ^{13}C NMR (100 MHz, $CDCl_3$): δ 156.5, 155.6, 82.7, 43.0, 41.5, 28.1, 13.9, 13.3; HRMS (ESI$^+$) *m/z*: $[M+Na]^+$ calcd for $C_{10}H_{20}N_2O_4^+$, 255.1315; found, 255.1320.

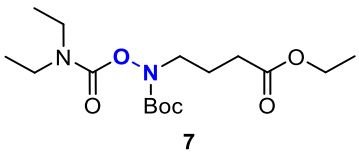

Ethyl 4-((*tert*-butoxycarbonyl)((diethylcarbamoyl)oxy)amino)butanoate (7). To a solution of **6** (7.00 g, 0.036 mol, 1.2 equiv) in 30 mL of DMF, ethyl 4-bromobutyrate (7 g, 0.03 mol, 1.0 equiv, abcr GmbH) was added followed by the addition of K_2CO_3 (6.25 g, 0.045 mol, 1.5 equiv). The reaction was stirred at 65 °C overnight. After addition of water,

the aqueous phase was extracted for 3 times with CH_2Cl_2. The combined organic layer was washed with brine and dried over sodium sulfate, filtered, and evaporated *in vacuo*. Crude product was purified by column chromatography to provide colorless oil **7** (8.3 g, 23.9 mmol, y = 80%); ^{1}H NMR (300 MHz, $CDCl_3$): δ 4.11 (q, *J* = 7.1 Hz, 2H), 3.65 (t, *J* = 6.5 Hz, 2H), 3.30 (q, *J* = 7.1 Hz, 4H), 2.39 (t, *J* = 7.5 Hz, 2H), 1.90 (p, *J* = 7.3 Hz, 0H), 1.45 (s, 9H), 1.23 (t, *J* = 7.1 Hz, 3H), 1.16 (t, *J* = 7.1 Hz, 6H); ^{13}C NMR (100 MHz, $CDCl_3$): δ 173.1, 155.0, 154.1, 81.8, 60.3, 49.6, 42.9, 41.7, 31.4, 28.2, 22.8, 14.2; HRMS (MALDI) *m/z*: $[M+H]^+$ calcd for $C_{16}H_{30}N_2O_6^+$, 347.2174; found, 347.2174.

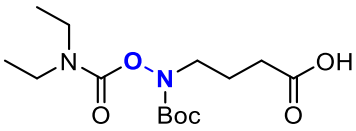

8

4-((*tert*-Butoxycarbonyl)((diethylcarbamoyl)oxy)amino)butanoic acid (8). To a solution of hydroxylamine carbamate ester **7** (1 g, 2.89 mmol, 1 equiv) in 20 mL THF, 1 M LiOH (20 mL, 832 mg, 19.8 mmol) was added. The reaction mixture was stirred at room temperature until completion for about 3 h. Subsequently, 40 mL of EtOAc was added and the reaction mixture was slowly neutralized with citric acid being careful not to exceed pH 7 in order to preserve the Boc protection on the amino group. Subsequently water was added and extracted with EtOAc (50 mL x 3). The combined organic layers were dried over Na_2SO_4, filtered, and concentrated *in vacuo* to give **8** as a pure colorless oil (650 mg, 2.04 mmol, y = 71%); ^{1}H-NMR (300 MHz, $CDCl_3$): δ 3.68 (t, *J* = 6.5 Hz, 2H), 3.31 (q, *J* = 7.1 Hz, 4H), 2.45 (t, *J* = 7.3 Hz, 2H), 1.91 (quint, *J* = 7.0 Hz, 2H), 1.46 (s, 9H), 1.18 (t, *J* = 7.0 Hz, 6H); ^{13}C NMR (100 MHz, $CDCl_3$): δ 178.1, 155.1, 154.2, 82.0, 49.5, 43.0, 41.6, 31.3, 28.2, 22.7, 14.1, 13.4; HRMS (ESI^+) *m/z*: $[M+H]^+$ calcd for $C_{14}H_{26}N_2O_6^+$, 319.1864; found, 319.1862.

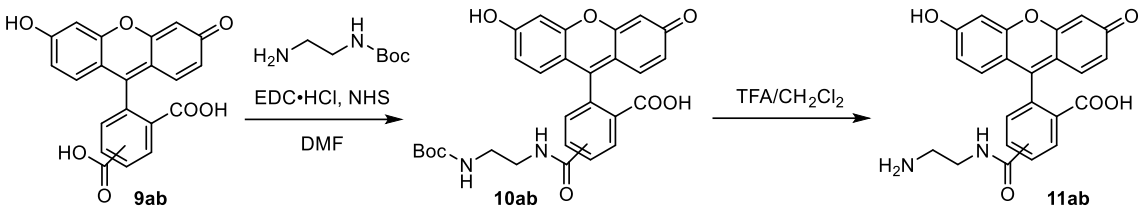

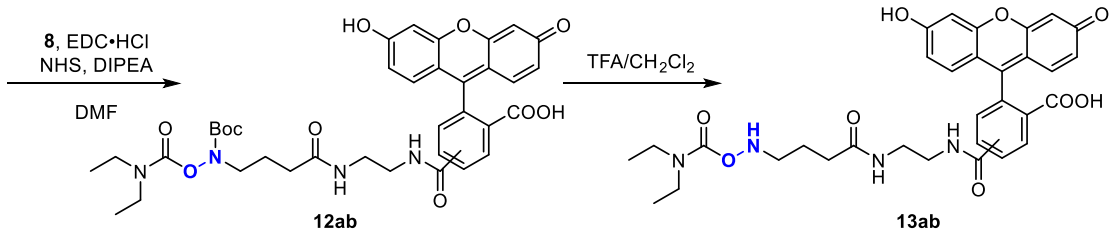

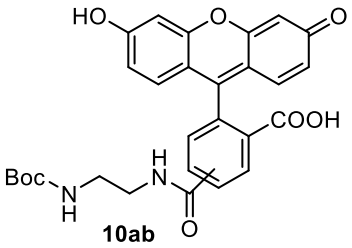

Coumpound 10ab. To a solution of a mixture of carboxyfluoresceins **9ab** (20 mg, 0.053 mmol, 1 equiv, Sigma-Aldrich) in 0.9 mL of dry DMF, EDC•HCl (40.8 mg, 0.213 mmol, 4 equiv, Tokyo Chemical Industry, Co., LTD.) and NHS (24.5 mg, 0.213 mmol, 4 equiv, Sigma-Aldrich) were added. The reaction mixture was stirred for 1 h under Ar atmosphere and then ethylene diamine (34.13 mg, 0.213 mmol, 4 equiv) was added and stirred for additional 4 h. Reaction mixture was purified by reverse phase HPLC using MeOH-water eluent system to provide yellow fluffy powder **10a** and **10b** (18 mg, 0.034 mmol, y = 64%); **10a**: ^{1}H NMR (300 MHz, methanol-d_4) δ 8.49 (s, 1H) 8.22 (dd, *J* = 8.1, 1.4 Hz, 1H, H6), 7.34 (d, *J* = 8.1 Hz, 1H), 6.78 (d, *J* = 2.2 Hz, 2H), 6.71 (d, *J* = 8.8 Hz, 2H), 6.62 (dd, *J* = 8.8, 2.3 Hz, 2H), 3.51 (t, *J* = 5.9 Hz, 2H), 3.32 (m, 2H) 1.43 (s, 9H); **10b**: ^{1}H NMR (300 MHz, methanol-d_4): δ 8.15 (d, *J* = 8.0 Hz, 1H), 8.10 (d, *J* = 8.1 Hz, 1H), 7.63 (s, 1H), 6.74 (d, *J* = 2.3 Hz, 2H,), 6.67 (d, *J* = 8.7 Hz), 6.59 (dd, *J* = 8.7, 2.3 Hz,), 3.38 (t, *J* = 5.2 Hz, 2H), 3.20 (t, *J* = 5.8 Hz, 2H), 1.31 (s, 10H); HRMS (ESI^{+}) *m/z*: [M+H]$^{+}$ calcd for $C_{28}H_{27}N_2O_8^{+}$, 519.1762; found, 519.1757.

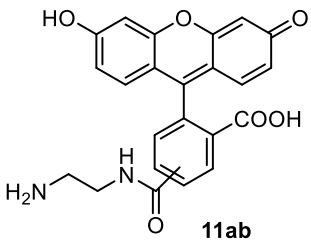

11ab

Compound 11ab. To a mixture of **10ab** (18 mg, 0.0347 mmol, 1 equiv), TFA (250 µL, Sigma-Aldrich) was added and stirred for 10 min at room temperature. Completion of the reaction was monitored by LC-MS. The resulting solution was immediately dried under nitrogen stream to dryness and used without further purification in the next step.

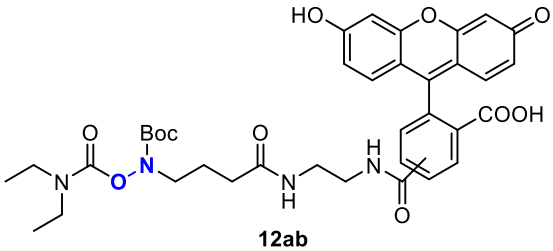

12ab

Compound 12ab. To a solution of a mixture of **11ab** (15 mg, 0.036 mmol, 1 equiv) in 0.35 mL of dry DMF, EDC•HCl (13.8 mg, 0.072 mmol, 2 equiv, Tokyo Chemical Industry, Co., LTD.) and NHS (8.3 mg, 0.072 mmol, 2 equiv, Sigma-Aldrich) were added. After stirring for 1 hour, a solution of **6** (17.1 mg, 0.054 mmol, 1.5 equiv) and DIPEA (20 µL, 0.108 mmol, 3 equiv, Acros Organics) in 0.11 mL of dry DMF were added and stirred for additional 18 h. Crude reaction mixture was purified by reverse phase HPLC with CH_3CN-H_2O gradient system (10% to 90% in 40 min), to provide yellow fluffy powder, **12a** and **8b** (7 mg, 9.5 µmol, y = 27%); IR (cm^{-1}): 2979, 1736, 1606, 1543, 1453, 1425, 1368, 1271, 1144, 994, 924, 852, 748, 667, 595, 568, 552 HRMS (MALDI) *m/z* calcd for $C_{35}H_{42}N_4NaO_{11}$: 741.2737, found 741.2742 $[M+Na]^+$, **10b**: ^{1}H NMR (400 MHz, methanol-d_4) δ 8.15 (d, *J* = 1.0 Hz, 2H), 7.66 (s, 1H), 6.81 (d, *J* = 2.2 Hz, 1H), 6.77 (d, *J* = 8.8 Hz, 1H), 6.66 (dd, *J* = 8.7, 2.2 Hz, 1H), 3.53-3.31 (m, 10H), 2.21 (t, *J* = 7.4 Hz, 2H), 1.75 (m, 2H), 1.41 (s, 9H, Boc), 1.16 (m, 6H); ^{13}C NMR (101 MHz, methanol-d_4) δ 175.7, 170.0, 168.4, 156.7, 155.9, 155.1, 141.9, 130.9, 130.5, 127.2, 124.9, 114.9, 112.0, 103.6, 83.4, 77.3, 50.6, 49.7, 49.6, 44.2, 42.9, 41.16, 39.79, 33.79, 28.46, 24.29, 14.48, 13.62, 6.60; a mixture of **10ab**: ^{1}H NMR (400 MHz, methanol-d_4) δ 8.48 (s, 1H, 5-isomer, H4), 8.21 (dd, *J* = 8.0, 1.6 Hz), 8.16 (dd, *J* = 8.0, 1.3 Hz), 8.13 (d, *J* = 8.2 Hz), 7.65 (s, 1H), 7.34 (d, *J* = 8.0, 1H), 6.78-6.62 (m, 12H), 3.68-2.55 (m, 20H), 2.31 (t, *J* = 7.5, 2H), 2.21 (t, *J* = 7.4, 2H), 1.88 (p, *J* = 6.9 Hz, 2H), 1.76 (p, *J* = 6.9 Hz, 2H), 1.44

(s, 9H), 1.42 (s, 9H), 1.16 (m, 12H); ^{13}C NMR (100 MHz, methanol-d_4) δ 175.8, 175.7, 170.1, 168.6, 168.4, 156.7, 155.9, 154.8, 137.9, 135.1, 130.8, 130.6, 130.5, 114.6, 111.7, 103.6, 83.4, 50.8, 50.6, 49.7, 49.6, 49.5, 49.4, 49.3, 49.2, 49.1, 49.0, 49.0, 48.9, 48.8, 48.7, 48.6, 48.4, 44.2, 42.9, 41.2, 41.2, 39.9, 39.8, 34.0, 33.8, 28.5, 28.5, 26.4, 26.3, 24.5, 24.3, 14.5, 13.6.

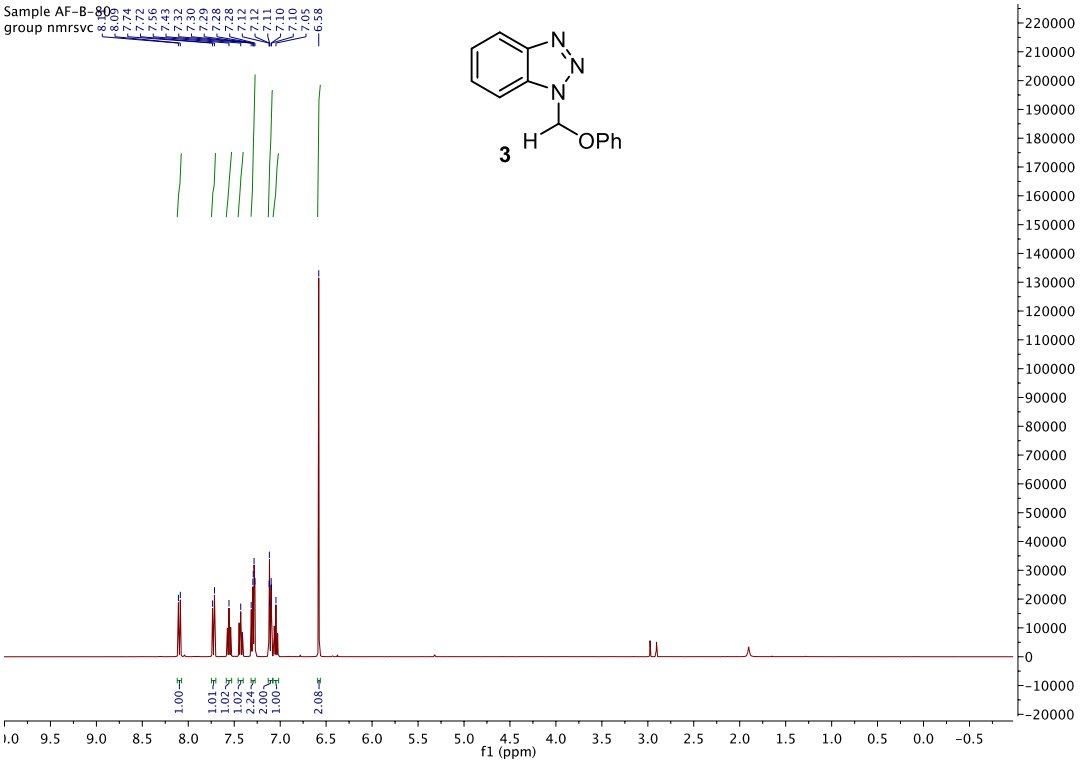

Figure 51. ^{1}H-NMR spectrum of **3** (in $CDCl_3$, 400 MHz).

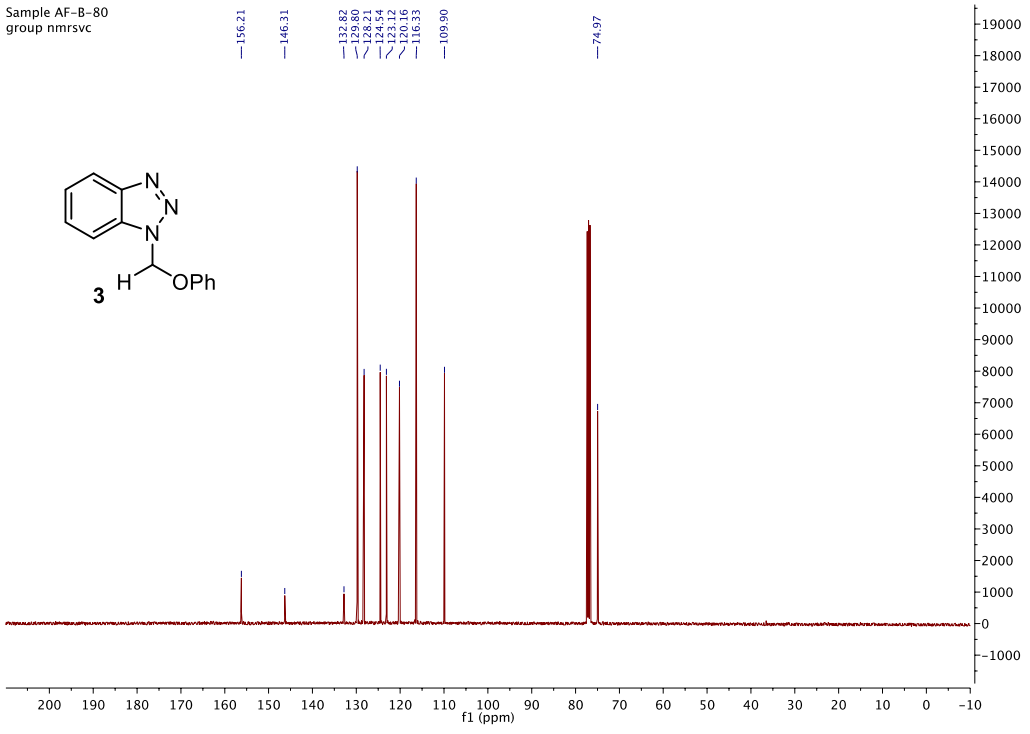

Figure 52. ^{13}C-NMR spectrum of **3** (in $CDCl_3$, 100 MHz).

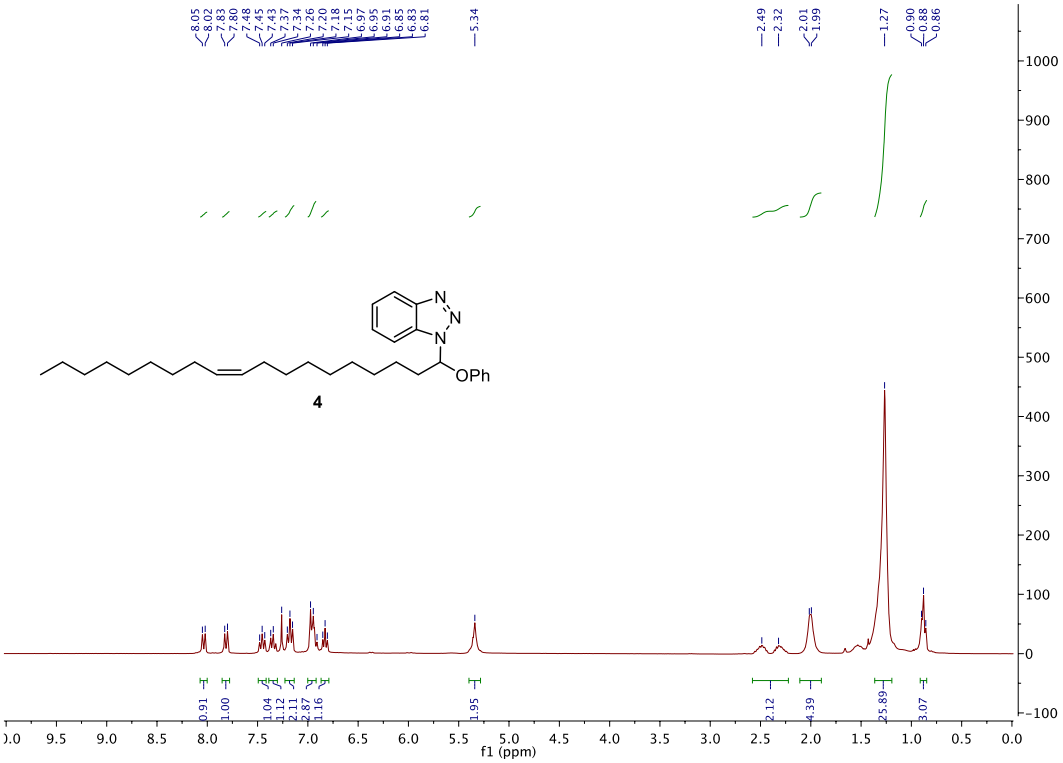

Figure 53. ^{1}H-NMR spectrum of **4** (in $CDCl_3$, 400 MHz).

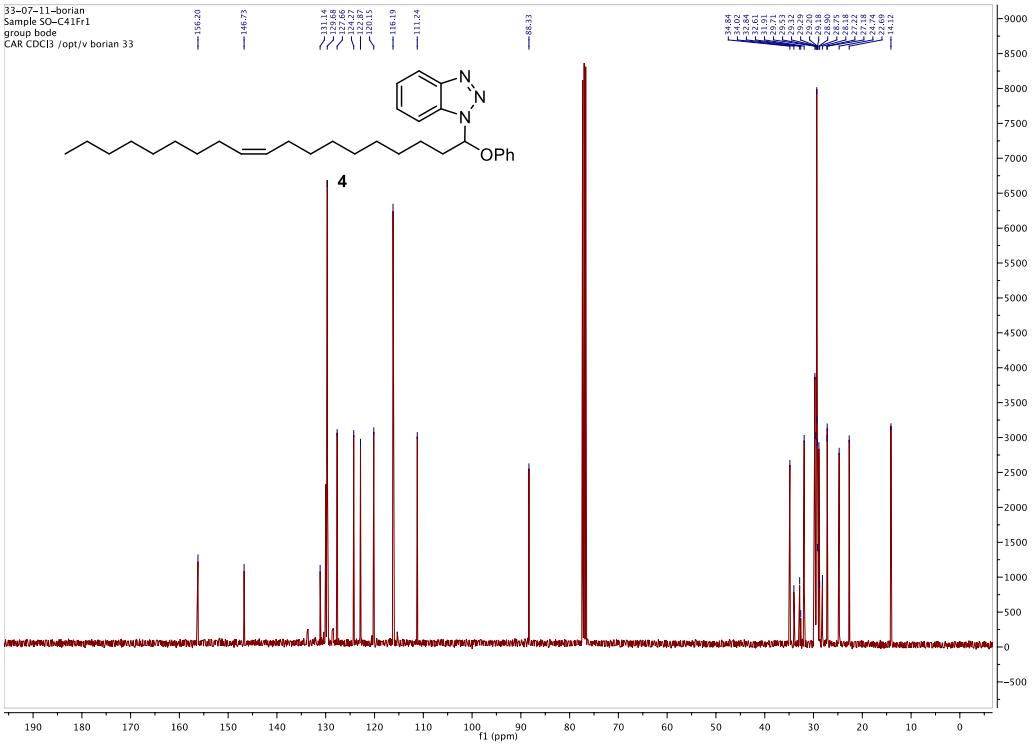

Figure 54. ^{13}C-NMR spectrum of **4** (in $CDCl_3$, 100 MHz).

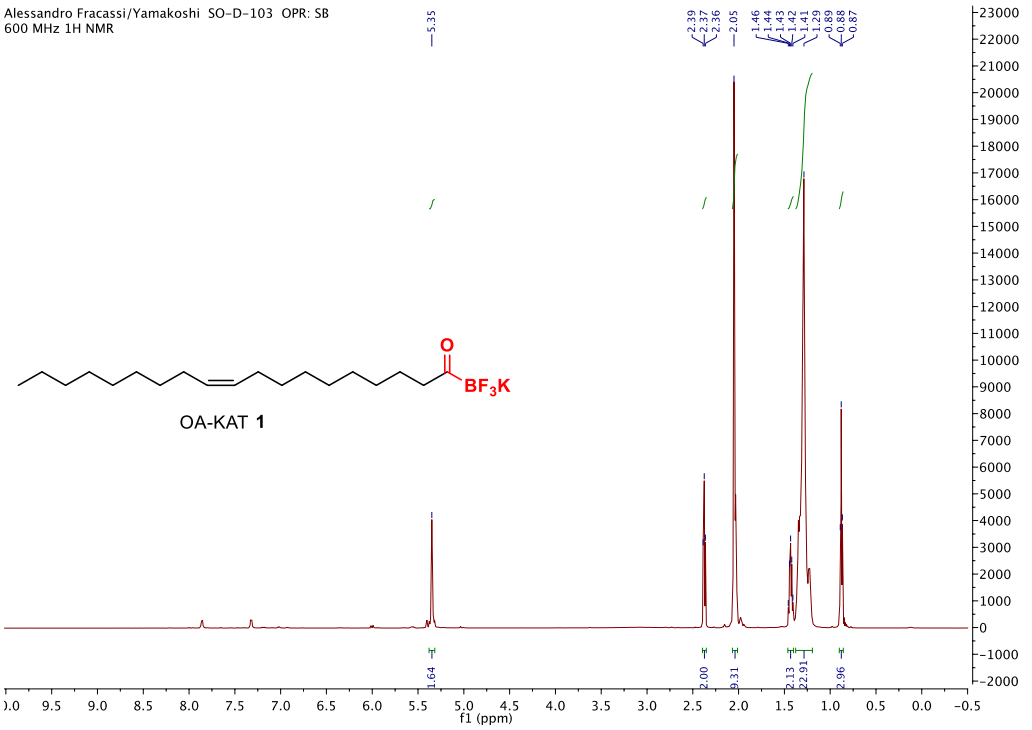

Figure 55. ^{1}H-NMR spectrum of **1** (in Acetone-d_6, 600 MHz).

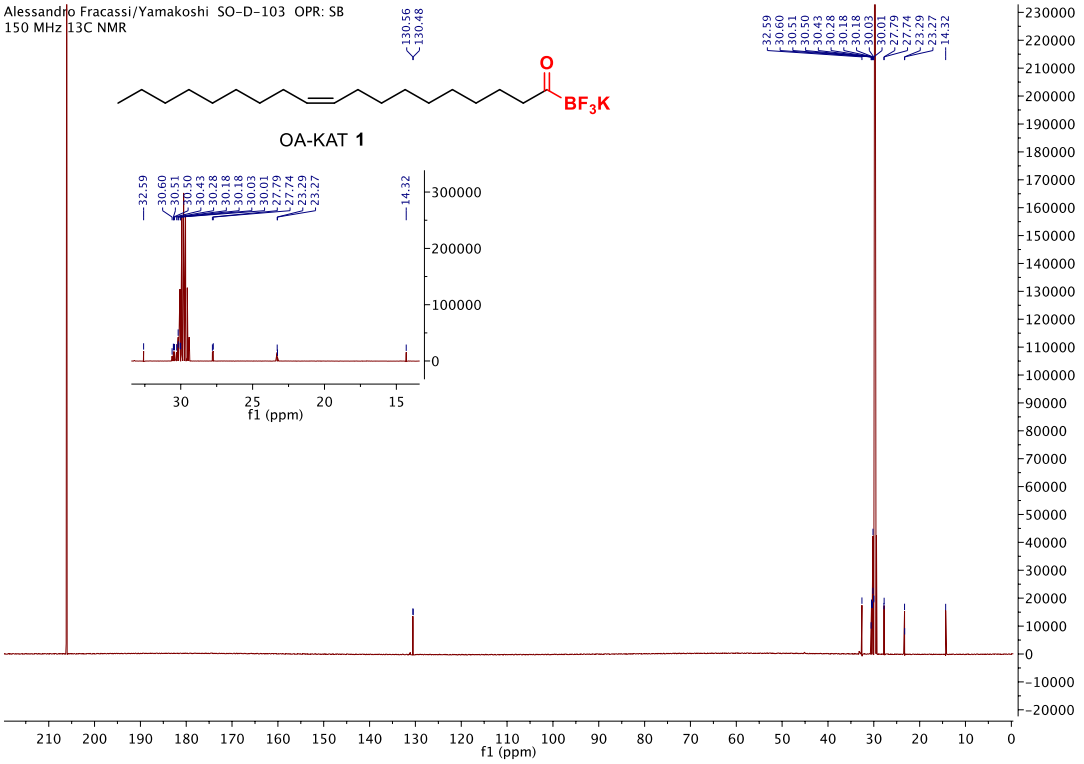

Figure 56. ^{13}C-NMR spectrum of **1** (in Acetone-d_6, 150 MHz).

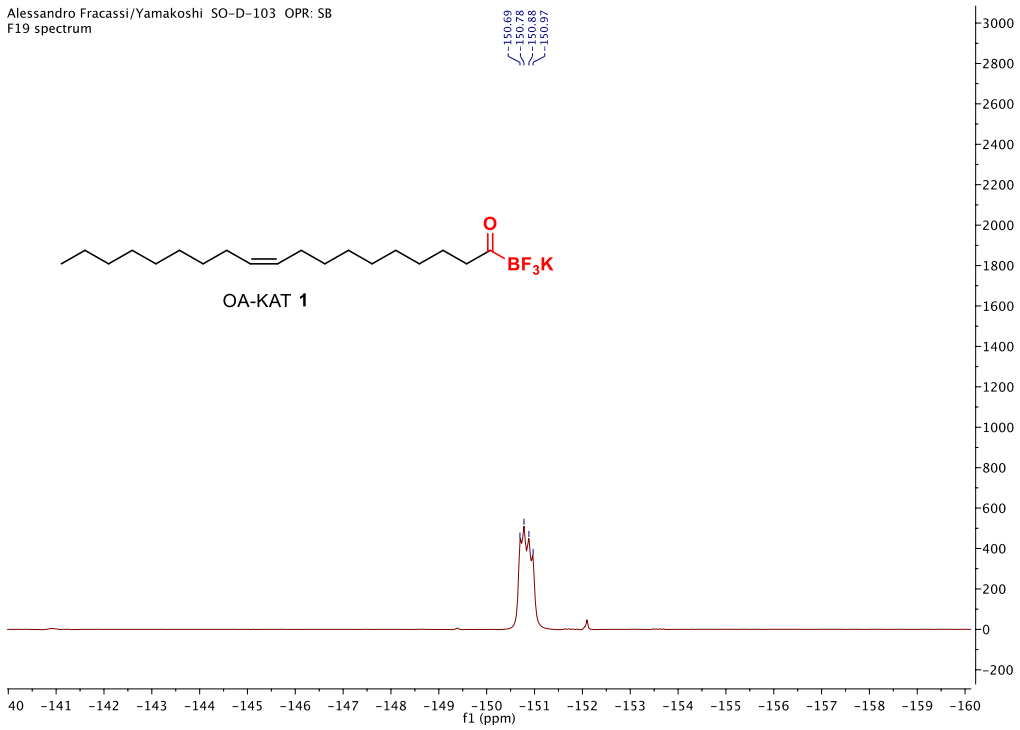

Figure 57. ^{19}F-NMR spectrum of **1** (in Acetone-d_6, 470 MHz).

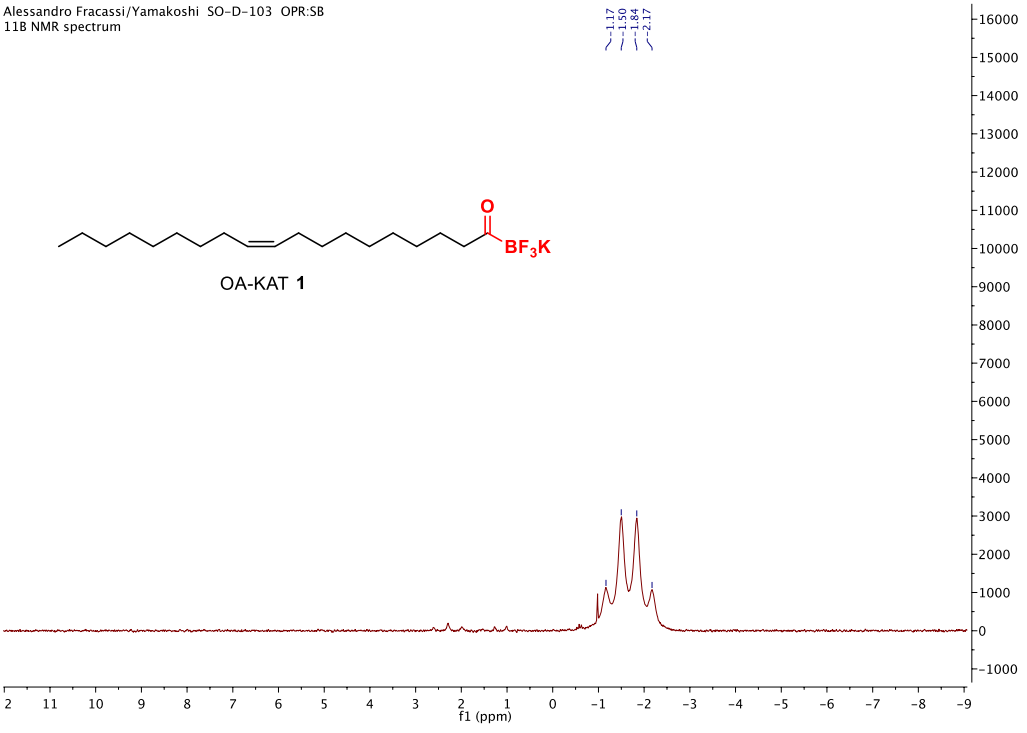

Figure 58. ^{11}B-NMR spectrum of **1** (in Acetone-d_6, 160 MHz).

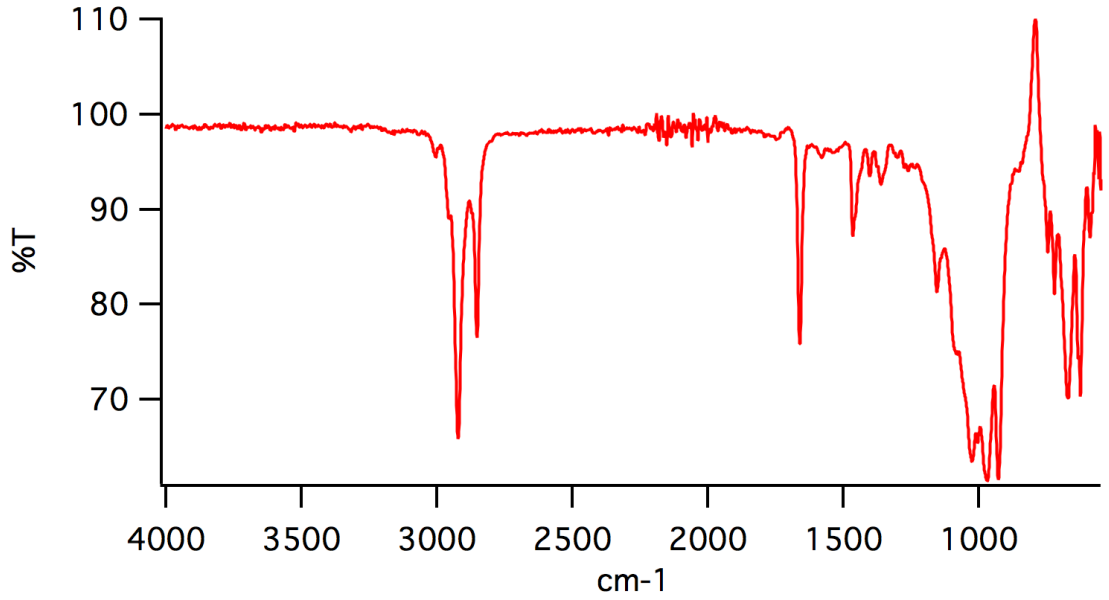

Figure 59. FT-IR spectrum of **1.**

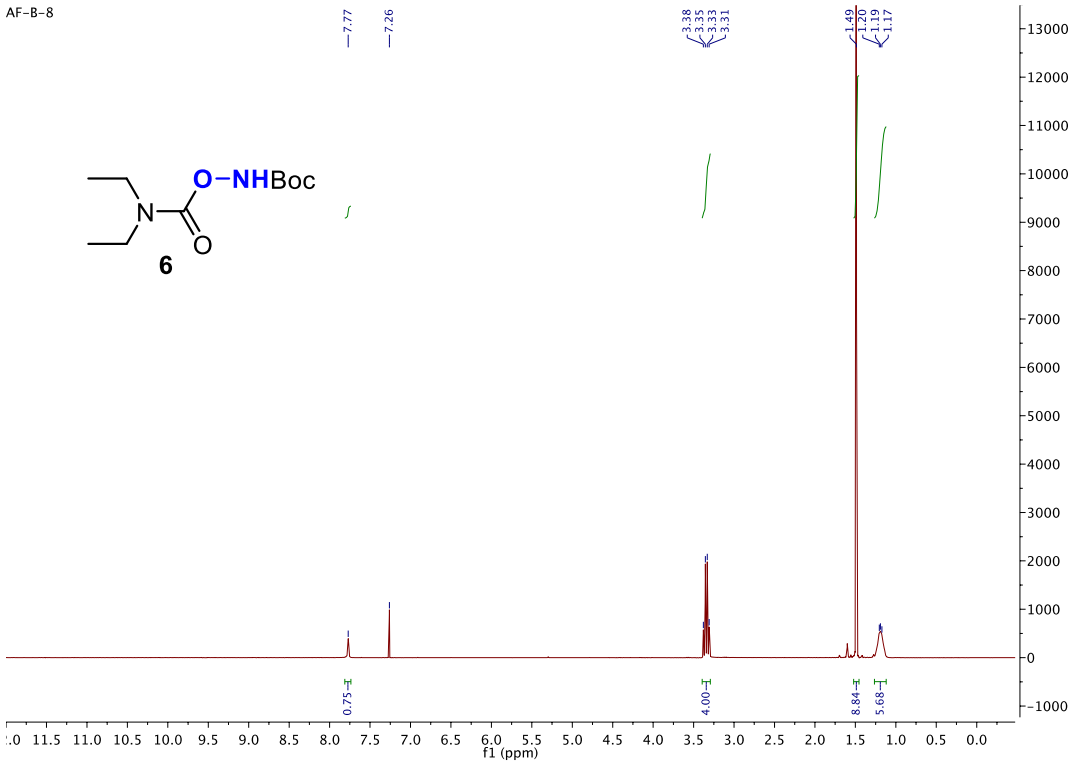

Figure 60. ^{1}H-NMR spectrum of **6** (in $CHCl_3$, 300 MHz).

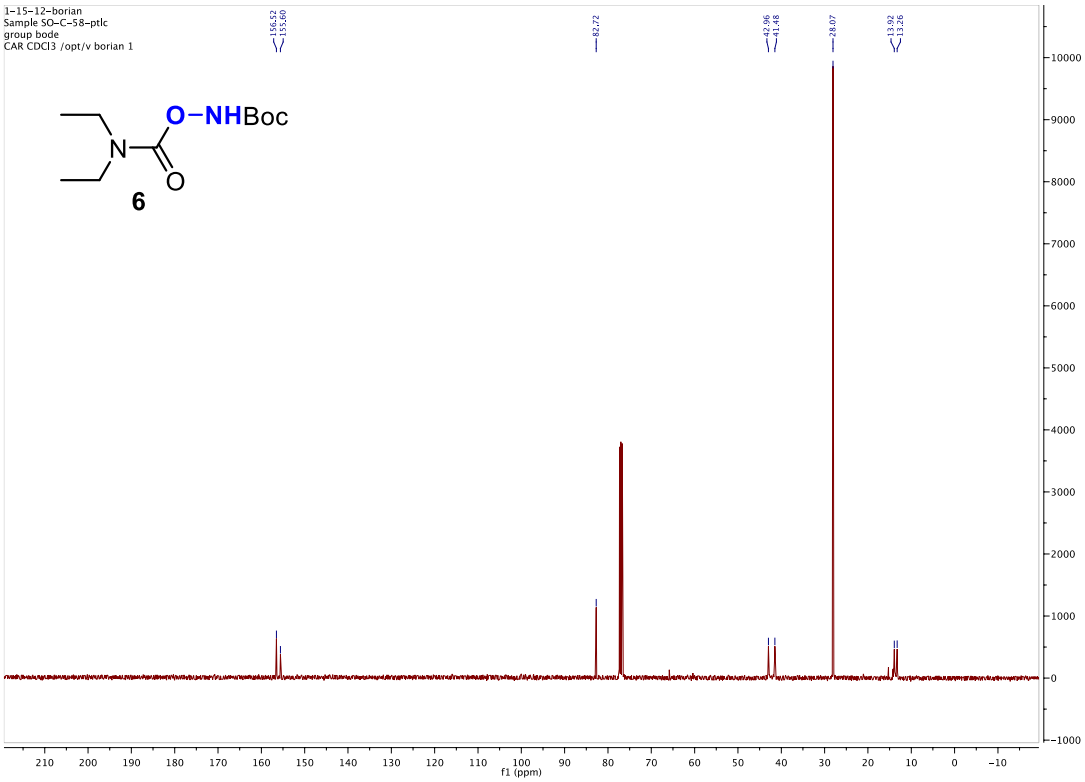

Figure 61. ^{13}C-NMR spectrum of **6** (in $CDCl_3$, 100 MHz).

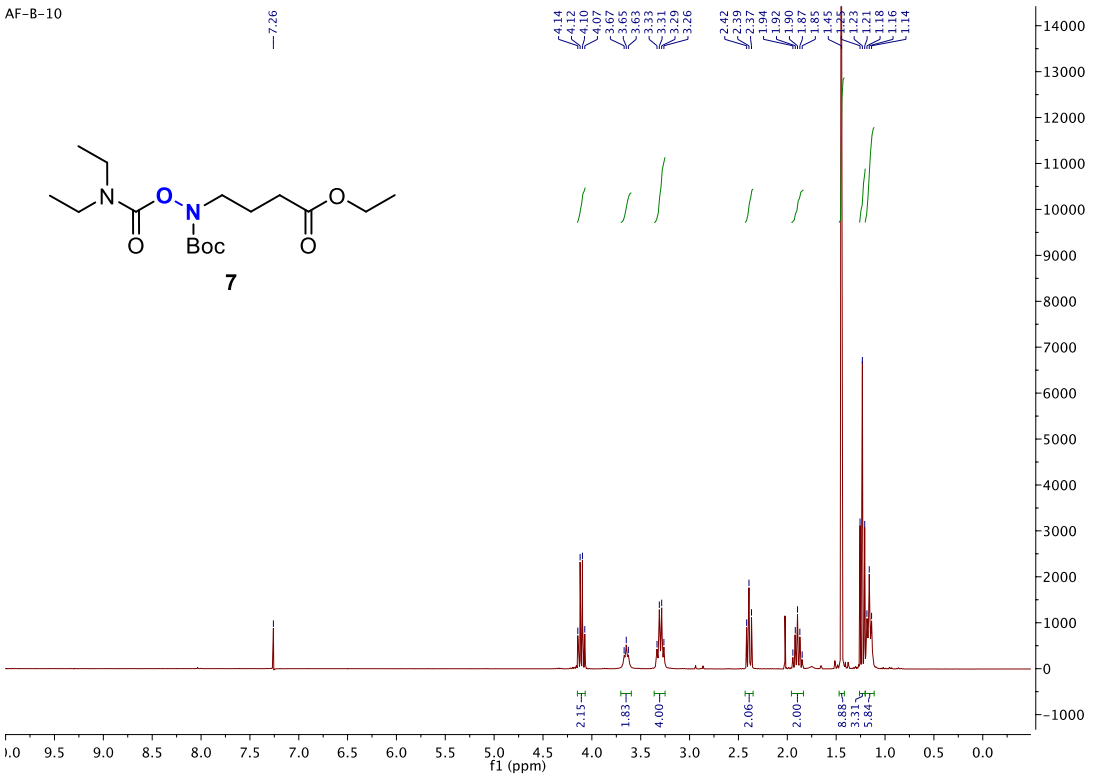

Figure 62. ^{1}H-NMR spectrum of **7** (in $CDCl_3$, 300 MHz).

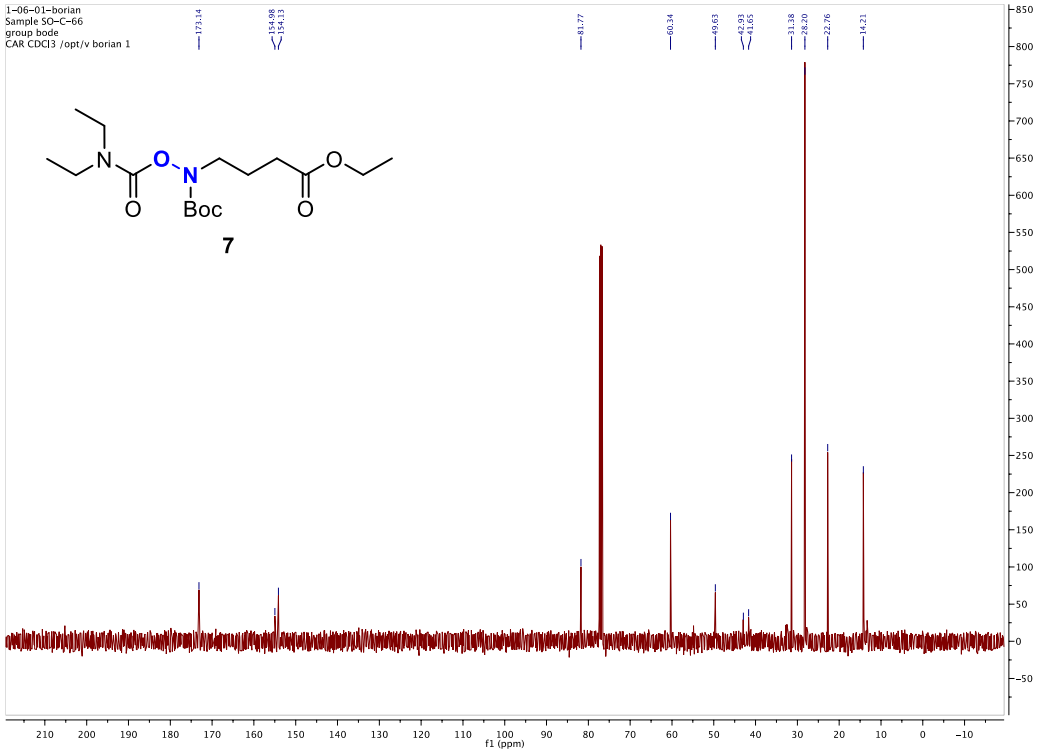

Figure 63. ^{13}C-NMR spectrum of **7** (in $CDCl_3$, 100 MHz).

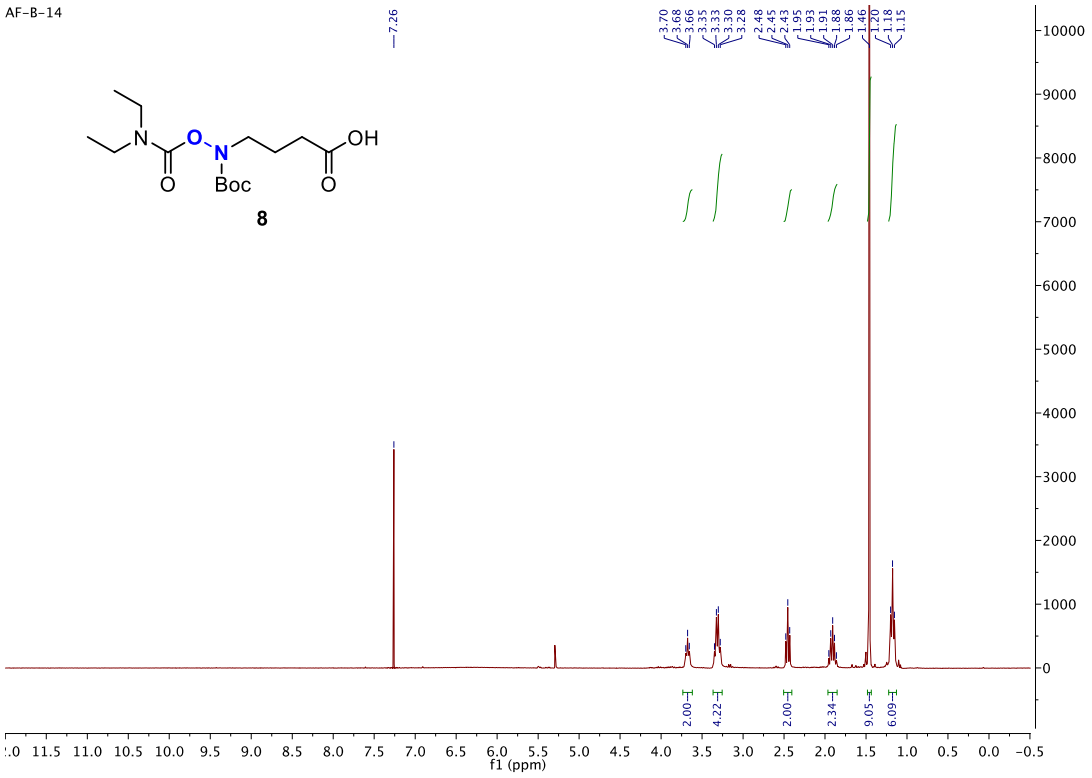

Figure 64. ^{1}H-NMR spectrum of **8** (in $CDCl_3$, 400 MHz).

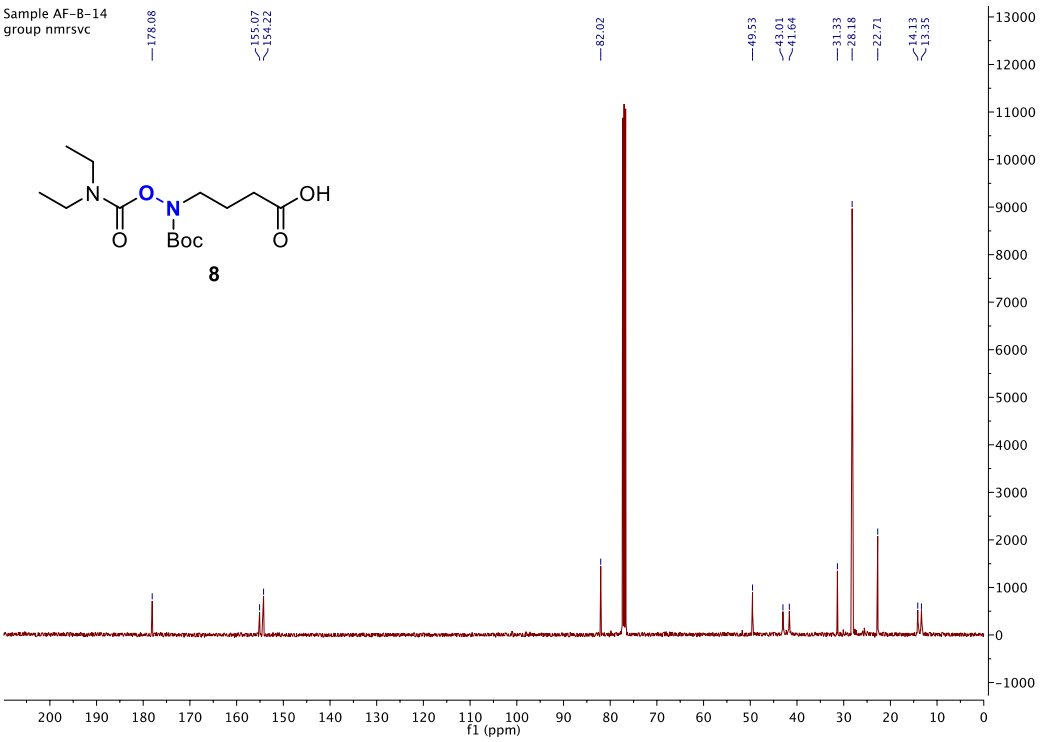

Figure 65. ^{13}C-NMR spectrum of **8** (in $CDCl_3$, 100 MHz).

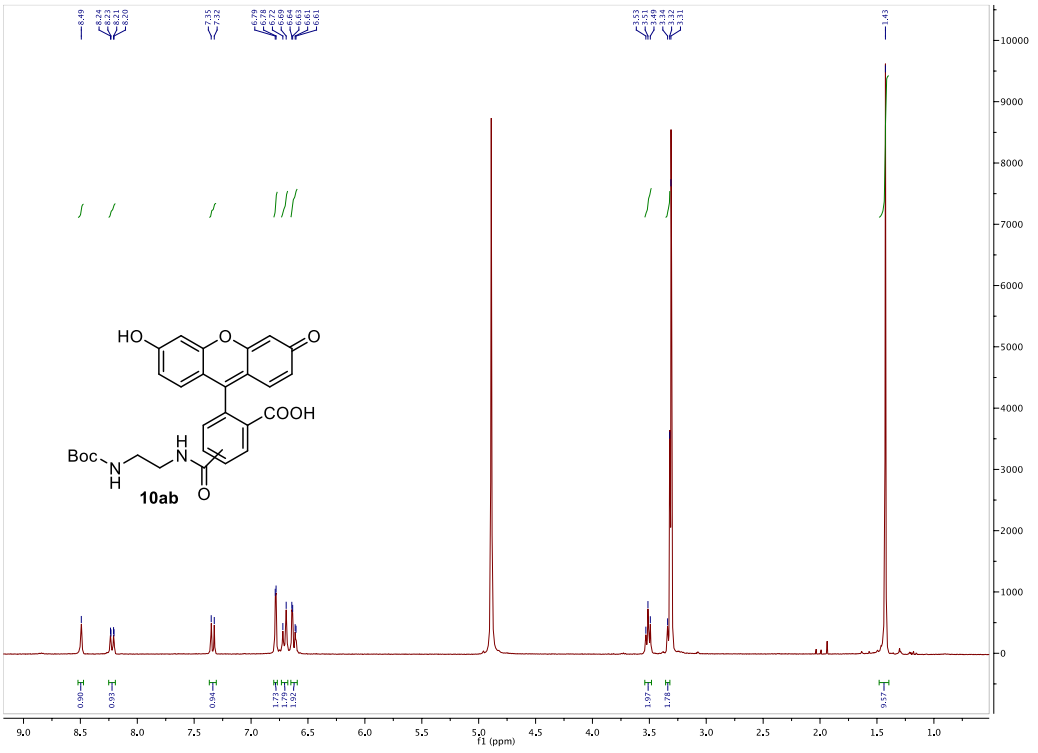

Figure 66. ^{1}H-NMR spectrum of **10ab** (in methanol-d_4, 300 MHz).

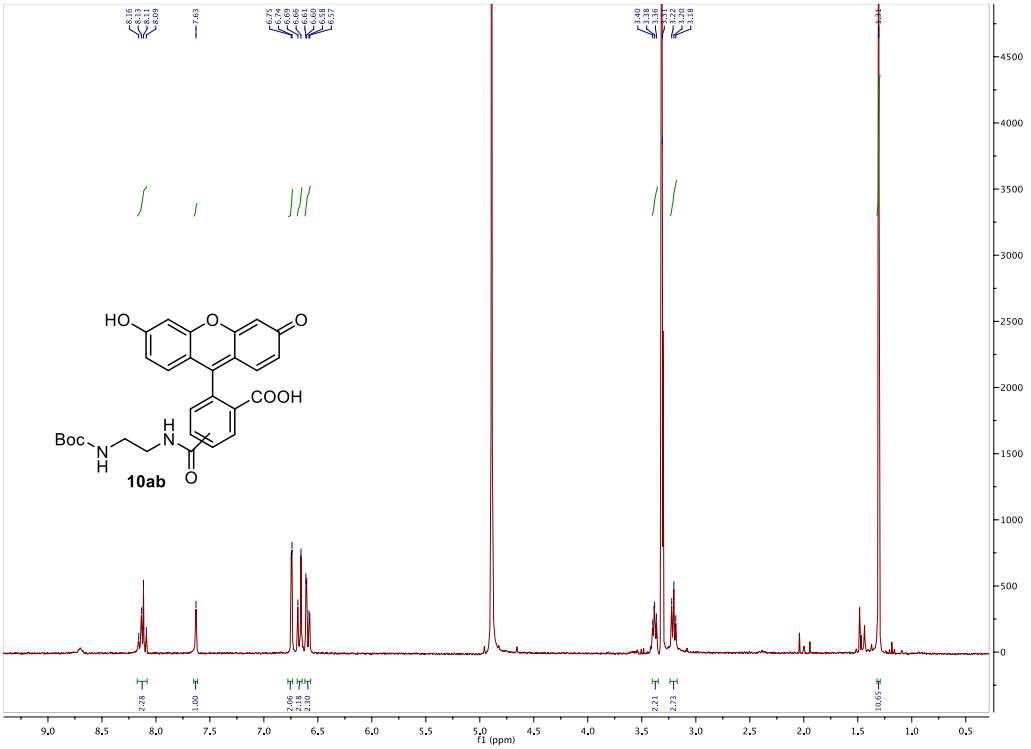

Figure 67. ^{1}H-NMR spectrum of **10ab** (in methanol-d_4, 300 MHz).

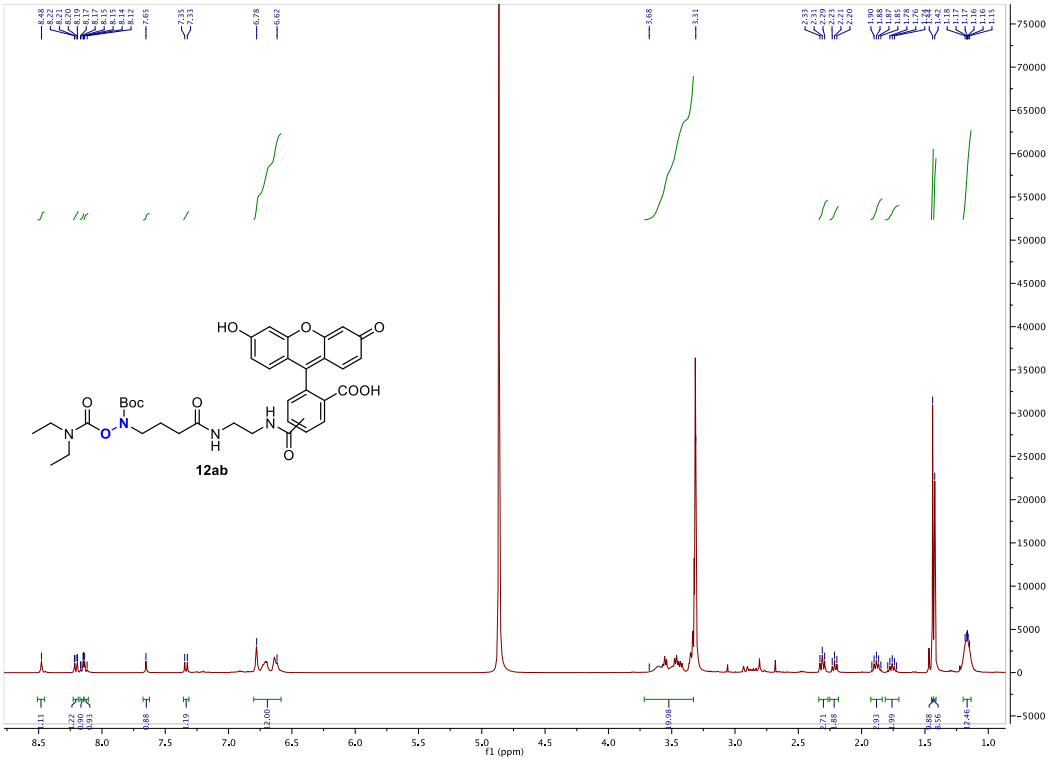

Figure 68. ^{1}H-NMR spectrum of compound **12ab** (methanol-d_4, 400 MHz).

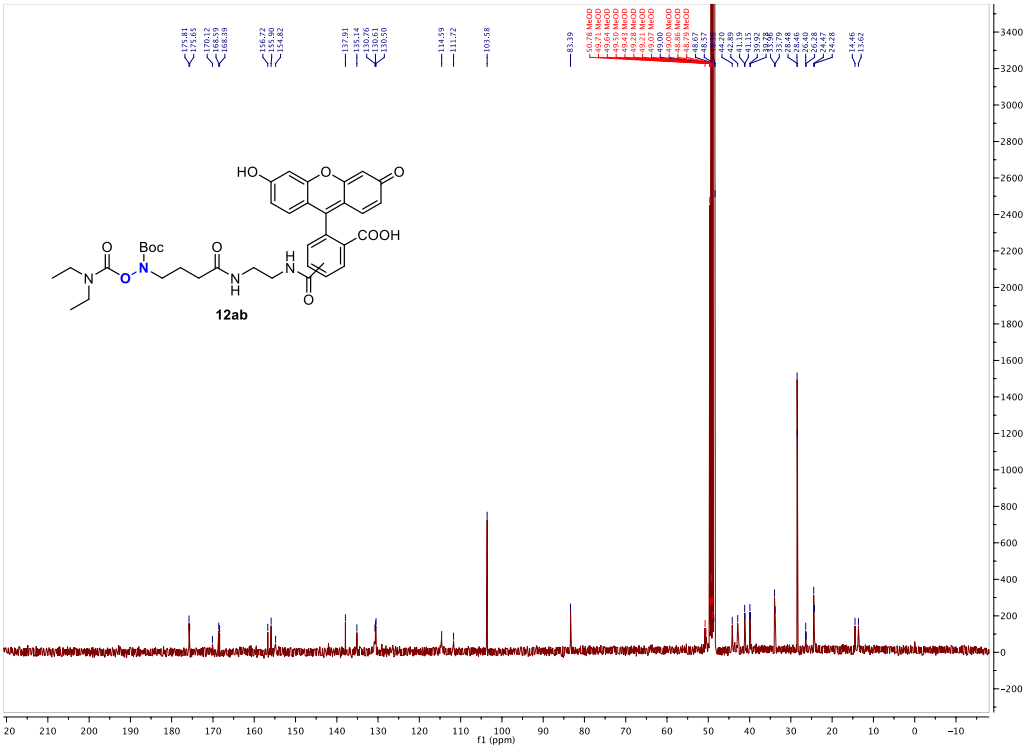

Figure 69. ^{13}C-NMR spectrum of a compound **12ab** (methanol-d_4, 100 MHz).

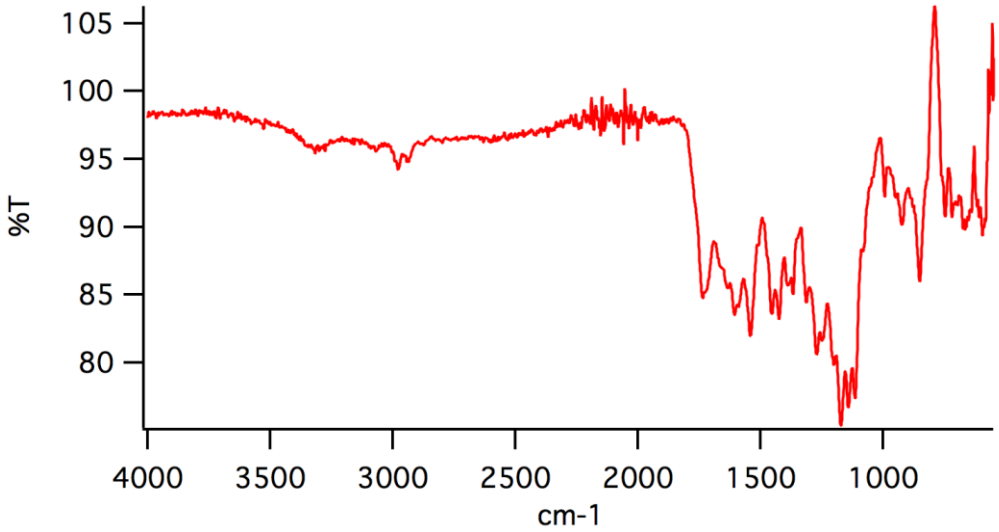

Figure 70. IR spectrum of compound **12ab**.

6.1.3 Synthesis of the compound in Chapter 3 and spectra

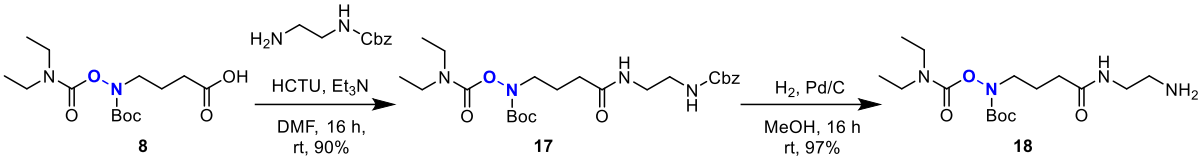

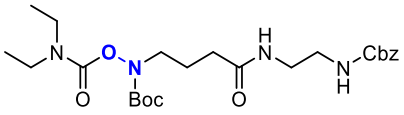

17

***tert*-Butyl(4-((2-(((benzyloxy)carbonyl)amino)ethyl)amino)-4-oxobutyl)((diethylcarbamoyl)oxy) carbamate (17).** Compound **8** (200 mg, 0.63 mmol, 1.0 equiv), Et_3N (270 µL, 1.9 mmol, 3.0 equiv) and HCTU (260 mg, 0.63 mmol, 1.0 equiv) were dissolved in 5 mL of DMF. After stirring the reaction mixture for 5 min at room temperature, benzyl (2-aminoethyl) carbamate (220 mg, 0.72 mmol, 1.1 equiv) was added and the reaction mixture was stirred overnight at room temperature. After the removal of DMF under reduced pressure, the crude mixture was extracted by CH_2Cl_2 and purified by a silica gel column chromatography (solvent: hexane-EtOAc) to provide **17** as a colorless oil (290 mg, 0.57 mmol, Y = 90%); IR (cm^{-1}): 3330 (N–H), 2977 (C–H), 2937 (C–H), 1718 (C=O), 1655, 1534 (C–N), 1423, 1367, 1264, 1144, 844, 1037, 845, 743, 698; ^{1}H NMR (400 MHz, in $CDCl_3$): δ 1.13 (m, CH_2CH_3, 6 H), 1.38 (s, $C(CH_3)_3$, 9 H), 1.84 (quin, $CH_2CH_2CH_2$, *J* = 6.5 Hz, 2H), 2.25 (t, $COCH_2CH_2$, *J* = 7.1 Hz, 2H), 3.27 (m, $CONHCH_2CH_2$, $OCONHCH_2$, 8H), 3.58 (t, $N(Boc)CH_2$, *J* = 6.2 Hz, 2H), 5.04 (s, OCH_2Ph, 2H) 5.78 (br.t, CH_2NHCbz, 1H), 6.52 (br.t, $CONHCH_2$, 1H), 7.31 (m, Ph, 5H); ^{13}C NMR (100 MHz, in $CDCl_3$): δ 13.3, 14.2, 23.6, 28.1, 33.3, 38.6, 39.9, 41.2, 41.68, 43.1, 49.2, 66.6, 82.2, 128.0, 128.2, 128.4, 136.6, 154.3, 155.5, 156.9, 173.3; HRMS (ESI^+) *m/z*: $[M+H]^+$ calcd for $C_{24}H_{39}N_4O_7^+$, 495.2813; found, 495.2819.

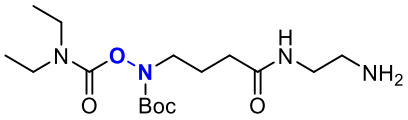

18

***tert*-Butyl (4-((2-aminoethyl)amino)-4-oxobutyl)((diethylcarbamoyl)oxy)carbamate (18).** Compound **17** (400 mg, 0.8 mmol, 1.0 equiv) was dissolved in MeOH (10 mL) in a Schlenk flask and 10% Pd/C (wt/wt) (20 mg, 0.019 mmol, 0.024 equiv) was added. The mixture was

stirred under H_2 atmosphere at room temperature for 16 h until completion of the reaction. Subsequently, EtOAc (10 mL) was added and the mixture was filtered on a pad of celite. The solvent was removed under reduced pressure and the crude product **18** (280 mg, 0.78 mmol, y = 97% in crude) was used without any further purification; IR (cm^{-1}): 2979 (C–H), 2938 (C–H), 1727 (C=O), 1675 (C=O), 1541 (C–N), 1424, 1368, 1269, 1201, 1171, 1140, 928, 835, 798, 746, 721; ^{1}H NMR (400 MHz, in $CDCl_3$): δ 1.13 (m, $CH_2C\mathbf{H_3}$, 6 H), 1.41 (s, $C(C\mathbf{H_3})_3$, 9 H), 1.86 (quin, $CH_2C\mathbf{H_2}CH_2$, *J* = 6.9 Hz, 2H), 2.27 (t, $COC\mathbf{H_2}CH_2$, *J* = 7.25 Hz, 2H), 2.81 (t, $CH_2C\mathbf{H_2}NH_2$, *J* = 5.8 Hz, 2H), 3.27 (m, $OCONHC\mathbf{H_2}$, 6H), 3.59 (t, $N(Boc)C\mathbf{H_2}$, *J* = 6.4 Hz, 2H), 6.71 (t, $CON\mathbf{H}CH_2$, *J* = 5.7 Hz, 1H); ^{13}C NMR (100 MHz, $CDCl_3$): δ 13.3, 14.1, 23.3, 28.2, 33.4, 41.3, 41.6, 41.6, 43.0, 49.5, 82.0, 154.3, 155.4, 173.3; HRMS (ESI^+) *m/z*: $[M+Na]^+$ calcd for $C_{16}H_{32}N_4O_5Na^+$, 383.2265; found, 383.2256.

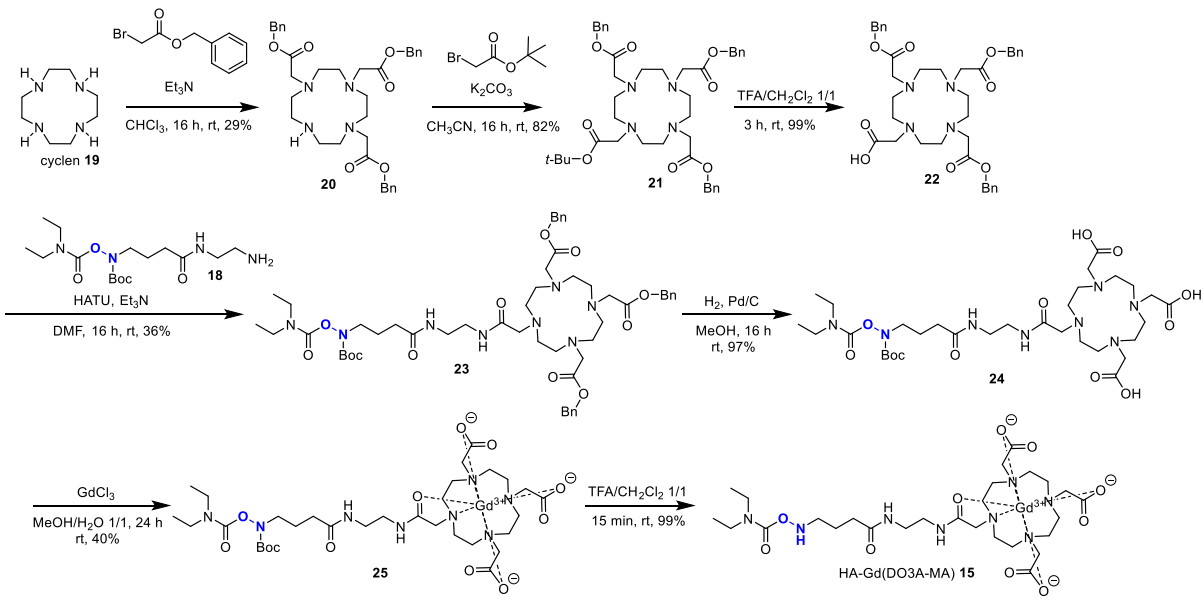

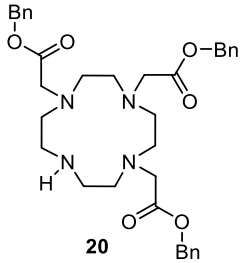

Tribenzyl 2,2',2''-(1,4,7,10-tetraazacyclododecane-1,4,7-triyl)triacetate (20). To a solution of cyclen (2.00 g, 11.6 mmol, 1.0 equiv, abcr GmbH, Karlruhe, Germany) and Et_3N (5.86 g, 58 mmol, 5.0 equiv) in $CHCl_3$ (300 mL), a solution of benzyl bromoacetate (7.97 g, 34.8 mmol, 3.0 equiv) in $CHCl_3$ (50 mL) was added at 0 °C dropwise using a syringe pump

over 30 min. After subsequently stirring overnight at room temperature, the solvent was removed and a crude mixture was extracted with CH_2Cl_2. The crude extract was purified by a silica column chromatography using CH_2Cl_2-MeOH as eluents to provide the colorless oil **20** (2.07 g, 3.36 mmol, Y = 29%); ^{1}H NMR (400 MHz, in $CDCl_3$): δ 2.83-2.87 (m, C**H**$_2$NCH$_2$COO, 12 H), 3.07 (t, NHC**H**$_2$, *J* = 4.1 Hz, 4 H), 3.40 (s, NC**H**$_2$COO, 2 H,), 3.47 (s, NC**H**$_2$COO, 4 H), 5.12 (s, OC**H**$_2$Ph, 6 H), 7.33 (m, Ph, 15 H); ^{13}C NMR (100 MHz, $CDCl_3$): δ 47.4, 48.7, 49.5, 51.6, 51.8, 57.3, 66.7, 128.5, 128.6, 128.6, 128.7, 128.8, 135.4, 135.4, 170.2, 171.0; HRMS (ESI$^+$) *m/z*: $[M+H]^+$ calcd for $C_{35}H_{45}N_4O_6^+$, 617.3334; found, 617.3338.

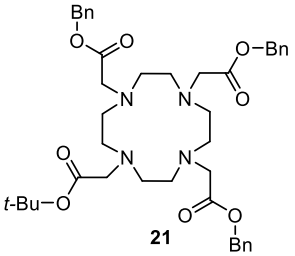

21

Tribenzyl 2,2',2''-(10-(2-(*tert*-butoxy)-2-oxoethyl)-1,4,7,10-tetraazacyclododecane-1,4,7-triyl)triacetate (21). To a solution of **S6** (2.0 g, 3.3 mmol, 1.0 equiv) in 40 mL of CH_3CN, K_2CO_3 (0.705 g, 5.0 mmol, 1.5 equiv) and tert-butyl bromoaceate (0.66 g, 3.3 mmol, 1.0 equiv) were added. The reaction mixture was stirred overnight at room temperature, filtered, and the solvent was removed under vacuum. The obtained crude mixture was purified by a silica column chromatography (CH_2Cl_2-MeOH) to provide compound **21** as a colorless oil (1.97 g, 2.7 mmol, Y = 82%); ^{1}H NMR (400 MHz, in $CDCl_3$): δ 1.40 (s, C(C**H**$_3$)$_3$ 9 H), 2.95-4.12 (m, C**H**$_2$NC**H**$_2$COO 24 H), 5.02 (m, OC**H**$_2$Ph 6 H), 7.29 (m, Ph, 15 H); ^{13}C NMR (100 MHz, in $CDCl_3$): δ 28.1, 55.2, 55.4, 56.0, 66.9, 67.0, 82.1, 128.4, 128.5, 128.6, 128.6, 128.7, 135.3, 173.3, 173.78, 173.82; HRMS (ESI$^+$) *m/z*: $[M+Na]^+$ calcd for $C_{41}H_{54}N_4O_8Na^+$, 753.3834; found, 753.3829.

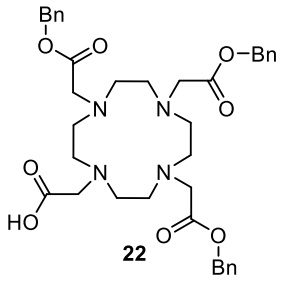

22

2-(4,7,10-Tris(2-(benzyloxy)-2-oxoethyl)-1,4,7,10-tetraazacyclododecan-1-yl)acetic acid (22). To a solution of compound **21** (1.8 g, 2.46 mmol, 1.0 equiv) in CH_2Cl_2 (3 mL), TFA (3 mL) was added. The reaction mixture was stirred for 3 h at room temperature. The solvent was removed by a flux of N_2 to provide crude **22** as a yellow oil (1.6 g, 2.6 mmol, Y ≥ 99%, the product was used without further purification); ^{1}H NMR (400 MHz, in DMSO-*d*$_6$): δ 1.91-3.74 (m, C**H**$_2$NC**H**$_2$COO, 24 H), 5.13 (m, OC**H**$_2$Ph, 6 H), 7.35 (m, Ph, 15 H); ^{13}C NMR (100 MHz, in DMSO-*d*$_6$): δ 55.4, 66.3, 66.4, 67.9, 128.5, 128.6, 128.6, 128.8, 128.8, 128.9, 128.9, 128.95, 128.99, 135.5, 136.2, 136.2, 158.0, 173.4; HRMS (ESI$^+$) *m/z*: [M+H]$^+$ calcd for $C_{37}H_{47}N_4O_8^+$, 675.3388; found, 675.3391.

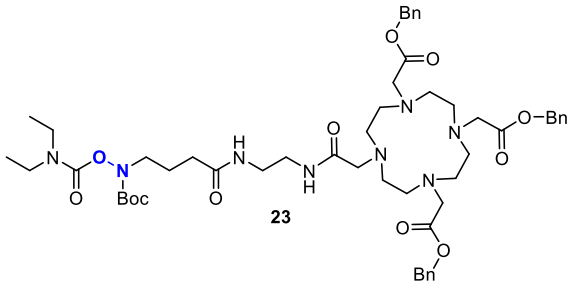

23

Tribenzyl2,2',2''-(10-(6-(*tert*-butoxycarbonyl)-3-ethyl-4,10,15-trioxo-5-oxa-3,6,11,14-tetraazahexadecan -16-yl)-1,4,7,10-tetraazacyclododecane-1,4,7-triyl)triacetate (23). To a solution of compound **22** (0.44 g, 0.65 mmol, 1.0 equiv) in DMF (10 mL), Et_3N (270 µL, 0.2 g, 1.95 mmol, 3.0 equiv) and HATU (0.247 g, 0.65 mmol, 1.0 equiv) were added. After stirring the solution for 5 min, compound **18** (0.26 g, 0.72 mmol, 1.1 equiv) was added and the reaction mixture was stirred overnight at room temperature. After the removal of DMF, the crude mixture was extracted with CH_2Cl_2 and the obtained crude mixture was purified by a silica gel column chromatography (CH_2Cl_2-MeOH) to provide **23** as a colorless solid (0.24 g, 0.23 mmol, y = 36%); IR (cm^{-1}): 3091.3 (N–H), 2979 (C–H), 1736 (C=O), 1686 (C=O), 1556 (C–N), 1457, 1392, 1367, 1200, 1165, 1090, 797, 747, 698; ^{1}H NMR (400 MHz, in $CDCl_3$): δ 1.17 (m, CH_2C**H**$_3$, 6 H), 1.45 (s, C(C**H**$_3$)$_3$, 9 H), 1.89 (quin, CH_2C**H**$_2$$CH_2$, *J* = 6.85 Hz, 2H**)**, 2.0-3.7 (m, C**H**$_2$NC**H**$_2$COO, NC**H**$_2$$CH_3$, N(Boc)C**H**$_2$, NHC**H**$_2$C**H**$_2$NH

,COC**H**$_2$CH$_2$, 34H), 5.13 (s, OC**H**$_2$Ph, 2 H), 5.20 (s, OC**H**$_2$Ph, 4 H), 6.43 (t, CON**H,** *J* = 5.9 Hz, 1H), 7.02 (t, CON**H,** *J* = 7.9 Hz, 1H), 7.31 (m, Ph, 15 H); ^{13}C NMR (100 MHz, $CDCl_3$): δ 13.4, 14.1, 23.2, 28.2, 32.9, 38.9, 39.7, 41.7, 43.0, 49.2, 55.2, 55.3, 55.5, 67.1, 82.0, 128.4, 128.5, 128.5, 128.6, 128.6, 128.7, 135.2, 135.4, 154.3, 155.5, 172.1, 173.3, 173.5; HRMS (ESI$^+$) *m/z*: $[M+Na]^+$ calcd for $C_{53}H_{76}N_8O_{12}Na^+$, 1039.5475; found, 1039.5470.

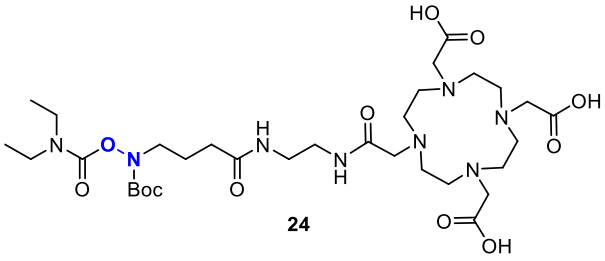

24

2,2',2''-(10-(6-(*tert*-Butoxycarbonyl)-3-ethyl-4,10,15-trioxo-5-oxa-3,6,11,14-tetraazahexadecan-16-yl)-1,4,7,10-tetraazacyclododecane-1,4,7-triyl)triacetic acid (24). Compound **23** (0.24 g, 0.24 mmol, 1.0 equiv) was dissolved in MeOH (10 mL) in a Schlenk flask and Pd/C (10%, wt.) (20 mg, 0.019 mmol, 0.08 equiv) was added. The reaction mixture was stirred under H_2 atmosphere at room temperature for 16 h until completion of the reaction. After addition of EtOAc (10 mL), the mixture was filtered on a pad of celite. The solvent was removed under reduced pressure to give the crude product **24** (164 mg, 0.22 mmol, y = 91% in crude), which was used without any further purification; IR (cm^{-1}): 3323 (O–H), 3094 (N–H), 2980 (C–H), 1730 (C=O), 1670 (C=O), 1462, 1426.1, 1394, 1370, 1273, 1189, 1143, 798, 719; ^{1}H NMR (400 MHz, DMSO-d_6): δ 1.10 (m, CH_2CH_3, 6 H), 1.38 (s, $C(CH_3)_3$, 9 H), 1.72 (quin, $CH_2CH_2CH_2$, *J* = 6.87 Hz, 2H), 2.14 (t, COC**H**$_2$CH$_2$, *J* = 7.19 Hz, 2H), 2.55-3.66 (m, C**H**$_2$NC**H**$_2$COO, NC**H**$_2$CH$_3$, N(Boc)C**H**$_2$, NHC**H**$_2$C**H**$_2$NH ,COC**H**$_2$CH$_2$, 34H); ^{13}C NMR (100 MHz, in DMSO-d_6): δ 13.8, 14.5, 23.5, 28.3, 32.7, 38.7, 41.6, 43.0, 49.9, 55.5, 81.4, 153.9, 154.9, 172.2; HRMS (ESI$^+$) *m/z*: $[M+H]^+$ calcd for $C_{32}H_{59}N_8O_{12}^+$ 747.4247; found, 747.4250.

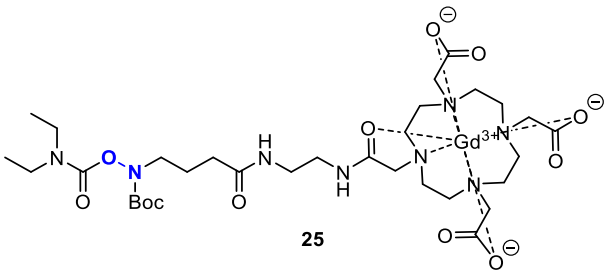

HA(Boc)-Gd(DO3A-MA) (25). To a solution of compound **24** (0.15 g, 0.20 mmol, 1.0 equiv) in MeOH (5 mL), a solution of $GdCl_3$ (0.058 mg, 0.22 mmol, 1,1 equiv, Alfa Aesar, Ward Hill, MA, USA) in water (5 mL) was added. The pH was slowly adjusted to 6.5 using 0.1 N NaOH. The reaction mixture was stirred for 24 h at room temperature. Subsequently, pH of the reaction mixture was adjusted to 9 using 0.1 N NaOH to remove free Gd^{3+} as a precipitate of $Gd(OH)_3$. The precipitate was removed by filtration and obtained crude mixture was purified by a reverse phase HPLC (column: Shiseido Capcell Pak C18 column (Φ30 x 250 mm), eluent: a gradient of CH_3CN-H_2O (10:90 to 90:10) over 40 min in the presence of 0.1% TFA). After the purity of obtained fraction was confirmed by an analytical HPLC (Figure S25) and the collected fraction was dried under vacuum to provide a colorless solid **25** (0.072 g, 0.08 mmol, Y = 40%); IR (cm^{-1}): 3282 (O–H), 3098 (N–H), 2980 (C–H), 2938 (C–H), 2877 (C–H), 1733 (C=O), 1625 (C=O), 1368, 1318, 1271, 1144, 1085, 1002, 934, 799, 717; HRMS (ESI^+) *m/z*: $[M+H]^+$ calcd for $C_{32}H_{56}Gd_1N_8O_{12}^+$, 902.3261; found, 902.3262.

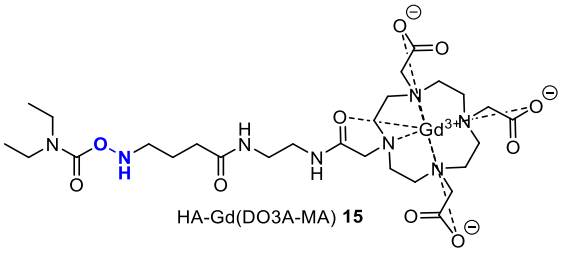

HA-Gd(DO3A-MA) (15). To a suspension of **25** (5 mg, 6.2 μmol, 1 equiv) in CH_2Cl_2 (0.5 mL), TFA (0.5 mL) was added. The reaction mixture was stirred at room temperature for 15 min to see the completion of reaction monitored by LC-MS (Figure S28b). The solvents were removed by N_2 flow to obtain colorless solids **15**; IR (cm^{-1}): 32723 (O–H), 3098 (N–H), 2875 (C–H), 2360 (C–H), 1749 (C=O), 1621 (C=O), 1406, 1317, 1269.9, 1132, 1082, 1001, 936, 903, 797, 705; HRMS: ($MALDI^+$) *m/z*: $[M+H]^+$ calcd for $C_{27}H_{48}Gd_1N_8O_{10}^+$, 802.2729, found: 802.275.

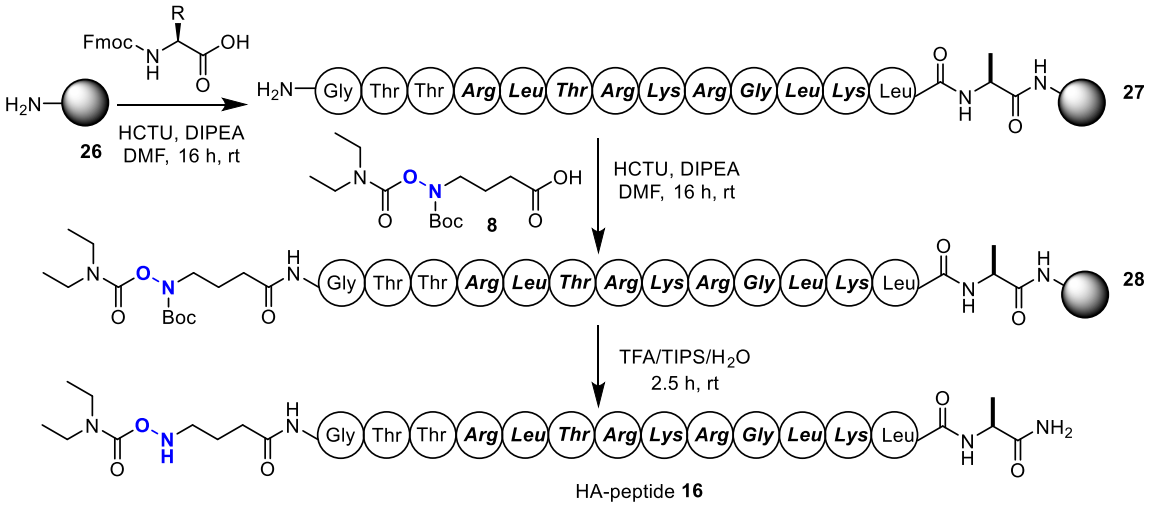

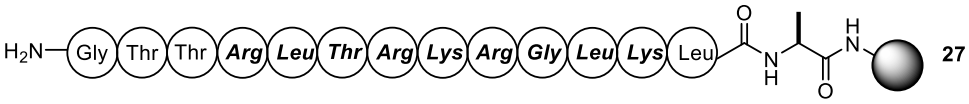

Peptide on resin 27. Peptide **27** was synthesized by solid phase peptide synthesis (SPPS) using Rink-amide-MBHA resin (1.0 g, 0.52 mmol•g^{-1}, 1.0 equiv, Chem-Impex, Wood Dale, IL, USA). The resin was initially allowed to swell in CH_2Cl_2 for 20 min before adding 20% (v/v) piperidine in DMF (15 mL) to remove the Fmoc group on the resin. Separately, DIPEA (0.9 mL, 5.2 mmol, 10 equiv) was added to a solution of an *N*-Fmoc amino acid (2.6 mmol, 5 equiv) and HCTU (1.075 g, 2.6 mmol, 5 equiv) in a minimal amount of DMF. After stirring for 5 min, an activated *N*-Fmoc amino acid solution was added to the deprotected resin above. The reaction mixture was shaken for 1 h at room temperature. The resin was subsequently washed with DMF (15 mL, 3 times) and CH_2Cl_2 (15 mL, 3 times). The unreacted free amine groups on the resin were capped with a solution of acetic anhydride 20% (v/v) in the presence of DIPEA 20% (v/v) in DMF by shaking for 20 min at room temperature. The Fmoc group of the *N*-terminus of the peptide was deprotected by 20% (v/v) piperidine in DMF for the addition of the next Fmoc-amino acid. This protocol was repeated to obtain the peptide on resin **27**.

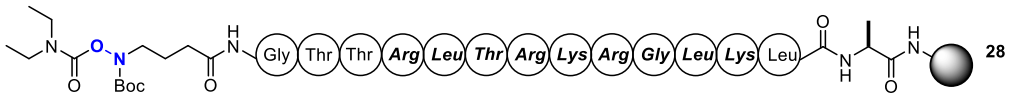

***N*-Boc-HA-peptide on resin 28.** To a solution of HA-COOH linker **8** (0.5 g, 1.56 mmol, 3.0 equiv) and HCTU (0.64 g, 1.56 mmol, 3.0 equiv) in the minimal amount of DMF, DIPEA (0.55 mL, 3.12 mmol, 6.0 equiv) was added. After stirring for 5 min, the reaction mixture was added to the peptide on resin **27** and shaken for 1 h at room temperature. The resin was washed with DMF (15 mL, 3 times) and CH_2Cl_2 (15 mL, 3 times) to obtain peptide **28** on resin.

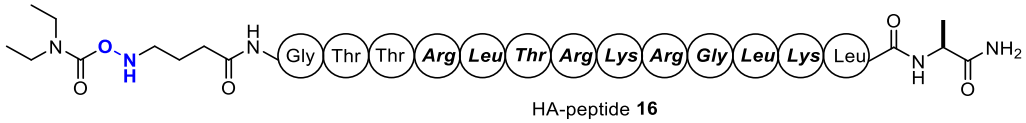

HA-peptide **16**

HA-peptide 16. To the HA-functionalized peptide on resin **28** (0.5 g), a mixture of TFA/TIPS/H_2O (95:2.5:2.5 (v/v/v), 5.0 mL) was added and the reaction mixture was stirred for 2.5 h at room temperature. The reaction mixture was filtered to remove the resin and the filtrate was concentrated under reduced pressure. The peptide, which was deprotected and cleaved from the resin, was collected by precipitation with Et_2O. After centrifuge, the supernatant was removed and the precipitate (crude peptide) was dried under vacuum and purified by a reverse phase HPLC (column: Shiseido Capcell Pak C18 column (Φ 30 mm x 250 mm) (Shiseido Co. Ltd., Tokyo, Japan), solvent system: CH_3CN-H_2O in the presence of 0.1% TFA (a gradient of CH_3CN-H_2O (v/v, 10:90 to 90:10) over 40 min). The corresponding fraction was collected and its purity was confirmed by analytical reverse phase HPLC (Figure S1). The collected fraction was lyophilized to provide the all-deprotected peptide **16** (0.17 g, 0.096 mmol, 37% yield in total for peptide synthesis); HRMS (MALDI$^+$, matrix: HCCA) *m/z*: $[M+H]^+$calcd for $C_{76}H_{145}N_{28}O_{20}^+$: 1770.1184, found 1770.1185.

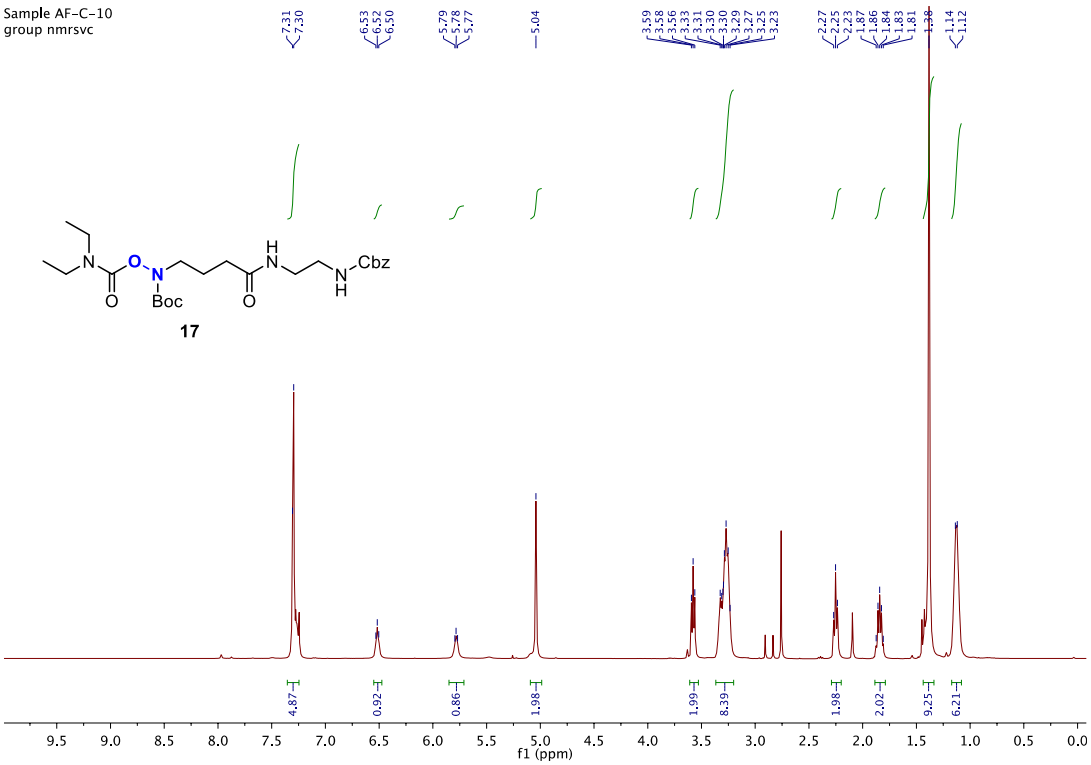

Figure 71. ^{1}H NMR spectrum of **17** (in $CDCl_3$, 400 MHz).

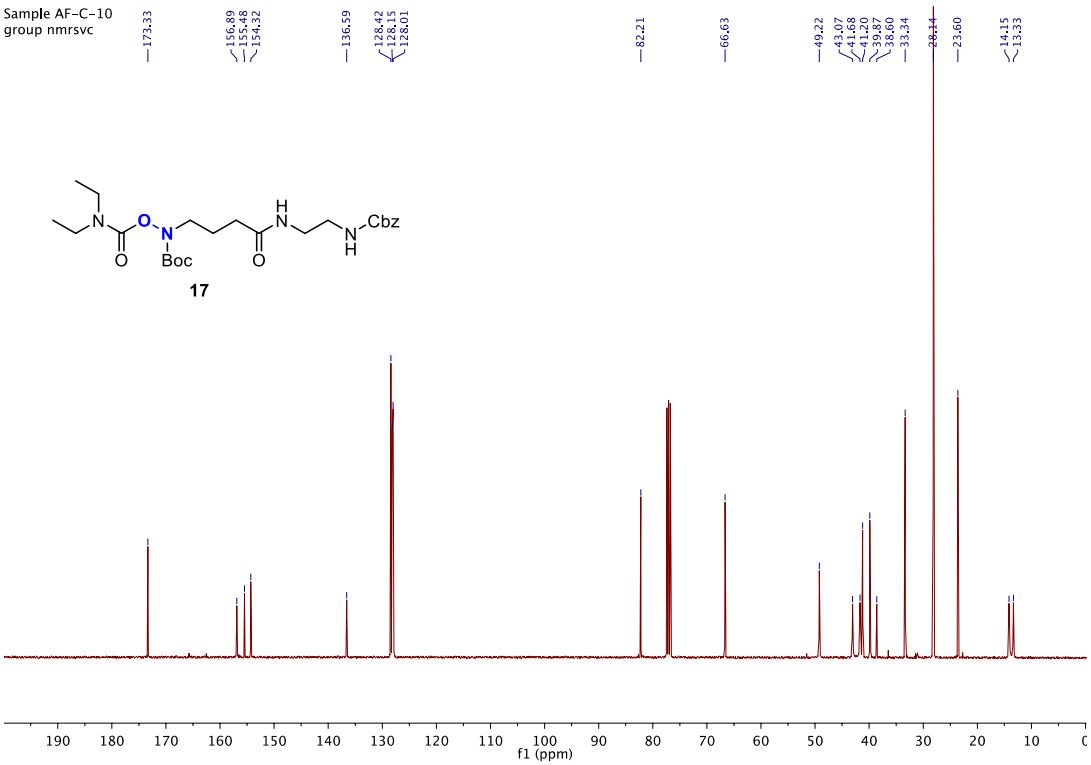

Figure 72. ^{13}C NMR spectrum of **17** (in $CDCl_3$, 100 MHz).

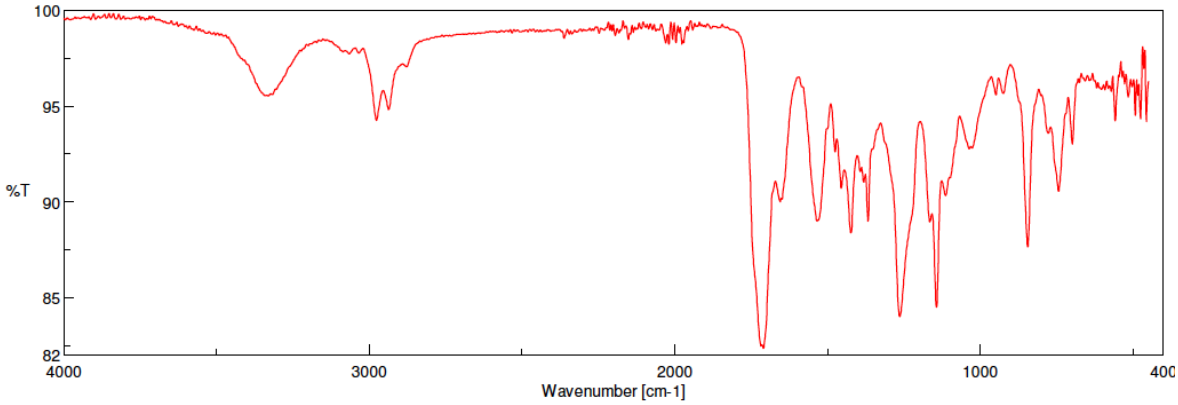

Figure 73. FT-IR ATR spectrum of **17**.

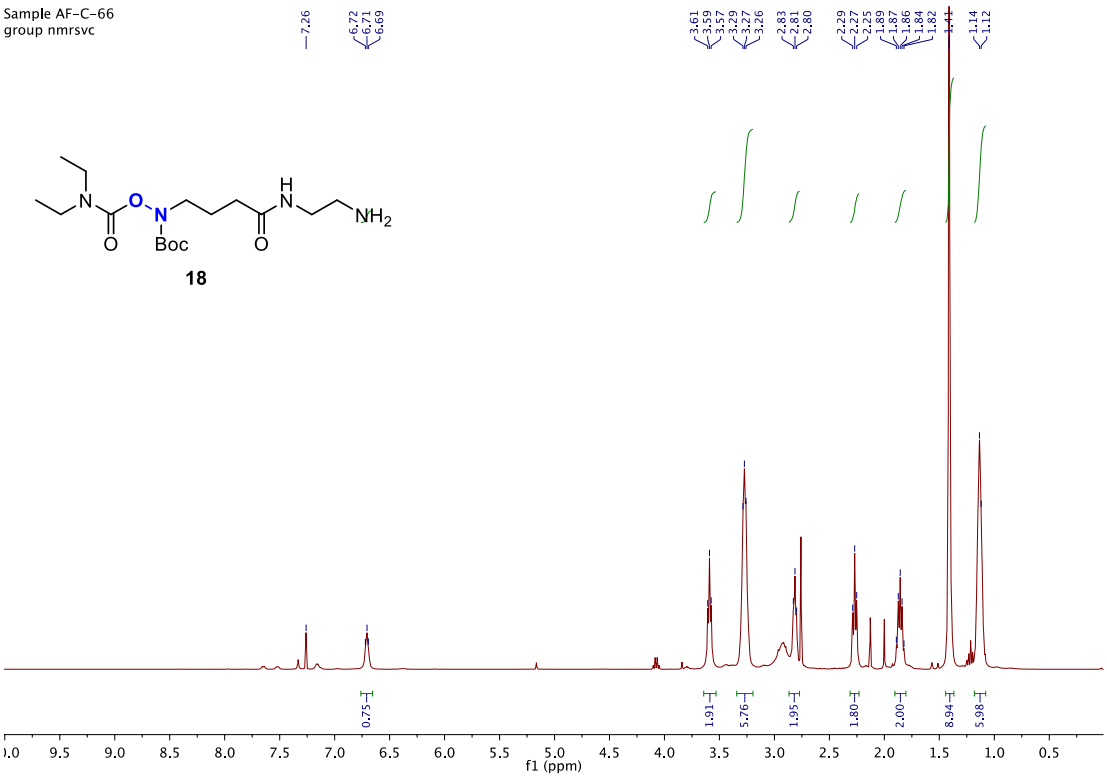

Figure 74. ^{1}H NMR spectrum of crude **18** (in $CDCl_3$, 400 MHz).

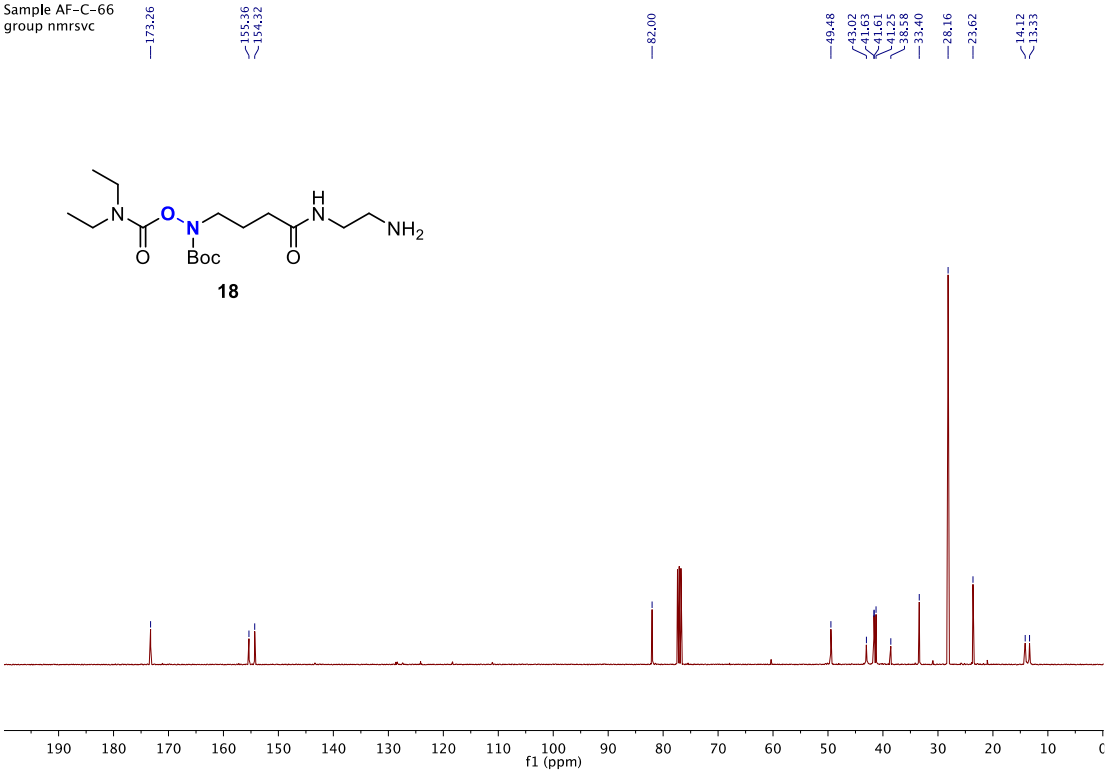

Figure 75. ^{13}C NMR spectrum of crude **18** (in $CDCl_3$, 100 MHz).

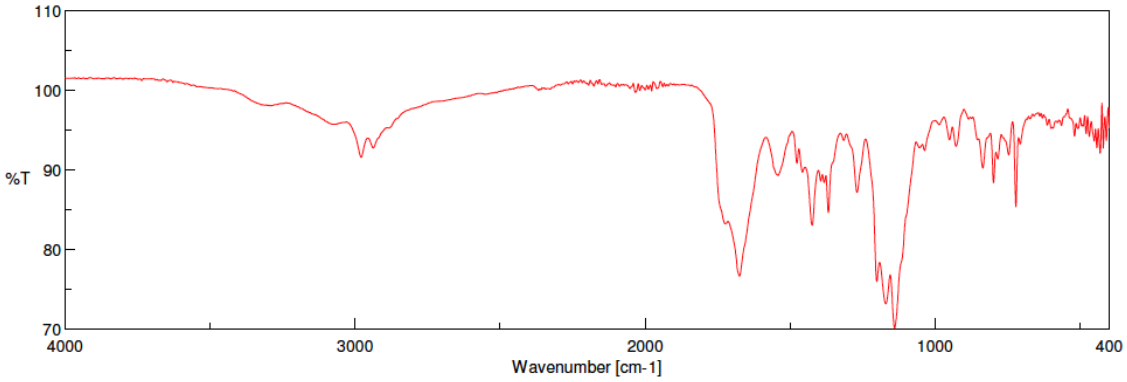

Figure 76. FT-IR ATR spectrum of crude **18**.

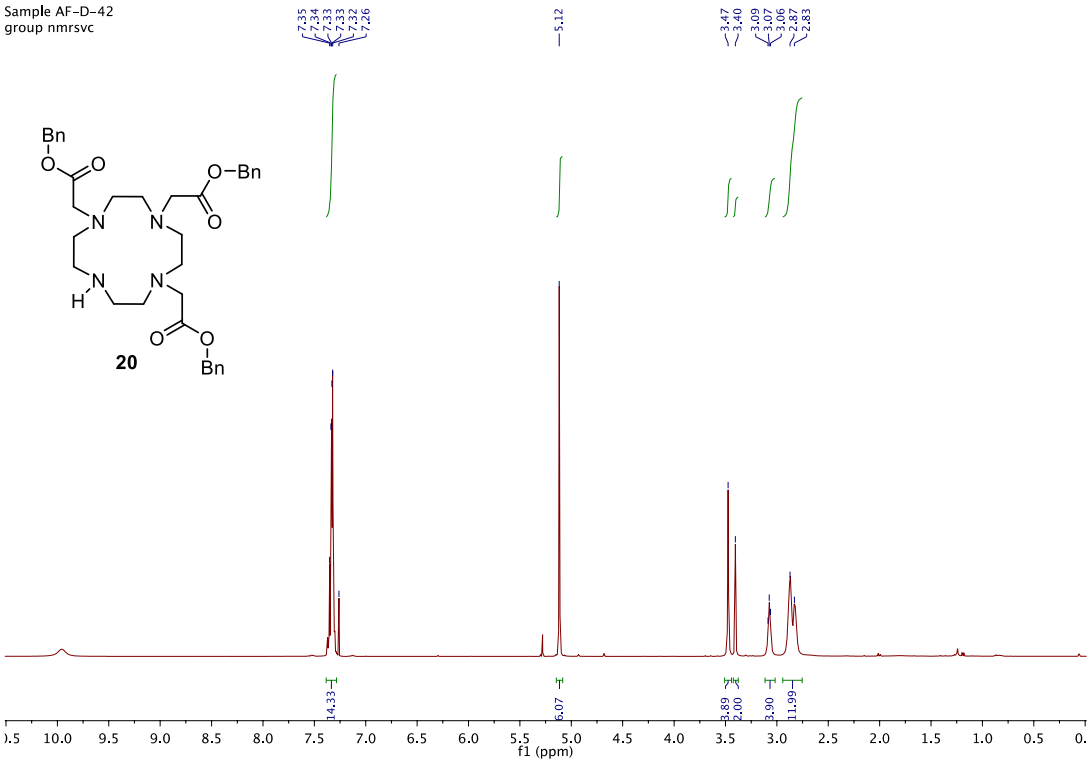

Figure 77. ^{1}H NMR spectrum of **20** (in $CDCl_3$, 400 MHz).

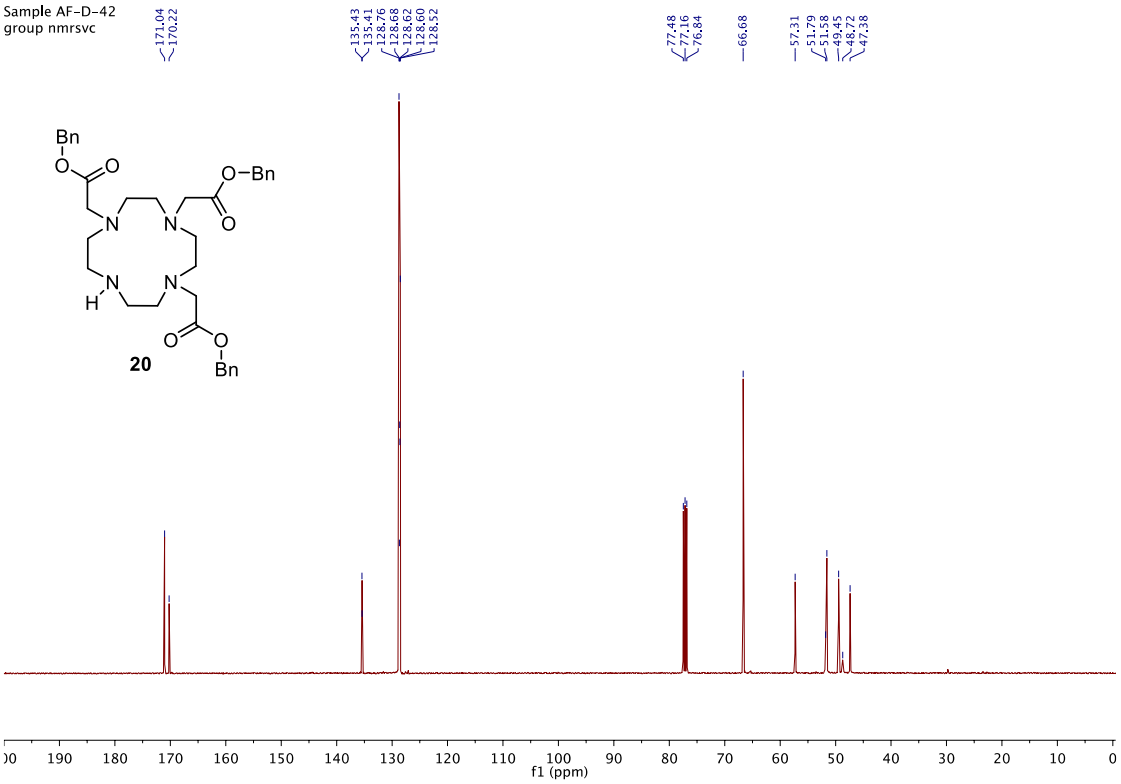

Figure 78. ^{13}C NMR spectrum of **20** (in $CDCl_3$, 100 MHz).

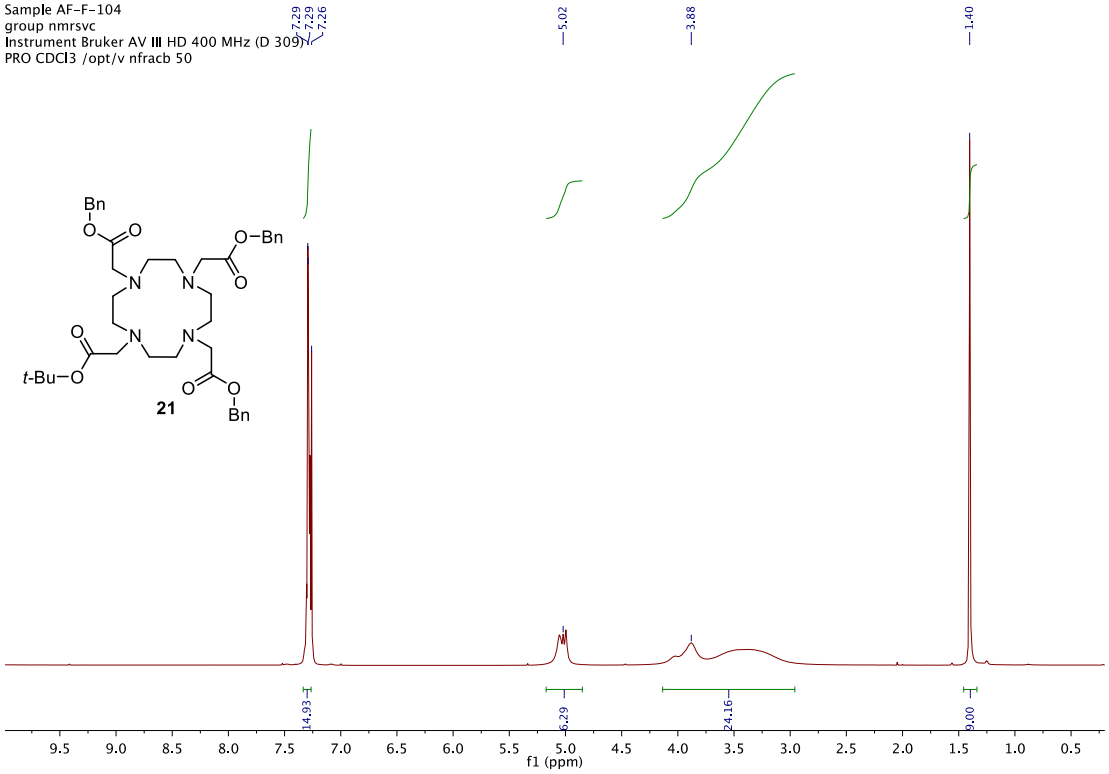

Figure 79. ^{1}H NMR spectrum of **21** (in $CDCl_3$, 400 MHz).

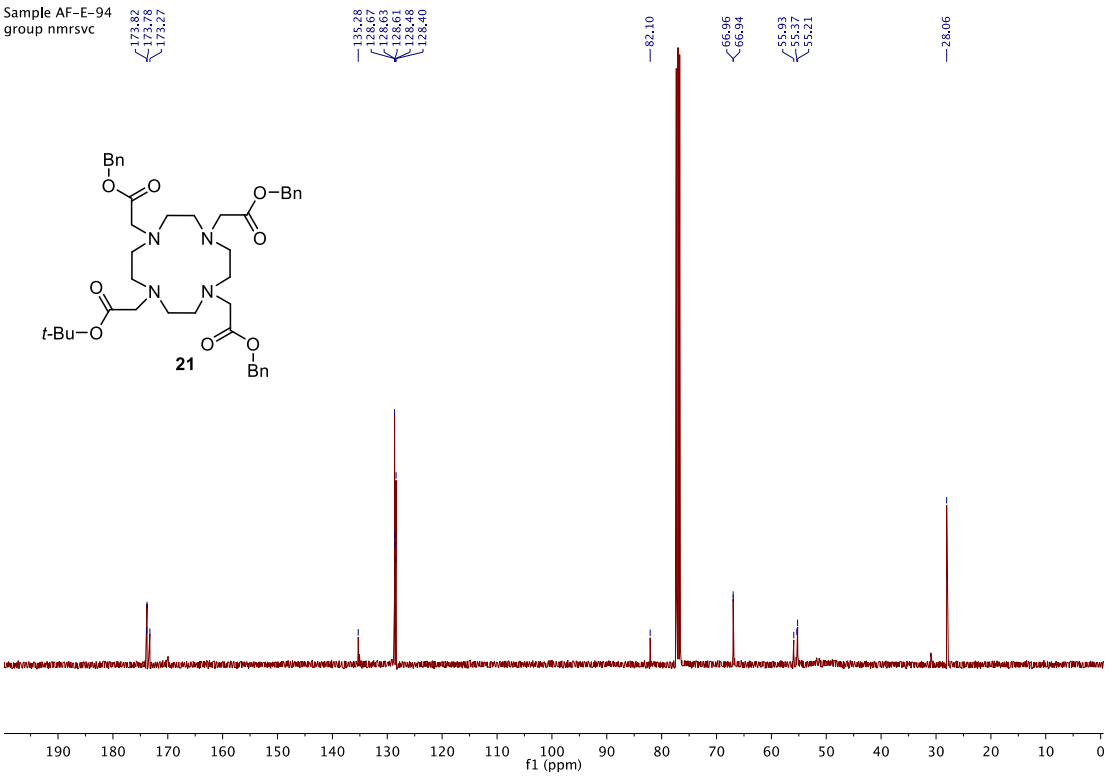

Figure 80. ^{13}C NMR spectrum of **21** (in $CDCl_3$, 100 MHz).

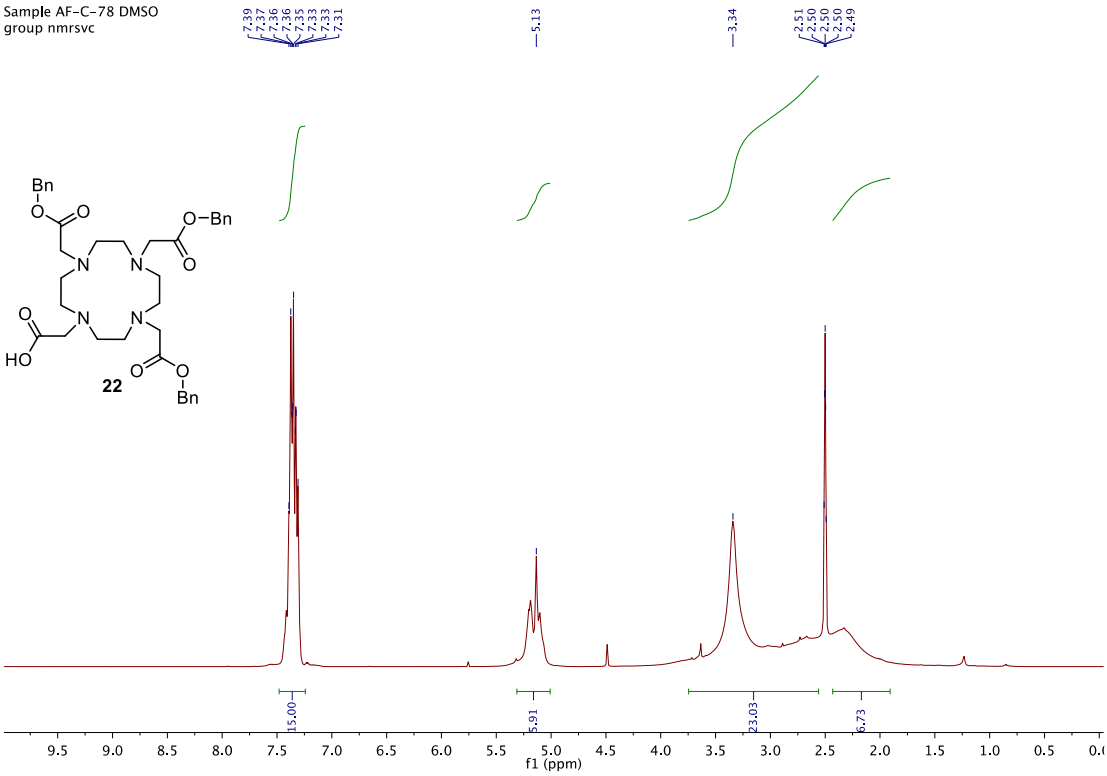

Figure 81. ^{1}H NMR spectrum of **22** (in DMSO-d_6, 400 MHz).

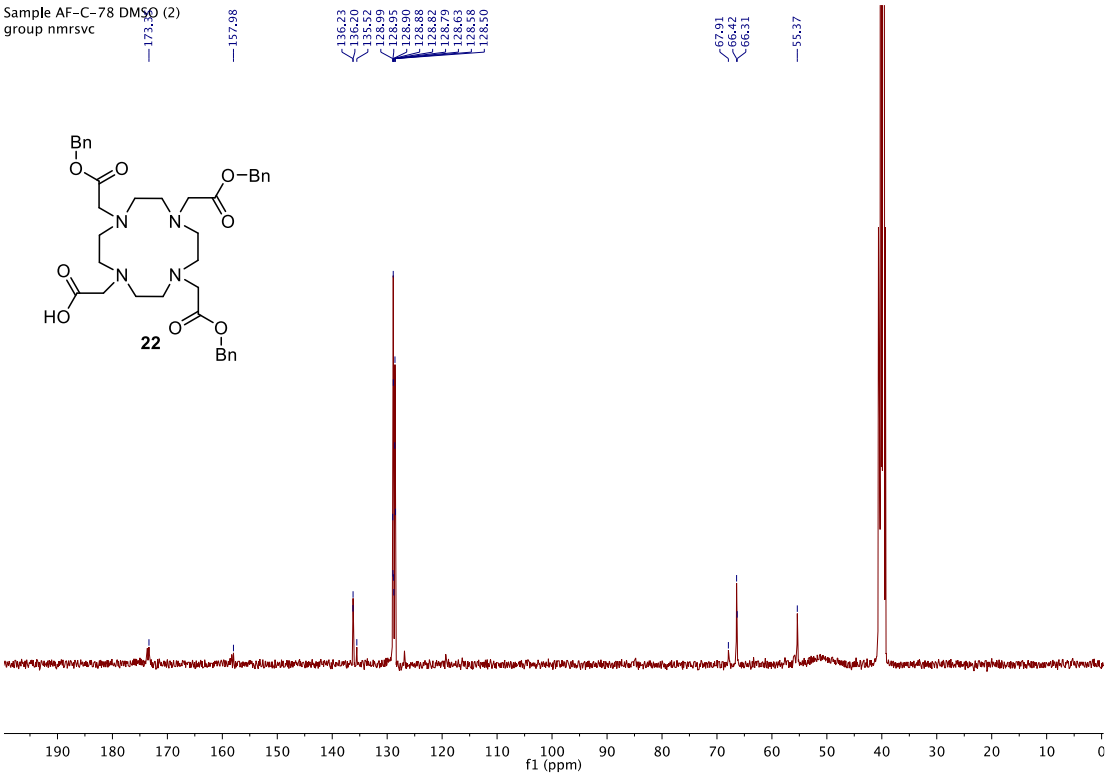

Figure 82. ^{13}C NMR spectrum of **22** (in DMSO-d_6, 100 MHz).

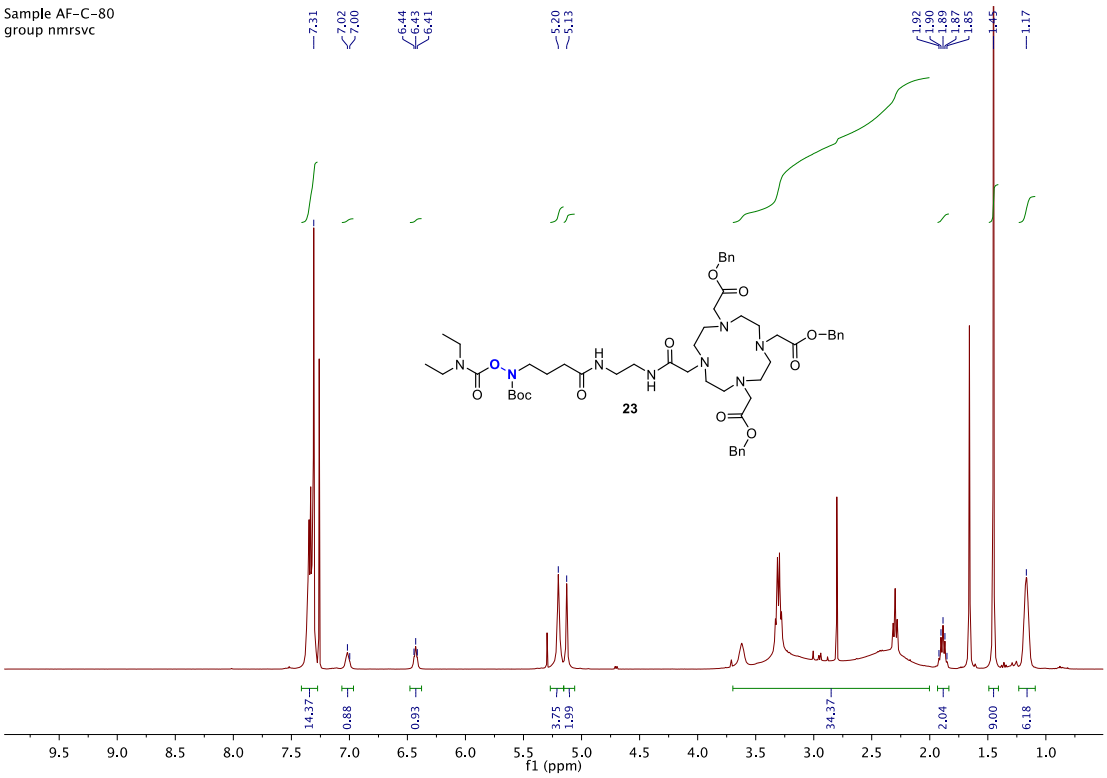

Figure 83. ^{1}H NMR spectrum of **23** (in $CDCl_3$, 400 MHz).

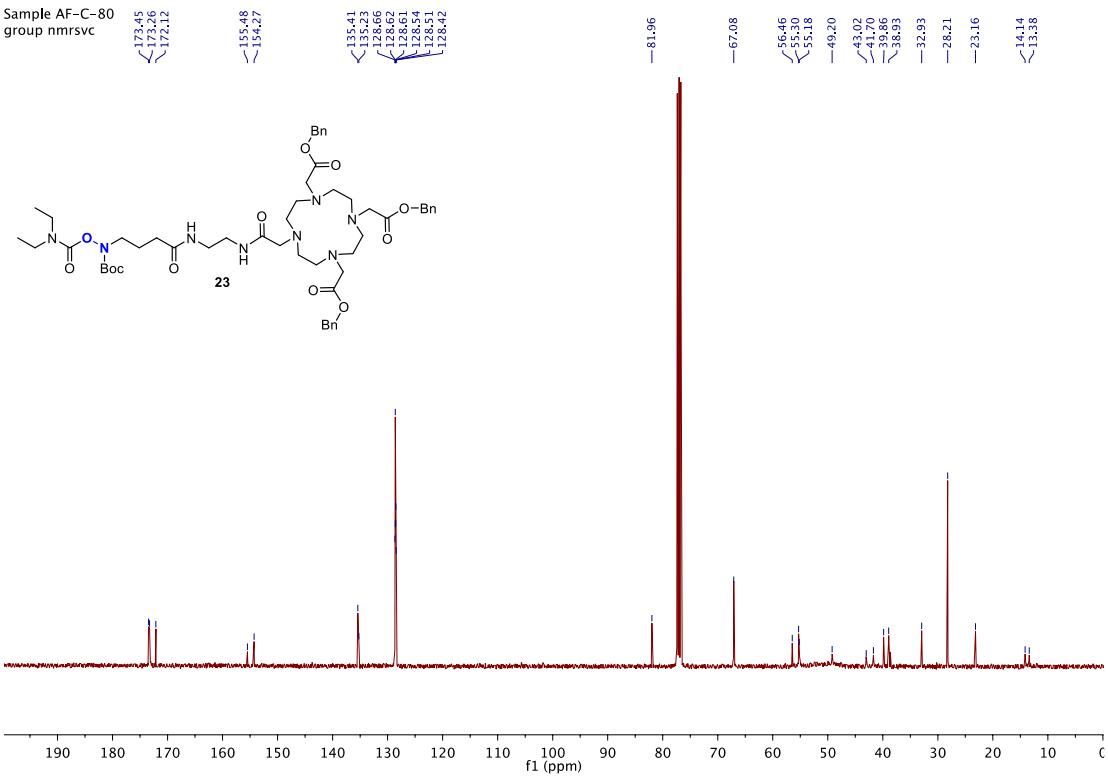

Figure 84. ^{13}C NMR spectrum of **23** (in $CDCl_3$, 100 MHz).

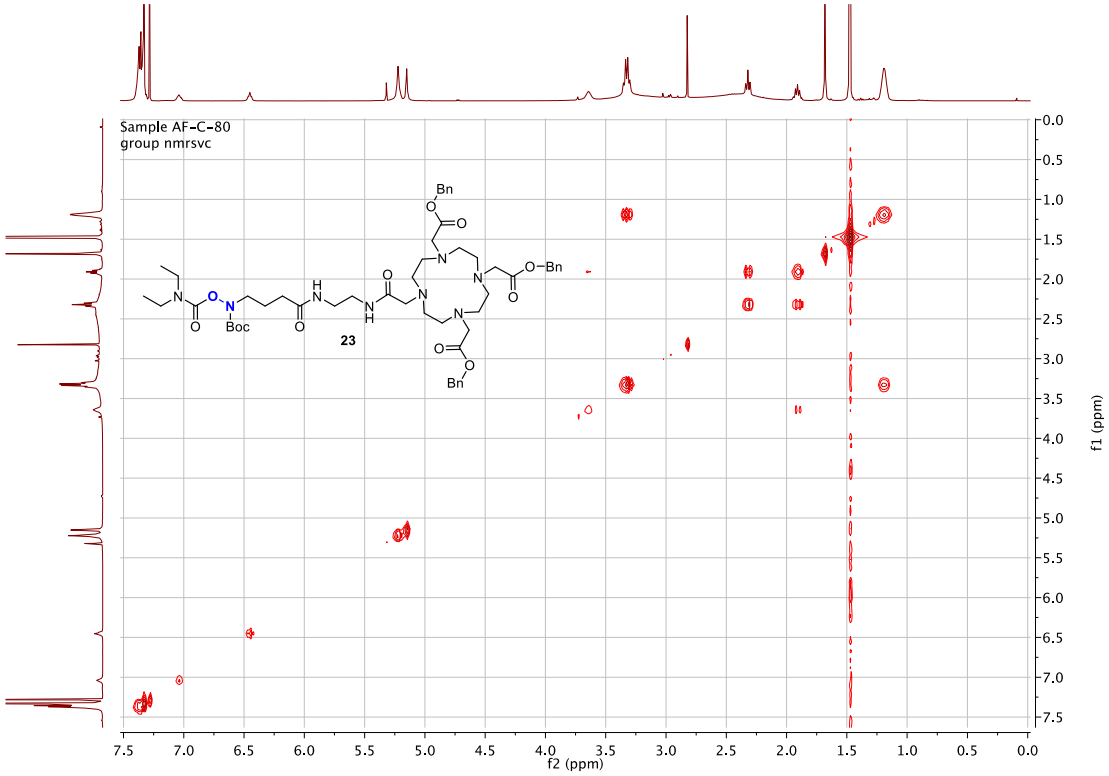

Figure 85. COSY spectrum of **23** (in $CDCl_3$, 400 MHz).

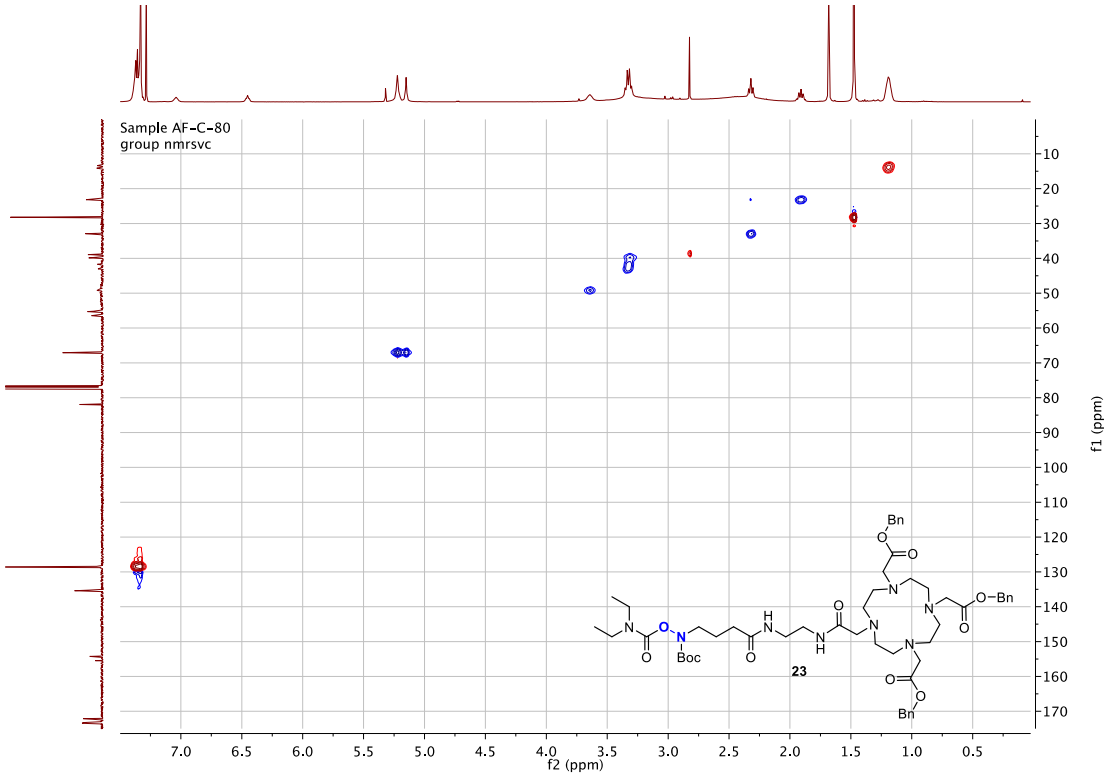

Figure 86. HSQC spectrum of **23** (in $CDCl_3$).

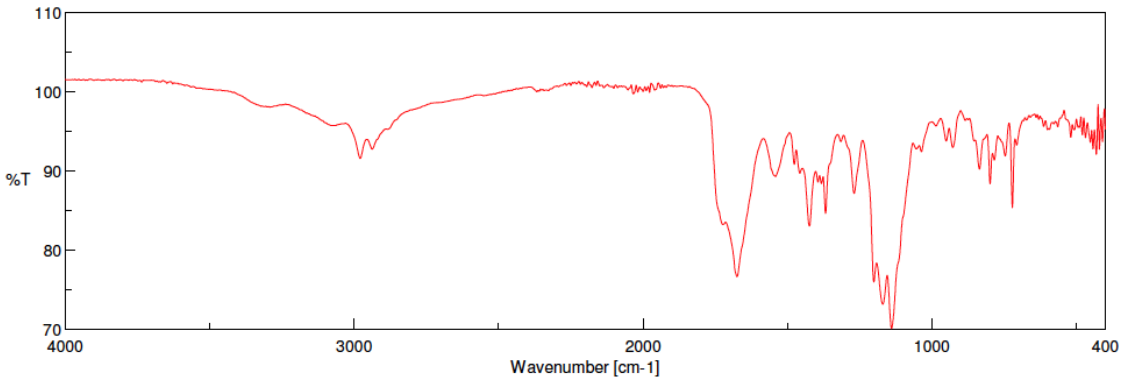

Figure 87. FT-IR ATR spectrum of **23**.

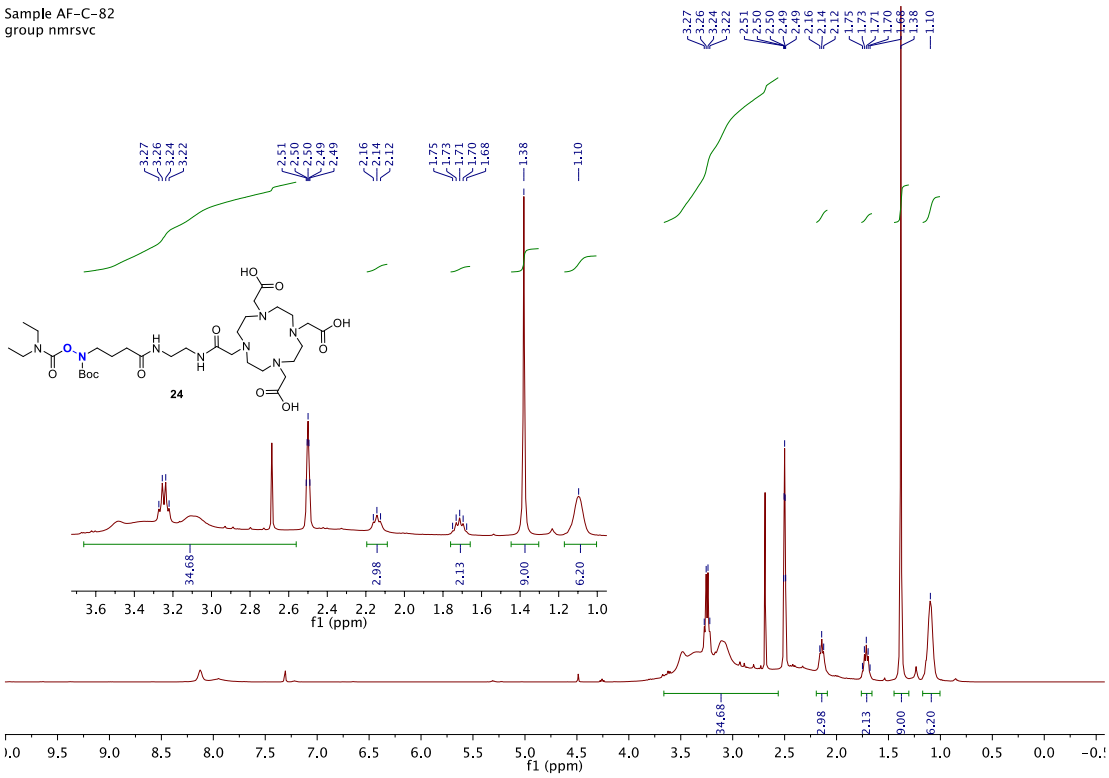

Figure 88. ^{1}H NMR spectrum of **24** (in DMSO-d_6, 400 MHz).

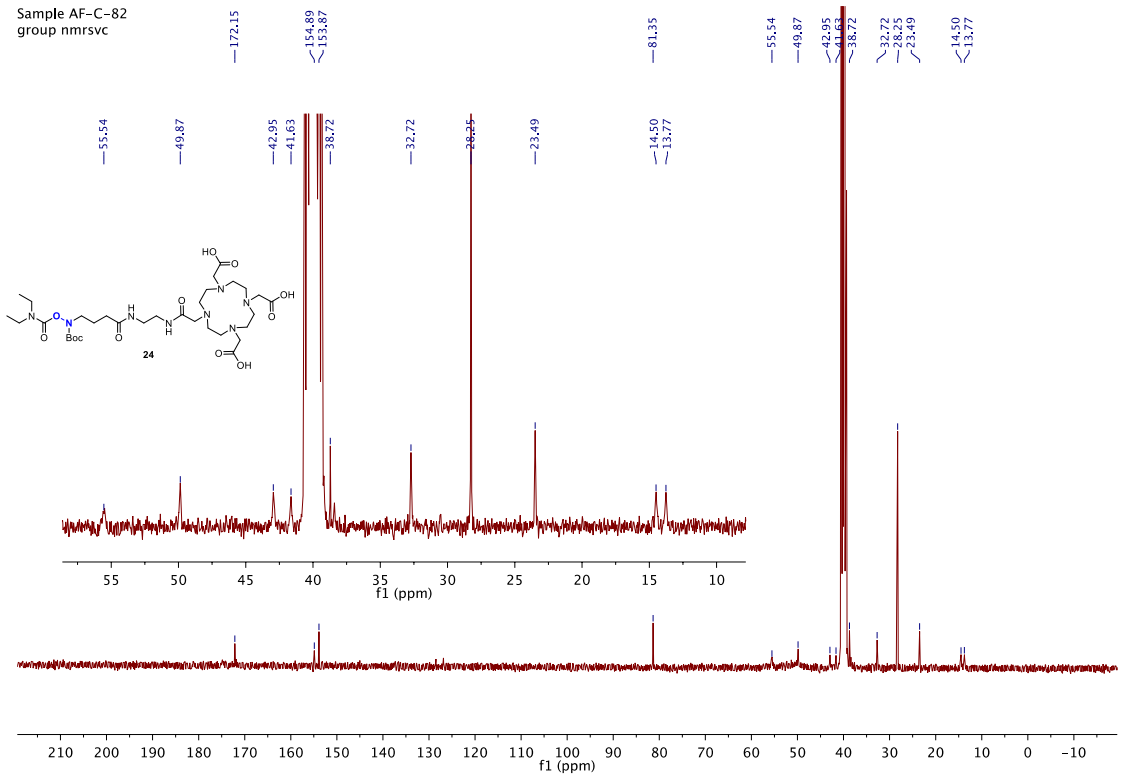

Figure 89. ^{13}C NMR spectrum of **24** (in DMSO-d_6, 100 MHz).

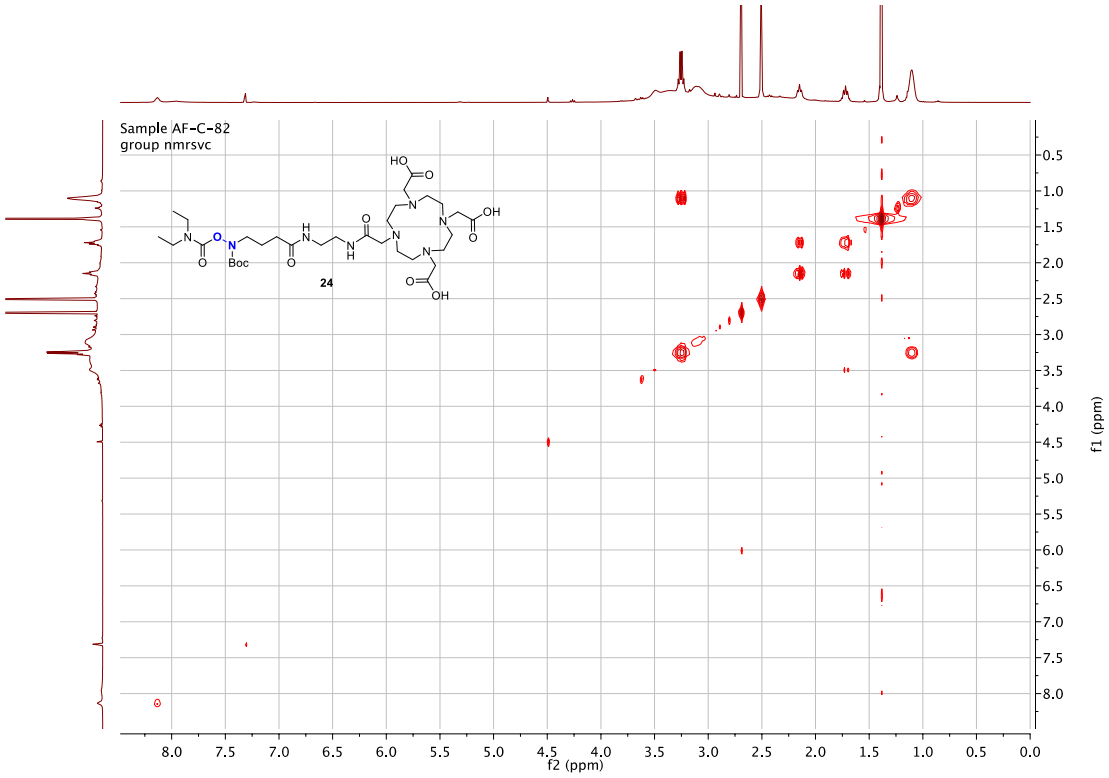

Figure 90. COSY spectrum of **24** (in DMSO-d_6, 400 MHz).

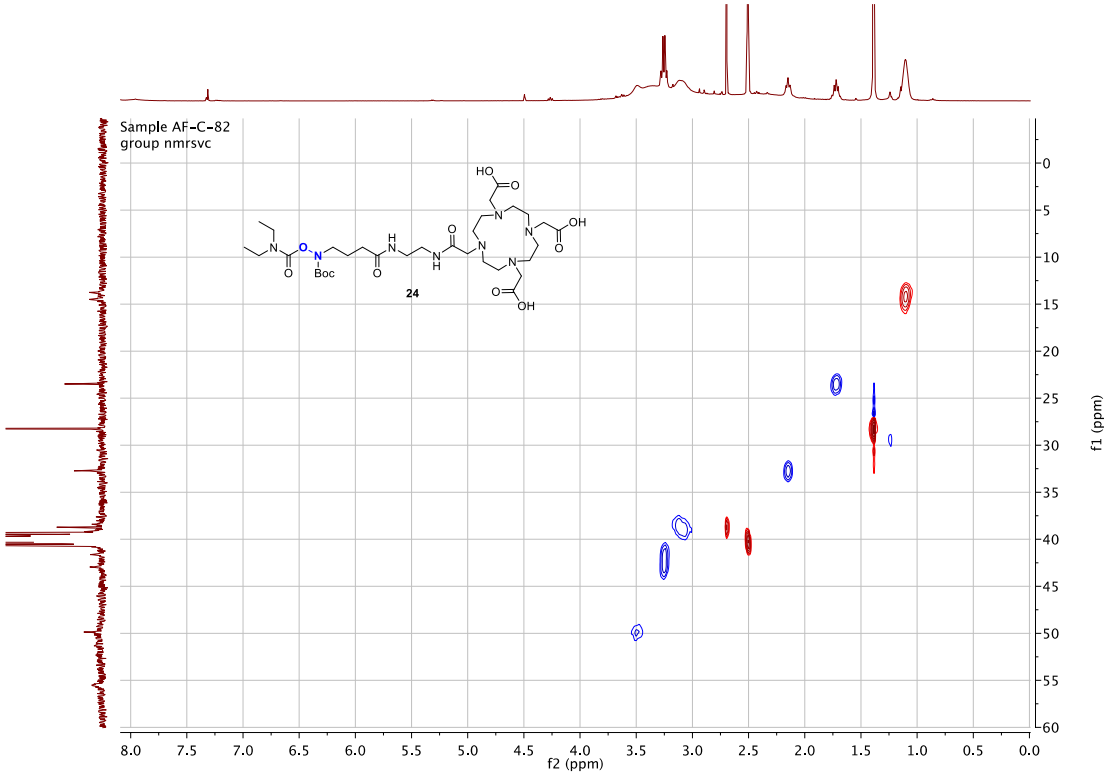

Figure 91. HSQC spectrum of **24** (in DMSO-d_6).

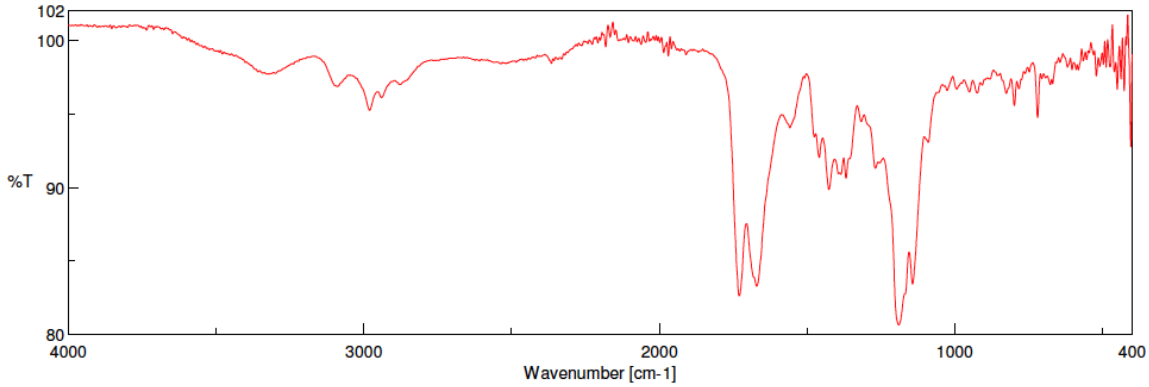

Figure 92. FT-IR ATR spectrum of **24**.

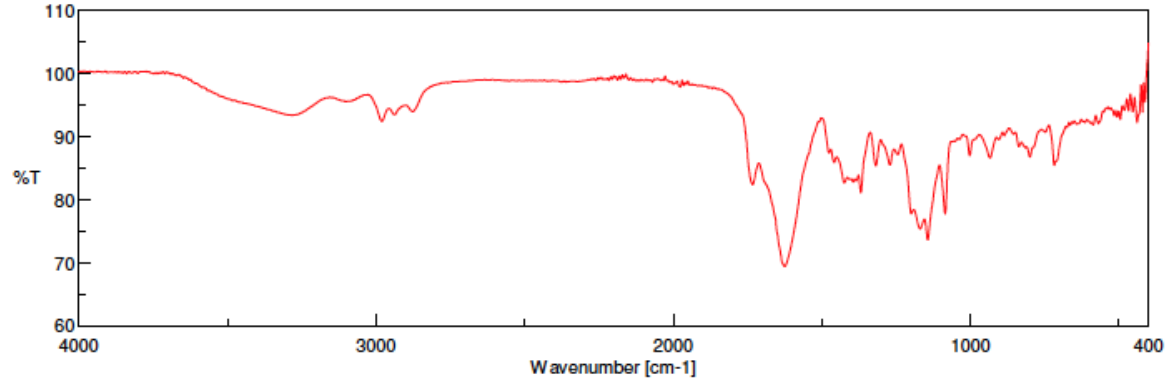

Figure 93. FT-IR ATR spectrum of **25**.

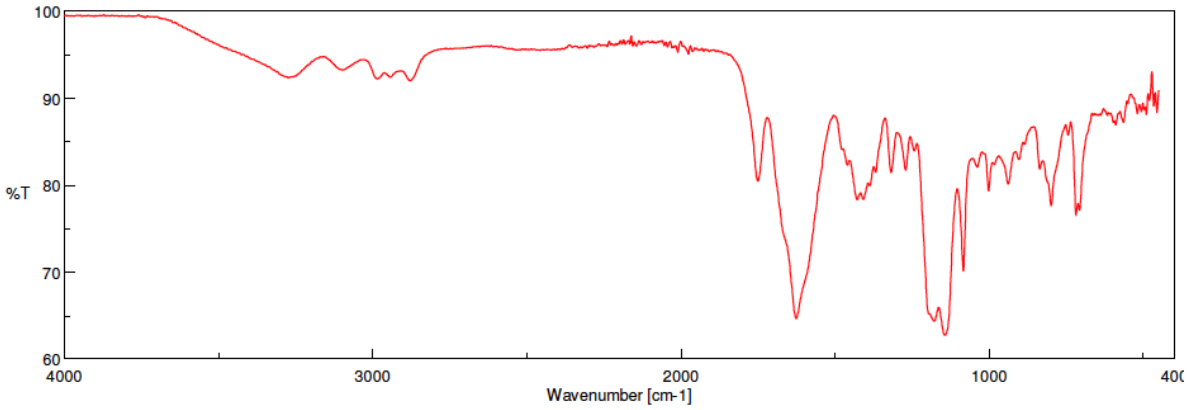

Figure 94. FT-IR ATR spectrum of compound **15**.

6.1.4 Synthesis of the compound in Chapter 4 and spectra

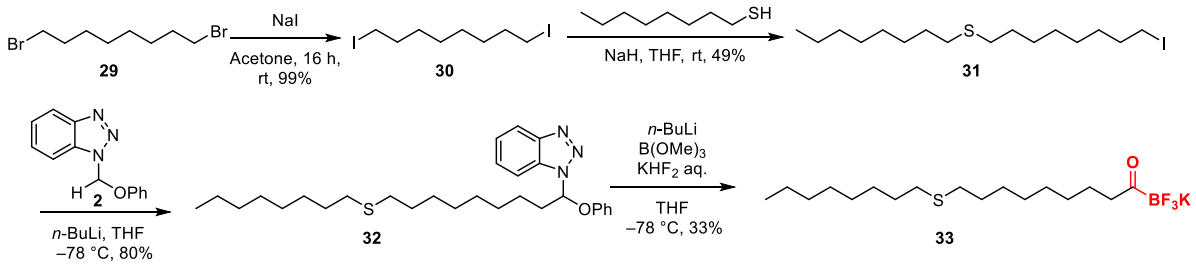

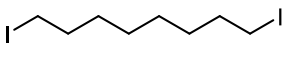

30

1,8-Diiodooctane (30). To a solution of **29** (5.00 g, 18.4 mmol, 1.0 equiv) in 70 mL of acetone, NaI (8.26 g, 55.1 mmol, 3.0 equiv) was added and the reaction mixture was stirred at room temperature overnight. After the removal of the solvent under reduced pressure, the crude mixture was extracted by hexane to provide **30** as a colorless solid (6.56 g, 17.9 mmol,

y = 98%); ^{1}H NMR (400 MHz, $CDCl_3$): δ 1.30-1.45 (m, 8 H), 1.82 (quin, C**H**$_2$CH_2I, *J* = 7.2 Hz, 4 H), 3.19 (t, C**H**$_2$I, *J* = 7.0 Hz, 4H), ^{13}C NMR (100 MHz, in $CDCl_3$): δ 33.5, 30.4, 28.3, 7.3; EIMS *m/z*: [M^+] calcd for $C_8H_{16}I_2$, 365.9336; found, 365.9333.

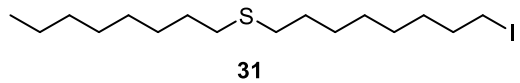

31

(8-Iodooctyl)(octyl)sulfane (31). To a dispersion of NaH (0.12 g, 5.0 mmol, 1.1 equiv) in 40 mL of THF, octanthiol (0.67 g, 4.6 mmol, 1.0 equiv) was added dropwise under N_2 atmosphere and the formation of a dense colorless dispersion was observed. After stirring the reaction mixture for 30 min at room temperature, compound **30** (2.0 g, 5.5 mmol, 1.2 equiv) was added and the reaction mixture was stirred at room temperature until the solution became completely transparent. After the removal of THF under reduced pressure, the crude mixture was extracted by CH_2Cl_2, and the crude extract was purified by silica gel column chromatography (solvent: 100% hexane) to provide **31** as a colorless wax (0.85 g, 2.2 mmol, y = 49%); IR (cm^{-1}): 2925 (C-H), 2852 (C-H), 1463, 1376, 1261, 1221, 1176, 721; ^{1}H NMR (400 MHz, in $CDCl_3$): δ 0.88 (t, CH_2C**H**$_3$, *J* = 6.9 Hz, 3H), 1.20-1.45 (m, 18H), 1.57 (quin, C**H**$_2$CH_2S, *J* = 7.9 Hz, 4H), 1.82 (quin, C**H**$_2$CH_2I, *J* = 7.4 Hz, 2H), 2.50 (broad, C**H**$_2$SC**H**$_2$, 4H), 3.18 (t, C**H**$_2$I, *J* = 7.1 Hz, 2H); ^{13}C NMR (100 MHz, in $CDCl_3$): δ 33.5, 32.3, 32.1, 31.8, 30.4, 29.8, 29.7, 29.24, 29.21, 29.04, 28.98, 28.8, 28.4, 22.7, 14.1, 7.3; HRMS (ESI^+) *m/z*: $[M+H]^+$ calcd for $C_{16}H_{34}IS^+$, 385.1420; found, 385.1425.

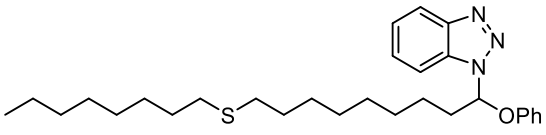

32

1-(9-(octylthio)-1-phenoxynonyl)-1*H*-benzo[*d*][1,2,3]triazole (32). To a solution of 1-(phenoxymethyl)-1*H*-benzotriazole **2** (0.75 g, 3.3 mmol, 1.5 equiv) in 45 mL of THF, *n*-BuLi (1.6 M in hexane, 4.1 mL, 3.5 mmol, 1.6 equiv, Sigma-Aldrich) was added slowly down the side of the flask at –78 °C under N_2 atomosphere and stirred for 1 h. Subsequently, a solution of the iodide **31** (0.85 g, 2.2 mmol, 1.0 equiv) in THF (5 mL) was added, and the reaction mixture was slowly brought to room temperature and stirred for 16 h. After removal of the solvent under reduced pressure, the crude mixture was extracted with CH_2Cl_2. The obtained crude extract was purified by silica gel column chromatography (solvent: hexane-EtOAc

(95:5)) to provide **32** as a colorless wax (0.85 g, 1.7 mmol, y = 77%); IR (cm^{-1}): 2922 (C–H), 2852, 1590, 1492, 1450, 1342, 1279, 1216, 1153, 1049, 1000, 929, 888, 803, 744, 689; ^{1}H NMR (400 MHz, in $CDCl_3$): δ 0.87 (t, $CH_2C\mathbf{H_3}$, *J* = 6.6 Hz, 3H), 1.20-1.45 (m, 20H), 1.54 (m, 5H), 2.30 (m, 1H), 2.47 (m, 5H), 6.82 (t, *J* = 6.8 Hz, 1H), 6.94 (m, 3H), 7.17 (t, *J* = 7.9 Hz, 1H), 7.34 (t, *J* = 7.6 Hz 1H), 7.45 (t, *J* = 7.4 Hz 1H), 7.81 (d, *J* = 8.0 Hz, 1H), 8.03 (d, *J* = 8.6 Hz, 1H); ^{13}C NMR (100 MHz, in $CDCl_3$): δ 22.7, 24.7, 28.8, 28.97, 29.03, 29.20, 29.21, 29.34, 29.65, 29.74, 31.8, 32.15, 32.21, 34.8, 88.3, 111.2, 116.2, 120.2, 122.9, 124.3, 127.7, 129.7, 131.1, 146.7, 156.2; HRMS (ESI^+) *m/z*: $[M+Na]^+$ calcd for $C_{29}H_{43}N_3OSNa^+$, 504.3019; found, 504.3011.

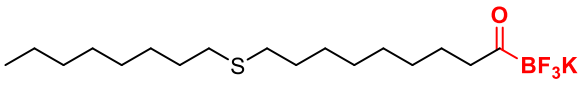

33

Potassium 9-(octylthio)-1-nonanoyltrifluoroborate (33). To a solution of compound **32** (0.85 g, 1.76 mmol, 1.1 equiv) in 40 mL of THF, *n*-BuLi (1.6 M in hexane, 4.1 mL, 1.6 mmol, 1.0 equiv) was added slowly down the side of the flask at –78 °C under N_2 atomosphere and stirred for 30 min. Subsequently, neat $B(OMe)_3$ (0.34 g, 3.2 mmol, 2.0 equiv) was added dropwise to the solution. The resulting reaction mixture was stirred for 1 h at –78 °C under N_2 atmosphere and then slowly brought to room temperature. The septum cap was then removed from the flask and KHF_2 aqueous solution (20 mL, saturated solution) was added slowly. The reaction mixture was vigorously stirred overnight, concentrated *in vacuo,* and then dried under high vacuum. The resulting solid was stirred in acetone and then filtered (repeated 3 times). The combined acetone filtrates were concentrated and diluted in Et_2O and stirred until precipitates formed. The precipitates were filtered, washed twice with Et_2O, and dried under high vacuum to give **33** as a colorless solid (0.21 g, 0.54 mmol, y = 33%); IR (cm^{-1}): 2921 (C-H), 2851 (C-H), 1651 (C=O), 1463, 1171, 1083, 1004, 949, 889, 831, 720, 635, 587; ^{1}H NMR (400 MHz, Acetone-d_6): δ 0.88 (t, $CH_2C\mathbf{H_3}$, *J* = 6.9 Hz, 3H), 1.18-1.46 (m, 20H), 1.56 (quin, $C\mathbf{H_2}CH_2S$- *J* = 7.8 Hz, 4H), 2.37 (t, $C\mathbf{H_2}COBF_3K$, *J* = 7.1 Hz, 2H), 2.50 (t, $C\mathbf{H_2}SC\mathbf{H_2}$, *J* = 7.3 Hz, 4H); ^{13}C NMR (100 MHz, Acetone-d_6): δ 31.7, 31.6, 31.5, 29.7, 29.65, 29.58, 29.55, 29.4, 29.1, 29.0, 28.6, 22.41, 22.38, 13.5; ^{13}C NMR (100 MHz, DMSO-d_6): δ 31.7, 31.58, 31.56, 29.68, 29.65, 29.6, 29.5, 29.1, 29.0, 28.72, 28.66, 22.7, 22.6, 14.4; ^{19}F NMR (376 MHz, Acetone-d_6): δ –150.8, ^{11}B NMR (128 MHz,

Acetone-d_6): δ –1.67, HRMS (MALDI$^-$) *m/z*: $[M-K]^-$ calcd for $C_{17}H_{33}BF_3OS^-$, 353.2306; found, 353.2309.

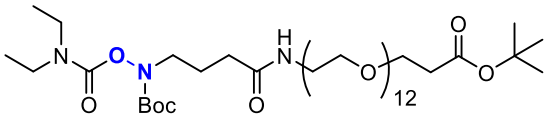

35

***tert*-Butyl protected carboxylate PEG hydroxylamine (35).** The hydroxylamine linker 34 (0.14 g, 0.44 mmol, 3.0 equiv), DIPEA (130 µL, 0.74 mmol, 5.0 equiv) and HATU (0.17 g, 0.44 mmol, 3.0 equiv) were dissolved in 5 mL of DMF. After stirring the mixture for 5 min at room temperature, *tert*-Butyl protected carboxylate PEG S5 (0.10 g, 0.15 mmol, 1.0 equiv) was added and the reaction mixture was stirred overnight at room temperature. After the removal of DMF under reduced pressure, the crude extract was purified by reverse phase HPLC (column: Shiseido Capcell Pak C18 column (Φ30 x 250 mm) CH_3CN-H_2O in the presence of 0.1% TFA (a gradient of CH_3CN-H_2O (v/v, 30:70 to 98:10) over 40 min). The collected fraction was lyophilized to provide compound 35 as a colorless oil (0.10 g, 0.10 mmol, y = 67%); IR (cm^{-1}): 2870 (C-H), 1728 (C=O), 1671 (C=O), 1538, 1456, 1422, 1366, 1350, 1254, 1098, 949, 849, 784, 748; ^{1}H NMR (400 MHz, in $CDCl_3$): δ 1.17 (broad, CH_2CH_3, 3H), 1.44 (s, Boc, 9H), 1.46 (s, Boc, 9H) 1.92 (quin, $CH_2CH_2CH_2$, *J* = 6.9 Hz, 2H), 2.33 (t, CH_2CON, *J* = 7.4 Hz, 2H), 2.49 (t, CH_2COO, 2H), 3.31 (m, CH_3CH_2, Hz, 4H), 3.45 (m, NCH_2CH_2O, 2H), 3.55 (t, NCH_2CH_2O, *J* = 5.3 Hz, 2H), 3.64 (m, OCH_2CH_2O, $N(Boc)CH_2$, 44H), 3.70 (t, OCH_2CH_2CO, *J* = 6.6 Hz, 2H); ^{13}C NMR (100 MHz, in $CDCl_3$): δ 170.9, 155.3, 154.3, 81.9, 80.5, 77.2, 70.6, 70.5, 70.4, 70.3, 69.7, 66.9, 49.6, 43.0, 41.7, 39.4, 36.3, 33.2, 28.2, 28.1 23.7, 14.2, 13.4; HRMS (MALDI$^+$) *m/z*: $[M+H]^+$ calcd for $C_{45}H_{88}N_3O_{19}^+$, 974.6007; found, 974.6018.

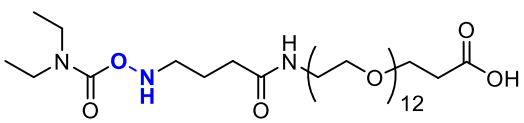

36

Carboxylate PEG hydroxylamine (**36**)**.** To a solution of compound **35** (1.8 g, 2.46 mmol, 1.0 equiv) in CH_2Cl_2 (3 mL), TFA (3 mL) was added. The reaction mixture was stirred for 3

h at room temperature. The solvent was removed by a flux of N_2 to provide crude **36** as a yellow oil (1.6 g, 2.6 mmol, y = 99%, the product was used without further purification);

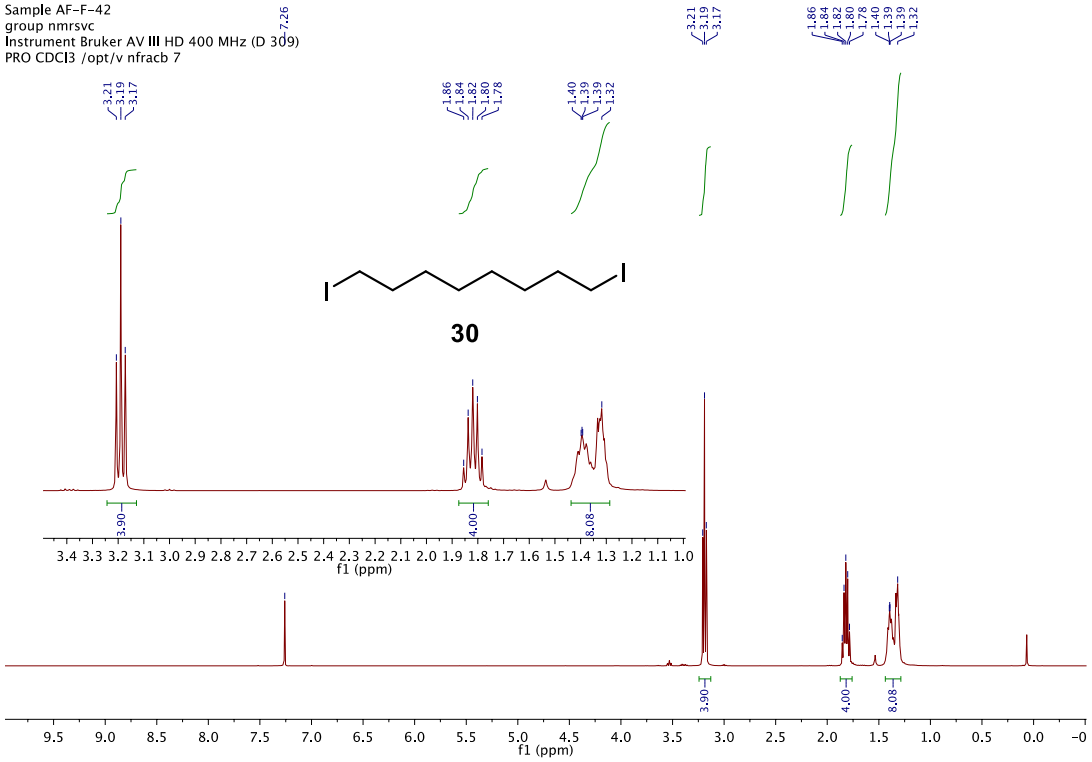

Figure 95. ^{1}H NMR spectrum of **30** (in $CDCl_3$, 400 MHz).

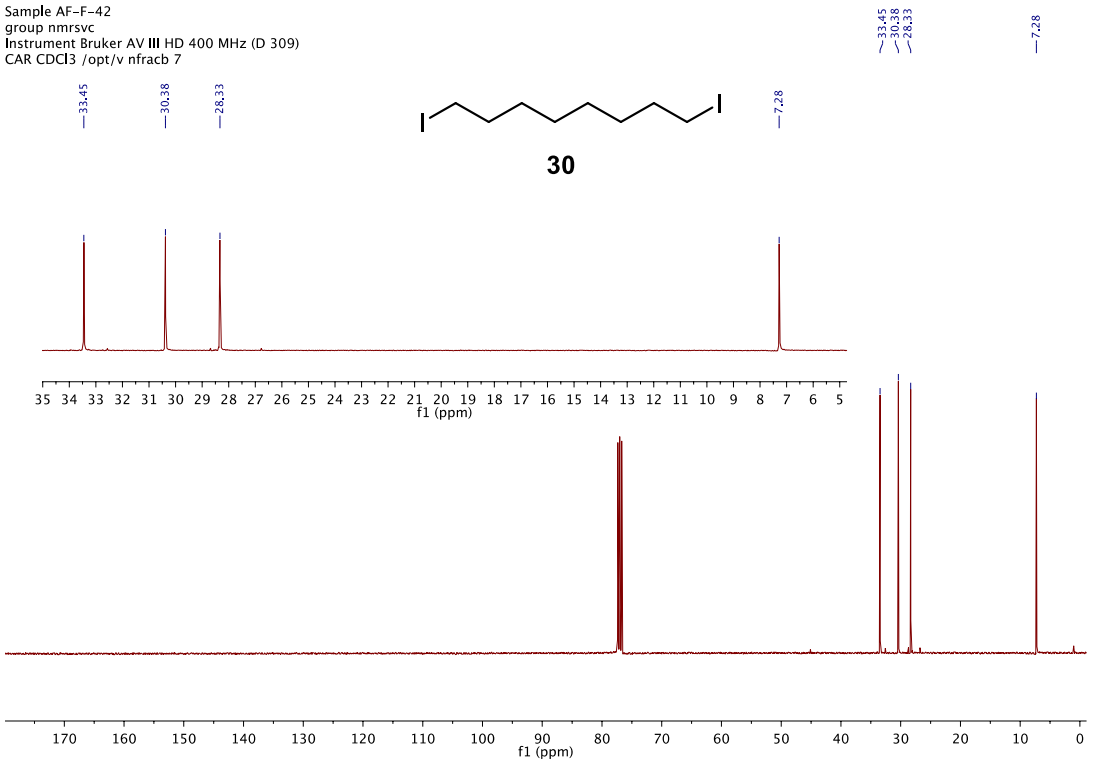

Figure 96. ^{13}C NMR spectrum of **30** (in $CDCl_3$, 100 MHz).

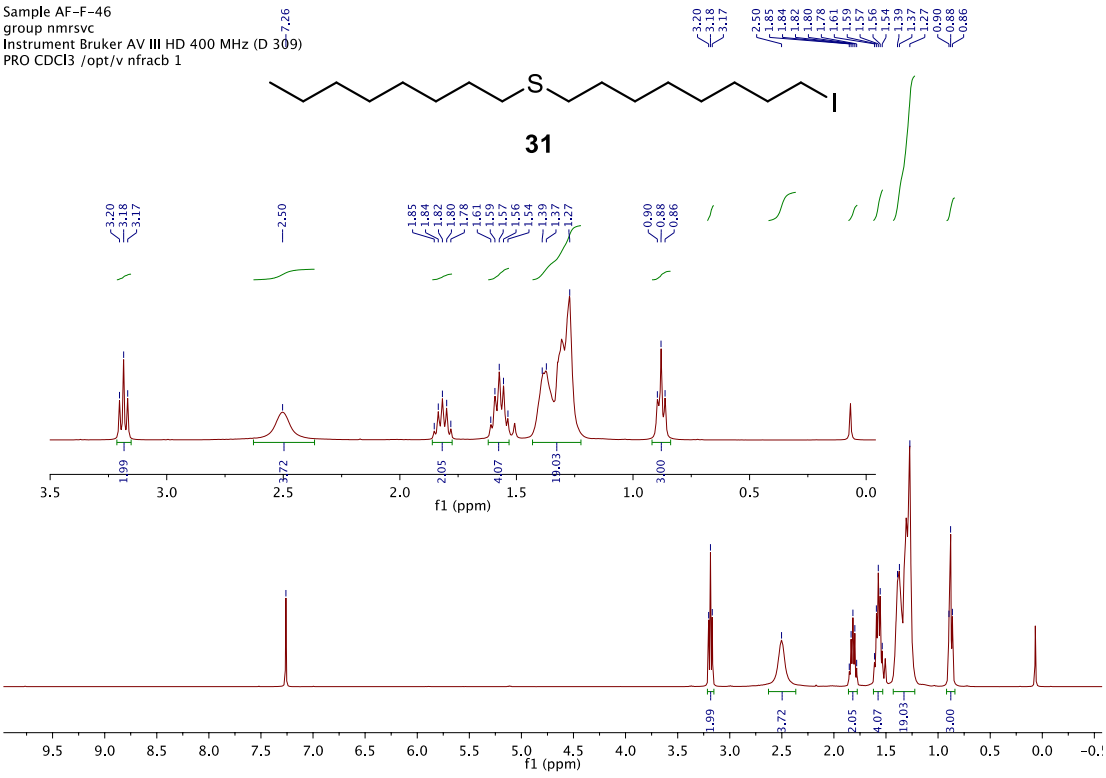

Figure 97. ^{1}H NMR spectrum of **31** (in $CDCl_3$, 400 MHz).

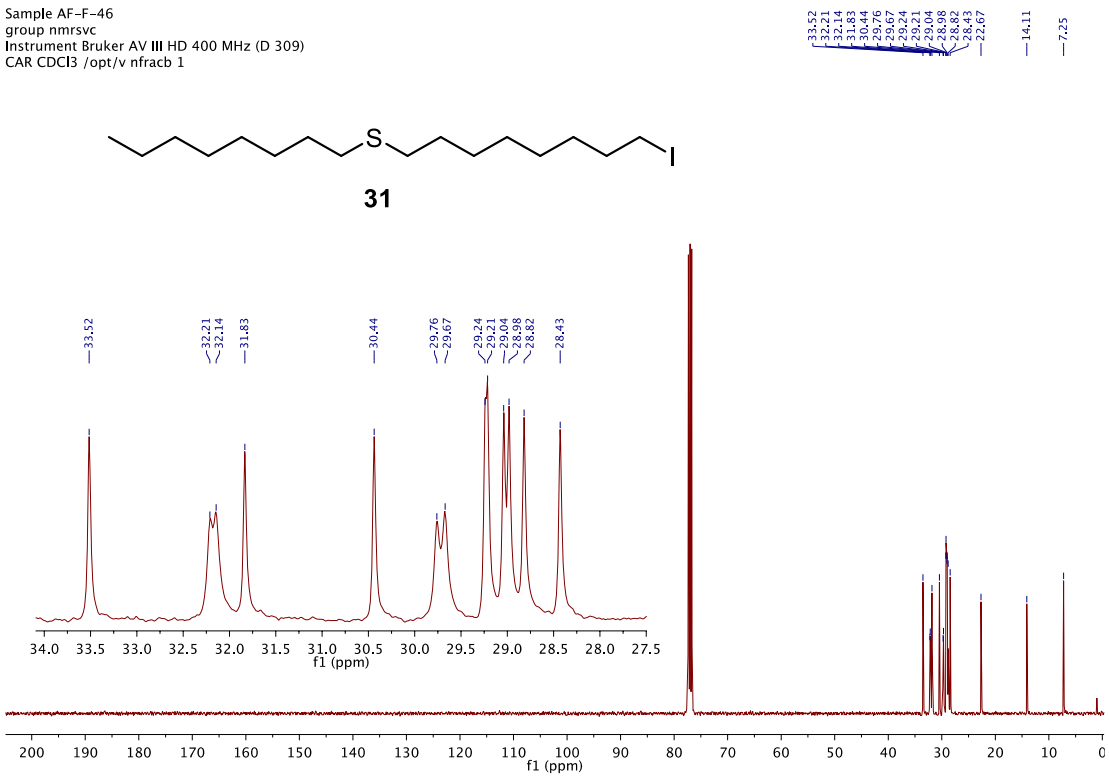

Figure 98. ^{13}C NMR spectrum of **31** (in $CDCl_3$, 100 MHz).

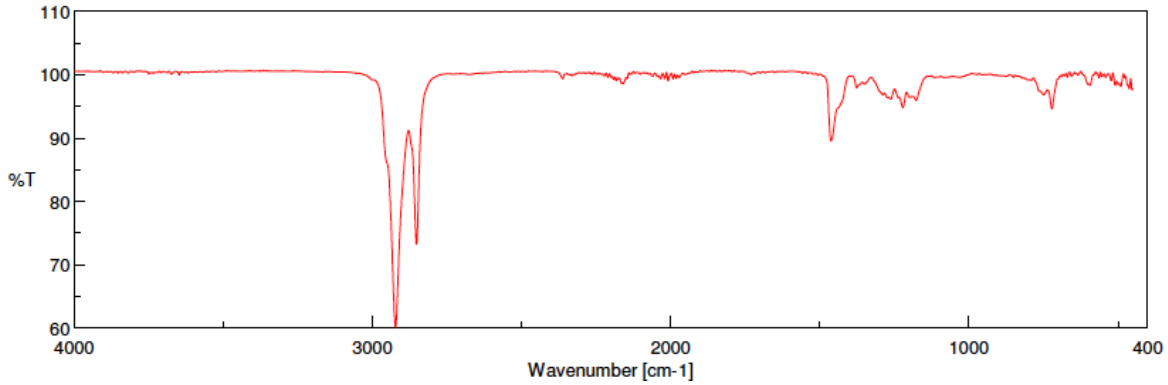

Figure 99. FT-IR ATR spectrum of **31**

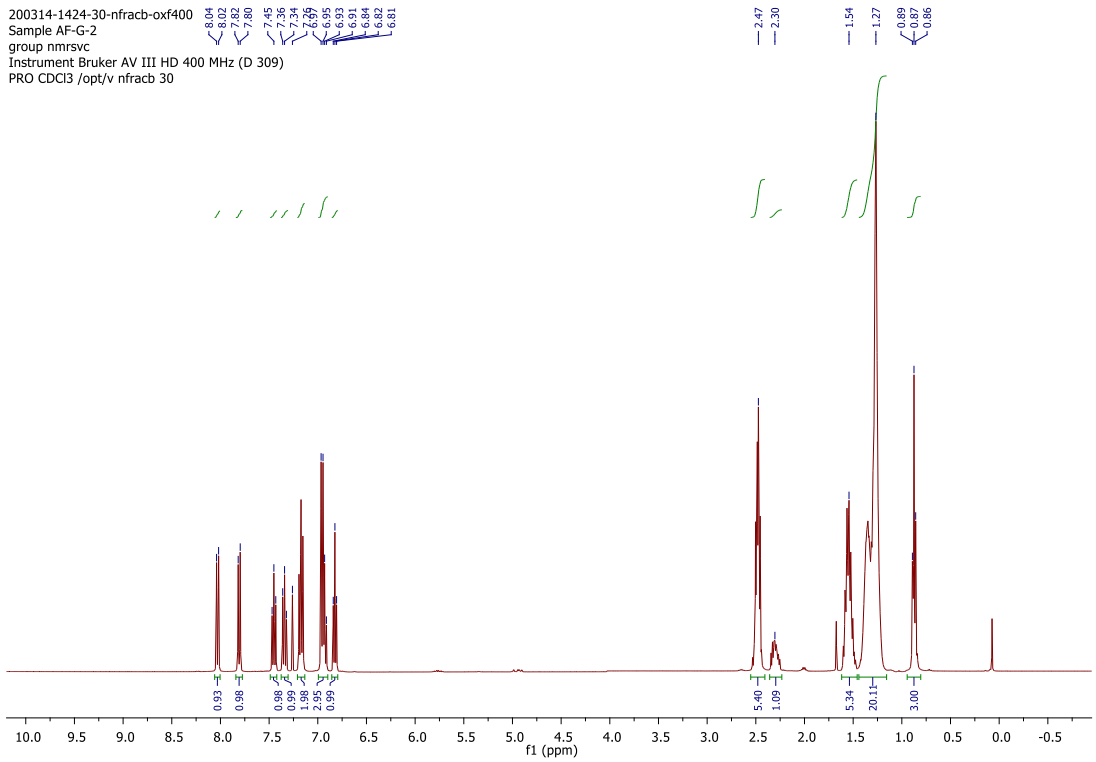

Figure 100. ^{1}H NMR spectrum of **32** (in $CDCl_3$, 400 MHz).

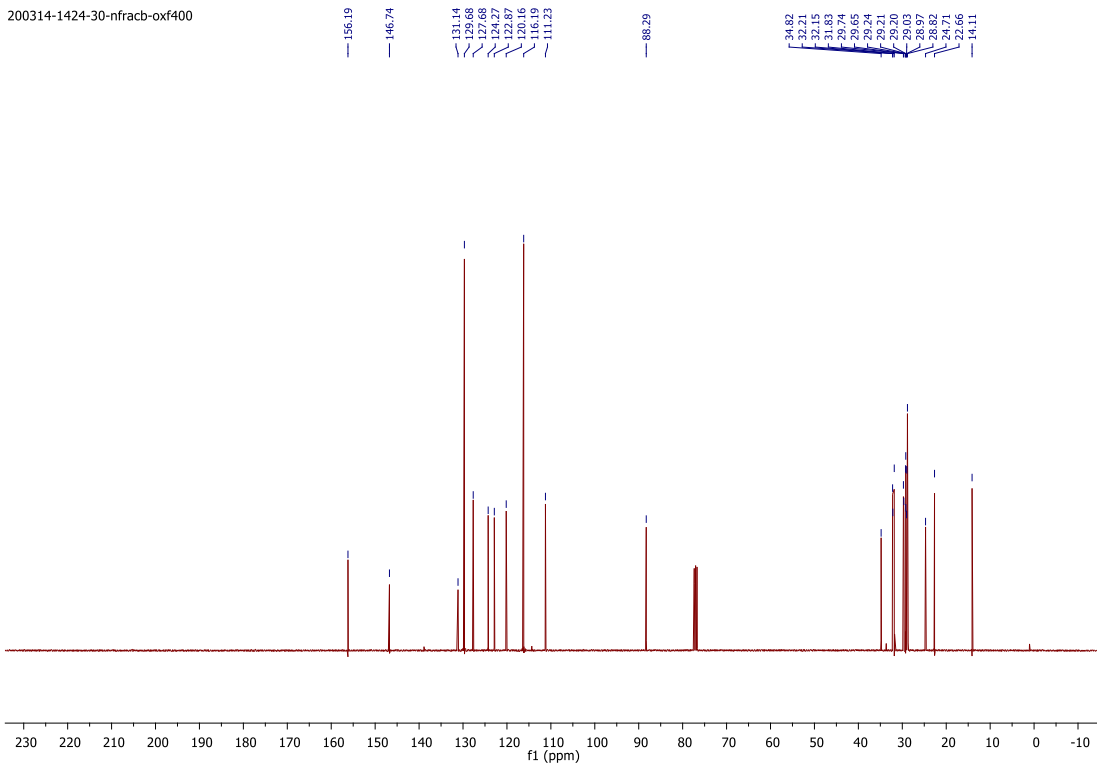

Figure 101. ^{13}C NMR spectrum of **32** (in $CDCl_3$, 100 MHz).

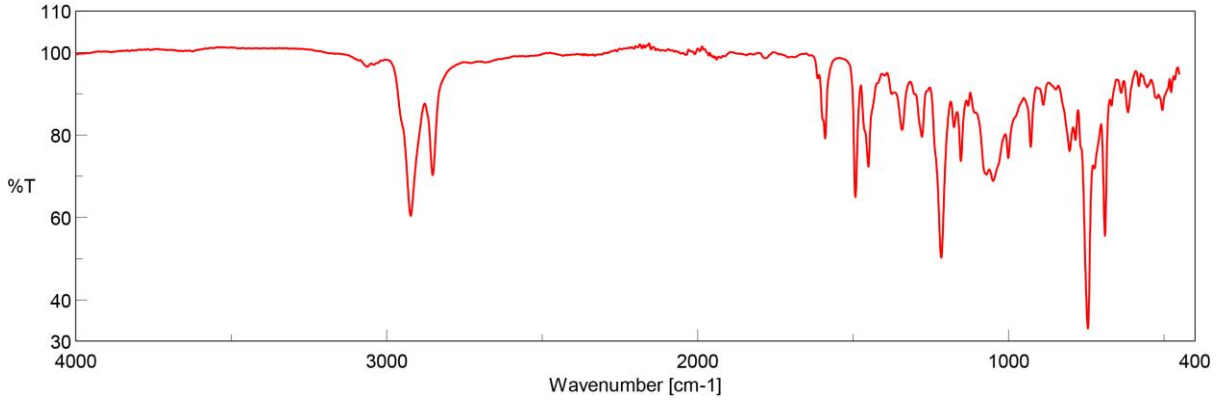

Figure 102. FT-IR ATR spectrum of **32**

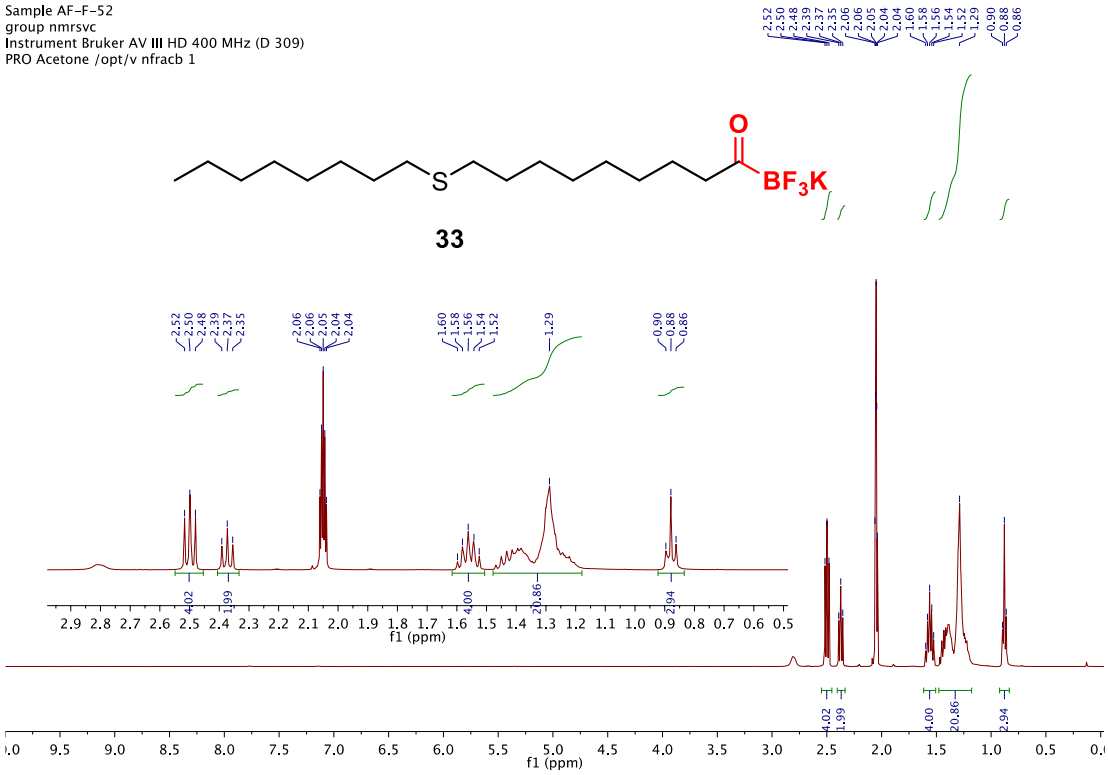

Figure 103. ^{1}H NMR spectrum of **33** (in Acetone- d_6, 400 MHz).

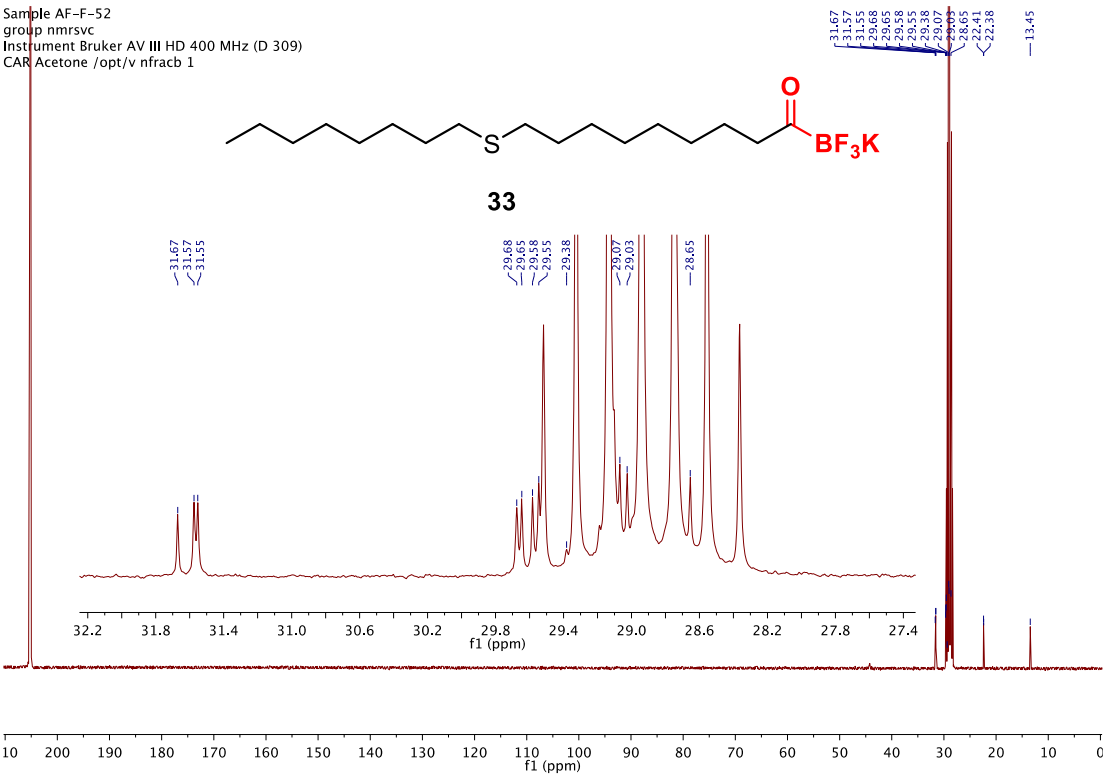

Figure 104. ^{13}C NMR spectrum of **33** (in Acetone- d_6, 100 MHz).

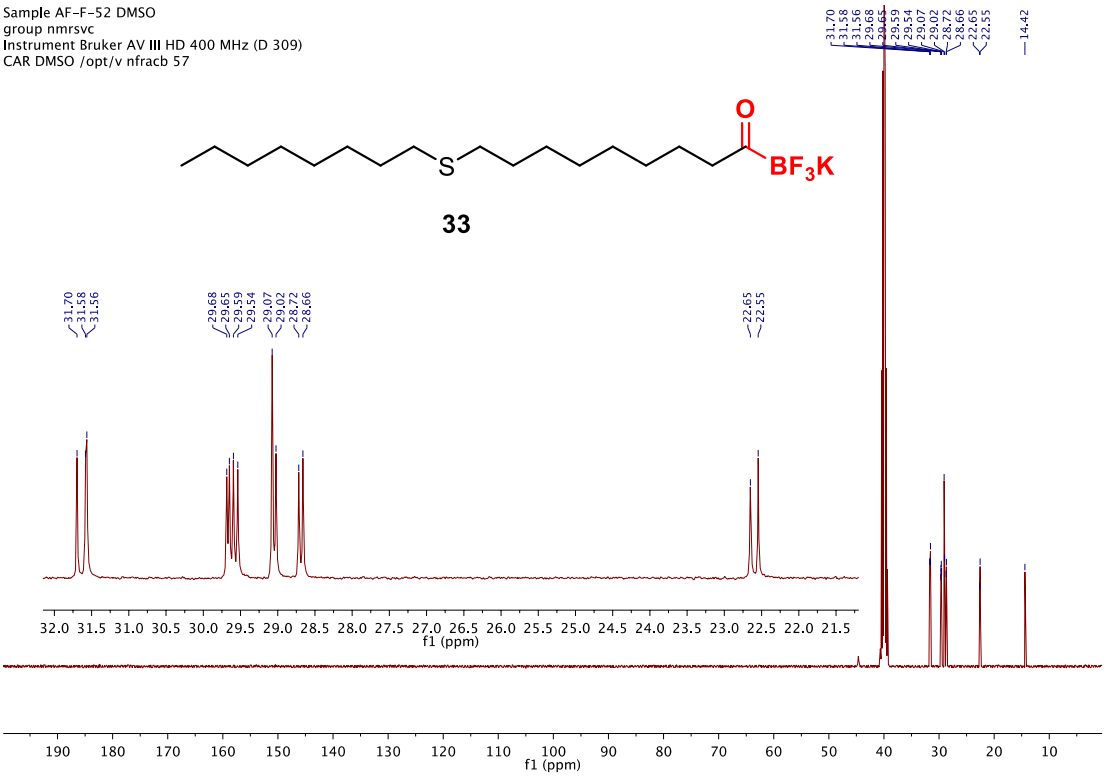

Figure 105. ^{13}C NMR spectrum of **33** (in DMSO-d_6, 100 MHz).

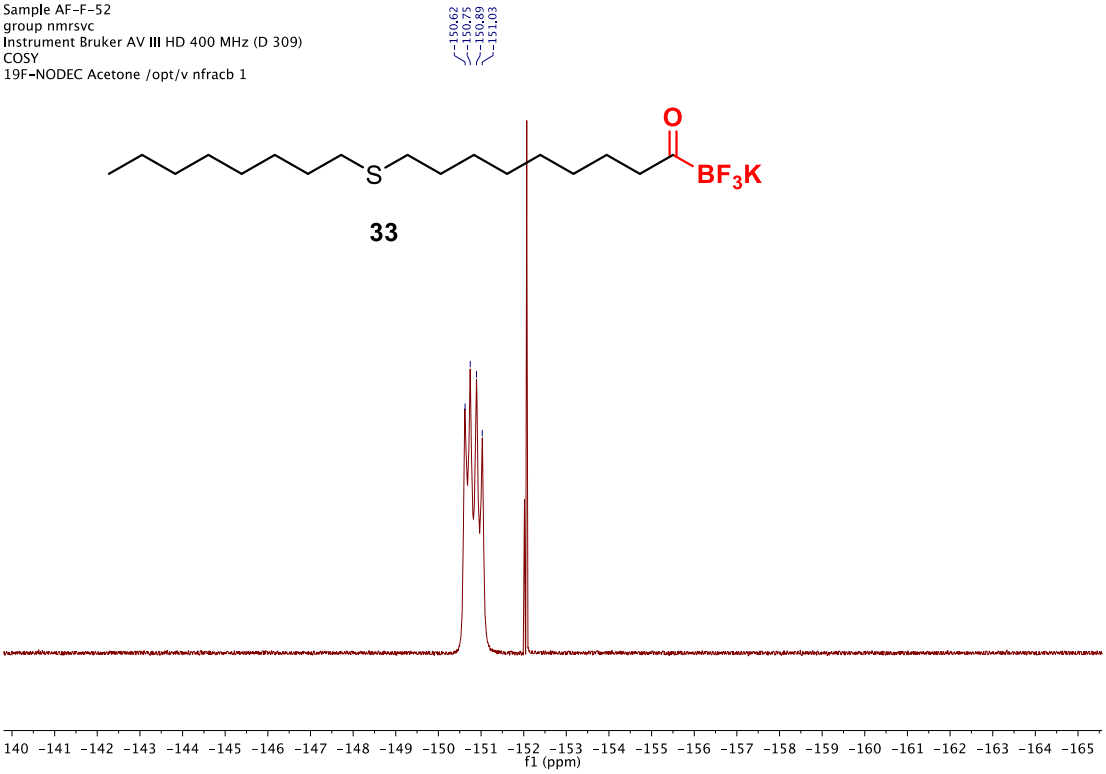

Figure 106. ^{19}F-NMR spectrum of **33** (in Acetone-d_6, 376 MHz).

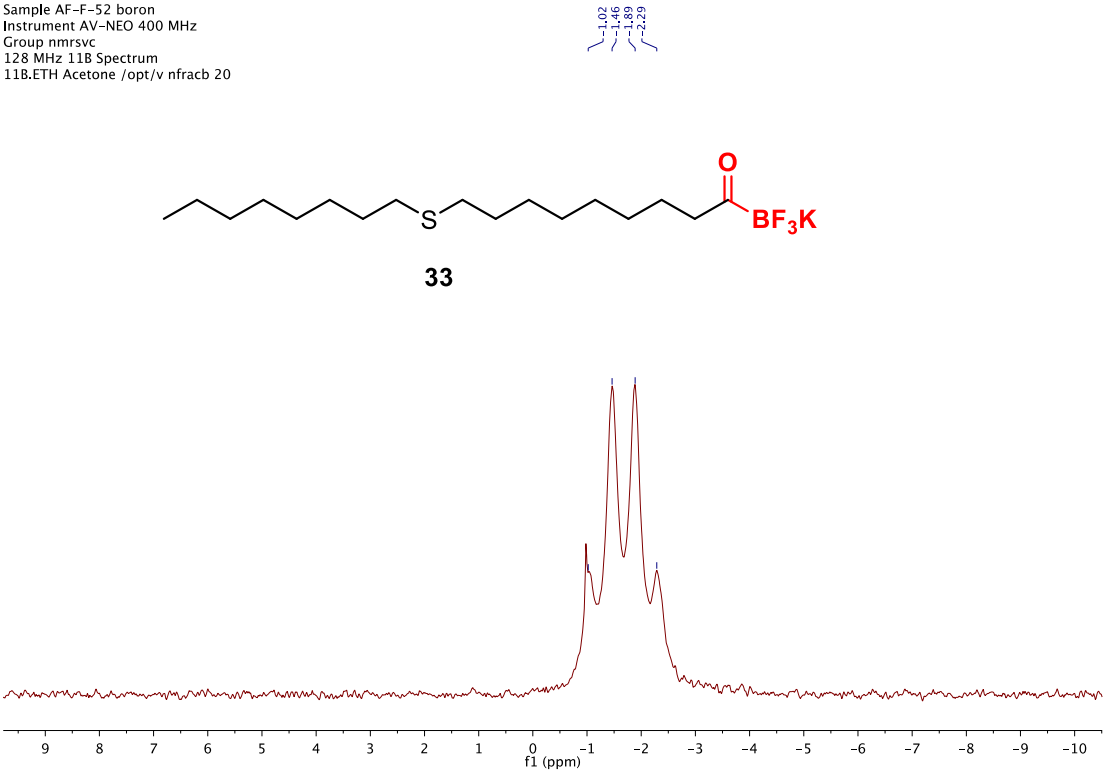

Figure 107. ^{11}B-NMR spectrum of **33** (in Acetone-d_6, 128 MHz).

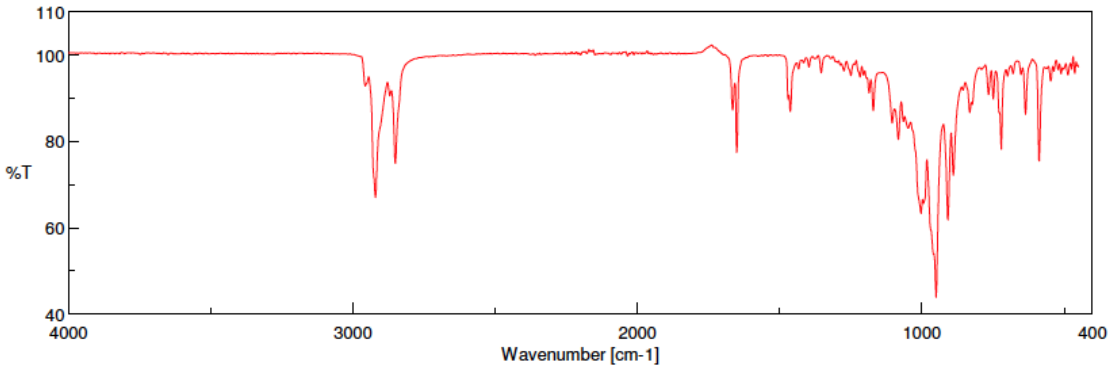

Figure 108. FT-IR ATR spectrum of **33**

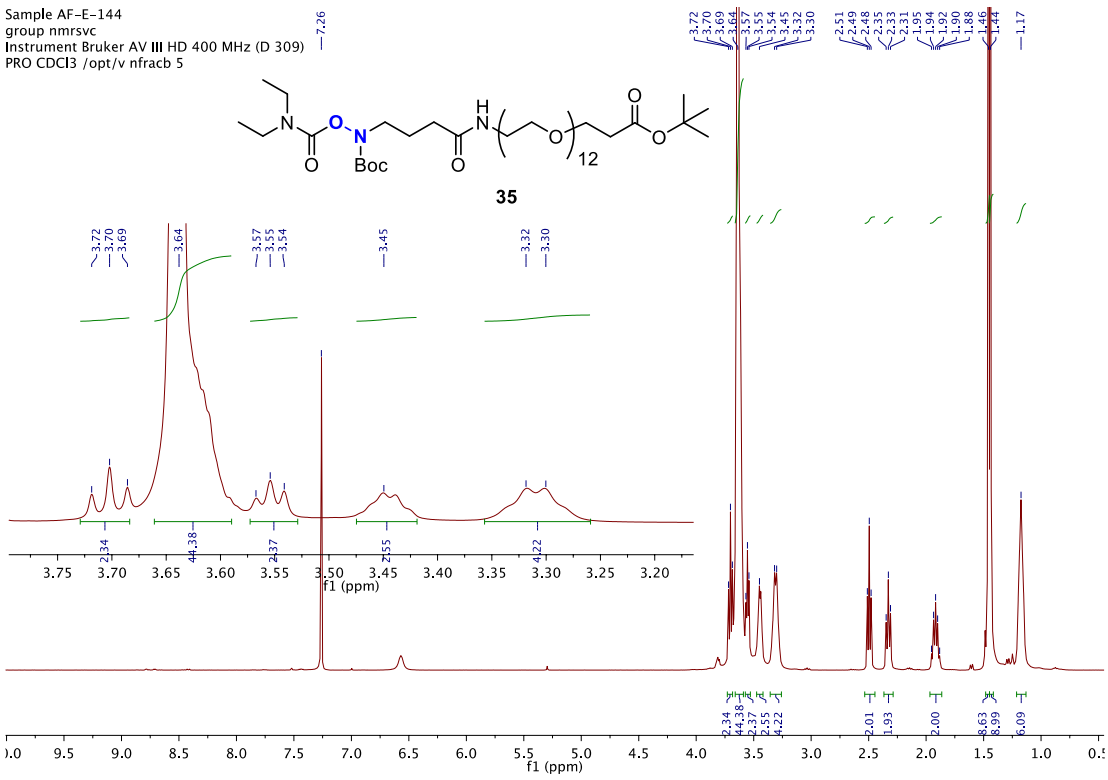

Figure 109. ^{1}H NMR spectrum of **35** (in $CDCl_3$, 400 MHz).

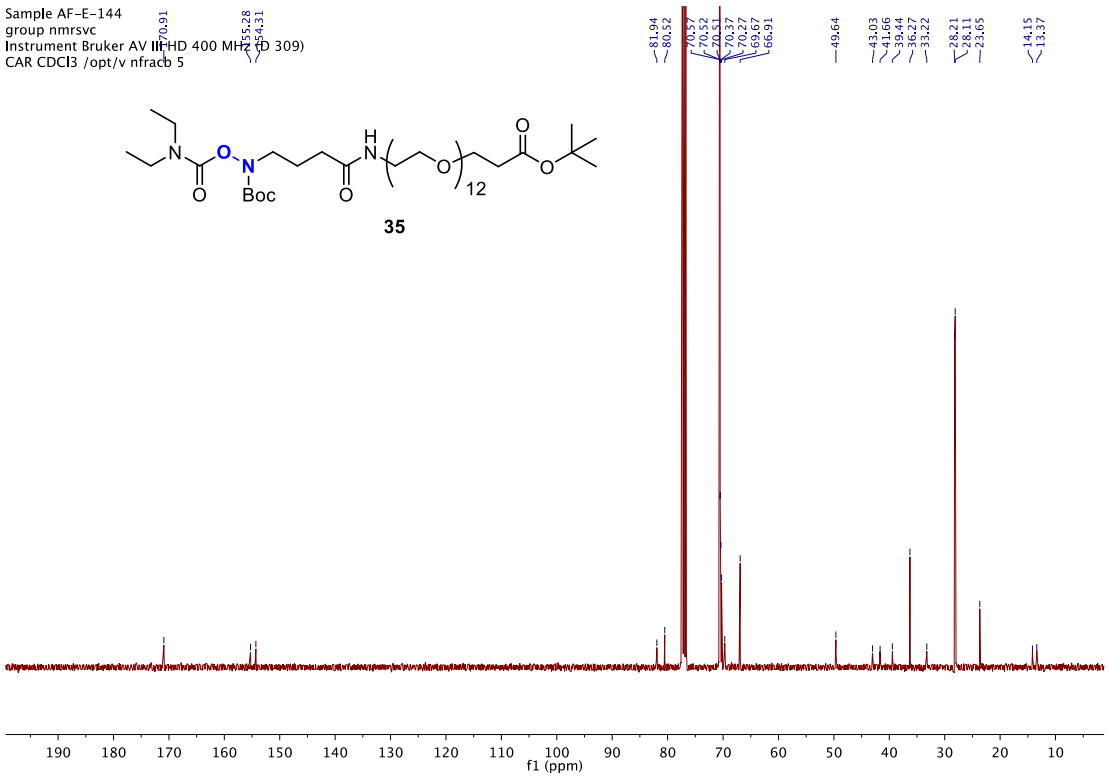

Figure 110. ^{13}C NMR spectrum of **35** (in $CDCl_3$, 100 MHz).

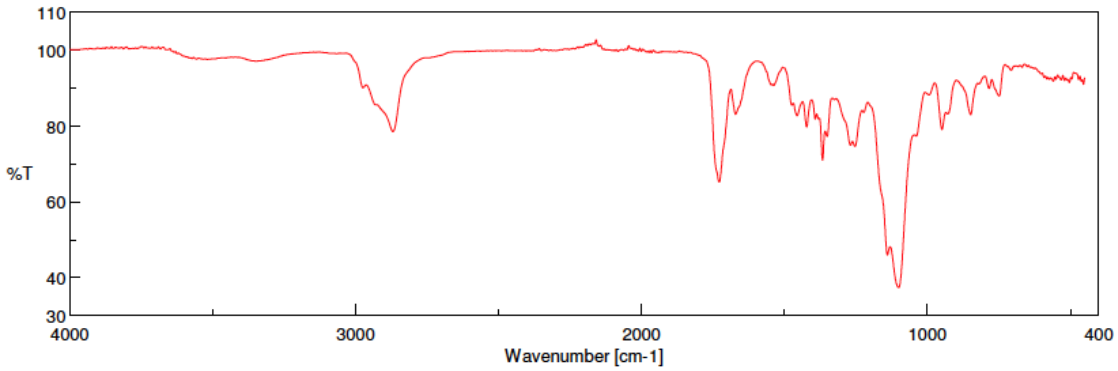

Figure 111. FT-IR ATR spectrum of **35**

6.2 Particle preparation and characterization

6.2.1 Preparation of LNP and LNP-KAT

To a solution of a mixture of three lipid substances – phosphatidylcholine from egg (PC, 33.8 mg, 44.5 μmol, Tokyo Chemical Industry, Co. LTD., Tokyo, Japan), triolein (TO, 29.2 mg, 33 μmol, Acros) and cholesteryl oleate (CO, 9.4 mg, 16.5 μmol, Alfa Aesar), in a ratio of PC-TO-CO (44.5:33:16.5, mol/mol/mol) in a mixture of $CHCl_3$-MeOH-acetone (2:1:1, v/v/v) (90 mL), the KAT derivative of oleic acid (OA-KAT **1**, 1.9 mg, 5 μmol, 5 mol% of total lipid) in MeOH-acetone (1:1, v/v) (30 mL) was added and thoroughly mixed in a round bottom flask. The solvents were slowly removed by rotary evaporator to make a thin lipid film on the bottom of the flask, which was further lyophilized overnight to remove all trace of organic solvents. To this dried thin film, 4 mL of Tris-HCl buffer (10 mM, pH 8.0, containing KF (10 mM) and BHT (1 mg L^{-1})) was added, mixed with a vortex mixer for 1 min, and treated under sonication in ice bath for 2 h using an EMMI® 40HC sonicator (EMAG-AG, Mörfelden-Walldorf, Germany). Obtained suspension of lipid mixture was extruded by a Lipex 10 mL extruder (Lipex Biomembranes, Burnaby, BC, Canada) for 10 times at 50 °C using two stacked polycarbonate membrane filters (pore sizes: 0.05 μm and 0.1 μm). The obtained nanoparticle suspension was filtered through a filter (0.45 μm, Chromafil® Xtra PTEF-45/25, Macherey Nagel GmbH & Co. KG, Düren, Germany), washed three times with Tris-HCl buffer (10 mM, pH 8.0) by spin filtering (Amicon centrifuge filter 50 kDa cutoff, Merck KGaA) to remove the free un-bound lipids, which were not incorporated into the particle. The filtrate (**LNP-KAT** particle) was kept in Tris-HCl buffer (10 mM, pH 8.0) at 4 ºC before being subjected to the surface functionalization.

6.2.2 DLS measurement

DLS measurements were performed with a Malvern Nano-ZetaSizer (Malvern Instruments Ltd, Malvern, Worcestershire, UK), equipped with a 5 mW HeNe laser (wavelength: 632.8 nm) and a digital logarithmic correlator. The normalized intensity autocorrelation functions were measured at an angle of 173 °. An aliquot (20 μL) of each obtained particle was diluted with Tris-HCl buffer (10 mM, pH 8.0) or phosphate buffer (10 mM, pH 8.0) to 0.8 – 1 mL for the measurements, which were carried out at 25 ºC.

6.2.3 Determination of Zeta-Potential

The measurements of the electrophoretic mobility to determine ζ-potential were carried out with a Malvern Nano-ZetaSizer equipped with a 5 mW HeNe laser (wavelength = 632.8 nm) also employed for size determination. The **LNP-KAT** were analyzed at 25 °C in Tris buffer (10 mM, pH 8.0).

6.2.4 TEM measurement

Samples for TEM measurements were prepared by diluting the LNP suspension with equal volume of 2% sodium phosphotungstate (pH 8) in a small test tube by gentle shaking by hand. The final concentration of LNP in the mixture was approximately 4 mg/mL (estimated by initially added lipid amount). One drop of this mixture was placed onto a Quantifoil carbon-coated grid (Quantifoil Instruments GmbH, Jena, Germany) that was glow-discharged for 15 s using Emitech K100X (Quorum Technologies Ltd, East Sussex, UK). It was then allowed to sit for 60 s followed by the removal of the excess fluid by touching the edge of the grid with filter paper. The samples were examined by a Morgagni 268 microscope (FEI, Hillsboro, OR, USA) operated at 100 kV.

6.2.5 cryoTEM measurement

The microscopical characterization of the particles in their hydrated state was carried out on a Tecnai F20 cryo-TEM (FEI/Thermo Fisher Scientific). The 300-mesh lacey carbon-coated copper grids (Quantifoil Micro Tools GmbH, Jena, Germany) were glow discharged using an Emitech K100X (Quorum Technologies Ltd., Laughton, GB) for 30 sec. An aliquot of particle suspension (3 μL) was applied onto the grids in a Vitrobot Mark II (FEI/Thermo Fisher Scientific) and the excess of the particles was removed by controlled blotting. A mixture of liquid ethane/propane was used for sample vitrification. The grids were then transferred on a Gatan cryo-transfer holder (Gatan, Inc., Pleasanton, CA, USA) into the microscope and kept at –180 °C during observation. Micrographs were recorded under low dose conditions (<500 e^{-}/nm^{2}) using a Falcon II 4K Camera (FEI Thermo Fisher Scientific), operating the microscope at 200 kV acceleration voltage in bright field mode.

6.2.6 CryoSEM imaging

Each particles suspension was filled into a 6-mm aluminium-planchette for carrying the sample and a second aluminium-planchette was used as a lid. The planchette sandwiches were frozen in a high-pressure freezer HPM 100 (Bal-Tec/Leica) and stored in liquid nitrogen. Due to weak cohesion of the samples the planchettes often broke apart already at this step. Vitrified specimen were then transferred and mounted under liquid nitrogen on the cryo-holder and finally transferred under liquid nitrogen into a precooled (–130 °C) freeze-fracturing system BAF 060 (Bal-Tec/Leica) at 1×10^{-6} mbar. Closed planchette sandwiches were broken apart. Coating was performed without previous etching with 2 nm tungsten at an elevation angle of 45° followed by 2 nm at 90°. Transfer to the precooled cryo-SEM (Zeiss Gemini 1530) was done under high vacuum ($<5 \times 10^{-6}$ mbar) with an air-lock shuttle. Cryo-SEM was performed in a field emission SEM Leo Gemini 1530 (Zeiss) equipped with a cold stage to maintain the specimen temperature at –120 °C (VCT Cryostage, Bal-Tec/Leica). Inlens-SE-signals at an acceleration voltage of 4 kV were used for image formation (acquisition). The contrast and brightness of the pictures were adjusted.

6.2.7 AFM measurements

Mica (Ted Pella Inc., Redding, CA, USA) was freshly cleaved with a scotch-tape to reveal a fresh layer devoid of organic contaminants. An aliquot (10 µL) of nanoparticles suspension was diluted 5 times with PBS (pH 7.4) and deposited onto the mica surface and left for 10 min for immobilization. Subsequently, 10% formalin solution (10 µL) was added and left additionally for 10 min. The substrate was washed with PBS (50 µL) to remove excess nanoparticles, and added with an additional aliquot (50 µL) of PBS, and kept for 30 min prior to AFM imaging. AFM imaging was performed on a Bruker Dimension Icon AFM (Bruker) in Peak Force Tapping mode in liquid with an SNL 10-A cantilever (Bruker, deflection sensitivity: 30 nm/V, spring constant: 0.35 N/m, frequency: 80 KHz). The engage setpoint was set to 0.05 V with initial imaging force at roughly 50-80 pN to make engage settings rather soft so that the tip underwent minimum impact when approaching the surface. Imaging was performed using a peak force frequency of 2 kHz, and peak force amplitude of 10 nm. Images were acquired at line rate of 1-1.2 Hz with 512 pixels per line. Data were analyzed using the Bruker Nanoscope Analysis (Bruker AXS, CA, USA) for line-by-line flattening and removal of tilt using first order polynomial.

6.2.8 Preparation of sLDL-Gd particle

To a mixture of 10 mM KF in phosphate buffer (10 mM, pH 5.8, 32 mL) and 0.1 M HCl (400 μL), a solution of HA-peptide **16** (0.48 μmol) in H_2O (200 μL) and a solution of HA-Gd(DO3A-MA) **15** (4.32 μmol) in H_2O (700 μL) were added. Subsequently, **LNP-KAT** particle (with estimated KAT content of 4.1 μmol by ICP-MS analysis of B) in 8 mL of Tris-HCl buffer (10 mM, pH 8.0) was added. The pH of reaction mixture was 5.2. The reaction was stirred overnight at room temperature. The crude mixture was concentrated to a volume of 1.5 mL by spin filtering (Amicon centrifuge filter 50 kDa cutoff) and washed with 5 mL of PBS (-) (pH 7.4) for three times to remove the unreacted compounds **15** and **16**. The obtained nanoparticles were reconstituted to 8 mL in PBS (-) (pH 7.4) for characterization.

6.2.9 MALDI-MS analysis of sLDL-Gd particle

The MALDI of the **sLDL-Gd** was recorded on a Bruker SolariX-FTICR 9.4 T MS (Bruker Daltonics). An aliquot (50 μL) of particles suspension of **sLDL-Gd** in PBS (pH 7.4) was dried by N_2 flow and reconstituted in 200 μL of a mixture of H_2O and CH_3CN (1:1, v/v). The mixture was then further diluted 10 times with a saturated solution of α-cyano-4-hydroxycinammic acid (HCCA) in a mixture of H_2O and CH_3CN (1:1, v/v) before the MALDI analysis.

6.2.10 ICP-MS for B and Gd contents in LNP-KAT and sLDL-Gd particles

The ICP-MS or ICP-OES analyses of B and Gd contents were measured on an Element XR sector-field inductively coupled plasma mass spectrometer (Thermo Fisher Scientific, Waltham, MA, USA) or a Horiba Ultra 2 inductively coupled plasma-optical emission spectrometry (Horiba Ltd., Kyoto, Japan). An aliquot (100 μL for B analysis and 20 μL for Gd^{3+} analysis) of each particle suspension was dried on a hot plate and digested by refluxing in conc. HNO_3 (1 mL) for 16 h. Subsequently, each sample was dried again and dissolved in 1.0 mL of 2% HNO_3 (v/v) (0.3 M) before being subjected to the ICP−MS or ICP-OES analyses. Calibration curves were prepared using standard solutions of B and Gd (Alfa Aesar B ICP standard and Gd ICP standard (Thermo Fisher (Kandel) GmbH, Kandel, Germany) in a concentration range of 5−200 μM. In case of ICP-MS measurements, samples were introduced into the mass spectrometer via a PFA nebulizer with an uptake rate of 50 $\mu L \cdot min^{-1}$ attached to a cyclonic glass spray chamber. In general, in this laboratory, long-term accuracy and precision are assessed using two secondary multielement standards: National

Research Council of Canada river standard SLRS-5 (now replaced by SLRS-6) and USGS shale standard SGR1. The concentrations obtained matched certified values to within 5−10% (2SD) for most of the elements of interest. In this laboratory, boron is not routinely measured, therefore no long-term data are available. However, the accuracy and precision within the analytical session were determined by repeat analysis of SRM NIST 1640 and were determined to be with 10 and 17% (2SD), respectively.

6.2.11 Relaxivity measurements

The Proton relaxivities at 60 MHz were measured on a Bruker WP80 NMR electromagnet adapted to variable field measurements and controlled by a Stelar SMARTracer PC-NMR console (Stelar s.r.l., Pavia, Italy). The temperature was monitored by a VTC91 temperature control unit and maintained by a gas flow. The temperature was determined by previous calibration with a Pt resistance temperature probe. Relaxivities at 400 MHz were measured on a Bruker AVANCE NMR spectrometer. The temperature was calculated according to previous calibration with ethylene glycol and methanol. The Gd concentration of the sample was 193 μM.

6.2.12 *In vitro cellular* incorporation tests

A fluorescent LNP was prepared for the cell incorporation tests with a protocol similar to that used for the preparation of **sLDL-Gd** (section 7.3.3 above). Instead of HA-Gd(DO3A-MA) **15**, HA-fluorescein **13** was used for the surface functionalization of the **LNP-KAT** particle, together with HA-peptide **16**, to provide **sLDL-Fl** particles. As a control, **LNP-Fl** particles without peptide moiety on the nanoparticle surface was used.

In vitro cellular incorporation tests were performed using two types of cell lines, THP-1 (human monocyte cell line) and RAW 264.7 (mouse macrophage cell line, a gift from Dr. Irie in Tokyo Metropolitan Institute of Medical Science). THP-1 cells were cultured in RPMI (Gibco 11875) with 10% heat-inactivated FBS and 0.1 mM 2-mercaptoethanol. RAW 264.7 cells were cultured in DMEM with 10% heat-inactivated FBS and 1 mM sodium pyruvate. Cells were pre-cultured in a 6-cm dish, inoculated in the 96-well microplates with 1-4 x 10^4 cells/well. Cells were incubated for 1 or 2 days and **sLDL-Fl** or **LNP-Fl** particles were added to the cells in logarithmic growth phase. RAW 264.7 cells were cultured and processed in Biosafety level 2 facility.

Assay with THP-1: After the co-incubation with **sLDL-Fl** or **LNP-Fl** for 5 or 20 h, cells were washed with PBS. After removing the excess particles in the medium, cells were washed with PBS and incorporated particles were examined by KEYENCE Fluorescence Microscope BZ-X700 (Keyence Co., Osaka, Japan) using 470 nm of excitation wavelength. Phase contrast images were simultaneously recoded. The incorporated cellular fluorescent intensities of three independent microscopic images at x20 magnification were quantified by Lumina Vision software 3.3 (Mitani Corporation, Fukui, Japan)

Assay with RAW 264.7: Cells were co-incubated with **sLDL-Fl** or **LNP-Fl** for 5 h and washed with PBS before the examination by fluorescence microscope. Subsequently, cells were incubated in the medium without particles for additional 16 h. After washing with PBS (-), the incorporated particles were examined as above.

6.2.13 *ex vivo* test of *apoE*$^{-/-}$ mice by ICP-MS

All the animal procedures were approved by the Institutional Animal Care and Use Committee (IACUC) of the University of Pennsylvania. The male *apoE*$^{-/-}$ mice were purchased from the Jackson Laboratory. The mice started receiving HFD (42% kcal from fat, Teklad#88137) at 8 weeks of age and the HFD was continued for two months. Prior to injection, **sLDL-Gd** sample was concentrated in filter tubes (50 kDa) by centrifugation (1000 rcf at 4 °C) to a suitable volume (0.25 mL) for the injection to a mouse. No aggregation was observed after the centrifugation. Under anesthesia, the **sLDL-Gd** particles were injected *via* a catheter placed in tail vein of the mouse. The mice were euthanized 48 h after the injection of **sLDL-Gd**. To obtain the clean aorta from, PBS buffer pH 7.4 was perfused in the blood stream from the left ventricle of the heart and the right atrium was gently cut in order to absorb the perfusion liquid by sterile gauzes. Under a dissection microscope, the presence of atheroplaques were clearly visible. The aorta was then dissected utilizing a dissecting microscope and the aortic arch was collected. The ICP-MS analysis of the Gd^{3+} content in the mice aorta (ng of Gd^{3+} per mg of dry tissue) was carried out in Pennsylvania Animal Diagnostic Laboratory System in New Bolton Center (Kennett Square, PA, USA).

6.2.14 *In vivo* MR imaging of *apoE*$^{-/-}$ mice (atherosclerosis model)

The same model mice as in section 7.3.12 were used in MR imaging. Under anesthesia, the **sLDL-Gd** particles were injected *via* a catheter placed in tail vein of the mouse. All MRI was

performed on a 9.4 T horizontal bore MR spectrometer (DirectDrive®, Agilent, Palo Alto, CA) equipped with a 12-cm (ID) gradient coil. The mouse was positioned prone in a quadrature volume radio frequency (RF) coil (ID = 3.5 cm, length = 8 cm, m2m imaging/Polarean) tuned to ^{1}H resonance frequency (400 MHz). During imaging, the mouse was sedated with 0.8−1% of isoflurane mixed with air (flow rate = 1 L/min). ECG, respiration and core temperature of the mouse were monitored by an MRI-compatible vital sign monitoring system (SA Inc, Long Island, New York). The rectal temperature was maintained at 37 ±0.2 °C by a feedback loop that turns on/off warm air directed into the magnet bore. Scout images were acquired to capture the aortic arch with three rising branches (LC, LS and BA). Then the image plane was placed to cut through the three aortic branching points. This image plane was used to acquire the "White Blood" (WB), where the blood signal in aorta lumen is not suppressed, as well as "Black Blood" (BB) images, where the blood signal is suppressed (thus black). To obtain WB image, ECG-gated multi-slice gradient echo sequence (TR = 1 heartbeat, about 120 ms, TE = 2.4 ms) was employed with FOV = 26 x 25 mm, matrix size = 192 x 128, slice thickness = 0.8 mm. To obtain BB images, ECG-gated multi-slice FLASH (Fast imaging with Low Angle Shot) (TR = 76 ms, TE =0.97 ms, FA=40 degree) was applied to the same slice. Due to long interval between MRI sessions, we relied on the unique anatomy of the aortic arch, its branching points, and other thoracic arteries in the imaging plane for the comparison of pre- and post-injection images. For images acquired after **sLDL-Gd** injection, BB was further combined with fat suppression option in the MRI protocol although such option is not necessary to detect enhancement.

6.3 Gold surface KAT ligation and characterization

6.3.1 Preparation of functionalized gold surfaces

Gold substrates were prepared by vapor evaporation of gold (99.99% purity, Umicore Thin Films Products, Liechtenstein) on freshly cleaned microscopic slides (area of 2 mm^2) using a sputter coating unit (BalTec AG, Leichtenstein). Firstly, a 10 nm layer of chromium (99.99% purity, Umicore Thin Films Products, Liechtenstein) was deposited on the glass slides to act as an adhesion layer, following which, 50 nm of gold was deposited at a rate of 0.05 nm/s to control the roughness of the sample. After depositon, the chamber was backfilled with research purity N_2, and the bare surfaces immediately used for surface modification. For the formation of thioether SAM, the gold substrates were immersed in a glass vial containing 1

mM solution of the thioether in ethanol for 20 h, at room temperature, in the dark. The substrates were taken out with a clean pair of tweezers and washed with ethanol to remove unbound molecules from the surface. For the KAT ligation on surface, the above prepared samples were immersed in a 0.5 mM solution of HA-PEG **36** in phosphate buffer (10 mM, pH 5.5, containing KF 10 mM) at room temperature for 16 h. The samples were then washed with MilliQ water and ethanol to remove any residual HA-PEG **36** non-covalently bound to the surface. These modified surfaces were stored under Ar atmosphere before characterisation by XPS, contact angle, and ellipsometry.

6.3.2 X-ray photoelectron spectroscopy (XPS)

A PHI Quantera SXM spectrometer (ULVAC-PHI, Chanhassen, MN) was used for the XPS measurements. All experiments were conducted at residual pressures lower than $3 \cdot 10^{-7}$ Pa. The X-ray source was a monochromatic Al Kα beam, with the emission angle being 45°. The nominal diameter of the X-ray beam was 100 µm. The analyzer was used in constant-analyzer-energy mode. The pass energy for survey spectra was 280 eV, while that used for narrow spectra was 69 eV, with an energy step size of 1 eV and 0.125 eV respectively. The energy scale of the spectrometer was calibrated according to ISO 15472:2014 with an accuracy of ±0.1 eV. The energy resolution, expressed as the full width at half maximum (FWHM) of the $Ag3d_{5/2}$ peak, was 0.71 eV at the pass energy used for narrow spectra. No charge compensation was applied. Peak fitting was performed with CasaXPS software (v2.3.18PR1.0, Casa Software Ltd, Teignmouth, UK). A linear function was used for background subtraction in the case of N1s and S2p spectra, while a Shirley background subtraction was employed in all other cases. Gaussian-Lorentzian functions were used for peak fitting, with the addition of a tail function T(5.5) for the Au4f peak.

The thickness of the organic layers adsorbed on gold was determined using the following equation:

$$d = ln\left(\frac{I_0}{I}\right)\lambda \cos\theta$$

where I_0 is the total area of the Au4f peak acquired on bare gold, I is its area when an adsorbed organic layer is present, λ is the inelastic mean free path of Au4f photo-electrons in an organic medium, determined according to the TPP-2M method, and θ is the emission angle (45°). Reference Au4f spectra were acquired on freshly template-stripped bare gold to

measure I_0, after 10 seconds of mild ion-argon sputtering at 3 keV and 3 μA, which was enough for the C1s and O1s signals in the survey spectra to be well below 5% of the most intense signal. This criterion is indicated in the ISO guidelines for defining a cleaned surface.

6.3.3 Contact angle measurements

Static water contact angles were measured by a goniometer (Ramé Hart Inc., Succasunna, NJ, USA) by adding 3 μL drop of water to the modified substrate at room temperature and ambient humidity. Angles were measured at three different spots on each sample.

6.3.4 Ellipsometry measurements

Ellipsometric data were obtained on a spectroscopic ellipsometer (spectroscopic ellipsometer (VASE M-2000F, LOT Oriel GmbH, Germany). The angle of incidence was 70˚ from the surface normal. The determination of Ψ (amplitude) and Δ (phase) as a function of wavelength (350−800 nm) was carried out by employing the WVASE32 software package (LOT Oriel GmbH), The *n* and *k* values were found to be 0.2 and 3.35 for the S-KAT **33** on gold surface. SAM on gold surface were analyzed based on a three-layer model (SiO_2/gold/Cauchy-SAM) based on the bulk dielectric function of gold. Thickness determination of SAM on gold was based on a Cauchy model: $n = A + B.\ \lambda^{-2}$, where *n* is the refractive index, λ is the wavelength, and $A = 1.45$, and $B = 0.01$ as values for thin and transparent organic films. Thickness values were obtained by averaging at least five measurements per sample.

6.3.5 Quartz Crystal Microbalance (QCM) measurements

QCM measurements were carried out using a QCM-D (Q-sense AG, Gothenburg, Sweden). A gold-coated quartz crystal was cleaned by sonication in isopropanol followed by UV/ozone treatment. EtOH was injected using a plastic syringe to obtain a stable baseline. After ca. 30 min, a filtered 1 mM EtOH solution of S-KAT **33** was injected. A drop in the oscillation frequency was observed and when no change was any further observed, pure EtOH was again injected to wash out the unbound molecules. Water was injected until the formation of a stable baseline and it was followed by an injection of phosphate buffer (10 mM, pH 5.5, containing KF 10 mM). Subsequently a filtered solution of the hydroxylamine derivative was injected and a sharp decrease of the oscillation frequency was observed. When no change was

any further observed, phosphate buffer was again injected to wash out the unbound reactants and the oscillation frequency was observed to not change and remain constant.

Chapter 7

References

7. References

(1) Barquera, S.; Pedroza-Tobías, A.; Medina, C.; Hernández-Barrera, L.; Bibbins-Domingo, K.; Lozano, R.; Moran, A. E. Global Overview of the Epidemiology of Atherosclerotic Cardiovascular Disease. *Arch. Med. Res.* **2015**, *46* (5), 328–338.

(2) Lusis, A. J. Atherosclerosis. *Nature* **2000**, *407* (6801), 233–241.

(3) Dod, H. S.; Bhardwaj, R.; Sajja, V.; Weidner, G.; Hobbs, G. R.; Konat, G. W.; Manivannan, S.; Gharib, W.; Warden, B. E.; Nanda, N. C.; et al. Effect of Intensive Lifestyle Changes on Endothelial Function and on Inflammatory Markers of Atherosclerosis. *Am. J. Cardiol.* **2010**, *105* (3), 362–367.

(4) Moore, K.; Sheedy, F.; Fisher, E. Macrophages in Atherosclerosis: A Dynamic Balance. *Nat. Rev. Immunol.* **2013**, *13* (10), 709–721.

(5) Hansson, G. K.; Hermansson, A. The Immune System in Atherosclerosis. *Nat. Immunol.* **2011**, *12* (3), 204–212.

(6) Athanasiou, L. S.; Fotiadis, D. I.; Michalis, L. K. Introduction. In *Atherosclerotic Plaque Characterization Methods Based on Coronary Imaging*; Elsevier, 2017; pp 1–21.

(7) Douglas, G.; Channon, K. M. The Pathogenesis of Atherosclerosis. *Medicine (Baltimore)* **2010**, *38* (8), 397–402.

(8) *Asymptomatic Atherosclerosis: Pathophysiology, Detection, and Treatment*; Naghavi, M., Ed.; Contemporary cardiology; Humana Press: New York, 2010.

(9) Myerburg, R. J.; Interian, A.; Mitrani, R. M.; Kessler, K. M.; Castellanos, A. Frequency of Sudden Cardiac Death and Profiles of Risk. *Am. J. Cardiol.* **1997**, *80* (5), 10F-19F.

(10) Sanz, J.; Fayad, Z. A. Imaging of Atherosclerotic Cardiovascular Disease. *Nature* **2008**, *451* (7181), 953.

(11) Tarkin, J. M.; Dweck, M. R.; Evans, N. R.; Takx, R. A. P.; Brown, A. J.; Tawakol, A.; Fayad, Z. A.; Rudd, J. H. F. Imaging Atherosclerosis. *Circ. Res.* **2016**, *118* (4), 750–769.

(12) Corti, R.; Fuster, V. Imaging of Atherosclerosis: Magnetic Resonance Imaging. *Eur. Heart J.* **2011**, *32* (14), 1709–1719.

(13) Yuan, C.; Kerwin, W. S. MRI of Atherosclerosis. *J. Magn. Reson. Imaging* **2004**, *19* (6), 710–719.

(14) Teresa Albelda, M.; Garcia-España, E.; Frias, J. C. Visualizing the Atherosclerotic Plaque: A Chemical Perspective. *Chem Soc Rev* **2014**, *43* (8), 2858–2876.

(15) Schoenhagen, P.; Halliburton, S. S.; Stillman, A. E.; Kuzmiak, S. A.; Nissen, S. E.; Tuzcu, E. M.; White, R. D. Noninvasive Imaging of Coronary Arteries: Current and Future Role of Multi–Detector Row CT. *Radiology* **2004**, *232* (1), 7–17.

(16) Voros, S.; Rinehart, S.; Qian, Z.; Joshi, P.; Vazquez, G.; Fischer, C.; Belur, P.; Hulten, E.; Villines, T. C. Coronary Atherosclerosis Imaging by Coronary CT Angiography: Current Status, Correlation With Intravascular Interrogation and Meta-Analysis. *JACC Cardiovasc. Imaging* **2011**, *4* (5), 537–548.

(17) Kolossváry, M.; Szilveszter, B.; Merkely, B.; Maurovich-Horvat, P. Plaque Imaging with CT—a Comprehensive Review on Coronary CT Angiography Based Risk Assessment. *Cardiovasc. Diagn. Ther.* **2017**, *7* (5), 489–506.

(18) Rosa, E. M. da; Kramer, C.; Castro, I. Association between Coronary Artery Atherosclerosis and the Intima-Media Thickness of the Common Carotid Artery Measured on Ultrasonography. *Arq. Bras. Cardiol.* **2003**, *80* (6), 589–592.

(19) Garcia-Garcia, H. M.; Costa, M. A.; Serruys, P. W. Imaging of Coronary Atherosclerosis: Intravascular Ultrasound. *Eur. Heart J.* **2010**, *31* (20), 2456–2469.

(20) Bertrand, M.-J.; Abran, M.; Maafi, F.; Busseuil, D.; Merlet, N.; Mihalache-Avram, T.; Geoffroy, P.; Tardif, P.-L.; Abulrob, A.; Arbabi-Ghahroudi, M.; et al. In Vivo Near-Infrared Fluorescence Imaging of Atherosclerosis Using Local Delivery of Novel Targeted Molecular Probes. *Sci. Rep.* **2019**, *9* (1), 1–12.
(21) Hilderbrand, S. A.; Weissleder, R. Near-Infrared Fluorescence: Application to in Vivo Molecular Imaging. *Curr. Opin. Chem. Biol.* **2010**, *14* (1), 71–79.
(22) Smith, A. M.; Mancini, M. C.; Nie, S. Bioimaging: Second Window for *in Vivo* Imaging. *Nat. Nanotechnol.* **2009**, *4* (11), 710–711.
(23) Fleg, J. L.; Stone, G. W.; Fayad, Z. A.; Granada, J. F.; Hatsukami, T. S.; Kolodgie, F. D.; Ohayon, J.; Pettigrew, R.; Sabatine, M. S.; Tearney, G. J.; et al. Detection of High-Risk Atherosclerotic Plaque. *JACC Cardiovasc. Imaging* **2012**, *5* (9), 941–955.
(24) Jager, N. A.; Westra, J.; Golestani, R.; van Dam, G. M.; Low, P. S.; Tio, R. A.; Slart, R. H. J. A.; Boersma, H. H.; Bijl, M.; Zeebregts, C. J. Folate Receptor- Imaging Using 99mTc-Folate to Explore Distribution of Polarized Macrophage Populations in Human Atherosclerotic Plaque. *J. Nucl. Med.* **2014**, *55* (12), 1945–1951.
(25) Glaudemans, A. W. J. M.; Bonanno, E.; Galli, F.; Zeebregts, C. J.; de Vries, E. F. J.; Koole, M.; Luurtsema, G.; Boersma, H. H.; Taurino, M.; Slart, R. H. J. A.; et al. In Vivo and in Vitro Evidence That 99mTc-HYNIC-Interleukin-2 Is Able to Detect T Lymphocytes in Vulnerable Atherosclerotic Plaques of the Carotid Artery. *Eur. J. Nucl. Med. Mol. Imaging* **2014**, *41* (9), 1710–1719.
(26) Brown, J. W. L.; Chard, D. T. The Role of MRI in the Evaluation of Secondary Progressive Multiple Sclerosis. *Expert Rev. Neurother.* **2016**, *16* (2), 157–171.
(27) Korolev, I. O. Alzheimer's Disease: A Clinical and Basic Science Review. **2014**, *04*, 10.
(28) Young, A. A.; Prince, J. L. Cardiovascular Magnetic Resonance: Deeper Insights Through Bioengineering. *Annu. Rev. Biomed. Eng.* **2013**, *15* (1), 433–461.
(29) Fayad, Z.; Fuster, V. Characterization of Atherosclerotic Plaques by Magnetic Resonance Imaging. *Ann. N. Y. Acad. Sci.* **2006**, *902* (1), 173–186.
(30) Merbach, A. S.; Helm, L.; Tóth, É. *The Chemistry of Contrast Agents in Medical Magnetic Resonance Imaging*; John Wiley & Sons, 2013.
(31) De León-Rodríguez, L. M.; Martins, A. F.; Pinho, M. C.; Rofsky, N. M.; Sherry, A. D. Basic MR Relaxation Mechanisms and Contrast Agent Design: MR Relaxation Mechanisms and Contrast Agents. *J. Magn. Reson. Imaging* **2015**, *42* (3), 545–565.
(32) Marcus, Y. Ionic Radii in Aqueous Solutions. *J. Solut. Chem.* **1983**, *12* (4), 271–275.
(33) Hermann, P.; Kotek, J.; Kubíček, V.; Lukeš, I. Gadolinium(Iii) Complexes as MRI Contrast Agents : Ligand Design and Properties of the Complexes. *Dalton Trans.* **2008**, *0* (23), 3027–3047.
(34) Laurent, S.; Elst, L. V.; Muller, R. N. Comparative Study of the Physicochemical Properties of Six Clinical Low Molecular Weight Gadolinium Contrast Agents. *Contrast Media Mol. Imaging* **2006**, *1* (3), 128–137.
(35) Amoroso, A. J.; Pope, S. J. A. Using Lanthanide Ions in Molecular Bioimaging. *Chem. Soc. Rev.* **2015**, *44* (14), 4723–4742.
(36) Werner, E. J.; Datta, A.; Jocher, C. J.; Raymond, K. N. High-Relaxivity MRI Contrast Agents: Where Coordination Chemistry Meets Medical Imaging. *Angew. Chem. Int. Ed.* **2008**, *47* (45), 8568–8580.
(37) Livramento, J. B.; Helm, L.; Sour, A.; O'Neil, C.; Merbach, A. E.; Tóth, É. A Benzene-Core Trinuclear Gd ^{III} Complex: Towards the Optimization of Relaxivity for MRI Contrast Agent Applications at High Magnetic Field. *Dalton Trans* **2008**, No. 9, 1195–1202.

(38) Paranawithana, N. N.; Martins, A. F.; Clavijo Jordan, V.; Zhao, P.; Chirayil, S.; Meloni, G.; Sherry, A. D. A Responsive Magnetic Resonance Imaging Contrast Agent for Detection of Excess Copper(II) in the Liver In Vivo. *J. Am. Chem. Soc.* **2019**, *141* (28), 11009–11018.
(39) Briley-Saebo, K. C.; Mulder, W. J. M.; Mani, V.; Hyafil, F.; Amirbekian, V.; Aguinaldo, J. G. S.; Fisher, E. A.; Fayad, Z. A. Magnetic Resonance Imaging of Vulnerable Atherosclerotic Plaques: Current Imaging Strategies and Molecular Imaging Probes. *J. Magn. Reson. Imaging* **2007**, *26* (3), 460–479.
(40) Buxton, D. B. Current Status of Nanotechnology Approaches for Cardiovascular Disease: A Personal Perspective. *Wiley Interdiscip. Rev. Nanomed. Nanobiotechnol.* **2009**, *1* (2), 149–155.
(41) Phinikaridou, A.; Andia, M.; Lacerda, S.; Lorrio, S.; Makowski, M.; Botnar, R. Molecular MRI of Atherosclerosis. *Molecules* **2013**, *18* (11), 14042–14069.
(42) Zhang, J.; Zu, Y.; Dhanasekara, C. S.; Li, J.; Wu, D.; Fan, Z.; Wang, S. Detection and Treatment of Atherosclerosis Using Nanoparticles: Detection and Treatment of Atherosclerosis Using Nanoparticles. *Wiley Interdiscip. Rev. Nanomed. Nanobiotechnol.* **2017**, *9* (1), e1412.
(43) Peer, D.; Karp, J. M.; Hong, S.; Farokhzad, O. C.; Margalit, R.; Langer, R. Nanocarriers as an Emerging Platform for Cancer Therapy. *Nat. Nanotechnol.* **2007**, *2* (12), 751–760.
(44) Ho Park, J.; Dehaini, D.; Zhou, J.; Holay, M.; H. Fang, R.; Zhang, L. Biomimetic Nanoparticle Technology for Cardiovascular Disease Detection and Treatment. *Nanoscale Horiz.* **2020**, *5* (1), 25–42.
(45) Wickline, S. A.; Neubauer, A. M.; Winter, P. M.; Caruthers, S. D.; Lanza, G. M. Molecular Imaging and Therapy of Atherosclerosis with Targeted Nanoparticles. *J. Magn. Reson. Imaging* **2007**, *25* (4), 667–680.
(46) Sato, N.; Kobayashi, H.; Hiraga, A.; Saga, T.; Togashi, K.; Konishi, J.; Brechbiel, M. W. Pharmacokinetics and Enhancement Patterns of Macromolecular MR Contrast Agents with Various Sizes of Polyamidoamine Dendrimer Cores. *Magn. Reson. Med.* **2001**, *46* (6), 1169–1173.
(47) Kobayashi, H.; Kawamoto, S.; Jo, S.-K.; Bryant, H. L.; Brechbiel, M. W.; Star, R. A. Macromolecular MRI Contrast Agents with Small Dendrimers: Pharmacokinetic Differences between Sizes and Cores. *Bioconjug. Chem.* **2003**, *14* (2), 388–394.
(48) Thiruppathi, R.; Mishra, S.; Ganapathy, M.; Padmanabhan, P.; Gulyás, B. Nanoparticle Functionalization and Its Potentials for Molecular Imaging. *Adv. Sci.* **2017**, *4* (3), 1600279.
(49) Bejarano, J.; Navarro-Marquez, M.; Morales-Zavala, F.; Morales, J. O.; Garcia-Carvajal, I.; Araya-Fuentes, E.; Flores, Y.; Verdejo, H. E.; Castro, P. F.; Lavandero, S.; et al. Nanoparticles for Diagnosis and Therapy of Atherosclerosis and Myocardial Infarction: Evolution toward Prospective Theranostic Approaches. *Theranostics* **2018**, *8* (17), 4710–4732.
(50) Allijn, I. E.; Leong, W.; Tang, J.; Gianella, A.; Mieszawska, A. J.; Fay, F.; Ma, G.; Russell, S.; Callo, C. B.; Gordon, R. E.; et al. Gold Nanocrystal Labeling Allows Low-Density Lipoprotein Imaging from the Subcellular to Macroscopic Level. *ACS Nano* **2013**, *7* (11), 9761–9770.
(51) Cormode, D. P.; Roessl, E.; Thran, A.; Skajaa, T.; Gordon, R. E.; Schlomka, J.-P.; Fuster, V.; Fisher, E. A.; Mulder, W. J. M.; Proksa, R.; et al. Atherosclerotic Plaque Composition: Analysis with Multicolor CT and Targeted Gold Nanoparticles. *Radiology* **2010**, *256* (3), 774–782.

(52) Lipinski, M. J.; Amirbekian, V.; Frias, J. C.; Aguinaldo, J. G. S.; Mani, V.; Briley-Saebo, K. C.; Fuster, V.; Fallon, J. T.; Fisher, E. A.; Fayad, Z. A. MRI to Detect Atherosclerosis with Gadolinium-Containing Immunomicelles Targeting the Macrophage Scavenger Receptor. *Magn. Reson. Med.* **2006**, *56* (3), 601–610.
(53) Mulder, W. J. M.; Strijkers, G. J.; Briley-Saboe, K. C.; Frias, J. C.; Aguinaldo, J. G. S.; Vucic, E.; Amirbekian, V.; Tang, C.; Chin, P. T. K.; Nicolay, K.; et al. Molecular Imaging of Macrophages in Atherosclerotic Plaques Using Bimodal PEG-Micelles. *Magn. Reson. Med.* **2007**, *58* (6), 1164–1170.
(54) Peters, D.; Kastantin, M.; Kotamraju, V. R.; Karmali, P. P.; Gujraty, K.; Tirrell, M.; Ruoslahti, E. Targeting Atherosclerosis by Using Modular, Multifunctional Micelles. *Proc. Natl. Acad. Sci.* **2009**, *106* (24), 9815–9819.
(55) Hanafy, N. A. N.; El-Kemary, M.; Leporatti, S. Micelles Structure Development as a Strategy to Improve Smart Cancer Therapy. *Cancers* **2018**, *10* (7).
(56) Terreno, E.; Sanino, A.; Carrera, C.; Castelli, D. D.; Giovenzana, G. B.; Lombardi, A.; Mazzon, R.; Milone, L.; Visigalli, M.; Aime, S. Determination of Water Permeability of Paramagnetic Liposomes of Interest in MRI Field. *J. Inorg. Biochem.* **2008**, *102* (5–6), 1112–1119.
(57) Mulder, W. J. M.; Douma, K.; Koning, G. A.; van Zandvoort, M. A.; Lutgens, E.; Daemen, M. J.; Nicolay, K.; Strijkers, G. J. Liposome-Enhanced MRI of Neointimal Lesions in the ApoE-KO Mouse. *Magn. Reson. Med.* **2006**, *55* (5), 1170–1174.
(58) Maiseyeu, A.; Mihai, G.; Kampfrath, T.; Simonetti, O. P.; Sen, C. K.; Roy, S.; Rajagopalan, S.; Parthasarathy, S. Gadolinium-Containing Phosphatidylserine Liposomes for Molecular Imaging of Atherosclerosis. *J. Lipid Res.* **2009**, *50* (11), 2157–2163.
(59) Mulder, W. J. M.; Strijkers, G. J.; van Tilborg, G. A. F.; Griffioen, A. W.; Nicolay, K. Lipid-Based Nanoparticles for Contrast-Enhanced MRI and Molecular Imaging. *NMR Biomed.* **2006**, *19* (1), 142–164.
(60) Thaxton, C. S.; Rink, J. S.; Naha, P. C.; Cormode, D. P. Lipoproteins and Lipoprotein Mimetics for Imaging and Drug Delivery. *Adv. Drug Deliv. Rev.* **2016**, *106*, 116–131.
(61) Jackson, R. L.; Morrisett, J. D.; Gotto, A. M. Lipoprotein Structure and Metabolism. *Physiol. Rev.* **1976**, *56* (2), 259–316. https://doi.org/10.1152/physrev.1976.56.2.259.
(62) Prassl, R.; Laggner, P. Molecular Structure of Low Density Lipoprotein: Current Status and Future Challenges. *Eur. Biophys. J.* **2009**, *38* (2), 145–158.
(63) Prassl, R.; Laggner, P. Lipoprotein Structure and Dynamics: Low Density Lipoprotein Viewed as a Highly Dynamic and Flexible Nanoparticle. In *Lipoproteins - Role in Health and Diseases*; Kostner, G., Ed.; InTech, 2012.
(64) Kuai, R.; Li, D.; Chen, Y. E.; Moon, J. J.; Schwendeman, A. High-Density Lipoproteins: Nature's Multifunctional Nanoparticles. *ACS Nano* **2016**, *10* (3), 3015–3041.
(65) Bricarello, D. A.; Smilowitz, J. T.; Zivkovic, A. M.; German, J. B.; Parikh, A. N. Reconstituted Lipoprotein: A Versatile Class of Biologically-Inspired Nanostructures. *ACS Nano* **2011**, *5* (1), 42–57.
(66) Zhu, C.; Xia, Y. Biomimetics: Reconstitution of Low-Density Lipoprotein for Targeted Drug Delivery and Related Theranostic Applications. *Chem. Soc. Rev.* **2017**, *46* (24), 7668–7682.
(67) Maric, S.; Lind, T. K.; Raida, M. R.; Bengtsson, E.; Fredrikson, G. N.; Rogers, S.; Moulin, M.; Haertlein, M.; Forsyth, V. T.; Wenk, M. R.; et al. Time-Resolved Small-Angle Neutron Scattering as a Probe for the Dynamics of Lipid Exchange between Human Lipoproteins and Naturally Derived Membranes. *Sci. Rep.* **2019**, *9* (1), 1–14.

(68) Frias, J. C.; Lipinski, M. J.; Lipinski, S. E.; Albelda, M. T. Modified Lipoproteins as Contrast Agents for Imaging of Atherosclerosis. *Contrast Media Mol. Imaging* **2007**, *2* (1), 16–23.
(69) Frias, J. C.; Williams, K. J.; Fisher, E. A.; Fayad, Z. A. Recombinant HDL-Like Nanoparticles: A Specific Contrast Agent for MRI of Atherosclerotic Plaques. *J. Am. Chem. Soc.* **2004**, *126* (50), 16316–16317.
(70) Oppi, S.; Lüscher, T. F.; Stein, S. Mouse Models for Atherosclerosis Research—Which Is My Line? *Front. Cardiovasc. Med.* **2019**, *6*.
(71) Yamakoshi, Y.; Qiao, H.; Lowell, A. N.; Woods, M.; Paulose, B.; Nakao, Y.; Zhang, H.; Liu, T.; Lund-Katz, S.; Zhou, R. LDL-Based Nanoparticles for Contrast Enhanced MRI of Atheroplaques in Mouse Models. *Chem. Commun.* **2011**, *47* (31), 8835.
(72) Lowell, A. N.; Qiao, H.; Liu, T.; Ishikawa, T.; Zhang, H.; Oriana, S.; Wang, M.; Ricciotti, E.; FitzGerald, G. A.; Zhou, R.; et al. Functionalized Low-Density Lipoprotein Nanoparticles for in Vivo Enhancement of Atherosclerosis on Magnetic Resonance Images. *Bioconjug. Chem.* **2012**, *23* (11), 2313–2319.
(73) Corbin, I. R.; Zheng, G. Mimicking Nature's Nanocarrier: Synthetic Low-Density Lipoprotein-like Nanoparticles for Cancer-Drug Delivery. *Nanomed.* **2007**, *2* (3), 375–380.
(74) Navab, M.; Shechter, I.; Anantharamaiah, G. M.; Reddy, S. T.; Van Lenten, B. J.; Fogelman, A. M. Structure and Function of HDL Mimetics. *Arterioscler. Thromb. Vasc. Biol.* **2010**, *30* (2), 164–168.
(75) Cormode, D. P.; Briley-Saebo, K. C.; Mulder, W. J. M.; Aguinaldo, J. G. S.; Barazza, A.; Ma, Y.; Fisher, E. A.; Fayad, Z. A. An ApoA-I Mimetic Peptide High-Density-Lipoprotein-Based MRI Contrast Agent for Atherosclerotic Plaque Composition Detection. *Small* **2008**, *4* (9), 1437–1444.
(76) Cormode, D. P.; Skajaa, T.; van Schooneveld, M. M.; Koole, R.; Jarzyna, P.; Lobatto, M. E.; Calcagno, C.; Barazza, A.; Gordon, R. E.; Zanzonico, P.; et al. Nanocrystal Core High-Density Lipoproteins: A Multimodality Contrast Agent Platform. *Nano Lett.* **2008**, *8* (11), 3715–3723.
(77) Cormode, D. P.; Chandrasekar, R.; Delshad, A.; Briley-Saebo, K. C.; Calcagno, C.; Barazza, A.; Mulder, W. J. M.; Fisher, E. A.; Fayad, Z. A. Comparison of Synthetic High Density Lipoprotein (HDL) Contrast Agents for MR Imaging of Atherosclerosis. *Bioconjug. Chem.* **2009**, *20* (5), 937–943.
(78) Briley-Saebo, K. C.; Geninatti-Crich, S.; Cormode, D. P.; Barazza, A.; Mulder, W. J. M.; Chen, W.; Giovenzana, G. B.; Fisher, E. A.; Aime, S.; Fayad, Z. A. High-Relaxivity Gadolinium-Modified High-Density Lipoproteins as Magnetic Resonance Imaging Contrast Agents. *J. Phys. Chem. B* **2009**, *113* (18), 6283–6289.
(79) Skajaa, T.; Cormode, D. P.; Falk, E.; Mulder, W. J. M.; Fisher, E. A.; Fayad, Z. A. High-Density Lipoprotein–Based Contrast Agents for Multimodal Imaging of Atherosclerosis. *Arterioscler. Thromb. Vasc. Biol.* **2010**, *30* (2), 169–176.
(80) Sanchez-Gaytan, B. L.; Fay, F.; Lobatto, M. E.; Tang, J.; Ouimet, M.; Kim, Y.; van der Staay, S. E. M.; van Rijs, S. M.; Priem, B.; Zhang, L.; et al. HDL-Mimetic PLGA Nanoparticle To Target Atherosclerosis Plaque Macrophages. *Bioconjug. Chem.* **2015**, *26* (3), 443–451.
(81) Ginsburg, G. S.; Small, D. M.; Atkinson, D. Microemulsions of Phospholipids and Cholesterol Esters. Protein-Free Models of Low Density Lipoprotein. *J. Biol. Chem.* **1982**, *257* (14), 8216–8227.
(82) Owens, M. D.; Halbert, G. W. Production and Characterization of Protein-Free Analogues of Low Density Lipoprotein. *Eur. J. Pharm. Biopharm.* **1995**, *41* (2), 120–126.

(83) Owens, M. D.; Baillie, G.; Halbert, G. W. Physicochemical Properties of Microemulsion Analogues of Low Density Lipoprotein Containing Amphiphatic Apoprotein B Receptor Sequences. *Int. J. Pharm.* **2001**, *228* (1–2), 109–117.
(84) Lundberg, B.; Hong, K.; Papahadjopoulos, D. Conjugation of Apolipoprotein B with Liposomes and Targeting to Cells in Culture. *Biochim. Biophys. Acta BBA - Biomembr.* **1993**, *1149* (2), 305–312.
(85) Knott, T. J.; Pease, R. J.; Powell, L. M.; Wallis, S. C.; Rall, S. C.; Innerarity, T. L.; Blackhart, B.; Taylor, W. H.; Marcel, Y.; Milne, R.; et al. Complete Protein Sequence and Identification of Structural Domains of Human Apolipoprotein B. *Nature* **1986**, *323* (6090), 734–738.
(86) Yang, C.-Y.; Chen, S.-H.; Gianturco, S. H.; Bradley, W. A.; Sparrow, J. T.; Tanimura, M.; Li, W.-H.; Sparrow, D. A.; DeLoof, H.; Rosseneu, M.; et al. Sequence, Structure, Receptor-Binding Domains and Internal Repeats of Human Apolipoprotein B-100. *Nature* **1986**, *323* (6090), 738–742.
(87) Baillie, G.; Owens, M. D.; Halbert, G. W. A Synthetic Low Density Lipoprotein Particle Capable of Supporting U937 Proliferation in Vitro. *J. Lipid. Res.* **2002**, *43*, 69-73.
(88) Hayavi, S.; Halbert, G. W. Synthetic Low-Density Lipoprotein, a Novel Biomimetic Lipid Supplement for Serum-Free Tissue Culture. *Biotechnol. Prog.* **2005**, *21* (4), 1262–1268.
(89) Hayavi, S.; Baillie, G.; Owens, M. D.; Halbert, G. W. Receptor Dependent Cellular Uptake of Synthetic Low Density Lipoprotein by Mammalian Cells in Serum-Free Tissue Culture. *J. Pharm. Pharmacol.* **2006**, *58* (10), 1337–1342.
(90) Nikanjam, M.; Blakely, E. A.; Bjornstad, K. A.; Shu, X.; Budinger, T. F.; Forte, T. M. Synthetic Nano-Low Density Lipoprotein as Targeted Drug Delivery Vehicle for Glioblastoma Multiforme. *Int. J. Pharm.* **2007**, *328* (1), 86–94.
(91) Nikanjam, M.; Gibbs, A. R.; Hunt, C. A.; Budinger, T. F.; Forte, T. M. Synthetic Nano-LDL with Paclitaxel Oleate as a Targeted Drug Delivery Vehicle for Glioblastoma Multiforme. *J. Controlled Release* **2007**, *124* (3), 163–171.
(92) García-Pinel, B.; Porras-Alcalá, C.; Ortega-Rodríguez, A.; Sarabia, F.; Prados, J.; Melguizo, C.; López-Romero, J. M. Lipid-Based Nanoparticles: Application and Recent Advances in Cancer Treatment. *Nanomaterials* **2019**, *9* (4).
(93) Alexis, F.; Pridgen, E.; Molnar, L. K.; Farokhzad, O. C. Factors Affecting the Clearance and Biodistribution of Polymeric Nanoparticles. *Mol. Pharm.* **2008**, *5* (4), 505–515.
(94) Weingart, J.; Vabbilisetty, P.; Sun, X.-L. Membrane Mimetic Surface Functionalization of Nanoparticles: Methods and Applications. *Adv. Colloid Interface Sci.* **2013**, *0*, 68–84.
(95) Doane, T.; Burda, C. Nanoparticle Mediated Non-Covalent Drug Delivery. *Adv. Drug Deliv. Rev.* **2013**, *65* (5), 607–621.
(96) Lynch, I.; Dawson, K. A. Protein-Nanoparticle Interactions. *Nano Today* **2008**, *3* (1), 40–47.
(97) Nair, D. P.; Podgórski, M.; Chatani, S.; Gong, T.; Xi, W.; Fenoli, C. R.; Bowman, C. N. The Thiol-Michael Addition Click Reaction: A Powerful and Widely Used Tool in Materials Chemistry. *Chem. Mater.* **2014**, *26* (1), 724–744.
(98) Li, N.; Binder, W. H. Click-Chemistry for Nanoparticle-Modification. *J. Mater. Chem.* **2011**, *21* (42), 16717.
(99) Lallana, E.; Fernandez-Megia, E.; Riguera, R. Surpassing the Use of Copper in the Click Functionalization of Polymeric Nanostructures: A Strain-Promoted Approach. *J. Am. Chem. Soc.* **2009**, *131* (16), 5748–5750.
(100) Saito, F.; Noda, H.; Bode, J. W. Critical Evaluation and Rate Constants of Chemoselective Ligation Reactions for Stoichiometric Conjugations in Water. *ACS Chem. Biol.* **2015**, *10* (4), 1026–1033.

(101) Kim, Y.; Ho, S. O.; Gassman, N. R.; Korlann, Y.; Landorf, E. V.; Collart, F. R.; Weiss, S. Efficient Site-Specific Labeling of Proteins via Cysteines. *Bioconjug. Chem.* **2008**, *19* (3), 786–791.
(102) Lainson, J. C.; Fuenmayor, M. F.; Johnston, S. A.; Diehnelt, C. W. Conjugation Approach To Produce a Staphylococcus Aureus Synbody with Activity in Serum. *Bioconjug. Chem.* **2015**, *26* (10), 2125–2132.
(103) Rostovtsev, V. V.; Green, L. G.; Fokin, V. V.; Sharpless, K. B. A Stepwise Huisgen Cycloaddition Process: Copper(I)-Catalyzed Regioselective "Ligation" of Azides and Terminal Alkynes. *Angew. Chem. Int. Ed.* **2002**, *41* (14), 2596–2599.
(104) Tornøe, C. W.; Christensen, C.; Meldal, M. Peptidotriazoles on Solid Phase: [1,2,3]-Triazoles by Regiospecific Copper(I)-Catalyzed 1,3-Dipolar Cycloadditions of Terminal Alkynes to Azides. *J. Org. Chem.* **2002**, *67* (9), 3057–3064.
(105) Ayouchia, H. B. E.; Bahsis, L.; Anane, H.; R. Domingo, L.; Stiriba, S.-E. Understanding the Mechanism and Regioselectivity of the Copper(i) Catalyzed [3 + 2] Cycloaddition Reaction between Azide and Alkyne: A Systematic DFT Study. *RSC Adv.* **2018**, *8* (14), 7670–7678.
(106) Shieh, P.; Bertozzi, C. R. Design Strategies for Bioorthogonal Smart Probes. *Org Biomol Chem* **2014**, *12* (46), 9307–9320.
(107) Wolbers, F.; Braak, P. ter; Gac, S. L.; Luttge, R.; Andersson, H.; Vermes, I.; Berg, A. van den. Viability Study of HL60 Cells in Contact with Commonly Used Microchip Materials. *ELECTROPHORESIS* **2006**, *27* (24), 5073–5080.
(108) Hong, V.; Steinmetz, N. F.; Manchester, M.; Finn, M. G. Labeling Live Cells by Copper-Catalyzed Alkyne−Azide Click Chemistry. *Bioconjug. Chem.* **2010**, *21* (10), 1912–1916.
(109) Agard, N. J.; Prescher, J. A.; Bertozzi, C. R. A Strain-Promoted [3 + 2] Azide−Alkyne Cycloaddition for Covalent Modification of Biomolecules in Living Systems. *J. Am. Chem. Soc.* **2004**, *126* (46), 15046–15047.
(110) Beatty, K. E.; Fisk, J. D.; Smart, B. P.; Lu, Y. Y.; Szychowski, J.; Hangauer, M. J.; Baskin, J. M.; Bertozzi, C. R.; Tirrell, D. A. Live-Cell Imaging of Cellular Proteins by a Strain-Promoted Azide–Alkyne Cycloaddition. *ChemBioChem* **2010**, *11* (15), 2092–2095.
(111) Pattabiraman, V. R.; Bode, J. W. Rethinking Amide Bond Synthesis. *Nature* **2011**, *480* (7378), 471–479.
(112) Bode, J. W.; Fox, R. M.; Baucom, K. D. Chemoselective Amide Ligations by Decarboxylative Condensations of N-Alkylhydroxylamines and α-Ketoacids. *Angew. Chem. Int. Ed.* **2006**, *45* (8), 1248–1252.
(113) Harmand, T. J.; Murar, C. E.; Bode, J. W. Protein Chemical Synthesis by α-Ketoacid–Hydroxylamine Ligation. *Nat. Protoc.* **2016**, *11* (6), 1130–1147.
(114) Bode, J. W. Chemical Protein Synthesis with the α-Ketoacid–Hydroxylamine Ligation. *Acc. Chem. Res.* **2017**, *50* (9), 2104–2115.
(115) Dumas, A. M.; Molander, G. A.; Bode, J. W. Amide-Forming Ligation of Acyltrifluoroborates and Hydroxylamines in Water. *Angew. Chem. Int. Ed.* **2012**, *51* (23), 5683–5686.
(116) Mazunin, D.; Broguiere, N.; Zenobi-Wong, M.; Bode, J. W. Synthesis of Biocompatible PEG Hydrogels by PH-Sensitive Potassium Acyltrifluoroborate (KAT) Amide Ligations. *ACS Biomater. Sci. Eng.* **2015**, *1* (6), 456–462.
(117) Noda, H.; Erős, G.; Bode, J. W. Rapid Ligations with Equimolar Reactants in Water with the Potassium Acyltrifluoroborate (KAT) Amide Formation. *J. Am. Chem. Soc.* **2014**, *136* (15), 5611–5614.

(118) White, C. J.; Bode, J. W. PEGylation and Dimerization of Expressed Proteins under Near Equimolar Conditions with Potassium 2-Pyridyl Acyltrifluoroborates. *ACS Cent. Sci.* **2018**, *4* (2), 197–206.
(119) Mazunin, D.; Bode, J. W. Potassium Acyltrifluoroborate (KAT) Ligations Are Orthogonal to Thiol- *Michael* and SPAAC Reactions: Covalent Dual Immobilization of Proteins onto Synthetic PEG Hydrogels. *Helv. Chim. Acta* **2017**, *100* (2), e1600311.
(120) Molander, G. A.; Raushel, J.; Ellis, N. M. Synthesis of an Acyltrifluoroborate and Its Fusion with Azides To Form Amides. *J. Org. Chem.* **2010**, *75* (12), 4304–4306.
(121) Dumas, A. M.; Bode, J. W. Synthesis of Acyltrifluoroborates. *Org. Lett.* **2012**, *14* (8), 2138–2141.
(122) Katritzky, A. R.; Lang, H.; Wang, Z.; Zhang, Z.; Song, H. Benzotriazole-Mediated Conversions of Aromatic and Heteroaromatic Aldehydes to Functionalized Ketones. *J. Org. Chem.* **1995**, *60* (23), 7619–7624.
(123) Katritzky, A. R.; Lang, H.; Wang, Z.; Lie, Z. Convenient Syntheses of Functionalized Dialkyl Ketones and Alkanoylsilanes: 1-(Benzotriazol-1-Yl)-1-Phenoxyalkanes as Alkanoyl Anion Equivalents. *J. Org. Chem.* **1996**, *61* (21), 7551–7557.
(124) Erős, G.; Kushida, Y.; Bode, J. W. A Reagent for the One-Step Preparation of Potassium Acyltrifluoroborates (KATs) from Aryl- and Heteroarylhalides. *Angew. Chem. Int. Ed.* **2014**, *53* (29), 7604–7607.
(125) Liu, S. M.; Wu, D.; Bode, J. W. One-Step Synthesis of Aliphatic Potassium Acyltrifluoroborates (KATs) from Organocuprates. *Org. Lett.* **2018**, *20* (8), 2378–2381.
(126) Oriana, S.; Fracassi, A.; Archer, C.; Yamakoshi, Y. Covalent Surface Modification of Lipid Nanoparticles by Rapid Potassium Acyltrifluoroborate Amide Ligation. *Langmuir* **2018**, *34* (44), 13244–13251.
(127) Cardenas-Benitez, B.; Djordjevic, I.; Hosseini, S.; Madou, M. J.; Martinez-Chapa, S. O. Review—Covalent Functionalization of Carbon Nanomaterials for Biosensor Applications: An Update. *J. Electrochem. Soc.* **2018**, *165* (3), B103–B117.
(128) Katritzky, A. R.; Kirichenko, K. Acyl Anion Synthons: Benzotriazole Stabilized Compared to Classical. *Arkivoc* **2006**, *4*, 119–151.
(129) Forte, G. M.; Nichols, A. V.; Glaeser, R. M. Electron Microscopy of Human Serum Lipoproteins Using Negative Staining. *Chem. Phys. Lipids* **1968**, *2* (4), 396–408.
(130) Bello, V.; Mattei, G.; Mazzoldi, P.; Vivenza, N.; Gasco, P.; Idee, J. M.; Robic, C.; Borsella, E. Transmission Electron Microscopy of Lipid Vesicles for Drug Delivery: Comparison between Positive and Negative Staining. *Microsc. Microanal.* **2010**, *16* (4), 456–461.
(131) Forte, T. M.; Nordhausen, R. W. [26] Electron Microscopy of Negatively Stained Lipoproteins. In *Methods in Enzymology*; Plasma Lipoproteins Part A: Preparation, Structure, and Molecular Biology; Academic Press, 1986; Vol. 128, pp 442–457.
(132) Friedrich, H.; Frederik, P. M.; de With, G.; Sommerdijk, N. A. J. M. Imaging of Self-Assembled Structures: Interpretation of TEM and Cryo-TEM Images. *Angew. Chem. Int. Ed.* **2010**, *49* (43), 7850–7858.
(133) Boren, J.; Lee, I.; Zhu, W.; Arnold, K.; Taylor, S.; Innerarity, T. L. Identification of the Low Density Lipoprotein Receptor-Binding Site in Apolipoprotein B100 and the Modulation of Its Binding Activity by the Carboxyl Terminus in Familial Defective Apo-B100. *J. Clin. Invest.* **1998**, *101* (5), 1084–1093.
(134) Ulman, A. Formation and Structure of Self-Assembled Monolayers. *Chem. Rev.* **1996**, *96* (4), 1533–1554.
(135) Love, J. C.; Estroff, L. A.; Kriebel, J. K.; Nuzzo, R. G.; Whitesides, G. M. Self-Assembled Monolayers of Thiolates on Metals as a Form of Nanotechnology. *Chem. Rev.* **2005**, *105* (4), 1103–1170.

(136) Devaraj, N. K.; Miller, G. P.; Ebina, W.; Kakaradov, B.; Collman, J. P.; Kool, E. T.; Chidsey, C. E. D. Chemoselective Covalent Coupling of Oligonucleotide Probes to Self-Assembled Monolayers. *J. Am. Chem. Soc.* **2005**, *127* (24), 8600–8601.
(137) Jewell, A. D.; Kyran, S. J.; Rabinovich, D.; Sykes, E. C. H. Effect of Head-Group Chemistry on Surface-Mediated Molecular Self-Assembly. *Chem. – Eur. J.* **2012**, *18* (23), 7169–7178.
(138) Ishida, T.; Hara, M.; Kojima, I.; Tsuneda, S.; Nishida, N.; Sasabe, H.; Knoll, W. High Resolution X-Ray Photoelectron Spectroscopy Measurements of Octadecanethiol Self-Assembled Monolayers on Au(111). *Langmuir* **1998**, *14* (8), 2092–2096.
(139) Porter, M. D.; Bright, T. B.; Allara, D. L.; Chidsey, C. E. D. Spontaneously Organized Molecular Assemblies. 4. Structural Characterization of n-Alkyl Thiol Monolayers on Gold by Optical Ellipsometry, Infrared Spectroscopy, and Electrochemistry. *J. Am. Chem. Soc.* **1987**, *109* (12), 3559–3568.
(140) McCrackin, F. L.; Passaglia, E.; Stromberg, R. R.; Steinberg, H. L. Measurement of the Thickness and Refractive Index of Very Thin Films and the Optical Properties of Surfaces by Ellipsometry.
(141) Marx, K. A. Quartz Crystal Microbalance: A Useful Tool for Studying Thin Polymer Films and Complex Biomolecular Systems at the Solution−Surface Interface. *Biomacromolecules* **2003**, *4* (5), 1099–1120.
(142) Sha, X.; Sun, C.; Xu, X.; Alexander, L.; Loll, P. J.; Penn, L. S. Quartz Crystal Microbalance (QCM): Useful for Developing Procedures for Immobilization of Proteins on Solid Surfaces. *Anal. Chem.* **2012**, *84* (23), 10298–10305.
(143) Aufray, M.; Roche, A. A. Is Gold Always Chemically Passive? *Appl. Surf. Sci.* **2008**, *254* (7), 1936–1941.
(144) Shiro, T.; Schuhmacher, A.; Jackl, M. K.; Bode, J. W. Facile Synthesis of α-Aminoboronic Acids from Amines and Potassium Acyltrifluoroborates (KATs) via Trifluoroborate-Iminiums (TIMs). *Chem. Sci.* **2018**, *9* (23), 5191–5196.
(145) Kurnik, M.; Ortega, G.; Dauphin-Ducharme, P.; Li, H.; Caceres, A.; Plaxco, K. W. Quantitative Measurements of Protein−surface Interaction Thermodynamics. *Proc. Natl. Acad. Sci.* **2018**, *115* (33), 8352–8357.